Università degli Studi di Palermo

AREA QUALITÀ, PROGRAMMAZIONE E SUPPORTO STRATEGICO
SETTORE STRATEGIA PER LA RICERCA
U. O. DOTTORATI

Dottorato di Ricerca in Scienze Fisiche e Chimiche
Dipartimento di Fisica e Chimica - Emilio Segrè
CHEM-03/A

ATOMIC AND ELECTRONIC STRUCTURE OF LEAD-FREE HALIDE PEROVSKITES PROBED WITH X-RAY ABSORPTION SPECTROSCOPY

IL DOTTORE
SIMONE VIRGA

IL COORDINATORE
MARCO CANNAS

IL TUTOR
FRANCESCO GIANNICI

IL CO TUTOR
ALESSANDRO LONGO

CICLO XXXVIII
ANNO CONSEGUIMENTO TITOLO 2026

Table of Contents

Table of Contents

List of Abbreviations

AFM	Atomic Force Microscopy
AZ	Aziridinium
BA	Butylammonium
BSv	Base Solvent
BzCl	Benzoyl Chloride
CB	Conduction Band
CBM	Conduction Band Minimum
CPE	Constant Phase Element
DFT	Density Functional Theory
DMA	Dimethylammonium
DMF	Dimethylformamide
DOS	Density of States
EBS	Extremely Brilliant Source
EIS	Electrochemical Impedance Spectroscopy
ESRF	European Synchrotron Radiation Facility
EXAFS	Extended X-ray Absorption Fine Structure
FA	Formamidinium
FAPI	$(FA)PbI_3$
FDM	Finite Difference Method
FEAI	1-trifluoro-ethyl ammonium iodide
GA	Guanidinium
GGA	Generalized Gradient Approximation
HDP	Halide Double Perovskite
HERFD	High Energy Resolution Fluorescence Detection
HI	Hot Injection
HP	Halide Perovskite
i-PA	isopropylammonium
ICP-OES	Inductively Coupled Plasma-Optical Emission Spectroscopy
ITO	Indium Tin Oxide
LARP	Ligand-Assisted Reprecipitation
LCD	Liquid Crystal Display

List of Abbreviations

LDA	Local Density Approximation
LED	Light Emitting Diode
LHP	Lead Halide Perovskite
LMCT	Ligand-to-Metal Charge Transfer
MA	Methylammonium
MAPBr	$(MA)PbBr_3$
MAPCl	$(MA)PbCl_3$
MAPI	$(MA)PbI_3$
MMCT	Metal-to-Metal Charge Transfer
MST	Multiple Scattering Theory
NC	Nanocrystal
NIR	Near-Infrared
OA	Oleic Acid
OAc	Acetate
ODE	1-Octadecene
OLAM	Oleylamine
OHP	Organic Halide Perovskite
OLHP	Organic Lead Halide Perovskite
PAW	Projector Augmented Wave
PBE	Perdew-Burke-Ernzerhof
PCE	Power Conversion Efficiency
pDOS	projected Density of States
PEA	Phenylethyl Ammonium
PEAI	$((PEA)_2(MA)_2)Pb_3I_{10}$
PET	Polyethylene Terephthalate
PLQY	Photoluminescence Quantum Yield
PSC	Perovskite Solar Cell
QLED	Quantum dot Light Emitting Diode
RIXS	Resonant Inelastic X-ray Scattering
SEM	Scanning Electron Microscopy
SOC	Spin-Orbit Coupling
STE	Self-Trapped Exciton
TEM	Transmission Electron Microscopy

List of Abbreviations

TMSCl	Trimethylsilyl Chloride
TMSO	Trimethylsulfoxonium
TZ	1,2,4-triazolium
UPS	Ultraviolet Photoelectron Spectroscopy
VB	Valence Band
VBM	Valence Band Maximum
XANES	X-ray Absorption Near Edge Structure
XAS	X-ray Spectroscopy
XRD	X-ray Diffraction
XRF	X-ray Fluorescence

1. Introduction

Partially adapted with permission from Coord. Chem. Rev. ***2026****, 552, 217470. Copyright 2026 Elsevier.*

1.1. Aim and Motivation

The increasing demand for energy is one of the major global challenges that modern societies need to address in the near future. The intensive use of fossil fuels has characterized technological development since the industrial revolution, ultimately leading to global climate imbalances and widespread environmental pollution.[1] The design and synthesis of new functional materials for renewable energy production, capable of promoting sustainable development and mitigating both greenhouse gas emissions and the use of fossil fuels, is therefore a central focus in the current research landscape at the intersection of chemistry, physics, and materials engineering.[2] However, despite the many positive achievements, energy from renewable sources still does not meet global demand.

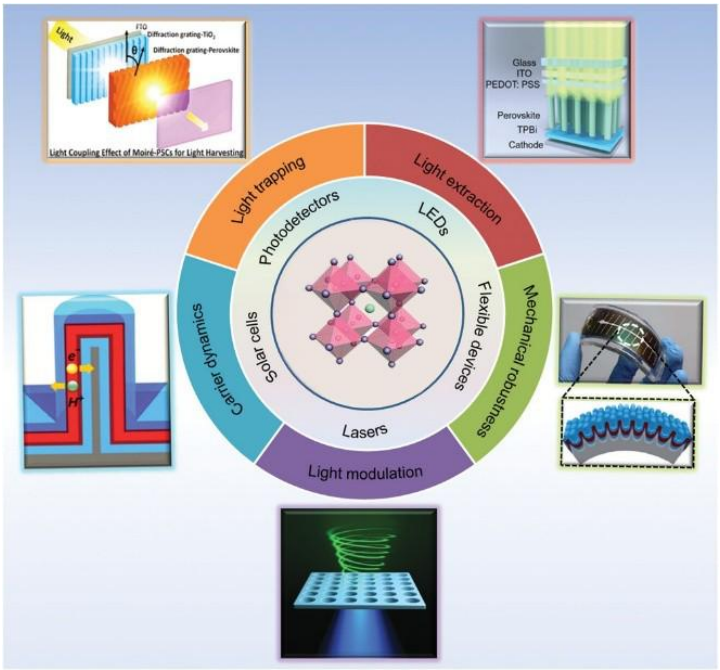

Figure 1.1. Examples of several applications of HPs in optoelectronic devices. Figure adapted from ref. [3], with permission from Wiley-VCH GmbH, Copyright 2022.

Semiconductors have been at the forefront of research in materials chemistry and engineering for decades, resulting in tailor-made materials with a broad diversity of light-matter interactions, and allowing remarkable progress. Materials with strong visible light absorption and good electrical properties can be employed in a variety of technologies besides photovoltaic devices (**Figure 1.1**), such as LEDs, flexible substrates for sensors, and microelectronics in general.[4,5] Advanced optoelectronic materials can modulate radiation emission and absorption in response to an applied electric field, thereby converting electrical energy into light and vice versa. All the aforementioned devices rely on semiconductors whose electrical properties can be enhanced by modifying their composition, structure, and size. Such modifications of existing semiconductors can lead to the creation of optimal materials for optoelectronic devices and expand their applicability to other technologies.

Over the years, research in materials chemistry has examined a wide range of semiconductors, typically inorganic and based on elements from groups III–IV–V of the periodic table. However, the reliance on scarce, expensive, and environmentally impactful elements has recently driven research toward more cost-effective, sustainable, and mechanically flexible alternatives, fostering the development of organic electronics.[4] Among the various semiconductors studied and designed over the past two decades, halides with a perovskite structure, ionic crystalline semiconductors composed of metal-halide anionic octahedra, have attracted increasing interest due to their promising electrical properties. In particular, fully inorganic and hybrid organic–inorganic lead-based halide perovskites, such as MAPI, represent some of the most studied systems in recent materials chemistry research, owing to their excellent optoelectronic properties and rich crystal chemistry.[6–10] Among these, strong optical absorption, relatively high carrier mobility, highly tunable bandgaps and high photoluminescence quantum yields,[9,11–17] make these materials promising candidates to replace traditional semiconductors in the fabrication of high-efficiency optoelectronic devices. Solar cell materials is one field in particular that LHPs have already impacted in depth, due to their steadily increasing efficiencies.[18–20] The combination of strong optical absorption and easily tunable bandgap, which can be precisely controlled over a wide range through compositional engineering, has enabled their application in specialized scenarios such as building-integrated photovoltaics.[21,22] The tunable bandgap and high photoluminescence quantum yields have further extended the applicability of LHPs to light-emitting devices. These materials can emit light across the entire visible spectrum and into the near-ultraviolet, enabling their use in LEDs,[23,24] lasers,[25] and displays.[26,27] The high

absorption coefficient and charge carrier mobility also make these materials promising for photodetectors,[28,29] as well as for X-ray and gamma-sensors,[30,31] where efficient photon-to-charge conversion and rapid photoresponse are critical. However, the poor air stability of the best performing LHPs and the high toxicity of lead hinder their large-scale implementation.[32–35]

The main purpose of this work is to explore and develop chemical strategies aimed at overcoming the intrinsic limitations of LHPs, following several different approaches. The first approach involved the substitution of the organic amines with TMSO, to improve the stability of lead-based perovskites. Afterwards, different strategies were pursued to replace lead. The substitution was first done using Sn(II), and then with a heterovalent approach, substituting divalent lead with monovalent (Ag^+, Na^+, and K^+) and trivalent (Bi^{3+} and In^{3+}) cations to obtain double perovskites. In addition, Cu^+ and Sb^{3+} were also used in an attempt to synthesize the double perovskite $Cs_2CuSbCl_6$, following the method recently reported by Zhou et al.,[36] to explain its very peculiar optical absorption spectrum. After design, synthesis and laboratory characterization, all the materials studied in this thesis, either bulk or nanoscale, were investigated using synchrotron-based techniques, with a particular focus on XAS, which represents an ideal complement to diffraction methods and enables detailed knowledge of the local structure around each cation. This line of investigation first started because despite the growing interest in halide perovskites, the application of XAS to these systems has so far remained relatively limited and with variable degrees of success. Core-level spectroscopies, such as XAS, provide fundamentally different insights compared to ones that focus on valence electrons, such as photoelectron spectroscopy (UPS or XPS). While the latter offer direct information on empty states near the bandgap, and localized at the surface, XAS enables bulk-averaged information to be obtained, making it an essential tool for the study of materials containing different cations, such as these. In the last years, XANES, potentially combined with HERFD-XANES, has proven to be a particularly powerful technique for assessing the local structure of metal halides with different compositions and dimensionality, effectively complementing conventional diffraction and electron microscopy techniques. Although X-ray spectroscopic methods now well-established tools in the study of chalcogenides and are routinely applied in areas such as heterogeneous catalysis or metallobiology, their application to halide perovskites has still remained somewhat limited until recently. Only in the past few years, studies specifically devoted XANES spectra of halide perovskites and lower-dimensional pseudo-perovskites have appeared. In particular, Pipitone et al. combined DFT calculations

with XAS experiments to understand the Bi^{3+} doping mechanism in one-dimensional lead iodide pseudo-perovskites containing the TMSO organic cation. The results confirmed that Pb^{2+} vacancies are indeed the primary ionic charge-compensation mechanism when it is replaced by bismuth.[37] Gardner and co-workers reported HERFD-XANES and RIXS spectra of MAPI, Cs_3Bi2I_9, $APbI_4$, and APb_2I_6: respectively, a 3D perovskite, two 2D edge-sharing layered pseudo-perovskites, and a 1D face-sharing pseudo-perovskite.[38–40] Smith et al. employed *in situ* XANES measurements to monitor the oxidation of Sn(II) to Sn(IV) in formamidinium-based thin films.[41] Vorwerk et al. applied many-body perturbation theory to assess the excitonic binding energy of core-holes at the low-energy I L_3-edge and Pb M_5-edge in MAPI, observing that the main spectral features are essentially determined by the inorganic Pb−I framework, as evidenced by comparison with PbI_2.[42] Drisdell et al. performed *ab initio* modeling of the metal HERFD-XANES spectra by constructing a statistical ensemble of snapshots of the MAPI/MAPBr structure through *ab initio* molecular dynamics. Their investigation showed that I/Br atoms are randomly distributed in MAPI/MAPBr solid solutions and that the spectra are highly sensitive to Pb−halide distances and octahedral tilting, while thermal motions dominate the energetically preferred structural conformations.[43]

The next sections of the introduction briefly outline the structure, properties, and applications of halide perovskites. The X-ray spectroscopic methods and their simulations are described in Chapter 2. Then, the discussion follows four published papers (forming the basis of chapters 3-6), plus one in preparation (integrated in Chapter 5). The state of the art on each specific theme is presented at the beginning of each chapter. These case studies, taken together, show how the combination of core X-ray spectroscopies and their simulations can provide a thorough understanding of the finer details of the atomic and electronic structure in halide perovskites.

1.2. Optoelectronic Properties of Semiconductors

Semiconductors with a wide range of light-response and electrical properties can be employed in various technologies, including photovoltaic devices, LEDs, flexible substrates for sensors, and microelectronics in general.[5] These materials can modulate the emission and absorption of radiation as a function of the applied electric field, thereby converting electrical energy into light radiation and vice versa. The design and synthesis of new functional materials in this field, capable of precisely tuning electronic and optical properties, is therefore central in current research, and is required for the development of more efficient and versatile devices, contributing to sustainable technological advancement. All the aforementioned devices rely on semiconductors whose electrical properties can be tuned through rational modification of their composition, structure, and also their grain size if in the sub-micrometer range, possibly expanding their applicability to other technologies. The two most established fields of application in optoelectronics are currently photovoltaic cells and LEDs. The former directly convert solar light into electrical energy and represent a potentially unlimited and emission-free energy source (**Figure 1.2a**). Photovoltaics undoubtedly represent a viable alternative to conventional energy sources, thanks to reduced emissions and the increasing competitiveness of costs. However, despite these advantages, the sector is not totally sustainable yet: significant challenges remain regarding material recovery, the management of the panels life cycle, and the overall environmental impact of the systems. Looking forward, it is essential to continue developing and optimizing recycling processes, enhance the efficiency of renewable materials, and conduct comprehensive life cycle assessments. By integrating these sustainable practices, the solar energy industry can further improve its environmental performance, ensuring that photovoltaic systems contribute to a cleaner and more sustainable future.[44,45] LEDs have been widely adopted for decades in various applications, including television, smartphone, and computer displays, and in the replacement of traditional lighting technologies. Their use is particularly helpful due to their superior efficiency and the ability to produce light with tunable spectral characteristics compared to incandescent and fluorescent bulbs.[46] LED devices, which convert electrical energy into visible light, consist of two semiconductors, p-type and n-type. Under the applied electric field, charge carriers move, meet, and recombine radiatively at the junction (**Figure 1.2b**).

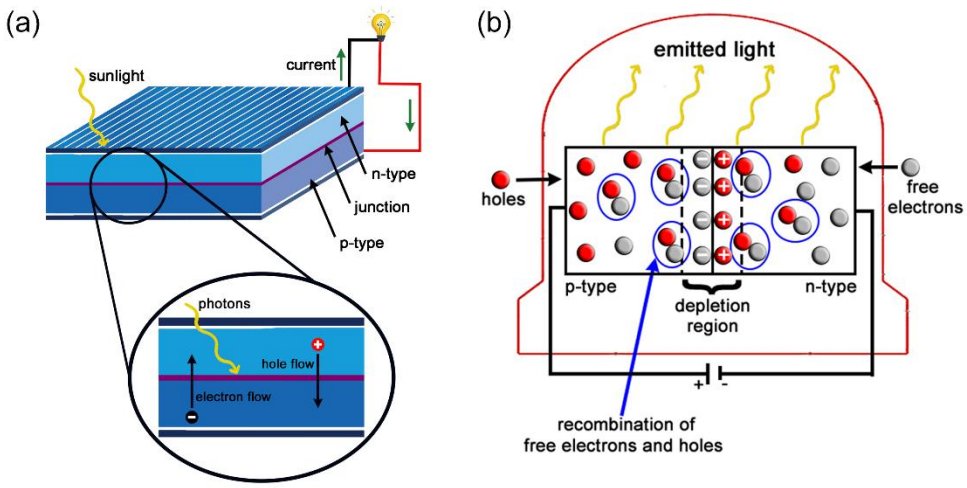

Figure 1.2. (a) In a photovoltaic cell, radiation striking a junction between semiconductors creates an electron-hole pair that is then separated and flows into an external circuit. (b) Light emission in an LED through radiative recombination of charges.

The spectrum of the emitted light depends on the electronic structure of the semiconductors, commonly described in terms of the energy gap between electronic levels, or band gap.[47] The main requirements for an efficient LED material are: 1) a direct bandgap in the range of approximately 1.6-3.2 eV; 2) low electrical resistivity; 3) efficient electronic transitions that do not involve interactions with lattice phonons; and 4) ease of material processing, such as the formation of a film or a pellet within a complete device. Conversely, devices that convert optical signals into electronic processes rely on materials that absorb radiation, generating electron-hole pairs which subsequently diffuse separately under the influence of an electric field, thus ideally reversing the operating principle described for LEDs. Typical examples include photodetectors and photovoltaic devices. Their performance depends on both the efficiency of electron-hole pair generation and the rate of charge-carrier separation.[46,48] Among the applications of semiconductors in sustainable energy production, thermoelectric devices occupy a particularly interesting niche not addressed by other technologies. In fact, they can exploit virtually any form of waste heat generated by various activities (such as body heat in wearable devices), even at low temperatures, and convert it into electricity.[49] A thermoelectric device consists of a pair of semiconductors arranged in parallel, with high electrical conductivity and low thermal conductivity, possessing positive and negative charge carriers, p- and n-type, respectively (**Figure 1.3**).

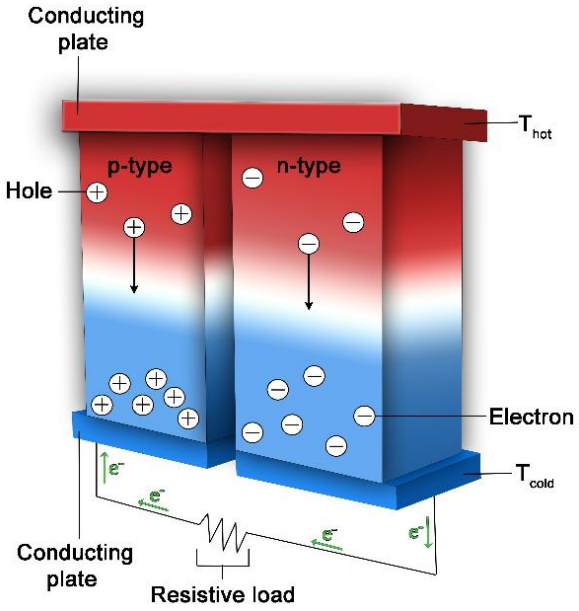

Figure 1.3. A thermoelectric device with two p- and n-semiconductors in parallel under a temperature gradient (blue to red). The semiconductors are connected at one side, while an electrical load closes the circuit at the other side.

When a temperature gradient is applied across the two materials, an electric field is generated. High electrical conductivity is required to minimize Joule heating, while low thermal conductivity is essential to maintain the temperature gradient across the device. These parameters, within a single material, must be optimized through various strategies such as doping, compositional tuning, and modification of structure and size.[2,49,50] To date, one of the fundamental limitations of thermoelectric materials lies in their ability to achieve high performance only at elevated temperatures, which restricts their use in room-temperature applications such as Peltier cells for small-scale refrigerations.[49] Precisely because of these limitations, research has progressively shifted toward other semiconductors and devices, capable of combining favorable electronic and optical properties with greater versatility and sustainability. Among these, HPs have recently attracted increasing attention due to their excellent optoelectronic properties, compositional tunability, and ease of synthesis, making them highly attractive for a broad range of optoelectronic applications.[3]

1.3. Halide Perovskites and Related Structures

HPs, particularly lead-based ones, as previously introduced, display remarkable optoelectronic properties, such as strong optical absorption, relatively high carrier mobility, long carrier diffusion lengths, low effective masses, tunable bandgaps, and considerable defect tolerance, featuring low-cost and straightforward processing.[9,11–17] These unique features have enabled rapid progress in the fabrication of high-performance devices, achieving impressive conversion efficiencies in solar cells (surpassing even those of single-crystal and polycrystalline silicon),[18–20,51,52] as well as in photodetectors,[29,53] X-rays, and gamma-sensors.[23,30,31,54] In their nanocrystalline form, HPs further benefit from quantum confinement effects and intrinsic band gap tunability, resulting in extremely narrow emission linewidths.[9,12,55–58] These features have facilitated their integration into advanced optoelectronic applications, including LCD television displays,[59–62] LEDs,[9,12,63–65] and lasers.[25,66–68] The prototype HP structure follows the general formula ABX_3, constructed from an almost-close packing of X anions, with metal cations occupying the A and B sites. The B-site hosts small cations with valence states ranging from +2 to +4, coordinated by six halides (X = Cl^-, Br^-, I^- and, more rarely, F^-) to form a three-dimensional framework of corner-sharing $[BX_6]^{4-}$ octahedra. The A-site cation sits in the cuboctahedral cavities and compensates charge (**Figure 1.4**).[69]

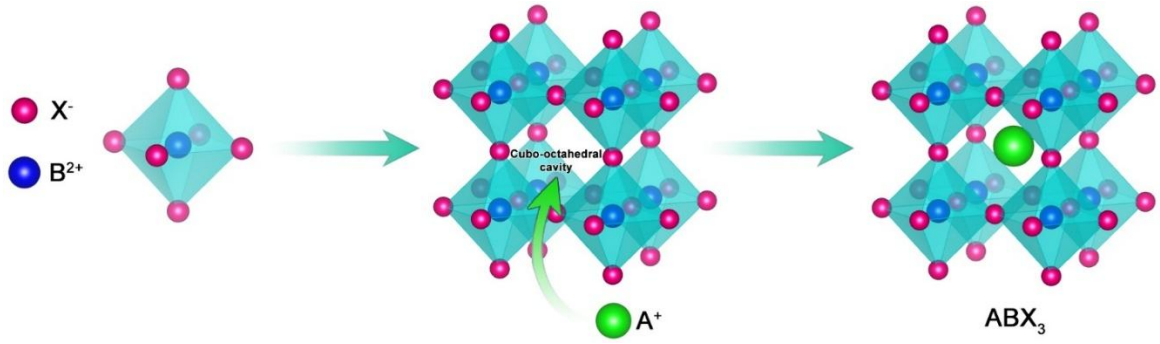

Figure 1.4. Schematic illustration of the cubic halide perovskite, and how it is built from simpler structural elements.

The structure got its name from the Russian mineralogist Lev Perovski, in honor of whom calcium titanate ($CaTiO_3$), the first representative of this structural family, was named. However, HPs, such as $CsPbX_3$, $RbPbX_3$ and $(CH_3NH_3)PbX_3$ (X = Cl^-, Br^-, I^-), were also

described very early in the literature (around 1890), following a comprehensive study on the synthesis of lead halide compounds from solutions including lead halides and cesium.[70–72] As with oxide perovskites, the structural stability of a perovskite-type phase for a given combination of cations and anions can be expressed by the Goldschmidt tolerance factor (t),[69] which defines the symmetry and stability of the structure. The tolerance factor accounts for variations in cation size and defines a general criterion for the formation of a perovskite-type phase. It is defined as:

$$t = \frac{(R_A + R_X)}{\sqrt{2}(R_B + R_X)} \qquad (1.1)$$

Where R_A, R_B and R_X are the ionic radii of the A and B cations and the X anion, respectively. Perovskites can crystallize in several possible symmetries, from cubic to triclinic. When the tolerance factor t is close to 1, the perovskite phase crystallizes in a cubic structure with the highest symmetry (space group: *Pm-3m*). When the A ion is smaller than the ideal value, the tolerance factor becomes less than 1, corresponding to a lower symmetry (e.g., orthorhombic) that results from the tilting of the [BX_6] octahedra to reduce the volume of the A-cavity. In contrast, when A is larger ($t > 1$), the B−X octahedral bond is distorted and elongates along the c axis, providing increased space for B-site cation mobility (e.g. hexagonal, or tetragonal symmetry).[73] It is worth noting that although originally developed for oxide perovskites, the tolerance factor remains a useful predictive tool for halide systems, and ad hoc corrections were developed to account for the partial covalency of the B−X bonds.[23,74,75]

The geometric constraints of the tolerance factor limit the compositional range of HPs to: 1) large monovalent A-site cations: Cs^+ or Rb^+ for fully inorganic HPs, and $CH(NH_2)_2^+$ (FA), $CH_3NH_3^+$ (MA), or $(CH_2)_2NH_2^+$ (AZ) for hybrid organic–inorganic HPs; 2) large B-site metal ions: post-transition divalent cations, typically lead (Pb^{2+}), tin (Sn^{2+}), or germanium (Ge^{2+}). Among these compositions, LHPs have been the most extensively studied over the past decade, thanks to their outstanding optical and electronic properties, which make them particularly attractive for optoelectronic applications. Within this group, cesium-based perovskite structures (e.g., $CsPbI_3$ shown in **Figure 1.5a**), were among the first to be investigated and are considered a model compound among fully inorganic perovskites.[51] In LHPs, chemical bonding, in particular the B−X interaction, plays a key role in determining optoelectronic properties. The higher ionicity of LHPs compared to conventional binary semiconductors (e.g., metal chalcogenides or pnictides) allows a simpler synthesis, and easier compositional tunability.[12] This high ionicity is also the origin of a key feature for

optoelectronic applications, i.e. their 'defect-tolerant' nature (**Figure 1.5b**). In LHPs the VBM arises from a mix of X np and Pb 6s orbitals, while the CBM is dominated by Pb 6p orbitals: this orbital mixing configuration ensures that defect states typically form shallow traps or remain embedded within the bands, minimally affecting radiative recombination and optical properties.[12] Unlike traditional semiconductors like silicon or metal chalcogenides, which require impurity levels in the ppb range to maintain adequate performance, lead HP-based photovoltaic devices can be fabricated from polycrystalline films using technical-grade precursors under ambient conditions, as they tolerate up to 1-2% of point defects without their properties degrading appreciably.[9] LHPs also exhibit significantly lower effective masses of the charge carriers compared to oxide perovskites, enabling high mobilities and optical absorption, due to the strong SOC.[76–78] These features, together with longer carrier diffusion lengths, and reduced nonradiative recombination, making these materials particularly suitable for photovoltaic applications.[79] Extremely high optical absorption coefficients[80] enable the fabrication of efficient thin-film solar cells with much thinner absorber layers (≈500 nm) compared to established Si thin-film technologies with similar PCEs.[81]

However, despite all these interesting properties, the actual application of $CsPbX_3$-type halide perovskites in PSCs has proven challenging for several reasons, including their high ionic conductivity that promotes ion migration in the cell. This creates vacancies or other defects, leading to recombination centers that reduce the performance of the solar cells.[9,82] Research efforts therefore shifted toward organic-inorganic hybrid perovskites, such as $MAPbI_3$ and $FAPbI_3$ (**Figure 1.5c-d**), in which the A-site is occupied by an organic cation (MA and FA cations, respectively), and which are now the undisputed leaders in terms of efficiency in the field of PSCs. In hybrid HPs, the interaction between the organic A-cation and the inorganic scaffold is still essentially ionic, while the possible presence of hydrogen bonds between the protonated amine group and the halide ions remains a topic of ongoing debate in the literature.[83–86]

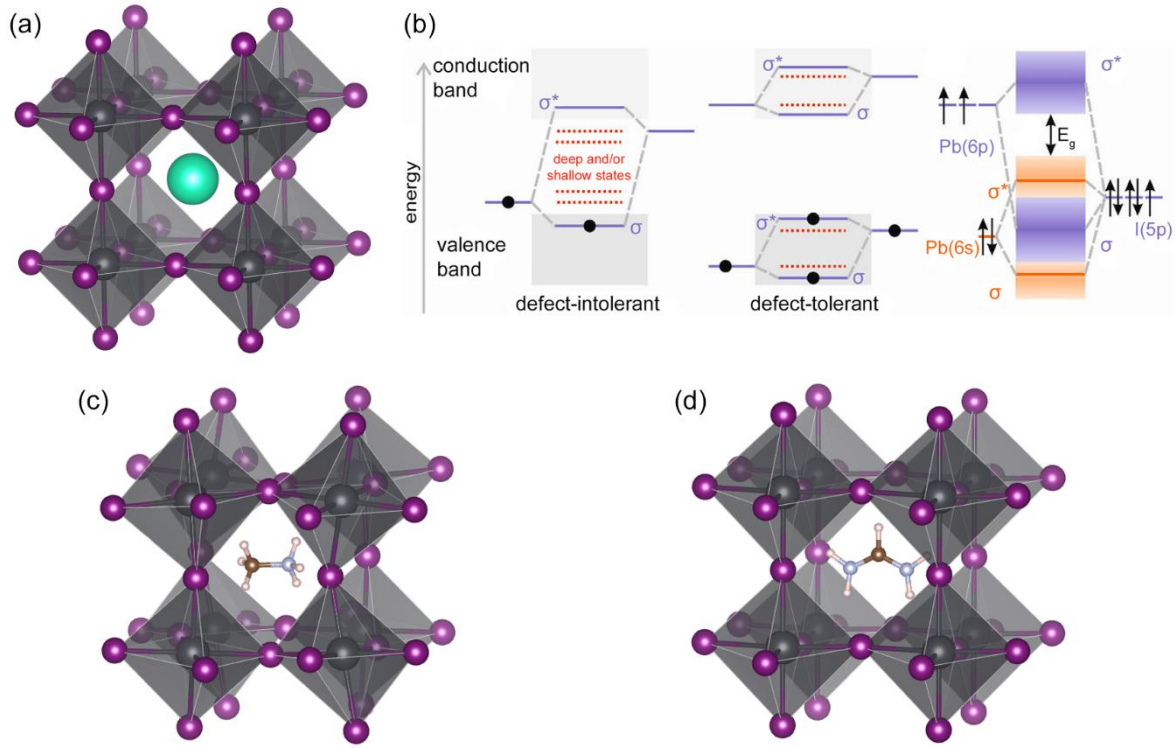

Figure 1.5. (a) Crystal structure of $CsPbI_3$. (b) Left and center panels: electronic energy level diagrams of semiconductors with two different limiting cases: defect-intolerant (typical of group IV and binary II-VI, IV-VI, III-V semiconductors) and defect-tolerant (as in ABX_3 HP). Defect states are depicted with red dotted lines. Right panel: Energy level diagram of $CsPbI_3$ with orbital hybridization between Pb and I atoms. (c-d) Crystal structures of (c) $MAPbI_3$ and (d) $FAPbI_3$. Iodine atoms are in violet, PbI_6 octahedra in grey. Cesium, carbon, nitrogen, and hydrogen atoms are in teal, brown, light grey and white, respectively. Panel b is adapted from ref. [12], published by the American Chemical Society, and distributed under the terms of the Standard ACS AuthorChoice/Editors' Choice usage agreement.

The band gap of lead-based hybrid HPs can be varied by varying the composition of both the A- and X-sites, as well as by controlling crystal symmetry through temperature.[87] MAPI in particular undergoes two phase transitions from high temperatures: the first, from cubic to tetragonal (space group: *I4/m*), at around 330 K, and from tetragonal to orthorhombic (space group: *Pnma*) at 161 K. The higher cubic symmetry observed at high temperature has been attributed to the rapid rotational motion of the $CH_3NH_3^+$ cations within the Pb–I framework.[88] In cubic MAPI the CBM sits at -3.93 eV, and the VBM at -5.43 eV, giving a band gap of 1.5 eV.[89] Upon transition to the lowest-symmetry orthorhombic phase, involving tilting of the PbI_6 octahedra along the c-axis and the ordering of $CH_3NH_3^+$, the direct band gap increases to 1.61 eV.[90] The position of the CBM at a higher symmetry has been shown to extend carrier lifetimes, suppress recombination, and promote exciton separation in $CH_3NH_3PbI_3$, thereby enhancing photovoltaic conversion efficiency.[91] The direct band gaps

of MAPBr and MAPCl, obtained by substituting Br or Cl for iodine, increase to 2.3 eV [92] and 2.67 eV,[93] respectively.

The substitution of the MA cation with FA leads to FAPI, which crystallizes in two phases depending on the orientation of the FA cation and the degree of distortion of the crystal lattice: the black α phase and the yellow δ phase.[94,95] The α-FAPI phase is a *Pm-3m* cubic structure, in which the FA cations exhibit high rotational mobility and are dynamically disordered within the octahedral framework.[96,97] This polymorph is characterized by excellent optoelectronic properties, with a bandgap around 1.47 eV.[98] In contrast, the δ-FAPI phase exhibits a non-perovskite hexagonal structure (space group: $P6_3mc$), in which the PbI_6 octahedra share faces rather than corners.[96] Owing to the preferred orientations of the FA cation, δ-FAPI shows superior structural stability and is therefore thermodynamically favored over the α phase within the typical operating temperature range of PSCs. As a result, α-FAPI readily undergoes a phase transition to δ-FAPI.[94,96] However, the δ phase has wide bandgap of approximately 2.48 eV, making it essentially inactive for photovoltaic applications.[97] Two further tetragonal polymorphs are stable at low temperatures (<285 K) and generally not relevant for practical applications.[95]

In any case, the use of both MAPI and FAPI is severely limited by their poor chemical stability, since they are highly sensitive to environmental factors, particularly oxygen and moisture.[32] Fully inorganic LHPs, on the other hand, exhibit superior chemical stability, suggesting that the organic molecule is the main source of vulnerability.[9,51] Nevertheless, even fully inorganic LHPs, despite being stable, still present a fundamental issue: the high toxicity of lead. All these challenges have driven the search for chemically more stable alternatives to MA and FA cations and, above all, for lead-free solutions.[32,99,100] In order to improve the chemical stability of OLHPs, a wide range of organic cations has been investigated as potential substitutes for MA and FA in the A-site of the perovskite lattice. Depending on the type and relative size of A-site cations, LHPs can form either three-dimensional structures or lower-dimensional phases.[101] Low-dimensional lead halides can crystallize in different stoichiometries and occur as two-dimensional, one-dimensional, or zero-dimensional structures (2D, 1D, and 0D) (**Figure 1.6**). As discussed by Akkerman and Manna, these compounds, particularly the 1D and 0D phases, usually share little in common with the a proper perovskite structure, and therefore should not be classified as such.[102]

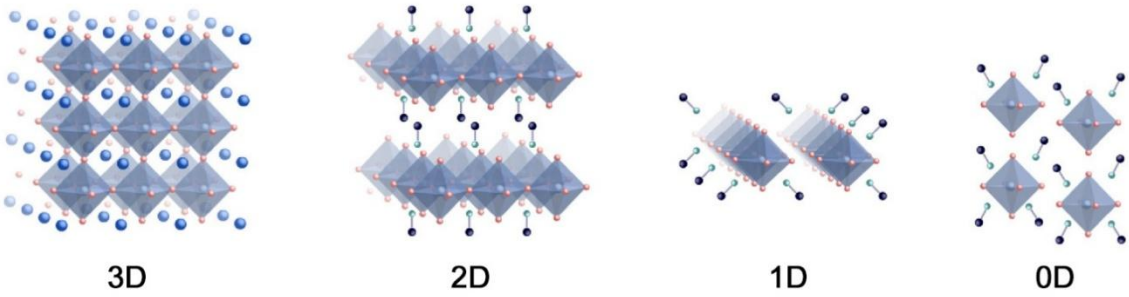

Figure 1.6. Schematic illustration of 3D and lower-dimensional "perovskites". Figure adapted from ref. [103], published by John Wiley & Sons Australia, distributed under the terms of the Creative Commons CC BY license.

Nevertheless, the liberal use of the term "perovskite" for these low-dimensional structures has become widely accepted, and it is now standard in the literature. Most small cations present in the low-dimensional structures are the same as those used in the synthesis of pure and mixed 3D perovskites, such as MA, FA, DMA, GA, etc.; however, more relaxed constraints for the tolerance factor in low-dimensional perovskites also allow the presence of larger cations like i-PA, TZ, and others.[104,105] The size and shape of the A-site cation influence the bond length and angles between the B and X species, thereby altering the arrangement of the surrounding $[BX_6]^{4-}$ octahedra, the crystal symmetry and, in extreme cases, even their connectivity. In 3D structures, A-site cation engineering is a useful approach to finely tune the octahedral tilting (analogously to the orthorhombic, tetragonal, or cubic phases in MAPI) and the physicochemical properties of OLHPs, without substantially modifying their optoelectronic properties. This has been made possible by the introduction of oversized A-site cations (resulting in $t > 1$), which do not necessarily fit within the structural constraints of the bulk lattice.[106]

Two-dimensional (2D) hybrid organic-inorganic LHPs are derived from 3D perovskites by removing inorganic layers along the (100), (110), or (111) (**Figure 1.7**) planes, where single or multiple corner-connected layers are separated by organic cations.

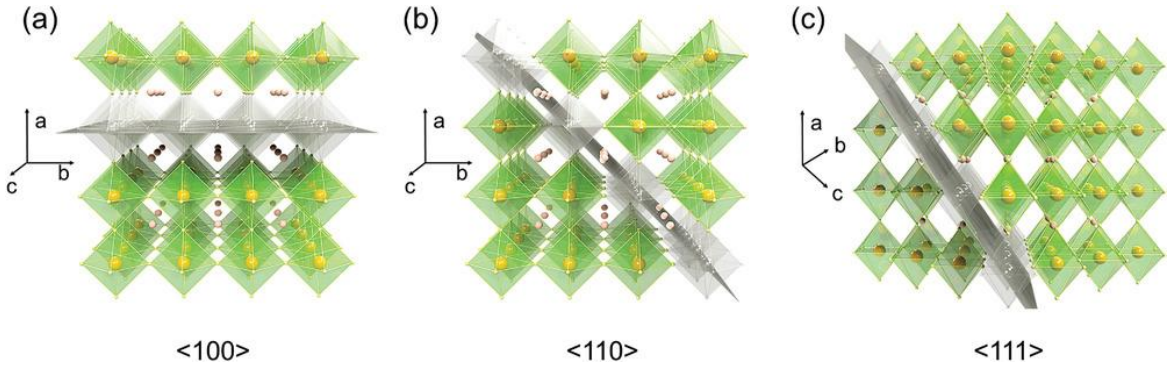

Figure 1.7. Structures of three types of 2D layered perovskite obtained by cutting a 3D perovskite structure along the ⟨100⟩, ⟨110⟩, and ⟨111⟩ planes, either with a larger spacer cation or with vacancies. Figure reproduced from ref. [107], with permission from Wiley-VCH GmbH, Copyright 2021.

Although the organic cations in 2D structure are larger than e.g. MA, they still need to fit into the frame of 2D inorganic layers, and the size of the organic molecule must be compatible with the square area defined by four corner-sharing lead halide octahedra, allowing the organic molecule to tilt and interlace between the inorganic layers.[108] 2D perovskites with slabs aligned to the (100) plane are the most represented type: among them, Ruddlesden-Popper phases have the general formula $A_{n-1}A'_2B_nX_{3n+1}$, where A are small cations that occupy the intralayer voids, and A' are interlayer organic cations, typically large primary amines with long alkyl chains, while n is the number of octahedral layers within each inorganic slab. In these structures, the monoammonium spacer is stabilized by electrostatic interactions with the inorganic slab on one end and by other noncovalent interactions (mainly van der Waals) on the other end. Dion-Jacobson phases ($A_{n-1}A'B_nX_{3n+1}$) have large diammonium cations as A' spacer cations instead, resulting in eclipsed stacking and enhanced stability due to stronger interaction between inorganic slabs and spacer cations at both ends, each stabilized via hydrogen bonding. The valence of the spacer cation then directs the formation of either kind of phase.[109–111] In general, all 2D structures exhibit significant charge-carrier quantum confinement effects in the layers, leading to the formation of both free excitons and self-trapped excited states upon photoexcitation.[112] Such anisotropic charge transport, combined with low phase purity, have limited the performance of PSCs employing these materials so far.[113]

One-dimensional (1D) structures exhibit various stoichiometries and consist of chains composed of $[PbX_6]^{4-}$ octahedra, and they typically form when the organic molecules cannot adopt close adjacent packing due to their shape.[108] The connectivity of lead halide octahedra

is essentially determined by the size and charge of the organic cations, and involves corner-sharing, edge-sharing, or face-sharing units (**Figure 1.8a**). The resulting octahedra chains can then be linear, step-like, bilinear, and tubular, and their chemical formulas depend on the connecting methods and the organic cations (**Figure 1.8b**).[114]

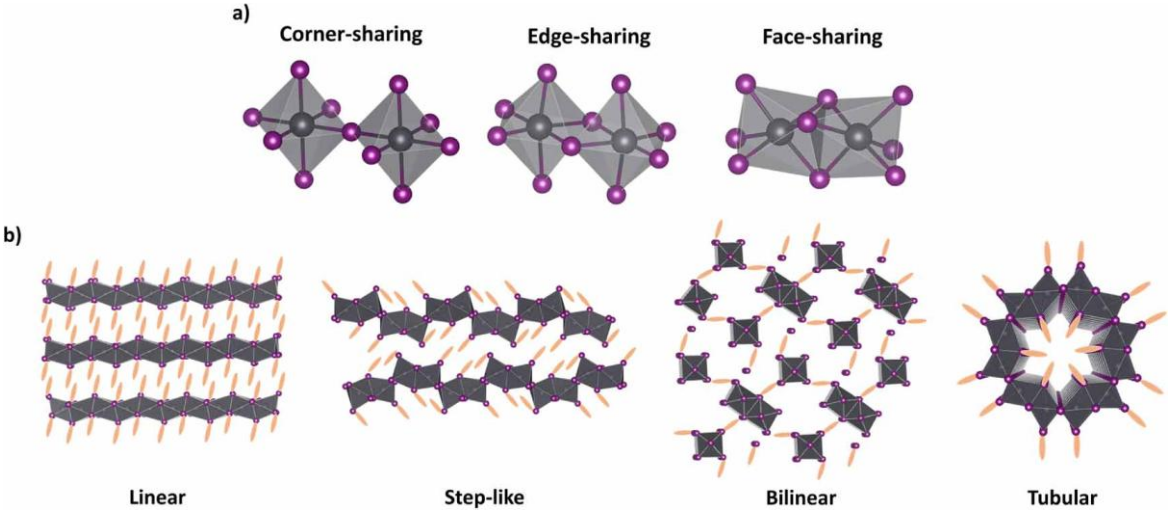

Figure 1.8. Examples of connectivity in 1D perovskites. (a) Basic connectivity of two octahedra, from lowest to highest number of structural elements in common. (b) Various motifs of connected octahedra sharing different number of structural elements, and arranged in different ways along one direction. Figure reproduced from ref. [[115]], published by IOP Publishing, distributed under the terms of the Creative Commons Attribution 4.0 license.

1D LHPs exhibit excellent stability due to the robust lattice structure arising from the "shoulder-to-shoulder" arrangement of PbX_6 octahedra and the protective effect of the organic cations that surround the chains.[114,116,117] In general, these materials exhibit high bandgaps and exciton binding energies, which may render them suitable for lighting systems such as LEDs and phosphors based on electron–hole recombination.[108,118] Although the high exciton energy hinders charge transport, combinations of 1D and 3D LHPs offer remarkable opportunities for advancing photovoltaics. By directly incorporating large organic cations into the 3D perovskite or post-depositing large cations onto the surface of a 3D perovskite film, environmentally stable multidimensional films with excellent photovoltaic properties can be achieved.[117,119] In zero-dimensional (0D) hybrid perovskites, the metal halide octahedra or metal halide clusters are fully surrounded and isolated by organic cations. In a sense, they can be regarded as core-shell systems, in which the negatively charged octahedra constitute the core and are encapsulated by organic cations as the shell. This structural

configuration explains their remarkable environmental stability.[120] This isolated structure prevents electronic interactions between neighboring octahedra, causing the optical properties to reflect essentially those of isolated octahedra or clusters. As a result, excitons are strongly confined within each octahedron, leading to a high binding energy, which increases radiative recombination in optoelectronic devices.[120,121] Furthermore, the broadband emission and large Stokes shifts characteristic make them advantageous in down conversion white LED applications as phosphors.[122] The wide variety of available A-site cations provides a robust platform for designing new materials with diverse electronic and photophysical properties. Despite some progress achieved so far, research on 1D and 0D LHPs can still discover potential applications of these materials, which largely remain to be explored.

1.4. Compositional Engineering of Halide Perovskites

To address the issue of high lead toxicity, that represents a barrier towards the eventual mass adoption of LHP-based devices, an ever-increasing number of studies have been devoted to the replacement of Pb in recent literature.[123] It has long been argued that the superior optical properties of Pb-based HPs are associated with the unique electronic configuration of Pb^{2+}, featuring the $6s^2$ lone pair. Initial investigations into the development of lead-free perovskites primarily focused on substituting Pb^{2+} with isovalent group IVA cations, such as Sn^{2+} or Ge^{2+} which maintain a similar electronic configuration.[124]

Ge-based perovskites, like $CsGeI_3$, $MAGeI_3$, and $FAGeI_3$, medium-to-wide band gap semiconductors. In particular, $CsGeI_3$ exhibits a direct band gap of approximately 1.6 eV, a value comparable to that of lead-based perovskites commonly employed in photovoltaic applications.[125] They do not exhibit phase transitions within the temperature range typically relevant for photovoltaic device operation, ensuring structural and optoelectronic stability under operating conditions.[126] Despite promising electronic properties, several challenges remain from an application perspective. In particular, the solubility of Ge-based perovskites in most polar organic solvents is unsatisfactory, which limits the achievable thin film quality, and in addition, the fabricated photovoltaic devices generally exhibit poor overall performance. This limitation is primarily associated with the intrinsic instability of Ge^{2+}, which, owing to its $4s^2$ outer shell, easily loses its lone pair, oxidizing to Ge^{4+}. The chemical stability of Ge-based perovskite materials is generally poor, and, consequently, the solar cells employing them have reached limited efficiency.[125]

Tin, on the other hand, represents the most promising candidate to replace lead, as it is chemically and structurally more similar to Pb^{2+} in its Sn^{2+} state (ionic radii Sn^{2+}: 1.35 Å; Pb^{2+}: 1.49 Å).[127] Unlike Ge-based perovskites, which exhibit trigonal crystal structures, Sn-based perovskites display cubic or pseudo-cubic crystal structures that closely resemble those of lead, highlighting the strong similarity between these two cations. $CsSnI_3$ exhibits three black and one yellow polymorphs. At room temperature, it adopts a black 3D distorted perovskite structure, in the orthorhombic *Pnma* space group.[128] This can coexist with the yellow phase, a non-perovskite orthorhombic structure with 1D double-chains. Above 351 K, a transition to a black tetragonal phase occurs, and finally, a black cubic phase forms above 425 K.[129] $MASnI_3$ forms a cubic *Pm-3m* structure, with a disordered MA cation,[130]

and lower symmetry polymorphs occur below 275 K.[131,132] $FASnI_3$ shows cubic or pseudo-cubic structures even at room temperature. Unlike FAPI, which is thermodynamically unstable and tends to form the yellow non-perovskite δ phase, cubic $FASnI_3$ is stable, transforming to an orthorhombic[133] or tetragonal phases at lower temperature.[124,134]

In principle, Sn-based perovskites with an optical bandgap in the range of 1.2-1.4 eV could achieve a PCE around 33% in ideal conditions.[135] In addition, Sn-based perovskites display similar, or even superior electronic and optical properties compared to Pb-based perovskites.[133,136] Despite these promising characteristics (discussed in detail in Chapter 3), Sn-based perovskite solar cells have achieved much lower efficiency so far compared to their Pb-based counterparts.[124] This can be attributed to the rapid oxidation of Sn^{2+} to Sn^{4+} (similar to what is observed with Ge) that induces unwanted p-type self-doping and compromising the cell efficiency.[127,137]

An alternative, and promising, route to replace Pb^{2+} is to substitute it with a pair of a monovalent and a trivalent cation, resulting in the ordered structure of HDPs, known as elpasolites. HDPs typically crystallize in a cubic structure, with the same a three-dimensional network of corner-sharing metal-halide octahedra as the aristotype perovskite.[138] Therefore, the structure of HDPs is the same as simple perovskites, but with a doubled unit cell, since each Pb^{2+} is replaced by two different B-site cations, leading to the general formula $A_2B^+B^{3+}X_6$ (**Figure 1.9**), where A is usually Cs^+, B^+ is a monovalent metal such as Cu^+, Ag^+, Na^+, or K^+, B^{3+} is a trivalent metal such as Bi^{3+}, In^{3+}, or Sb^{3+}, and X^- is a halide.[139,140] An alternative approach, still within the context of HDPs, involves replacing two Pb^{2+} sites with a tetravalent cation and one vacancy, yielding compounds with the formula $A_2(V)B^{4+}X_6$ (**Figure 1.9**). This opens a very broad compositional space, extending potentially to a very large section of the periodic table, and several combinations have already been explored in depth. **Figure 1.9** shows that nearly all elements of the periodic table can in principle be used in HDPs. For instance, alkali metal cations could occupy either the A-site or the B-site. In practice, however, Cs^+ is employed as the A-site cation, while Li^+ and Na^+ primarily occupy the B^+-site. Among trivalent metals, the most commonly used include various transition metals, which can also occupy the B^+-site,[141] group 13 elements, including Al,[142] In,[143] and Tl (also usable in the B^+-site),[144] and Sb and Bi from group 15.[145–147] The incorporation of trivalent cations further extends the applicability to lanthanides and some actinides.[148]

For HDPs featuring tetravalent cations alternating with vacancies, a wide range of cations can be used, primarily among transition metals, group 14 elements, and certain group 16 elements.

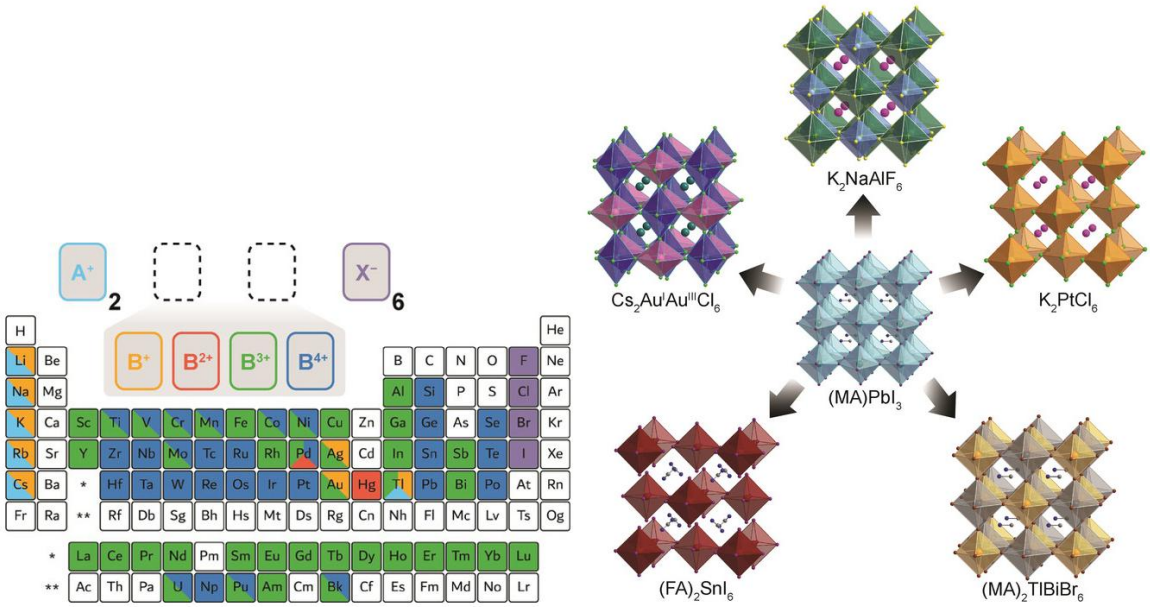

Figure 1.9. (left) Compositional diversity of 3D HPDs. Different valence states are indicated with different colors. (right) The aristotype perovskite MAPI is shown in the middle. Surrounding it, several examples of double perovskite structures of the $A_2B^+B^{3+}X_6$ and $A_2VB^{4+}X_6$ types. Sodium atoms are in dark green, aluminum in light blue, platinum in dark orange, bismuth in light-orange, thallium in black, tin in dark red, gold(III) in dark blue, gold(I) in light pink, lead in turquoise, potassium in magenta, cesium in teal, iodine in purple, bromine in brown, chlorine in green, fluorine in yellow, carbon in gray, and nitrogen in blue; H atoms are omitted. Figure reproduced from ref. [149], with permission from Wiley-VCH GmbH, Copyright 2021.

The crystallographic stability of HDPs is typically assessed using three geometric factors: the Goldschmidt tolerance factor (t), modified versions of which were proposed to extend its applicability to more complex structures,[150,151] the octahedral factor (μ), and, more recently, the τ paramerer, which also accounts for the oxidation state of the A-site cation. All these parameters are primarily based on ionic radii and provide a first-order approach towards predicting structural stability. However, their effectiveness may be limited in the presence of structural disorder, alloying, or defects. While useful as preliminary screening tools, geometric descriptors do not always accurately predict real stability, and must be complemented by a thermodynamic assessment to predict stability.[99] To date, HDPs have shown promise in photovoltaic applications,[143,152–154] as well as in lighting and display

technologies.[155–158] These materials also exhibit improved air and moisture stability compared to their ABX_3 counterpart.[152,159,160] However, while the former typically exhibit direct band gaps with CBM and VBM of opposite parity, HDPs display more diverse electronic behaviors, which can be primarily tuned by modifying the elements at the B^+- and B^{3+}-site. Many examples have been reported in recent literature.[155,158,161–165] For example, in bulk $Cs_2Ag_{0.60}Na_{0.40}InCl_6$ doped with 4% Bi^{3+}, a significant PLQY of 86% was reported and attributed to the Jahn-Teller distortion of $AgCl_6$ octahedra in the excited state. This distortion reduces the inversion symmetry of the electron wave function at the Ag site, thereby altering the parity of STEs and enabling radiative recombination.[157] Kovalenko and co-workers achieved a record PLQY of up to 93% and bright blue emission upon doping $Cs_2NaInCl_6$ and Cs_2KInCl_6 with Sb^{3+}, using single-crystal and powder samples, respectively.[156] Another highly promising approach involves reducing conventional perovskites to the sub-micrometer scale, where they display outstanding light-emission properties in QLED applications. NCs exhibit quantum confinement effects that can be harnessed to finely tune their optical properties, thereby providing additional opportunities beyond compositional modulation.[58]

A thorough rationalization of the properties of HDPs as a function of composition can be challenging: due to their high compositional flexibility and possible doping strategies, multiple cations can be present in the B^+ and B^{3+} sites. Many HDPs, particularly those that are alloyed, exhibit defects and local distortions that can significantly influence properties. The most important defect types include vacancies, interstitials, and antisite substitutions, all of which affect the electronic and structural features.[166] Halide vacancies, are among the most common defects due to their relatively low formation energies, and they create shallow or deep trap states within the bandgap, affecting the material's conductivity and, in some cases, inducing significant structural relaxation. Cs or Ag vacancies, on the other hand, act as acceptors, creating holes that induce p-type behavior.[167] Antisite defects, such as Ag on a Bi site and vice versa, are also common and introduce electronic defect states in the bandgap, promote lattice distortions and increase nonradiative recombination.[168] Local distortions further affect the overlap between metal–halide orbitals, directly impacting the electronic structure and charge-carrier dynamics, which are crucial factors for device performance and efficiency.[166] Understanding and controlling all these factors is essential to eventually optimize HDPs for optoelectronic applications.

2. X-Ray Absorption Spectroscopy and its Simulation

2.1. Basics of X-ray Absorption

Since their discovery, X-rays have represented a fundamental tool for the scientific community, to explore and understand the structure of materials. Established techniques based on X-rays, like XRD for the determination of the long-range atomic arrangement in a crystal lattice, have benefitted from almost a century of theoretical and experimental development, and today they are an essential tool in research and manufacturing. In general, X-rays represent an indispensable tool for correlating the crystalline structure with the properties in functional materials.[169]

For instance, in the field of optoelectronic materials, a detailed knowledge of crystalline order is essential to assess phase purity, and to understand and optimize electronic and optical properties.[170] However, research on new materials for optoelectronic applications, as well as the modification of existing ones, is rapidly advancing and understanding optical and electrical processes must rely on the study of both their long-range and short-range structure, which becomes increasingly complex as research progresses. To overcome the limitations of conventional X-ray techniques, the need for more advanced technologies has emerged over time. In this context, a highly brilliant and collimated X-ray source can be used to address these challenges, as it provides unique methods and techniques for understanding the complexity of materials.

Synchrotron radiation (made up mostly of X-rays) is generated in large scale facilities where electrons are kept in a round orbit at relativistic speeds and therefore undergo continuous direction changes, emitting electromagnetic radiation in a narrow cone tangent to the orbit.[171,172] A modern synchrotron source consists of four components: a linear accelerator (linac), a booster ring, a storage ring, and the beamlines (**Figure 2.1a**).

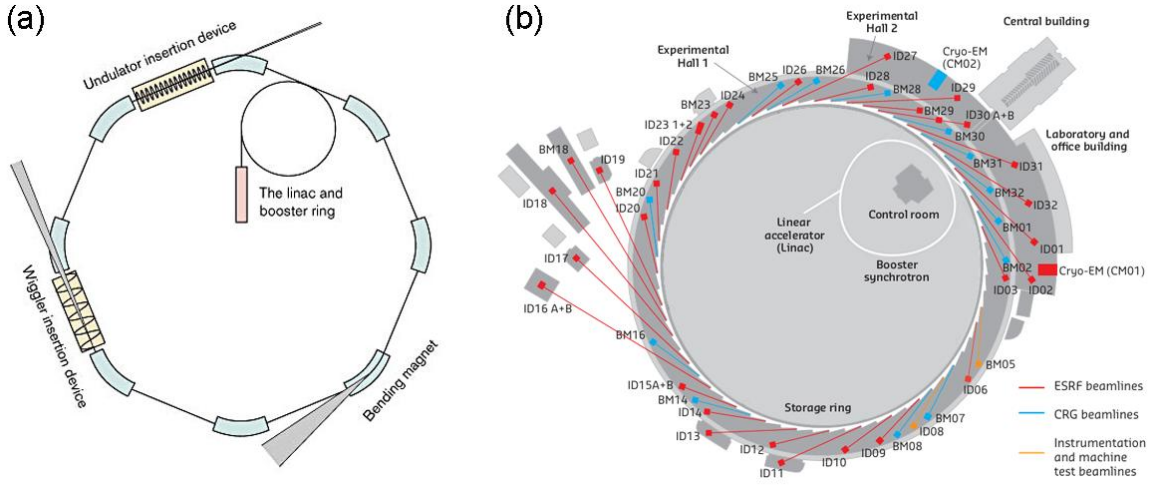

Figure 2.1. (a) Schematic of a synchrotron radiation source showing the linac, booster and the storage ring, and the magnetic devices that produce X-ray radiation. (b) An overview of the ESRF synchrotron storage ring, showing the linac where electrons are produced, the booster synchrotron where electrons are accelerated to high speed before being injected into the storage ring with a circumference of almost 900 m, and all the beamlines tange to it. Panel a is reproduced with permission from ref. [173], published by Elsevier Ltd, Copyright 1999. Panel b is reproduced from [174].

The linac generates a stream of electrons accelerated by electric fields. Then, an intermediate ring booster is used to bring particles to relativistic speeds. Once in the storage ring, electrons are kept along a circular path by magnetic fields produced by electromagnets or permanent magnets. In fact, the structure of a synchrotron facility resembles a polygon rather than a perfect circle. Three types of magnetic devices are commonly used to produce synchrotron radiation: bending magnets, wigglers and undulators. Bending magnets force electrons, moving at speeds close to that of light, to follow a curved path. This change in direction causes the electrons to emit radiation in a fan-like pattern, covering a broad range of wavelengths. Wigglers are an enhanced form of bending magnets: they employ a series of strong magnetic fields to make electrons oscillate in a zig-zag fashion along their path, generating more intense radiation over a wider energy range compared to bending magnets. Undulators are similar to wigglers but use weaker and more closely aligned magnetic fields, causing the electrons to move in a sharper, wave-like pattern. This results in a narrower, more focused radiation beam with a specific wavelength range, making it particularly useful for experiments that require nearly monochromatic and brilliant light source. Wigglers and undulators (collectively referred to as insertion devices) constitute the straight sections of the storage rings, and they generate radiation that is much more intense and collimated than that of bending magnets.[171,175] The most recent dedicated synchrotron radiation facilities are

specifically designed with many straight sections optimized to produce high-brilliance radiation from insertion devices. One of the most advanced synchrotron facilities worldwide is the ESRF, located in Grenoble, France (**Figure 2.1b**), where most of the XAS experiments of this work were performed. Recently, the ESRF underwent a major infrastructure upgrade known as the EBS, which has provided the scientific community with a unique high-energy, ultra-low-emittance synchrotron light source, together with new cutting-edge beamlines. With the introduction of advanced technological components and a new storage ring, the brilliance and coherence of X-ray beams were increased by approximately two orders of magnitude compared to previous-generation sources, marking the beginning of a new era in X-ray science with the ESRF–EBS source. This enables an extremely accurate exploration of materials down to the atomic scale with sub-micrometer spatial resolution, and therefore allows researchers to address a wide variety of scientific issues, encompassing pressing global challenges, e.g. the development of more sustainable and efficient materials for energy technologies that are environmentally friendly, economically viable, and capable of reducing climate and environmental impact.[176,177]

Among the various techniques available at synchrotron facilities, X-ray absorption spectroscopy is an ideal complement to the X-ray diffraction for studying optoelectronic materials. While the latter provides information on long-range structure, XAS enables the investigation, at the atomic scale, of the local structure (up to about 0.1 nm) surrounding a single atomic species. Being a spectroscopic method, XAS requires a monochromatic, brilliant and tunable X-ray source: although some measurements might in principle be performed using laboratory X-ray sources, most experiments greatly benefit from the use of synchrotron light.[178] XAS is highly sensitive to the oxidation state, coordination geometry, as well as to the bonding distances, coordination numbers, and nature of the atoms surrounding the selected element. Thanks to this sensitivity, it represents an effective and relatively straightforward tool for determining both the chemical state and the local atomic structure of a specific atomic species.[179] XAS imposes few restrictions on the nature of the analyzable samples, so it is readily applicable to a wide variety of materials: almost every element in the periodic table can be probed, there is no constraint on the crystallinity of the material, and, due to the high penetration depth of X-rays, the technique is not inherently surface-sensitive as it happens instead with photoelectron spectroscopy. Moreover, measurements can be performed even for absorbing atoms that are present in trace amounts or at very low concentrations.[180]

The fundamental principle of XAS involves tuning the energy of incident X-rays around the binding energy of the core electrons in the atoms of interest, inducing electronic transitions from the core to unoccupied states, thereby providing detailed information on the atom's electronic structure. During a XAS experiment, an X-ray photon is absorbed by a tightly bound core electron (e.g., an electron in the 1s orbital of a given atom), provided that the photon energy exceeds the electron binding energy (**Figure 2.2a**). The absorption results in the ejection of the electron into an unoccupied bound state below the ionization threshold or into the continuum, thereby generating either an electron in a higher-lying state or a photoelectron, plus a core-level electron vacancy, called "core-hole". In the μ(E) spectrum, sudden increases called absorption edges are observed, each corresponding to the excitation of a different core-level electron into the continuum. Since each element has well-defined binding energies for its core electrons, the specific atom to be analyzed can be selected by tuning the X-ray energy to its absorption edge. Depending on the incident energy, different interactions between X-ray and the investigated matter are triggered, thus determining their applications. (**Figure 2.2b**).[178,180] Provided the photon energy is high enough, the photoelectron propagates as a wave that interacts with the surrounding atoms, and undergoes partial scattering. The interference between the outgoing and scattered waves eventually modulates the X-ray absorption probability in an oscillatory manner, giving rise to characteristic variations in the absorption coefficient μ(E) that is measured in a XAS experiment.

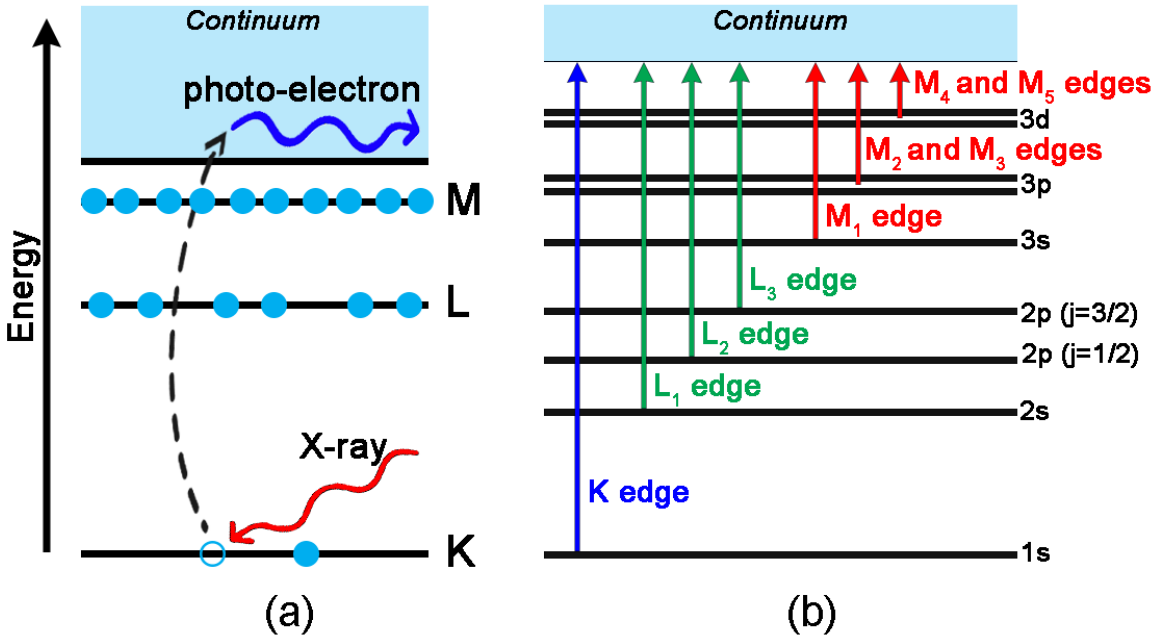

Figure 2.2. (a) The photoelectric effect, in which an X-ray is absorbed and a core-level electron is promoted out of the atom. (b) Transitions that contribute to XAS edges.

As shown in **Figure 2.3**, the XAS spectrum is usually interpreted separately in two regions: XANES and EXAFS. Although both regions share the same physical origin, this distinction is useful for data interpretation. The XANES region, within approximately 50 eV of the edge and usually comprising less intense pre-edge features, is particularly sensitive to the formal oxidation state and coordination chemistry of the absorbing atom, whereas the EXAFS region, consisting of oscillations arising from interference between the outgoing and back-scattered photoelectron waves, can extend up to 1000 eV beyond the edge and is used to determine interatomic distances, coordination numbers, and the nature of atoms surrounding the absorbing atom.[178,180]

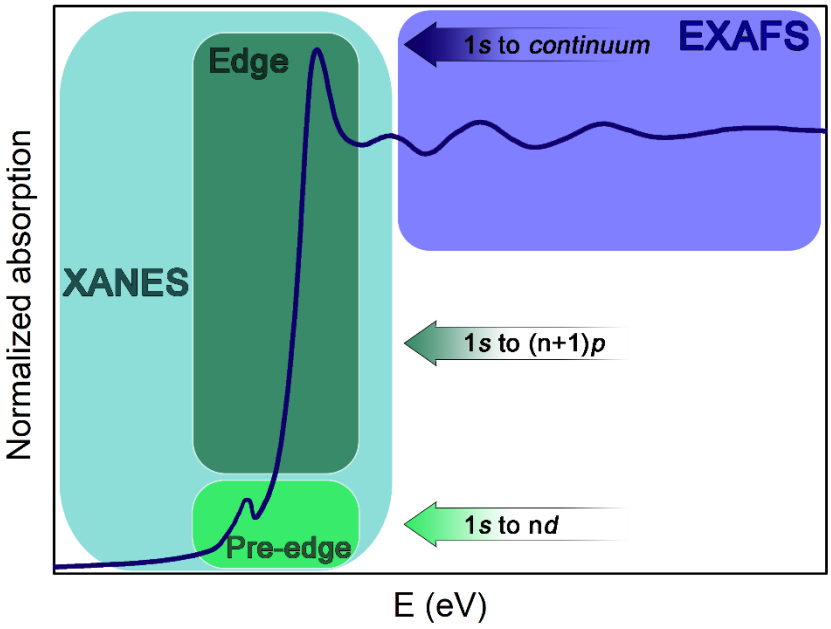

Figure 2.3. Example of a XAS spectrum at the K-edge, showing the three spectral regions (pre-edge, edge, and post-edge), with the corresponding electron excitations giving rise to them.

X-rays can be broadly classified into three categories, hard, tender, and soft, based on their energy ranges, penetration capabilities, and suitability for probing different material properties, from bulk structures to surface-sensitive layers. Hard X-rays possess the highest energies, typically ranging from 5 keV to 100 keV or higher. These X-rays have shorter wavelengths, which enable deep penetration into materials, making them particularly useful for probing the internal structures of dense objects. In most cases, hard and tender X-rays provide detailed bulk information on the electronic environment and atomic structure of materials averaging over up to tens of cubic micrometers. This penetrating power is crucial in applications such as hard XAS, where the K and L_3 edges of heavy elements commonly used in HPs, such as Pb, Sn, Bi, and Sb, are studied, as hard X-rays allow probing the electronic states of atoms within the bulk of the sample.[181–183] Hard X-rays are extensively used in EXAFS analysis, and their ability to probe bulk properties without significant surface interference makes them indispensable for the study of complex systems where detailed knowledge of the bulk electronic structure is essential. On the other hand, soft X-rays possess lower energies, typically ranging from 0.1 keV to 1 keV, so they are less penetrating and are absorbed near the surface of materials. This property makes them particularly suitable for more surface-sensitive studies. Soft-XAS is especially useful for investigating the electronic structure of surface layers or thin films, specifically accessing the L-edges of transition

metals. Although soft-XAS, is also employed, its application is generally limited to ex situ analyses due to the low penetration depth of soft X-ray photons. While soft-XAS offers certain advantages, such as providing information on different electronic transitions, its use is constrained by the need for vacuum conditions and other physical limitations. Therefore, complementary techniques are often required to achieve a more comprehensive understanding of the electronic structure of various materials. Tender X-rays occupy an intermediate position between hard and soft X-rays, with energies approximately ranging from 1 keV to 5 keV, although some overlap with the soft X-ray range can occur. This energy range allows a balance between surface sensitivity and penetration depth.

In order to overcome the limitations of soft-XAS and to provide complementary approaches to hard-XAS, a broad range of experimental techniques (e.g. RIXS, HERFD, XES, etc.), collectively referred to as photon-in photon-out, have emerged recently to make use of the secondary fluorescence radiation from the sample. This eventually overcomes some of the limitations of conventional XAS. Their principles are outlined in the next section.

2.2. Fluorescence Detection and HERFD

Following an absorption event, the excited state typically decays within a few femtoseconds via X-ray fluorescence, in which an electron from a higher-lying level fills the core-hole, emitting a photon with characteristic energy. Some fluorescence de-excitation mechanisms are depicted in **Figure 2.4**. The fluorescence energy equals the energy difference between the initial and final state.

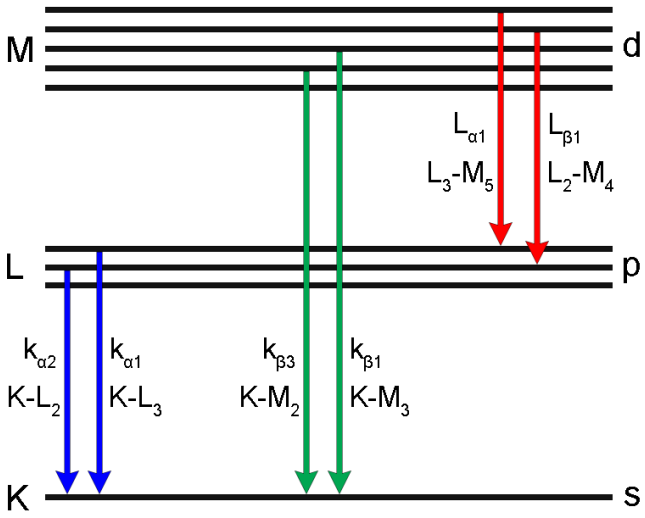

Figure 2.4. Electron de-excitation transitions to fill a 1s core-hole (in blue and green), or a 2p core-hole (in red), together their corresponding fluorescence lines expressed in both Siegbahn notation (with Greek letters) and IUPAC notation (with initial and final states).

The formalism for photon-in photon-out techniques is similar to inelastic scattering, as energy is transferred between the incident photon and the sample, and are then measured from the emitted photon. In this process, a photon of energy $\hbar\omega_{in}$, is scattered by the sample exiting with energy $\hbar\omega_{out}$. The energy $\hbar\omega = \hbar(\omega_{in}-\omega_{out})$ is transferred to the sample that consequently undergoes a transition from the ground state. The process can be a direct one-step process, i.e. not involving an intermediate state, giving rise to either elastic or inelastic Raman or Compton scattering. If the process involves the annihilation of the incident photon, an intermediate excited state with a certain lifetime is reached, which subsequently decays upon emission of fluorescence radiation. In this second case, the absorption process is

element-selective (i.e. like direct X-ray absorption) if the intermediate state is represented by an electron configuration that contains a hole in a core-level (e.g. 1s) of the element of interest. In **Figure 2.5** the ground, intermediate and final states are outlined for the case of a Mn^{3+} cation, connected by different direct and indirect transitions. Each of them probes different states and therefore provides different pieces of information on the electronic structure, and indirectly on the atomic structure.[184]

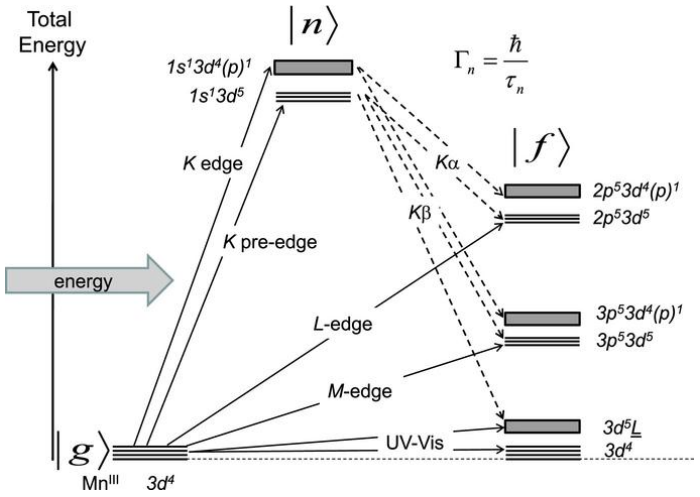

Figure 2.5. Total energy diagram depicting electronic transitions in a solid system containing Mn(III). The energy levels for the ground (|g⟩), intermediate (|n⟩) and final (|f⟩) states are represented using a single-particle picture of the electronic transitions. Black lines indicate that each configuration corresponds to a collection of several many-body states. Rectangles symbolize a band state, where the notation *(p)* represents mixed states between the atomic 4p level and the bands of the solid. The notation $\underline{L}$ corresponds to a hole created on a ligand orbital. Solid-line arrows indicate the absorption edge that allows the corresponding excited state to be reached directly, i.e., in one step. Dashed-line arrows indicate the emission line that allows excited states of lower energies to be reached in a second step, i.e., after a core-hole has been primarily created. Figure reproduced with permission from ref. [184], published by IOP Publishing, Copyright 2014.

X-ray fluorescence radiation can be acquired using solid-state detectors, such as germanium detectors (Ge-SSD) or silicon drift detectors (SDD) as shown in **Figure 2.6a**.[185] Since the fluorescence intensity is proportional to the absorption coefficient, the XAS spectrum can be acquired indirectly through fluorescence, instead of directly using the Beer-Lambert law. For instance, X-ray fluorescence was employed to compare the core excitations of MAPI thin film and PbI_2 by acquiring XANES spectra at the low-energy I $L_{2,3}$ and Pb $M_{4,5}$ edges

by collecting the I $L_{\alpha,\beta}$ and Pb $M_{\alpha,\beta}$ emission line: in this work, it was demonstrated that the fingerprints of the core excitations in MAPI are largely determined by its inorganic component, while the organic groups have a negligible influence.[42] In another study, fluorescence XANES at the Sn K-edge was used to investigate in situ the oxidation mechanisms induced by O_2 and H_2O in tin-based perovskites.[41]

A significant recent breakthrough in XANES spectroscopy is represented by high-resolution detection made possible by the use of Bragg-type crystal analyzers (**Figure 2.6b**). HERFD-XANES, a photon-in photon-out technique, is a very powerful tool to obtain bulk information on the local and electronic structure of complex systems in thin films, solids and liquids alike, including local distortions and defects often present in HPs. This technique improves the intrinsic energy resolution of the fluorescence spectrum, and therefore reveals subtle features not accessible with conventional XAS detection in either transmission or fluorescence mode. This technique also addresses issues of self-/over-absorption observed in conventional XANES spectra, which can cover most spectral features, and it is particularly advantageous for the analysis of heavy elements. Moreover, the high energy resolution improves the overall signal-to-noise ratio, making HERFD-XANES an ideal technique for the investigation of dilute samples and complex systems.

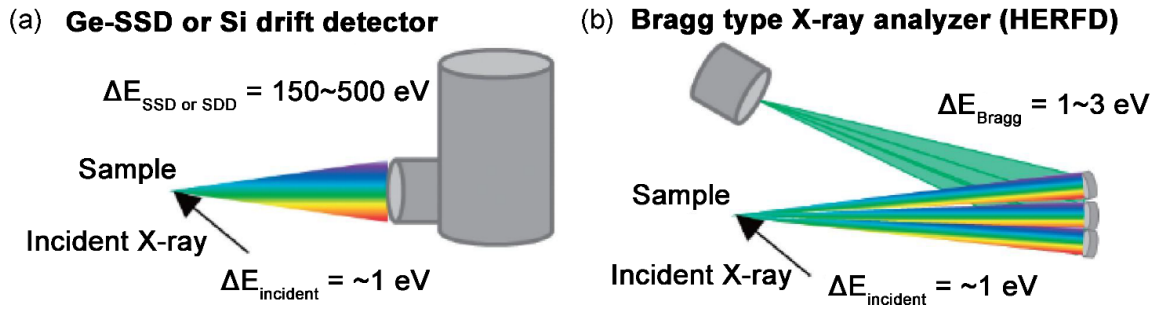

Figure 2.6. Schematic view of X-ray emission/fluorescence detection using (a) Ge solid-state detector or Si drift detector and (b) Bragg-type crystal analyzer used in HERFD-XANES. Figure reproduced with permission from ref. [185], published by Oxford University Press, Copyright 2021.

In a HERFD-XANES experiment, the spectrum is collected indirectly by measuring the intensity of a single fluorescence line, corresponding to a single decay process of the excited state (e.g. K-L_3, which in spectroscopic notation indicates the filling of a core-hole in the K

state with a higher lying electron from the L_3 state). For HERFD-XANES spectra, the incident energy is scanned across the absorption edge while the analyzer crystals remains fixed at the maximum intensity of the emission line. The spectroscopic resolution of a XAS experiment is a function of both the beamline optics and the so-called lifetime broadening, due to the short lifetime of the core-hole created by the primary photoexcitation event (typically less than 1 fs). The beamline optics provide a Gaussian contribution to the lineshape, and lifetime broadening provides a Lorentzian contribution. By collecting fluorescence photons exclusively at a specific emission line using a Bragg-type crystal monochromator (**Figure 2.6b**) composed of a series of analyzer crystals (i.e., in the HERFD setup), the energy resolution is drastically improved, yielding higher-resolution spectra in the pre-edge and edge regions compared to conventional XAS measurements.[186] Compared to the normal X-ray absorption, measuring the X-ray absorption spectrum at a fixed emission energy the effective lifetime related broadening can be described by:

$$\Gamma_{exp} \approx \frac{1}{\sqrt{(\frac{1}{\Gamma_n})^2+(\frac{1}{\Gamma_f})^2}} \quad (2.1)$$

where (Γ_n) and (Γ_f) are the intermediate and final core-hole lifetime broadenings, respectively. In these conditions, the observed spectra are no longer dependent on the short lifetime of the core-hole created by the primary photoexcitation event but depend on the much longer lifetime of the intermediate core-hole instead.[187]

As an example, **Figure 2.7** compares the La L_1-edge XANES spectra of $LaAlO_3$ measured in transmission and in HERFD modes using two different fluorescence lines. The energy bandwidth of the incident X-rays, monochromatized using a Si(111) double-crystal monochromator, was approximately 1 eV, while the natural width of the La L_1-edge due to the core-hole is 4.1 eV. On the contrary, the natural width of the La N_3-edge is 1.5 eV. Consequently, the La L_1-edge HERFD-XANES spectrum measured by collecting the La $L_{\gamma 3}$ (L_1-N_3) line exhibits a much improved energy resolution that is dominated by the N_3 hole.

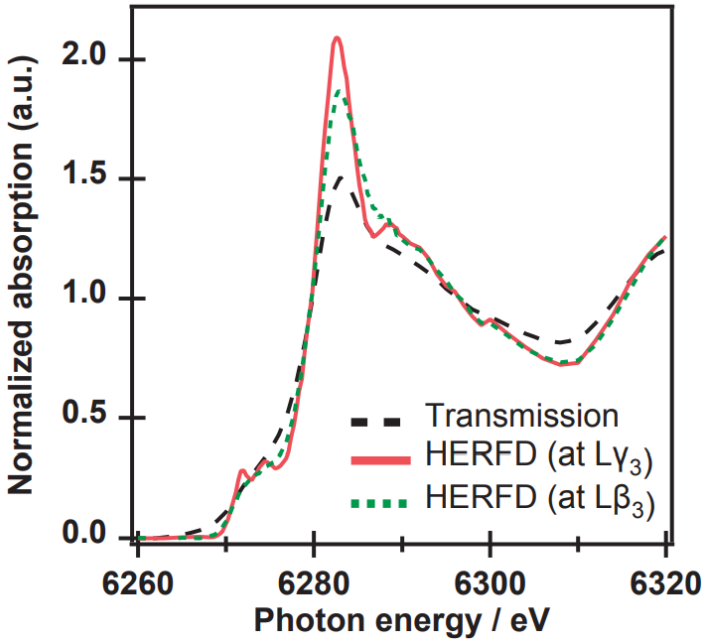

Figure 2.7. La L_1-edge XANES spectrum of $LaAlO_3$ in transmission mode (black) and HERFD-XANES spectra acquired the $L_{\beta 3}$ or $L_{\gamma 3}$ lines (green and red, respectively) highlighting the different energy resolution. Figure reproduced with permission from ref. [185], published by Oxford University Press, Copyright 2021.

It should be noted that a HERFD-XANES spectrum represent a cross-section on the wider two-dimensional plane of RIXS.[185] Therefore, the HERFD-XANES spectrum is just a particular case of RIXS in which the emitted energy is kept constant (and therefore, the energy transfer increases linearly with the incident energy).[188] As an example, an experimental 1s2p RIXS plane is shown in **Figure 2.8**, where the axes represent the incident energy ($\hbar\omega_{in}$) and the energy transfer ($\hbar\omega_{in} - \hbar\omega_{out}$). The transition to energy continuum above the localized states (main absorption edge) appears as a broad streak along the diagonal at higher energy, while the transitions to localized states (pre-edge features) appear as spot resonances at well defined positions in the plane. The two groups of diagonal features visible in **Figure 2.8** are vertically split by the 2p spin–orbit interaction in the final state, corresponding to the $K_{\alpha 1}$ and $K_{\alpha 2}$ emission lines (i.e. $K-L_3$ and $K-L_2$). A diagonal cut will then give the HERFD-XANES spectrum. The improvement in resolving the spectral features (sharpening effect), discussed previously, is striking at the $L_{2,3}$ edges of 5d elements when compared to standard XANES while at K pre-edge of 3d elements allows to detect finer details due to the strong reduction of the background signal.[184]

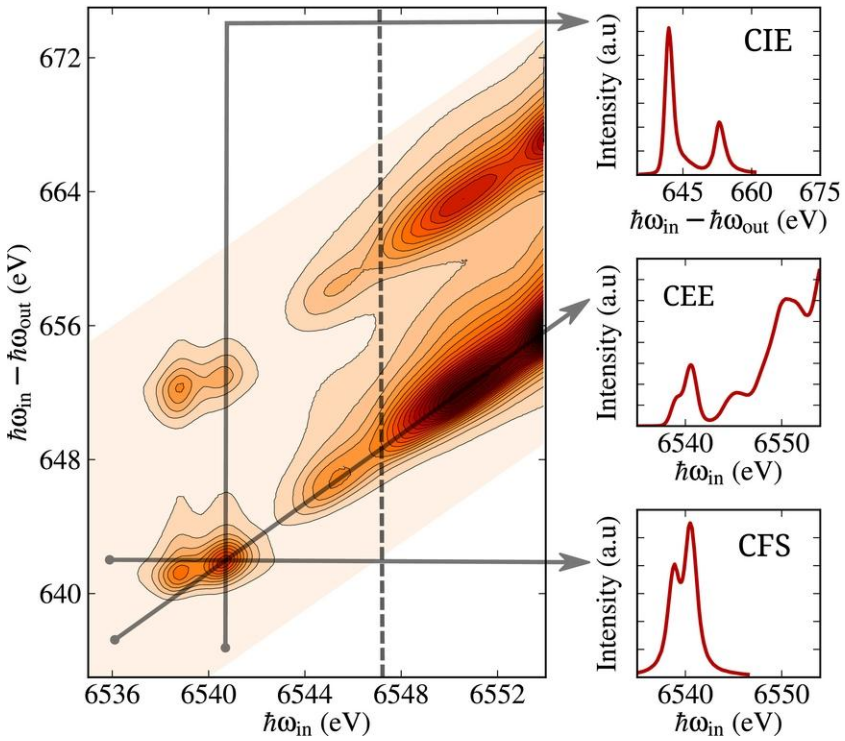

Figure 2.8. 1s2p RIXS intensity plane for a $Ga_{0.97}Mn_{0.03}N$ thin film. The insets show line cuts in three main directions: the emission spectrum is measured at constant incident energy (CIE), HERFD-XAS is measured at constant emitted energy (CEE). The vertical dashed line indicates the position of the Mn K-edge. Figure reproduced with permission from [184], published by IOP Publishing, Copyright 2014.

In conclusion, XAS measurements in HERFD mode enable a more advanced analysis of local electronic and geometric structures. In the field of LHPs and their lead-free alternatives, HERFD-XANES was applied to three 2D OLHPs of the $APbI_4$ type to obtain detailed insights into the electronic structure and band energy profiles at the interface with titanium dioxide, by analyzing the I L_1-edge.[38] The results show orbital narrowing when comparing the 2D OLHPs, the layered precursor PbI_2, and the conventional MAPI, highlighting that the different localizations of the band-edge states and narrow-band states are clearly due to the decreased dimensionality of the layered 2D structures. HERFD-XANES data at the I L_1-edge was also used to follow the transition from 2D to 1D induced by dimethylformamide intercalation in an OLHP.[39] Drisdell et al. combined HERFD-XANES with DFT calculations to achieve a molecular-scale understanding of the local structure and its role in defining the optoelectronic properties of $CH_3NH_3Pb(I_{1-x}Br_x)_3$ perovskites, analyzing the Pb L_1- and L3-edges, and Br and I K-edges.[43] The spectra probe ligand field splitting in the unoccupied *d* states of the material, located well above the conduction band minimum, showing high sensitivity to the halide identity, Pb–halide bond length, and Pb–halide octahedral tilting, particularly at the apical halide sites. The results indicate that in these mixed halide

compositions, the halides are randomly distributed without preferred octahedral sites, and thermal tilting motions dominate over any preferred structural distortions as a function of halide composition. HERFD-XANES was also employed for lead-free alternative materials such as halide bismuth compounds, which have attracted attention due to their potential in optoelectronic applications and rich structural chemistry. By analyzing the Bi L_1- and L_3-edges, respectively, HERFD-XANES was applied to $Cs_3Bi_3I_9$ and its related precursors BiI_3 and CsI to understand its electronic structure at the atomic level, providing insights into the chemistry and band-edge properties.[40]

These studies in fact are the very few examples of HERFD-XANES in this field, and in general this technique has remained much less applied than conventional XAS: even more rarely applied in the tender X-ray range due to technical challenges that require dedicated instrumental solutions. Tender X-rays can be defined as encompassing the K-edges of elements from Al to O, i.e., from 1.5 to 4.5 keV. It also include the K-edges of P, S, Cl, Ar, K, and Ca, and the L-edges of transition metals and other heavy elements such as In and Sb. Tender X-rays require special attention due to their limited penetration depth. Consequently, the path of the X-rays through air must be minimized or eliminated, and X-ray windows must be extremely thin. Monochromators are often based on Bragg optics using perfect crystals, as gratings employed in the soft X-ray range rapidly lose reflection efficiency with increasing energy. Many experimental stations worldwide, including free-electron lasers, develop and install instruments adapted to the tender X-ray range, and the ID26 tender spectrometer is discussed in more detail in the next section.[189]

2.3. XAS Experiments

In the following chapters, the results obtained in a series of XAS experiments at different synchrotron facilities are described. The experiments at the Pb and Bi L_3-edges (discussed in Chapter 3) and at the Sn K-edge (discussed in Chapter 4) were performed both at Elettra Sincrotrone Trieste (Trieste, Italy) and at the ESRF (Grenoble, France). The Cu K-edge measurements (discussed in Chapter 6) were acquired at the ESRF, as were the Cl and K K-edges, and Sb, In and Ag L_3-edge: all these measurements in the tender X-ray range (discussed in Chapters 5 and Chapter 6) were acquired in HERFD-XANES mode, under vacuum. Finally, the Sb K-edge XAS spectra (discussed in Chapter 6) were acquired at Synchrotron SOLEIL (Saint-Aubin, France). Data reduction was performed with Athena[190] and with Pymca[191] for HERFD-XANES, and the EXAFS analysis was performed with Viper[192] using theoretical scattering paths generated with FEFF9.[193]

The tender X-ray spectrometer at the ESRF ID26 beamline (**Figure 2.9**), used for the acquisition of all HERFD-XANES spectra discussed in this thesis, is more complicated than the setup for a conventional XAS experiment, and it warrants a separate description. It employs a point-to-point focusing geometry with vertical scattering planes.[194] It is equipped with eleven high-quality analyzer crystals (cylindrical Si, Ge, $LiNbO_3$, and β-SiO_2 single crystals) that monochromatize the emitted radiation, covering an emitted energy range between 1.5 keV and 5.5 keV, which is eventually collected with either a gas detector or a hybrid-photon-counting solid state detector.[195] The resulting energy bandwidth is close to or below the core-hole lifetime broadening of the measured emission lines. Sagittal focusing is achieved via a "pantograph" mounted on a sagittal plate, which is rotated to reach the Bragg angle. The pantograph allows the use of cylindrical crystals instead of spherical ones, whose fabrication is less demanding, more cost-effective, and with reduced figure errors. The ultra-high vacuum of the spectrometer minimizes X-ray attenuation in the tender X-ray energy range. These features make ID26 one of the best performing and sought-after beamlines in the world for the application of HERFD-XANES.[189,194]

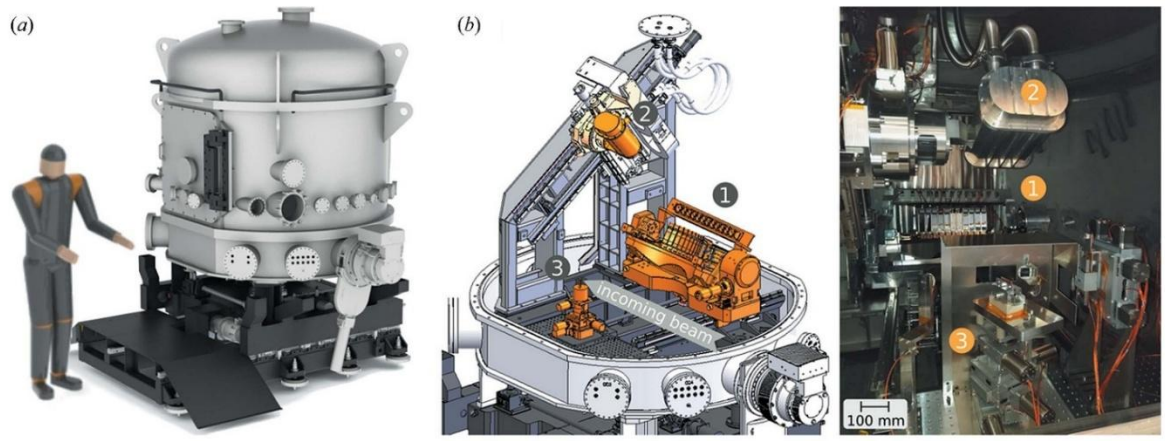

Figure 2.9. Layout of the TEXS spectrometer at the ID26 beamline of ESRF. (a) 3D rendering of the external view. (b) Internal view as 3D drawing (left, upper parts of the vacuum vessel are removed for clarity) and photograph (right), showing the spectrometer frame with the main sub-assemblies: analyzer table (1), detector (2) and sample environment (3). The incoming beam direction (X) is represented with a grey arrow. Figure reproduced from ref. [194], with permission from International Union of Crystallography, Copyright 2020.

On the whole, the results discussed in the following chapters represent one of the first systematic applications of XAS to HPs, and, to the best of our knowledge, the first application of HERFD-XANES to HDP NCs. To prevent possible radiation damage[43] or decomposition into simple halides,[196] the very small size of the synchrotron microbeam was exploited to track the time evolution of the absorption edges through repeated scans and minimized by performing fast scans at different sample positions. A comparison between the spectra collected on fresh and previously irradiated spots revealed the emergence of incipient damage at the Sb L_3-edge after several tens of seconds, while the other edges remained essentially unchanged (**Figure 2.10**).

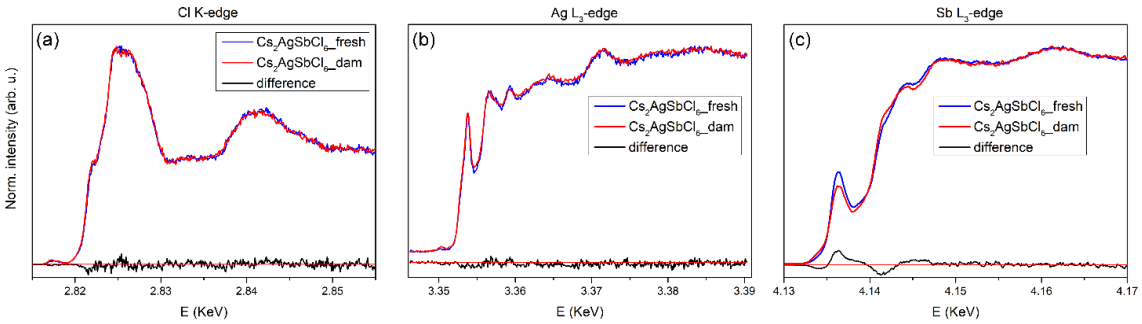

Figure 2.10. Assessment of radiation damage in HERFD-XANES measurements on $Cs_2AgSbCl_6$ at ID26. Spectra averaged over about 100 fresh spots (blue), and over the same spots that were already exposed to the beam once (red), along with their difference (black), at the a) Cl K-edge, b) Ag L_3-edge and c) Sb L_3-edge. While Cl and Ag edges do not show significant evidence of damage, a non-random difference is evident at the Sb L_3-edge.

The success of this initial study that proved the samples do not degrade significantly (which is not obvious under a very brilliant tender X-ray beam), led to a second experiment, carried out at the end of 2025, in which the Ag and In L_3-edges and the K and Cl K-edges (3.3–5.0 keV) were analyzed through the corresponding L_3M_5 and KL_3 emission lines (discussed in Chapter 5). The combined set of these data, complemented by X-ray diffraction measurements, enabled an extremely accurate structural characterization of each sample. Although the acquisition of a XAS spectrum itself may be relatively straightforward, a full understanding of the data analysis is often challenging, especially in the XANES region. A particularly useful tool for understanding these data is represented by *ab initio* simulations, which allow for the refinement of both 1) a local structural model providing an accurate assessment of the distortions and structural variations induced by cation substitution, and 2) the electronic features of the absorbing atom and of its coordination shell. The theoretical framework of ab initio XANES simulations is outlined in the following section.

2.4. Simulation of XANES Spectra

Ab initio simulations of the XANES spectra were performed using the FDMNES code, which allows simulations of X-ray absorption or scattering spectroscopies at energies close to the characteristic absorption edges.[197] FDMNES is a DFT code that employs the LDA to calculate the core-hole excited states (optionally with self-consistency using the SCF procedure), possibly with the addition of the Hubbard correction (LDA+U) for a better description of electronic correlation in *d* orbitals of transition metals or *f* orbitals of lanthanides. FDMNES exploits the space group symmetry to identify equivalent atoms in the unit cell of periodic crystalline systems, thus reducing the computational time significantly when crystalline solids are treated. Two different approaches are available to calculate XAS spectra:[198] 1) the FDM method represents a general approach to solve differential equations and, in the context of XANES, the Schrödinger equation, by discretizing it on a three-dimensional grid that spans the volume around the absorbing atom. The computational region is bounded by an outer sphere in which the potential is assumed to be constant. Within this framework, the wave function is calculated at every grid point, and the potential is unconstrained in shape, thereby avoiding the widely used muffin-tin approximation. Inside the atomic core, the potential can be represented using a multipole expansion, typically reduced to the dominant spherical term. This is because, in this region, the potential exhibits frequent variations due to the actual distribution of charges around the atom. In the outer regions, farther from the nucleus, the potential varies more gradually, and the electron wave function can be treated in a simpler way: for this reason, there the potential is assumed to be constant or spherically symmetric. The potential is then calculated using LDA, and no further approximations are introduced, requiring significant computation time.[199,200] 2) The MST method, on the other hand, is based on the muffin-tin approximation, in which the potential is assumed to be spherically symmetric around the atoms and constant between neighboring atoms beyond a certain distance from the nucleus. This approximation allows the use of Green's functions to rapidly compute scattering amplitudes and, consequently, absorption spectra, making the method far more efficient than FDM computationally. However, this comes at the expense of accuracy, as the shape of the potential is constrained. In practice, MST is preferable for extended solids or very large clusters where the use of FDM would become prohibitively time-consuming.[198,199] This approximation is used in most codes for XAS and EXAFS analysis (e.g. FEFF), and while it may lead to less accurate results, it nevertheless allows for much faster calculations.

In this thesis, all XANES simulations were carried out with the FDMNES software,[198] employing the MST method for all simulations on extended solids where, due to the large number of atoms, the FDM approach would result in prohibitively long computation times. The FDM approach was instead used for the XANES simulations of isolated [PbI_6] and [BiI_6] octahedra (discussed in Chapter 3), and for isolated $CuCl_n$ clusters (discussed in Chapter 6). For the Cu K-edge simulations in isolated $CuCl_n$ clusters, the semi-empirical screening parameter was also employed: this parameter models the screening of the core-hole created upon photoelectron excitation. At the K-edge, when a 1s electron is promoted to an unoccupied state, the positively charged core-hole strongly perturbs the local potential of the photoabsorbing atom. The screening parameter, which can vary between 0 (no screening) and 1 (full screening), then introduces an additional electron into the lowest unoccupied state of the excited atom, as if originating from the bonds with neighboring atoms, and thus compensates the core-hole reducing its perturbative effect on the potential. A screening value of 0 therefore corresponds approximately to an atom with an effective charge of +1, whereas a value of 1 restores the atom to an almost neutral charge state, effectively simulating maximal charge transfer from the surrounding atoms. In this context, the use of the screening parameter aims to reproduce the degree of hybridization between the copper *d* orbitals and the chlorine *p* orbitals, capturing both the nature of the copper center and the possible charge transfer along the Cu–Cl bond. A low screening value can indicate a higher positive charge on the copper atom, and therefore a higher basicity. Consequently, variations in the screening value can help reproduce the spectral features and provide insights into electronic modifications. It is worth noting that this parameter does not describe a dynamic process; i.e., the charge transfer does not occur in response to photon absorption, but it is an intrinsic property of the system, already present before the photoexcitation event.

3. Substitution of the Organic Cation in OLHP

*Adapted with permission from J. Phys. Chem. C **2023**, 127, 18058−18066. Copyright 2023 American Chemical Society.*

3.1. Introduction: Influence of the Organic Cation on Stability

Hybrid LHPs containing MA and FA are fundamentally limited by their poor stability under ambient conditions, which has been attributed to the presence of the amines, since inorganic HPs display much better stability.[9,32,51] One of the main vulnerabilities of MAPI is exposure to moisture. The absorption of water by the hybrid perovskite leads to the formation of CH_3NH_3I and PbI_2. Subsequently, CH_3NH_3I further decomposes into CH_3NH_2 and HI. In the presence of oxygen, HI can decompose into I_2 and H_2O, or under UV light, it can decompose into H_2 and I_2. Continuous consumption of HI therefore drives the complete degradation of the perovskite. Besides hydrolysis, thermal stability is also a critical aspect for MAPI. This OLHP typically undergoes degradation or phase transformations under prolonged high-temperature stress, primarily due to the low thermal conductivity of $MAPbI_3$ films, attributed to the MA cation, which prevents rapid dissipation of the generated heat in the PSCs. MAPI also exhibits three symmetries from higher to lower temperatures: cubic, tetragonal, and orthorhombic. Therefore, accurate temperature control is also an important factor for OLHP stability.[32] To address this issue, a wide range of organic cations has been investigated as potential substitutes for MA and FA in the A-site of LHPs. Depending on the type and relative size of the constituent ions, LHPs can form either three-dimensional structures or can crystallize into layered, one-dimensional, or zero-dimensional structures.[101,183,201–203] Smith et al.[204] synthesized a PEAI 2D perovskite, which was employed in PSCs exhibiting a PCE of 4.71% and remaining stable for 46 days, in contrast to the 3D OLHPs discussed previously. The benefits of incorporating PEA into 3D HPs were also reported by Lee et al.[205] The presence of wide-bandgap PEA-based quasi-2D perovskite is good for reducing

defect density and slowing down the degradation. Other than PEA, BA can also be used to fabricate 2D perovskites. A BA based Ruddlesden–Popper/3D heterostructure was recently tested along with molecule passivation to improve α-$FAPbI_3$ films for high-performance and ambient-air-stable PSCs.[206]

Other large organic cation–based additives include FEAI and imidazolium iodide, which are likely to result in the formation of 1D structures. Bi et al.[207] reported FEAI additive in $MAPbI_3$ with the possible formation of 1D $FEAPbI_3$ perovskite that enhanced the overall perovskite morphology and stability of the perovskite devices. Imidazolium iodide was also shown as an effective additive in a perovskite precursor to boost PSC performance via defect passivation.[208] The use of a wide range of mixed organic cations at the A site of OLHPs, together with the incorporation of additives, can influence perovskite crystallization and film formation, defect passivation in the bulk and/or at the surface, as well as the structural and energetic tuning of interfaces.[201] Many of these routes also lead to the formation of low-dimensional structures, in which additives are also incorporated in the lattice. Consequently, a comprehensive knowledge of the structure is crucial for the eventual development and optimization of optoelectronic devices. Although materials research has predominantly focused on low-bandgap compositions, wide-bandgap (>1.7 eV) halide perovskites have progressively emerged in recent years as promising candidates for several alternative applications.[209,210]

In this chapter the replacement of the commonly employed organic cations (such as MA and FA) with TMSO is discussed. The replacement imparts improved stability to these materials under ambient conditions for at least one month, followed by the subsequent doping of the B site with Bi^{3+}. $(TMSO)PbI_3$ and $(TMSO)_3Bi_2I_9$ form a solid solution with a monodimensional perovskite-like structure based on face-sharing octahedra, incorporating either Pb^{2+}, Bi^{3+}, or a metal cation vacancy, the latter required to preserve charge neutrality. Their rich defect chemistry and the ordering of metal cation sites have been described in detail in recent works.[183,202] The reduced connectivity of the octahedra in one dimension could in fact hinder their applicability in photovoltaics, while applications in thermoelectricity generation could be foreseen considering the very low thermal conductivity of lower-dimensional perovskite-like structures.[211]

To further investigate the local structure of these one-dimensional halide pseudo-perovskite materials, a comprehensive modeling of the near-edge spectra of both the metal and iodine atoms was therefore carried out. *Ab initio* simulations of the spectra and pDOS were carried

out using a bottom-up approach, which allowed the establishment of generally applicable criteria. The analysis was carried out starting from the $[PbI_6]^{4-}$ and $[BiI_6]^{3-}$ octahedral units, which constitute common building blocks in any pseudo-perovskite, and was progressively extended to the full $(TMSO)_3Pb_{3x}Bi_{2(1-x)}I_9$ structure. All possible Pb/Bi substitution patterns in a supercell containing eight metal sites were included to account for multiple scattering effects between neighboring metals. Finally, the simulations were compared with experimental XANES spectra, demonstrating that these can be effectively modeled using $[PbI_6]^{4-}$ and $[BiI_6]^{3-}$ units, while also providing indirect information on the long-range structural organization.

3.2. Synthesis and Characterization of Pb/Bi OHP

$(TMSO)_3Pb_{3x}Bi_{2(1-x)}I_9$ powders were prepared by precipitation from an aqueous solution, dissolving the corresponding metal oxides in hydroiodic acid. After complete solubilization, TMSO was added, inducing the immediate precipitation of the product, which was subsequently filtered and dried. The synthesis method, described in detail in the Appendix, is shown in **Scheme 3.1**.

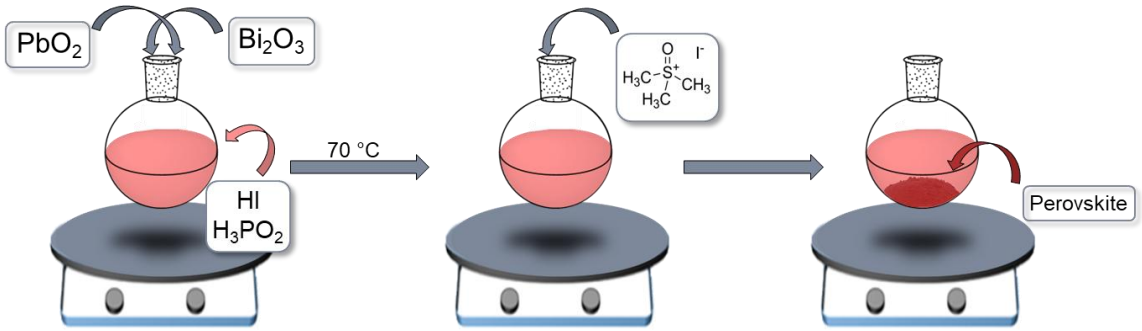

Scheme 3.1. Scheme of the synthesis of all samples.

$(TMSO)PbI_3$ crystallizes in the orthorhombic *Pnma* space group. Each Pb^{2+} cation is octahedrally coordinated by six iodide anions, forming $[PbI_6]^{4-}$ octahedra. These octahedra share faces, with each iodide anion bridging two Pb^{2+} cations and Pb−I bond lengths ranging from 3.16 to 3.26 Å. This arrangement gives rise to infinite one-dimensional $[PbI_3]^{\infty}$ polyanionic chains aligned along the *a*-axis (**Figure 3.1a**). These chains are interspersed with $TMSO^+$ cations, resulting in a one-dimensional pseudo-perovskite structure. In contrast, the Bi-based phase, $(TMSO)_3Bi_2I_9$, features $[Bi_2I_9]^{3-}$ clusters spaced by vacant sites along the *a*-axis (**Figure 3.1b**). These ordered sequences alternate fully populated and vacant metal sites in a 2:1 ratio, where the average space group *Pnma* is retained.

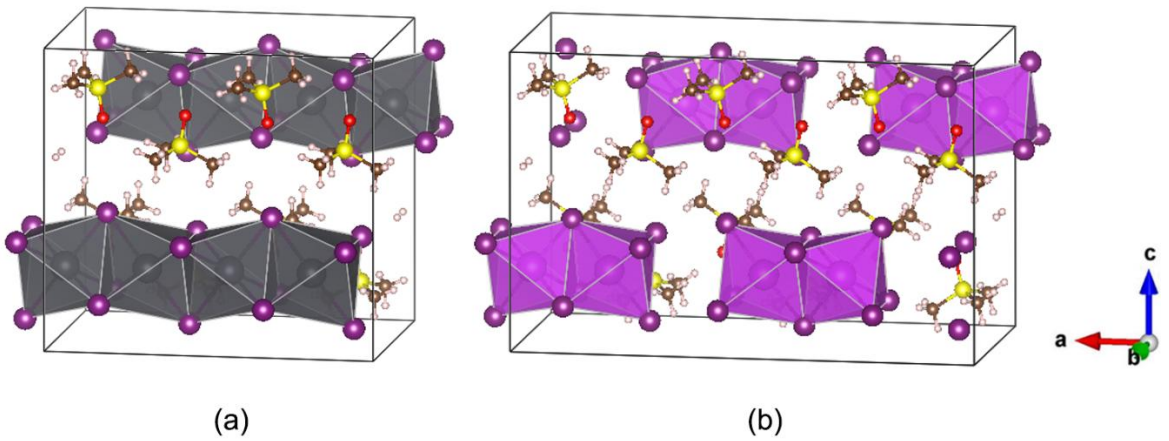

Figure 3.1. (a) An undoped $TMSOPbI_3$ 2 x 1 x 1 supercell, with composition $TMSO_8Pb_8I_{24}$. (b) $(TMSO)_3Bi_2I_9$ 3 x 1 x 1 supercell. Iodine atoms are in violet, PbI_6 octahedra are in grey, BiI_6 octahedra in pink. Carbon, sulfur, oxygen, and hydrogen atoms are in grey, yellow, red, and white, respectively. The octahedral chains are aligned along the *a* crystallographic axis.

The mixed-metal phases, prepared by combining Bi^{3+} and Pb^{2+} in various molar ratios, are structurally isomorphous with the parent compounds. The stoichiometry of the two end-member compounds was determined from TG profiles, where the weight losses due to (TMSO)I release were fully resolved.[202] For Pb-based compounds, a 1:1 TMSO/Pb ratio was observed, while Bi-based compounds conformed to a 3:2 TMSO/Bi ratio, yielding formulas $(TMSO)PbI_3$ and $(TMSO)_3Bi_2I_9$, respectively. Thermal analysis indicates also that these materials are stable up to 200 °C, with no phase transitions between 25 and 200 °C, an important distinction from traditional perovskites, which often feature complex phase behavior. To obtain precise stoichiometries for the mixed-metal phases, ICP-OES analysis was conducted on the six mixed samples (**Table 3.1**).

Table 3.1. Crystal structure and stoichiometry of all samples, with Bi % expressed as Bi/(Bi+Pb), and as x in $(TMSO)_3Pb_{3x}Bi_{2(1-x)}I_9$. Uncertainty is reported in parentheses.

Labels	Bi%	x	Crystal data				Formula
			a (Å)	b (Å)	c (Å)	V (Å^3)	
Pb100	0	1	7.8126(1)	11.2000(4)	14.3970(4)	1259.76(4)	$(TMSO)PbI_3$
Pb92	8	0.89	7.7831(2)	11.2007(3)	14.3886(4)	1254.34(6)	$(TMSO)_3Pb_{2.67}Bi_{0.22}I_9$
Pb90	10	0.87	7.7735(1)	11.2069(6)	14.4185(1)	1256.10(2)	$(TMSO)_3Pb_{2.61}Bi_{0.26}I_9$
Pb78	22	0.71	7.7279(9)	11.2116	14.4034(6)	1247.96(2)	$(TMSO)_3Pb_{2.13}Bi_{0.58}I_9$
Pb66	34	0.56	7.6862(4)	11.2090(2)	14.3912(3)	1239.87(8)	$(TMSO)_3Pb_{1.68}Bi_{0.88}I_9$
Pb42	58	0.33	7.5930(4)	11.2147(2)	14.3958(2)	1225.84(7)	$(TMSO)_3Pb_{0.99}Bi_{1.34}I_9$
Pb22	78	0.17	7.5223(2)	11.2199(4)	14.4041(3)	1215.70(9)	$(TMSO)_3Pb_{0.51}Bi_{1.66}I_9$
Pb0	100	0	7.4530(1)	11.2169(2)	14.4009(2)	1203.92(3)	$(TMSO)_3Bi_2I_9$

The XRD analysis shows minor and predictable variations in peak position and intensity upon changing the stoichiometry of the material, showing that this solid solution essentially follows Vegard's law. For all the mixed species the derived unit cell parameters follow distinct trends as a function of the Bi/Pb ratio. In particular, the *b* and *c* parameters (normal to the metal halide chains) are essentially unaffected by the extent of substitution; the *a* parameter, by contrast, decreases linearly with increasing Bi content (**Table 3.1**). This observation aligns with the nearly constant *b* and *c* parameters (i.e., the cross-section of the polyanionic metal iodide chains), while the relative ionic sizes and presence of vacant sites shrink the average periodicity along *a*.

The difference in valence between Bi^{3+} and Pb^{2+} requires some charge compensation mechanism to preserve electroneutrality. This can occur via either ionic (e.g., vacancies or interstitials) or electronic (e.g., excess electrons or holes) compensation. The unit cell contains four formula units of $(TMSO)PbI_3$, corresponding to a stoichiometry of $(TMSO)_4Pb_4I_{12}$, with the four Pb^{2+} ions arranged in two parallel linear chains. The crystallographic structure was replicated along the *a*-axis (the shortest axis), generating a 2 × 1 × 1 supercell with the composition $(TMSO)_8Pb_8I_{24}$. This replication yields two linear chains, each containing four Pb^{2+} sites. three charge compensation mechanisms involving negatively charged ionic defects are considered, and described by the following Kröger-Vink equations:

Substitution of the Organic Cation in OLHP

1. **Lead vacancy:** V''_{Pb}

$$3Pb^{x}_{Pb} + 2BiI_3 \rightarrow 2Bi^{\bullet}_{Pb} + V''_{Pb} + 3PbI_2 \quad (3.1)$$

2. **TMSO vacancy**: V'_{TMSO}

$$TMSO^{x}_{TMSO} + Pb^{x}_{Pb} + 2BiI_3 \rightarrow Bi^{\bullet}_{Pb} + V'_{TMSO} + PbI_2 \quad (3.2)$$

3. **Iodine interstitial**: I'_i

$$Pb^{x}_{Pb} + BiI_3 \rightarrow Bi^{\bullet}_{Pb} + I'_i + PbI_2 \quad (3.3)$$

Among the three mechanisms, the one involving the lead vacancy (V''_{Pb}, mechanism (3.1)) is the most favorable, and it is also the only one that directly alters the composition of the chains along the *a*-axis, reproduces the experimental contraction well. In contrast, mechanisms (ii) and (iii) mainly affect the *b* and *c* axes, due to the presence of interstitial iodide or altered TMSO stacking, and fail to reproduce the experimentally observed trends.

Therefore, mechanism (3.1), in which three Pb^{2+} ions are replaced by two Bi^{3+} ions, resulting in one vacant cation site (V''_{Pb}), emerges as the most consistent with experimental data and the solid solutions are best described by the general formula $(TMSO)_3Pb_{3x}Bi_{2(1-x)}I_9$ ($0 \leq x \leq 1$), with x = 1 and x = 0 representing the pure Pb and Bi end-members, respectively.

The Pb/Bi/vacancy alternation is both nonperiodic and nonrandom, and it can be modeled to some extent as correlated disorder governed by a second-order stochastic matrix. For a $(TMSO)_8Pb_2Bi_4I_{24}$ composition, there are 16 possible dispositions of Pb/Bi/vacancy in the eight metal cation sites of a 2 × 1 × 1 supercell, labeled A to R. The configurational energy is then due to the different interaction terms between cation pairs (i.e., the next-nearest-neighbor Pb−Pb, Bi−Bi, Pb−Bi, etc. correlations), as summarized in **Table 3.2**. Configuration A (**Figure 3.2**) exhibits the lowest energy and is therefore the most probable among all the configurations considered. This stability can be attributed to the presence of Bi–V pairs, which are energetically the most favorable and effectively reduce the overall energy of the system. At the same time, the absence of Pb–V and Bi–Bi pairs, associated with the highest energetic contributions, further enhances the structural stabilization, making configuration A the most likely from an energetic standpoint.

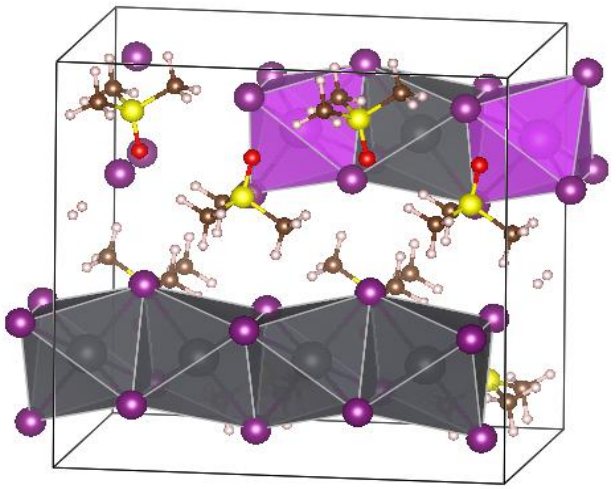

Figure 3.2. Doped $TMSO_8Pb_5Bi_2I_{24}$ supercell, in configuration A. Iodine atoms are in violet, PbI_6 octahedra are in grey, BiI_6 octahedra in pink. Carbon, sulfur, oxygen, and hydrogen atoms are in grey, yellow, red, and white, respectively.

Table 3.2. Energy of all different configurations in $(TMSO)_8Pb_2Bi_4I_{24}$, relative to lowest-energy configuration "A", calculated with periodic DFT at the PBE level. Data taken from ref. [183].

Configuration	Energy (eV)
A	0
B	0.58
C	0.58
D	0.56
E	0.48
F	0.52
G	1.11
H	1.04
I	0.97
L	1.03
M	1.48
N	1.39
O	1.39
P	1.47
Q	1.39
R	1.54

3.3. X-ray Absorption Spectroscopy of Pb/Bi OHP

The following structural models were used to compute the XANES spectra at the Pb and Bi L_3 edges: (1) isolated MI_6 octahedra (M = Pb or Bi); (2) 2 × 1 × 1 supercells with composition $(TMSO)_8Pb_2Bi_4I_{24}$, including all possible Pb/Bi arrangements in the eight metal cation sites, described in detail in ref [183]. XANES spectra were then calculated for all configurations (**Figure 3.3**).

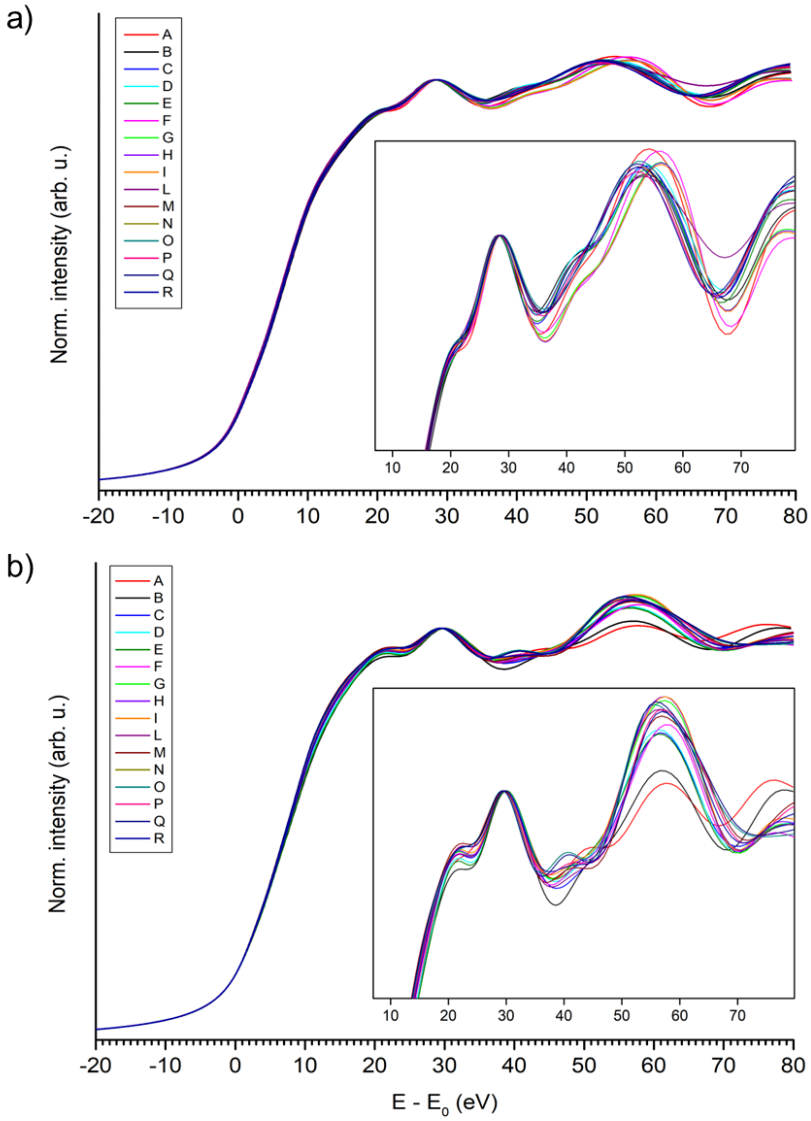

Figure 3.3. XANES spectra of all configurations at the Pb L_3-edge (a) and Bi L_3-edge (b).

For iodine, XANES spectra were simulated at the L_1-edge (**Figure 3.4a**): this absorption edge corresponds to the iodine 2s orbital, therefore probing dipole allowed transitions to 5p

states, which are hybridized with metal 6s in the Pb/Bi–I bonds. The simulated I L_1 spectra show substantial differences in the intensity of the white line and reflect the electronic density of states of the empty 5p orbitals of iodine. Compared to literature I L_1 spectra of 3D and 2D perovskites,[38] each octahedral face is shared here between two neighboring octahedra, and the local coordination of iodine atoms gives rise to a much different edge shape. The onset of the L_1 edge also correlates well with the position of the conduction band minimum. For instance, the energy of the I L_1 edge increases from configuration O to configurations A and B: the conduction band minimum also increases from configuration O to configurations A and B. The absence of any pre-edge shoulder at low energy reflects the purely ionic interaction between $TMSO^+$ and iodide, with no mixing with the I p states.[183]

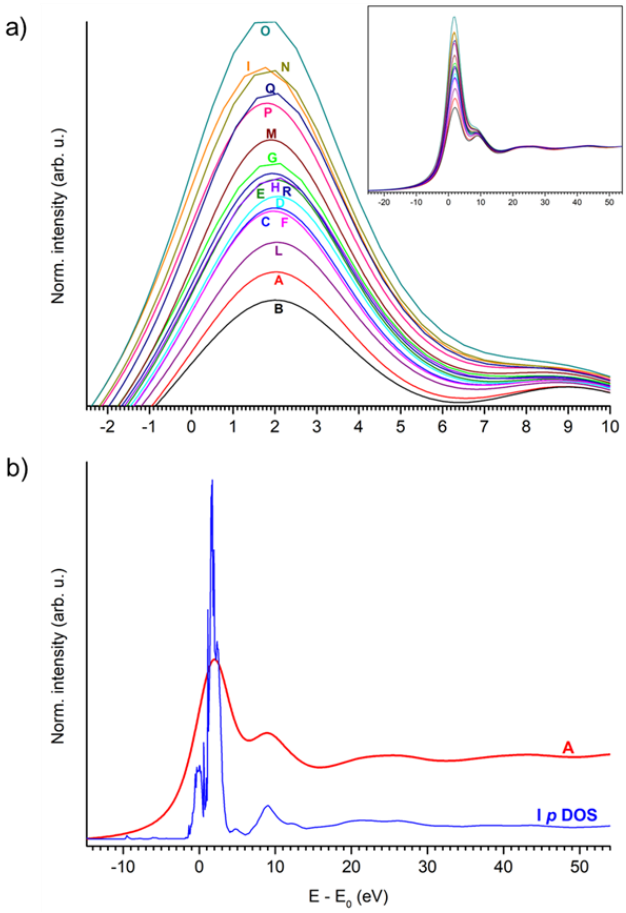

Figure 3.4. (a) XANES spectra, at the I L_1-edge, of all configurations; (b) I L_1-edge spectra of A configuration (red) and the average of the p DOS (blue) of all iodine atoms.

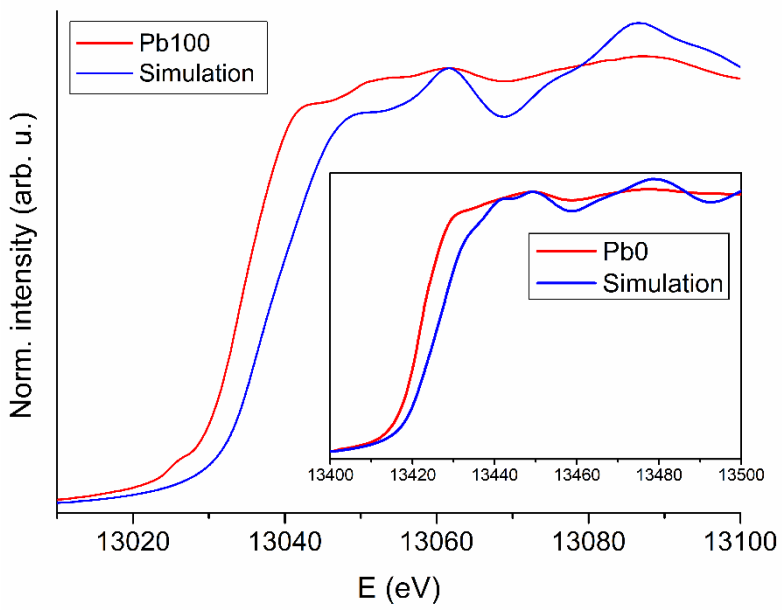

Figure 3.5. Experimental (red) Pb L_3-edge and simulated (blue) XANES spectrum of $(TMSO)PbI_3$. Inset: experimental spectrum (red) on Bi L_3-edge and simulated (blue) XANES spectrum of $(TMSO)_3Bi_2I_9$.

The experimental Pb and Bi L_3-edge spectra of the end members $(TMSO)PbI_3$ and $(TMSO)_3Bi_2I_9$ (**Figure 3.5**) were compared with simulations from the respective crystal structures in **Figure 3.1**. For mixed samples, a first comparison shows that all samples are very different from PbI_2 and BiI_3, and therefore, the decomposition to simple iodides from radiation damage can be reasonably excluded (**Figure 3.6**). All Pb near-edge features of samples look similar (**Figure 3.6a**), while Bi shows varying intensities for the edge features (three peaks up to 25 eV after the edge) depending on the Pb/Bi content (**Figure 3.6b**). In general, configuration A is the one that resembles more the experimental data of all mixed samples for Pb and Bi L_3-edges, as seen especially in the position and intensity of maxima and minima >30 eV above the edge. This configuration features maximum segregation of Bi and vacancy defects in linear clusters [Bi−V−Bi], and having the lowest configurational energy it has the highest probability of being represented in an average ensemble in the bulk.

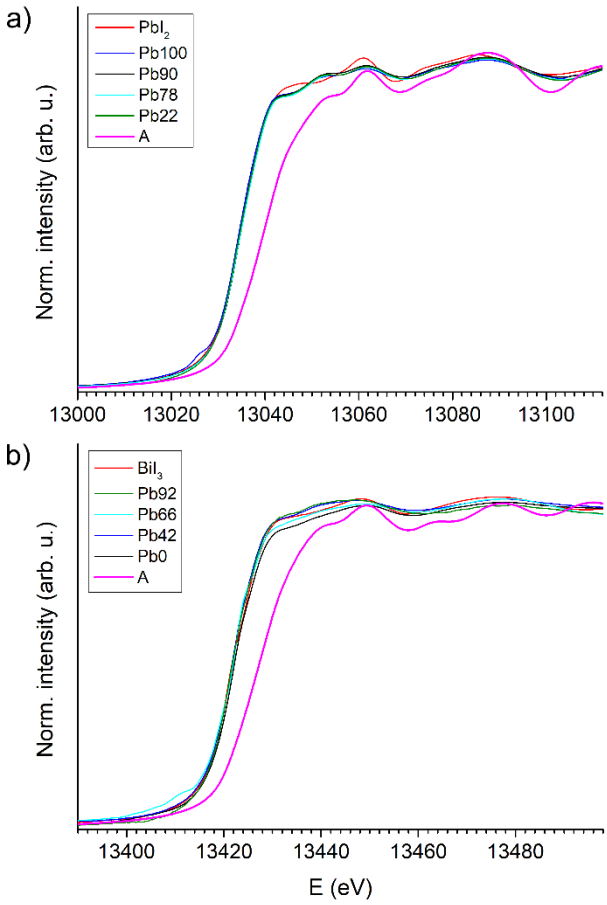

Figure 3.6. (a) experimental XANES spectra on Pb L_3-edge compared to the precursor PbI_2, and the simulated spectrum of configuration A (magenta); (b) experimental XANES spectra on Bi L_3-edge compared to the precursor BiI_3, and the simulated spectrum of configuration A (magenta).

The different A-R configurations essentially differ for the weight of various metal−metal inter-octahedral multiple scattering paths, while the nearest neighbor distances are the same in all of them. After assessing how different configurations affect the near-edge spectra, we now look into the role of each MI_6 octahedron. We extracted the octahedra of configuration A (five PbI_6 and two BiI_6, depicted in **Figure 3.7a**) to simulate their Pb and Bi XANES spectra (**Figure 3.7b**). With this approach, we can first evaluate whether an experimental XANES spectrum can be explained by the individual octahedra, or the whole configuration is needed. The essential features of the complete spectrum are still recognized in the spectrum of the isolated single octahedra, but important differences are evident in all portions of the spectrum, from the main edge to further peaks.

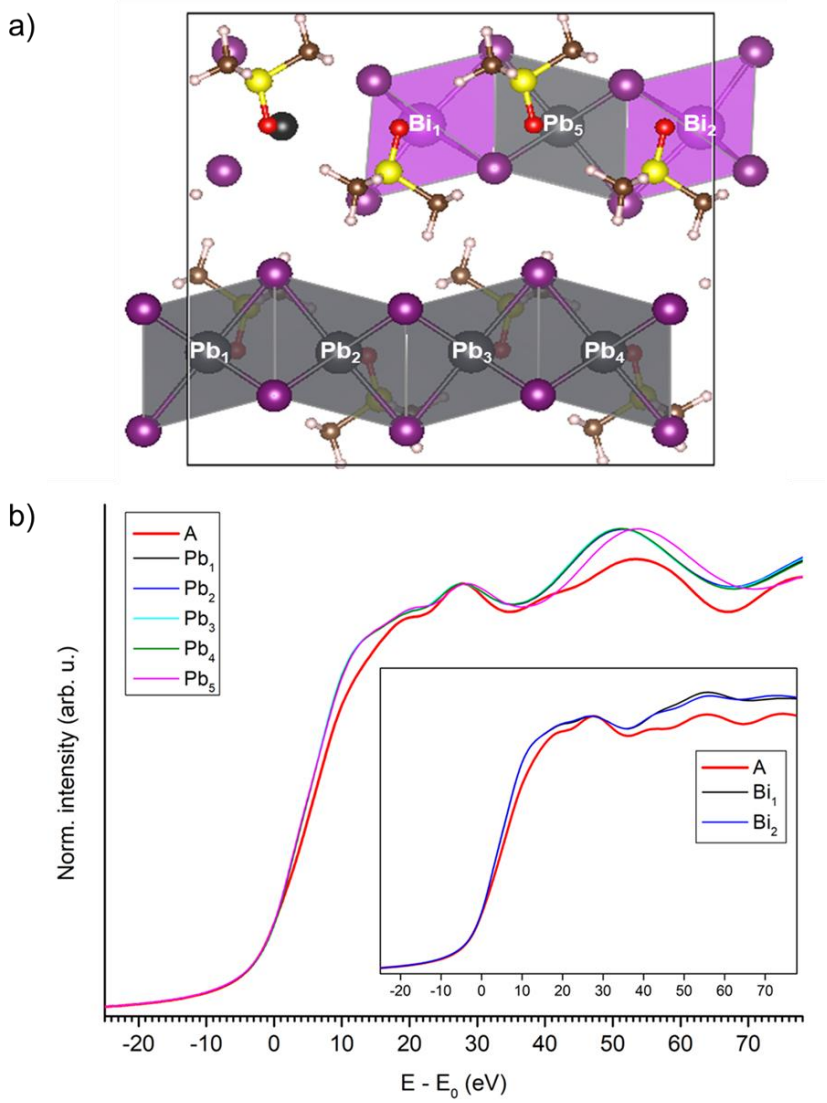

Figure 3.7. (a) Configuration A. Bi atoms are depicted in magenta, Pb atoms in grey and vacancy in black. Iodine, carbon, sulfur, oxygen, and hydrogen atoms are in violet, grey, yellow, red, and white, respectively. (b) Simulated XANES spectra of configuration A compared with its individual component octahedra at the Pb L_3-edge (main panel) and Bi L_3-edge (inset).

Comparing the experimental spectrum of mixed samples with the simulated spectra of configuration A and its octahedra (**Figure 3.8**), the individual octahedra (e.g., Pb3 and Bi2) are almost sufficient to explain all features of the experimental spectra in the edge region. In particular, the main edge features are much better reproduced by a single octahedron than the complete structure involving M−I−M intra-octahedral paths, a surprising observation for a well-crystallized compound. This corroborates the general observation that the crystal structure is only a snapshot that does not fully capture the reality of a "wobbly" ensemble, and it is likely to underestimate both static and dynamic disorder.[212] This observation

motivates the following investigation, based on the reduction of the structure to a sum of its octahedral units.

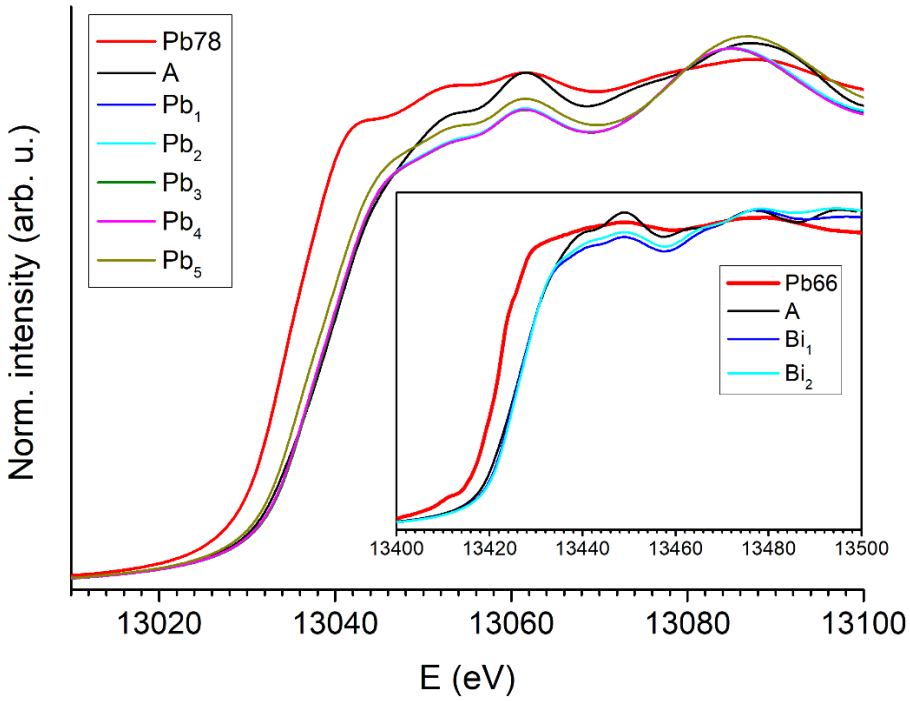

Figure 3.8. Experimental XANES spectra (thick red line) compared with the configuration A (black line) and individual octahedra (color lines) at the Pb L_3-edge (main panel) and Bi L_3-edge (inset).

3.4. XANES Simulations of Octahedral Units

Simulations of the XANES spectra were then carried out on a series of distorted isolated PbI_6 and BiI_6 octahedra starting from pristine regular ones. The possible applied distortions were: 1) skewing of one iodine atom; 2) isotropic compression and expansion; 3) anisotropic elongation/compression along one axis; 4) change of I−M−I bond angles. The effects of each modification on the Pb spectra are described in detail in the following: Bi spectra display mostly the same effects.

Iodine Skewing. The distortion of the octahedron caused by the displacement of an iodine atom along the *y*-axis, as shown in the inset of **Figure 3.9a**, results in a reduction of the I−M−I angle by approximately 6-7% at each step. From the initial 90° angle in the undistorted PbI_6 octahedron, the angle decreases to 68.2° in PbI_6_A_4 (inset of **Figure 3.9a**). To maintain a constant octahedral volume, the Pb−I bond length must increase, reaching 3.45 Å in PbI_6_A_4 compared to 3.2 Å in the undistorted PbI_6. This distortion does not cause significant variations in the XAS spectra, as it involves only a 7% elongation of a single Pb−I bond. With increasing distortion, a leftward shift of approximately 0.3 eV of the main peak is observed, along with shallower minima (**Figure 3.9a**).

Isotropic compression. An isotropic reduction of the octahedral volume by approximately 2-3% per step (inset of **Figure 3.9b**) is observed in PbI_6_B_4. This volume contraction causes a rightward shift of about 1 eV of the main XAS peak with each step, accompanied by deeper minima (**Figure 3.9b**).

Isotropic expansion. The octahedral volume increases by approximately 2.3% per step (inset of **Figure 3.9c**). From an initial volume of 43.7 $Å^3$, it reaches 47.92 $Å^3$ in PbI_6_D_4. This volume expansion causes a leftward shift of the main peak in the XAS spectra by about 1 eV per step (**Figure 3.9c**). In this case, the minimum also become systematically shallower.

Rotation. Rotation of an equatorial bond axis leads to the reduction of two bond angles and the increase of the other two by approximately 5° per step. From the initial 90° configuration, the angles become 65° and 115° in PbI_6_G_5 (inset of **Figure 3.9d**). In this case, no variations in bond lengths occur, and therefore no significant changes are observed in the calculated spectra, as multiple-scattering effects remain nearly unchanged (**Figure 3.9d**).

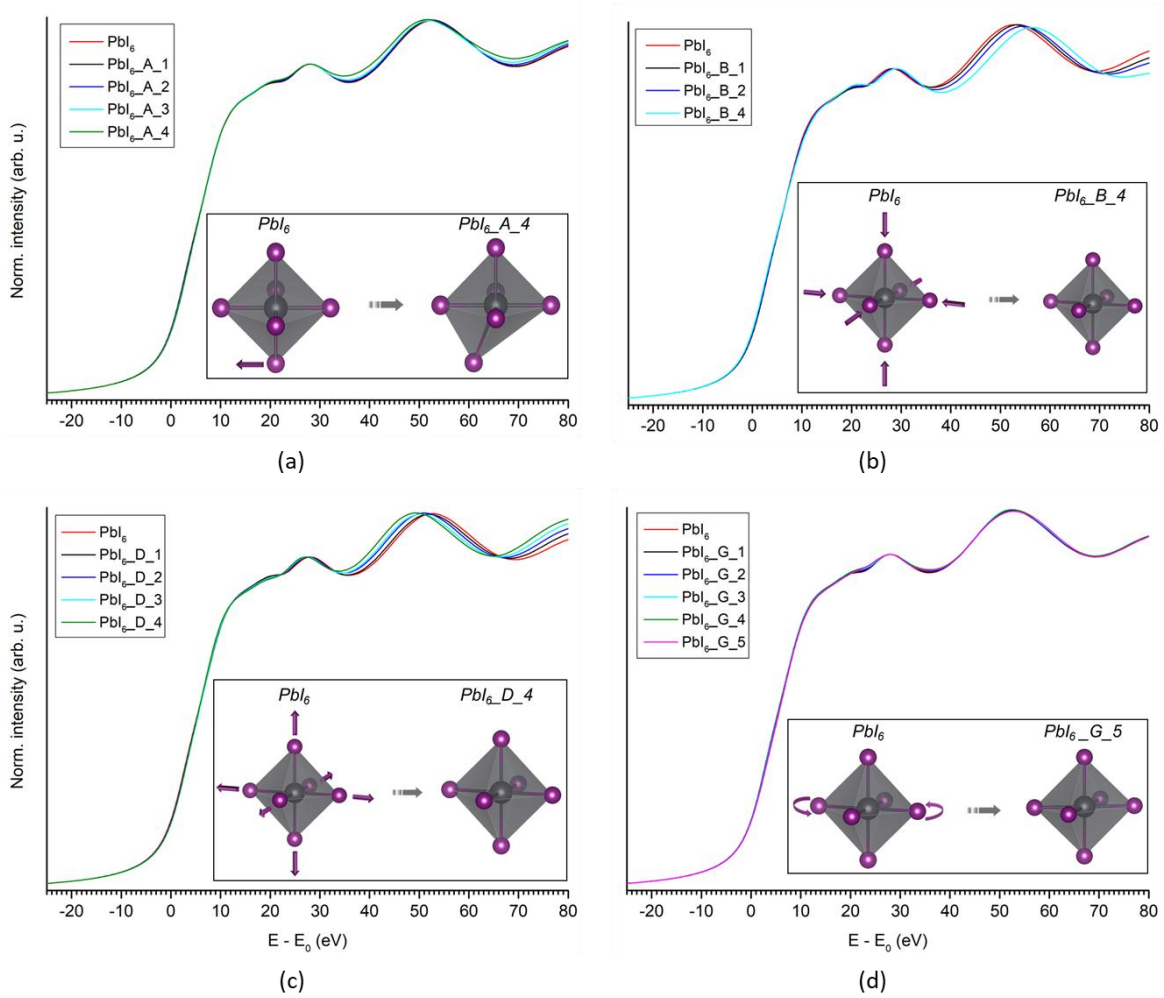

Figure 3.9. Pb L_3-edge simulated XANES spectra of reference PbI_6 octahedron, and different modes of octahedral distortion: (a) skewing; (b) isotropic compression; (c) isotropic expansion; (d) symmetric change of the equatorial I−Pb−I angle.

Axial compression. Compression of the octahedron along the axial bonds leads to a reduction of 0.05 Å per step. From an initial bond length of 3.2 Å, the Pb−I distance decreases to 2.75 Å in PbI_6_C_9 (inset of **Figure 3.10a**). In this case, the variation of the two axial Pb−I bonds is significant and induces a change in symmetry, which results in noticeable modifications in the XAS spectra. As the axial bonds become shorter, the main absorption peak shifts toward higher energy, its intensity decreases, and the absorption edge increases. In PbI_6_C_9, where the distortion is most pronounced, multiple-scattering effects become evident (**Figure 3.10a**).

Axial elongation. Elongation of the octahedron along the axial bonds results in an increase of 0.05 Å per step. From a bond length of 3.2 Å, the Pb−I distance extends to 3.65 Å in PbI_6_E_9 (inset of **Figure 3.10b**). Here, the variation of the two axial Pb−I bonds is less

significant than in the compression case, since the interaction between neighboring atoms becomes weaker. As the axial bonds lengthen, a slight leftward shift of the main peak is observed, along with a mild decrease in peak intensity and an increase of the absorption edge (**Figure 3.10b**).

Equatorial elongation and axial compression. In this case, the axial bonds are compressed while the equatorial ones are elongated by 0.05 Å per step. From initial bond lengths of 3.2 Å, the axial Pb−I distances decrease to 2.9 Å, while the equatorial ones increase to 3.5 Å in PbI_6_F_6 (inset of **Figure 3.10c**). This results in a strong symmetry distortion that profoundly affects the XANES spectra (**Figure 3.10c**).

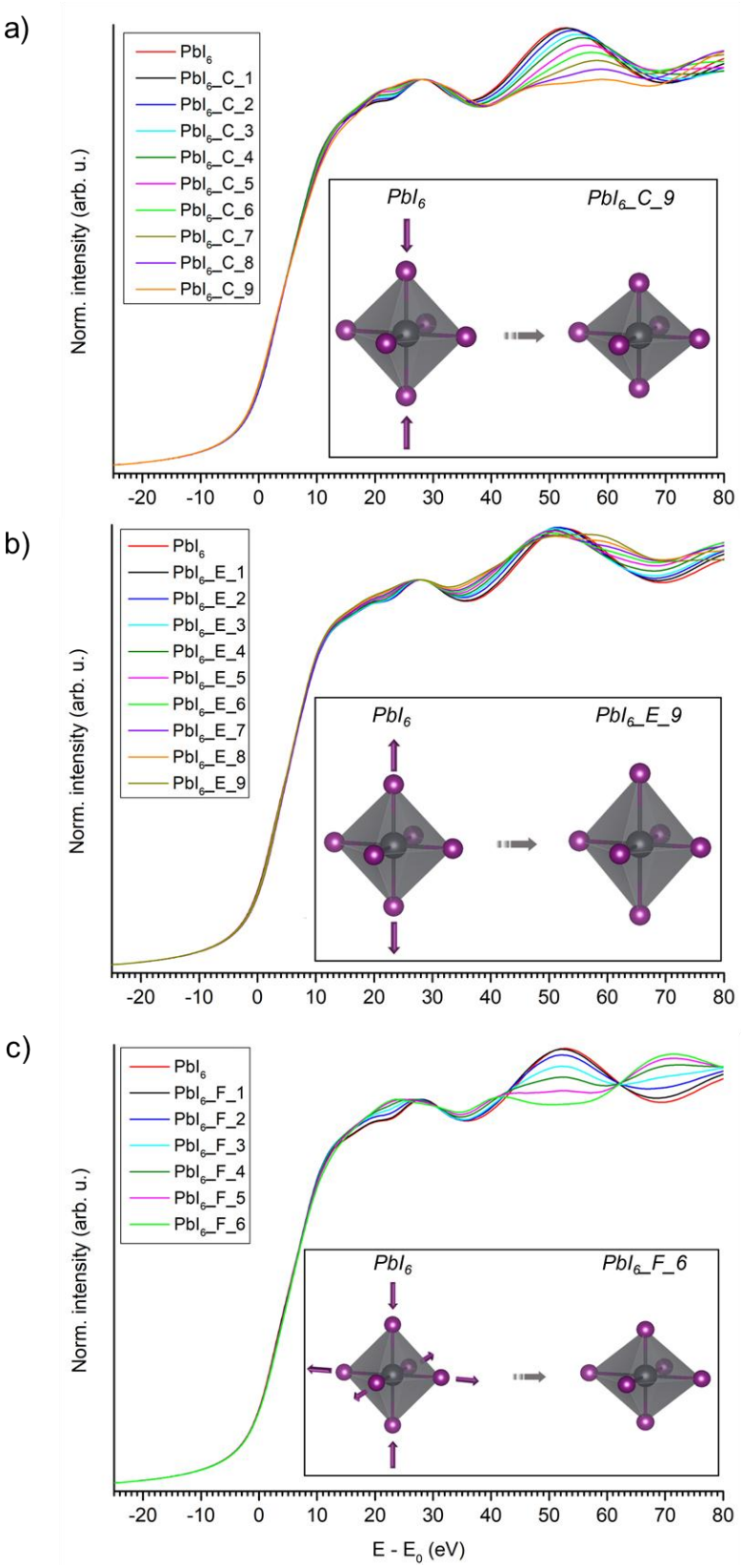

Figure 3.10. Pb L_3-edge simulated XANES spectra of reference PbI_6 octahedron, and further different modes of octahedral distortion: (a) axial compression; (b) axial elongation; (c) axial compression and equatorial elongation.

The three distortion modes illustrated in **Figure 3.10** have the most pronounced effects on the XANES spectra, and all lead to a reduction in symmetry from the Oh to the D_4h point groups. In contrast, the strong symmetry reduction induced by the displacement of a single iodine atom (**Figure 3.9a**) has only a minor influence on the XANES spectrum. It can therefore be concluded that the spectral features are dominated by the presence and relative length of collinear intra-octahedral I−M−I paths.

To gain deeper insight into the influence of the metal−iodine distance on the XANES spectra, the partial pDOS onto the absorber was analyzed for all PbI_6 octahedra. Among these, the simulated spectra showing substantial differences from the undistorted PbI_6 were selected, namely PbI_6_C_9, PbI_6_E_9, and PbI_6_F_6, and compared with the corresponding calculated d-orbital densities of states. In an undistorted PbI_6 octahedron, the d_z^2 and d_x^2−y^2 states are degenerate (**Figure 3.11a**); in octahedra with different axial/equatorial bond lengths (**Figure 3.11b-d**), geometric distortion breaks both the symmetry and this degeneracy, resulting in a flattening of the edge features. The d_x^2−y^2 DOS retains a sharp peak for distortion modes involving axial compression (PbI_6_C_9 and PbI_6_F_6), whereas for axial elongation (PbI_6_E_9, resembling a Jahn-Teller-like distortion) the two DOS components are simply shifted relative to each other, yielding a smoother edge.

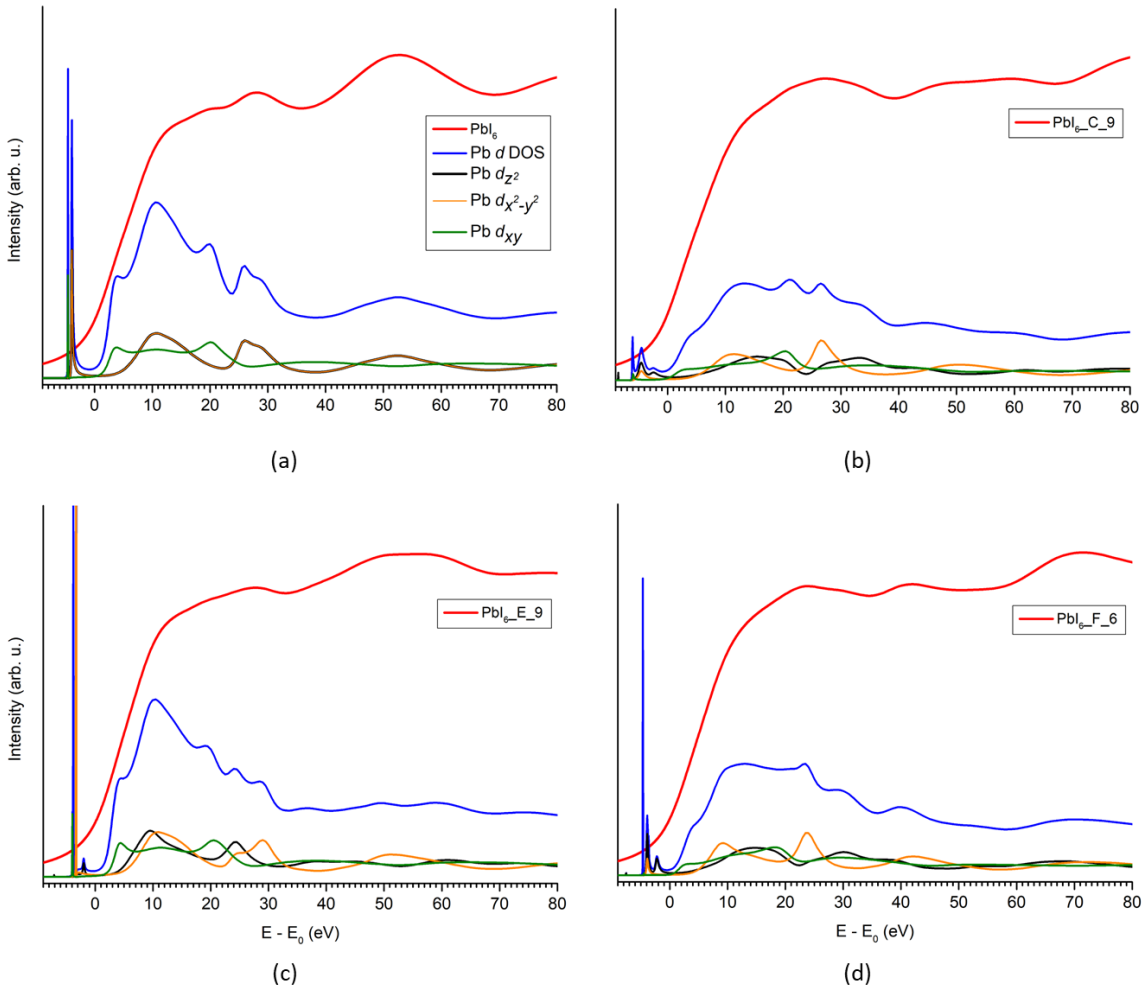

Figure 3.11. Pb L_3-edge simulated XANES spectra and DOS of d orbitals of: (a) reference PbI_6 octahedron; (b) axial compression; (c) axial elongation; (d) equatorial elongation and axial compression.

All the above observations indicate that the modifications in absorption edges are predominantly local in nature and are mainly governed by the relative lengths of the collinear intra-octahedral I−M−I paths. This suggests that XANES or HERFD-XANES signals could be modeled in terms of relatively simple distortion modes, both in static and in situ/operando studies of halide perovskites.

In this context, numerous recent empirical attempts have been made to correlate XAFS spectra with synthesis parameters or post-synthetic treatments. However, the non-systematic selection of coordination shells and fitting parameters, along with their large variability (Pb−I distances ranging from 3.09 to 3.47 Å in multi-shell fits, 3.13 Å in single-shell fits, or even 2.4-2.8 Å; disorder factors between 0.006 and 0.019 Å²), has so far hindered the establishment of reliable structure-property relationships for practical use of core-level

spectroscopies. In general, EXAFS data for hybrid halide perovskites provide information for only a single coordination shell.

Conversely, the near-edge portion of the spectrum is far less affected by static and dynamic disorder, and its sensitivity to symmetry and overall geometry (whether or not multiple-scattering contributions are involved, as observed here) makes it an ideal complement to diffraction-based analyses. Understanding structure-property relationships is thus crucial for the future development of halide perovskites toward higher-efficiency solar cells and other emerging applications.

The evidence gathered so far from EXAFS data, highly susceptible to the strong static disorder typical of lead halide perovskites, has proven inconclusive and ineffective in establishing correlations with functional properties or even with other structural features. In contrast, near-edge spectroscopic techniques (XANES and HERFD-XANES) can provide valuable insights into octahedral symmetry and cation arrangement in mixed halide perovskites of different dimensionalities, although they require more rigorous simulation approaches.

One-dimensional hybrid pseudo-perovskite solid solutions $(TMSO)_3Pb_{3x}Bi_{2(1-x)}I_9$ were investigated, obtained by replacing the conventional organic cations commonly used in OLHPs with TMSO, followed by subsequent doping of the B-site with Bi^{3+}. The substitution of the organic cation imparts enhanced stability to the resulting $TMSOPbI_3$ perovskite under ambient conditions for at least one month, overcoming the typical stability limitations associated with more common cations such as MA and FA. Lead and bismuth ions share a similar electronic configuration and ionic radius, however, due to their different charges, the positively charged Bi^{3+} defects are compensated by Pb^{2+} vacancies. As detailed in recent studies on these materials,[183,202] the introduction of Bi^{3+} promotes the formation of point defects that preferentially cluster in Bi−(V)−Bi arrangements along the linear metal halide chains, generating localized states below the conduction band, which are observed as a reduction of the band gap in optical absorption experiments.

Using these one-dimensional Pb/Bi perovskite solid solutions as model compounds, we demonstrated that XANES spectra of different absorption edges are highly sensitive to subtle structural features of the local metal−halogen coordination geometry, while remaining largely unaffected by long-range multiple-scattering effects that typically dominate the near-edge region. In addition, correlations between the atomic and the electronic structure close to the Fermi level can be established on a case-by-case basis, as exemplified for the iodine

L_1-edge. Extending this approach in the future to other halide perovskites should enable direct structural correlations, providing a valuable complement to other spectroscopic and diffraction techniques.

3.5. Appendix

Materials

Hydroiodic acid (HI,57% w/w aqueous stabilized with 1.5 w/w H_3PO_2), hypophosphorous acid (H_3PO_2, 50% w/w aqueous solution), lead oxide (PbO, 99%), and trimethylsulfoxonium iodide ($((CH_3)_3SO)I$, >98%) were purchased from Alfa Aesar. Anhydrous ethanol (C_2H_6O, >99%), bismuth oxide (Bi_2O_3, 99.9%), and isopropyl alcohol (C_3H_8O, 99.7%) were purchased from Sigma-Aldrich. All materials were used without further purification.

$(TMSO)_3Pb_{3x}Bi_{2(1-x)}I_9$ synthesis

Samples with general formula $(TMSO)_3Pb_{3x}Bi_{2(1-x)}I_9$ were synthetized through precipitation from aqueous solution. The corresponding metal oxides were dissolved in 5 mL of HI and 1 mL of H_3PO_2. The stoichiometric quantities for each reaction are described in **Table A 3.1**. The solutions were heated to 70 °C to dissolve all-metal oxides, resulting in a clear solution. (TMSO)I powder was added to the solutions, causing the immediate precipitation of a powder. All powders were decanted for 24 h and then filtered, under vacuum, through 0.45 μm polypropylene filters (Millipore) and washed with anhydrous ethanol. The powders obtained were dried at 40 °C overnight.

Table A 3.1. Stoichiometric quantities used for $(TMSO)_3Pb_{3x}Bi_{2(1-x)}I_9$ synthesis.

Label	Formula	$TMSO^+$ mmol	Pb^{2+} mmol	Bi^{3+} mmol
Pb100	$(TMSO)PbI_3$	1	1	--
Pb92	$(TMSO)_3Pb_{2.67}Bi_{0.22}I_9$	1	0.75	0.25
Pb90	$(TMSO)_3Pb_{2.61}Bi_{0.26}I_9$	1	0.7	0.3
Pb78	$(TMSO)_3Pb_{2.13}Bi_{0.58}I_9$	1	0.6	0.4
Pb66	$(TMSO)_3Pb_{1.68}Bi_{0.88}I_9$	1	0.5	0.5
Pb42	$(TMSO)_3Pb_{0.99}Bi_{1.34}I_9$	1	0.25	0.75
Pb22	$(TMSO)_3Pb_{0.51}Bi_{1.66}I_9$	1	0.15	0.85
Pb0	$(TMSO)_3Bi_2I_9$	1	--	1

XRD patterns of $(TMSO)_3Pb_{3x}Bi_{2(1-x)}I_9$ powders were acquired with a Rigaku Miniflex 600 diffractometer using Ni-filtered Cu Kα radiation (λ=1.5418 Å) and analyzed with Rietveld refinement using GSAS-II.[213] All samples were refined with an orthorhombic *Pnma* structure and all lattice parameters obtained from refining are reported in **Table 3.2**. The Rietveld refinements of P100, Pb92, Pb66, Pb42 and Pb0 samples are reported in Ref. [202]. Here, are reported the refinements of the Pb100 sample after one month, as well as those of the samples synthesized subsequently, namely Pb90, Pb78, and Pb22 (**Figure A 3.1**-**Figure A 3.4**).

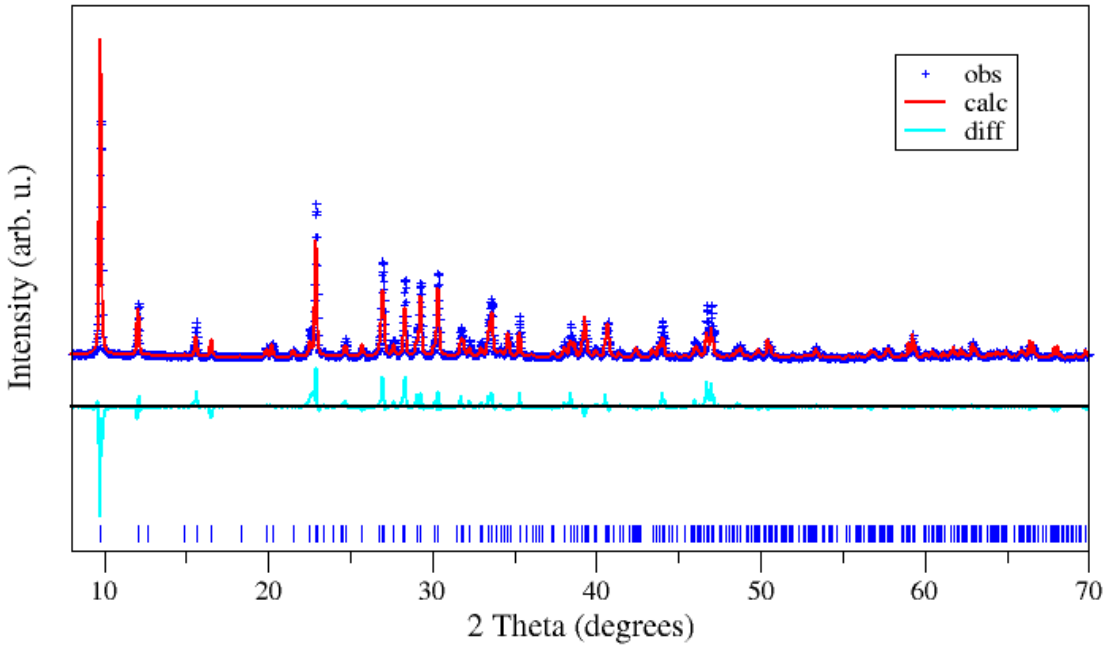

Figure A 3.1. Rietveld refinement plot for $(TMSO)PbI_3$ (Pb100) after one month. Experimental data (blue), calculated pattern (red), residual (cyan).

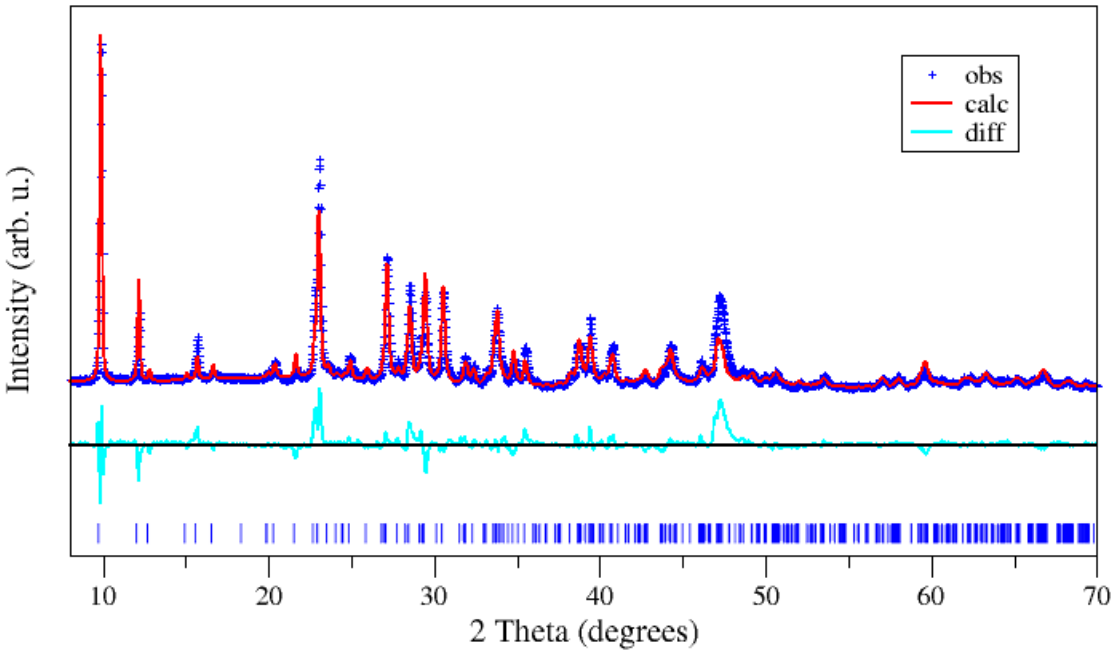

Figure A 3.2. Rietveld refinement plot for $(TMSO)_3Pb_{2.61}Bi_{0.26}I_9$ (Pb90). Experimental data (blue), calculated pattern (red), residual (cyan).

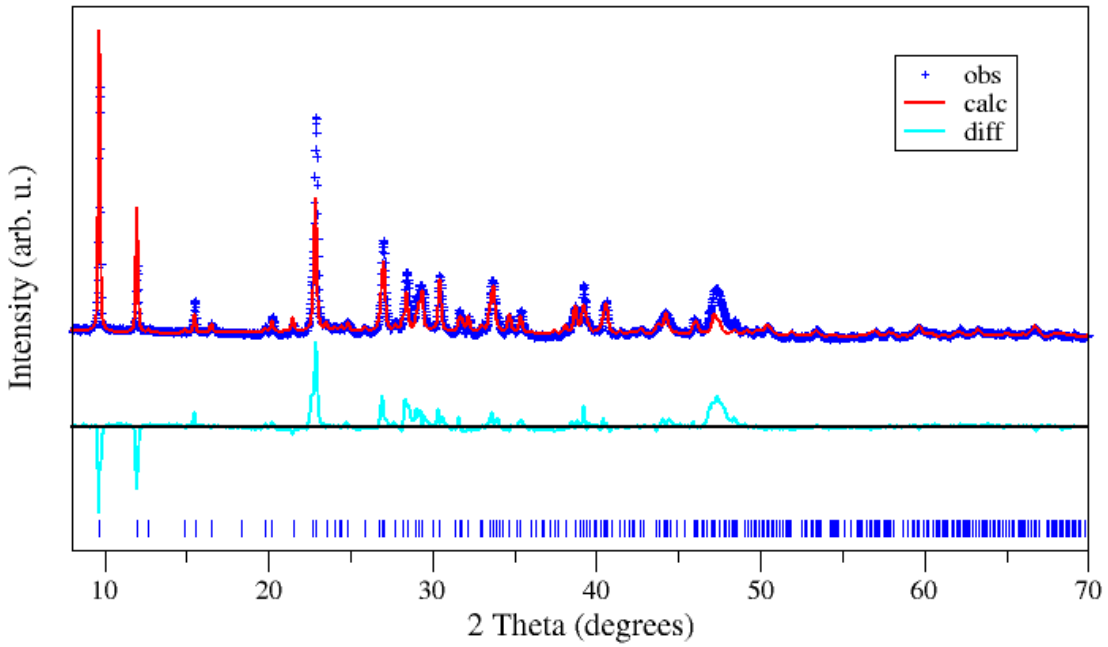

Figure A 3.3. Rietveld refinement plot for $(TMSO)_3Pb_{2.13}Bi_{0.58}I_9$ (Pb78). Experimental data (blue), calculated pattern (red), residual (cyan).

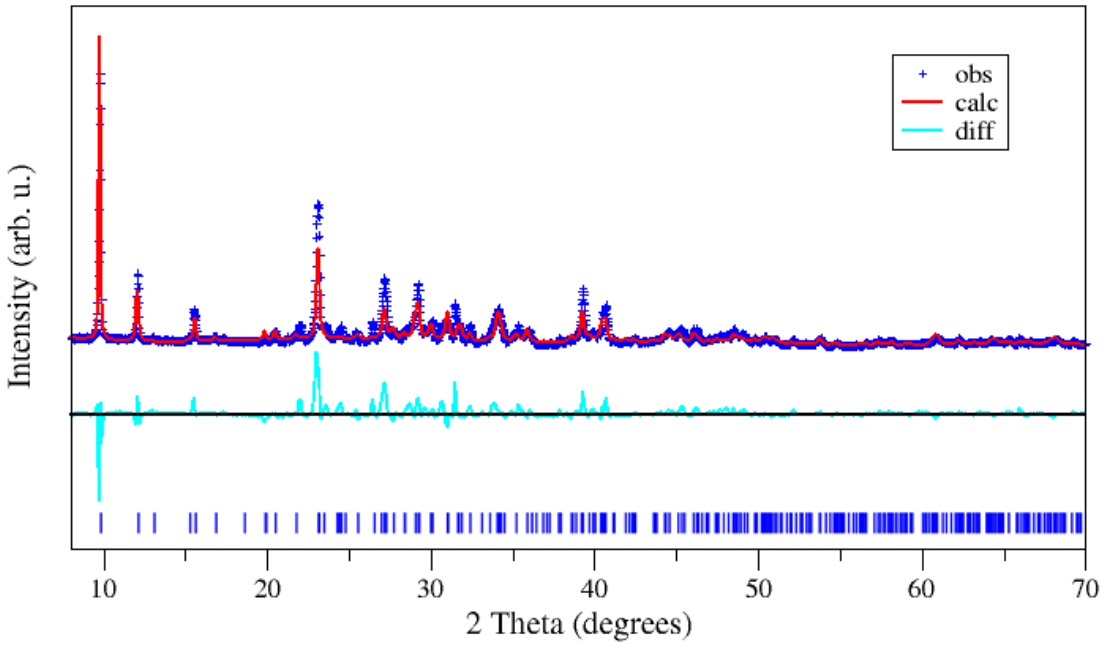

Figure A 3.4. Rietveld refinement plot for $(TMSO)_3Pb_{0.51}Bi_{1.66}I_9$ (Pb22). Experimental data (blue), calculated pattern (red), residual (cyan).

ICP-OES

ICP-OES was performed to accurately quantify Bi in the $(TMSO)_3Pb_{3x}Bi_{2(1-x)}I_9$ powders using a Perkin-Elmer Optima 2100 ICP-OES spectrometer equipped with an autosampler model S10. WinLab 32 software (Perkin-Elmer) was used for the acquisition and processing of the data. The emission wavelengths used was 190.171 nm. Calibration curves were obtained by diluting a multielement standard solution. For the analysis, 10 mg were mineralized in 10 mL of concentrated HNO_3 until half of the volume evaporated. The remaining liquid was recovered quantitatively in a 25 mL graduated flask, then filled with distilled water. The obtained stoichiometries, reported in **Table 3.1**, are reported with two significant digits for simplicity, although the ions concentration measurements are accurate to the 10^{-3} level.

XAS

XAS spectra were acquired at the Pb and Bi L_3-edge at the XAFS beamline of Elettra Sincrotrone Trieste, and at the BM08 beamline of ESRF. Spectra were acquired in transmission mode on samples cooled at 80 K with a liquid nitrogen cryostat. Ionization chambers were filled with Ar/N_2 mixtures at different pressure to achieve 20% absorption

on I_0 and 60% on I_t. A double crystal Si (111) monochromator, with Pt-coated mirrors, was used to achieve a ΔE energy resolution around 1.4 eV. The data were collected with an energy step of 5 eV in the pre-edge region, 0.4 eV in the XANES region and with a constant k-step of 0.04 $Å^{-1}$ in the postedge region. Each sample was measured on a grid of nine spots ca. 1 mm apart to minimize beam exposure, with each scan lasting about 30 min, and all scans were averaged afterward. For each sample, pellets were prepared by dilution with boron nitride.

XANES Simulations

The XANES spectra of $[PbI_6]$ (**Figure 3.9**-**Figure 3.10**) and $[BiI_6]$ (**Figure A 3.5**) isolated octahedra were simulated with the FDM approach, with a R_{max} of 4 Å, fixing the vacuum potential parameter Vmax at -6.0 eV to account for the potential outside the cluster. The XANES spectra of the extended solids were simulated with periodic boundary conditions using the *Green* function approach with muffin tin potentials, where the SCF function and the R_{max} parameter were increased until convergence, achieved around 8-9 Å.

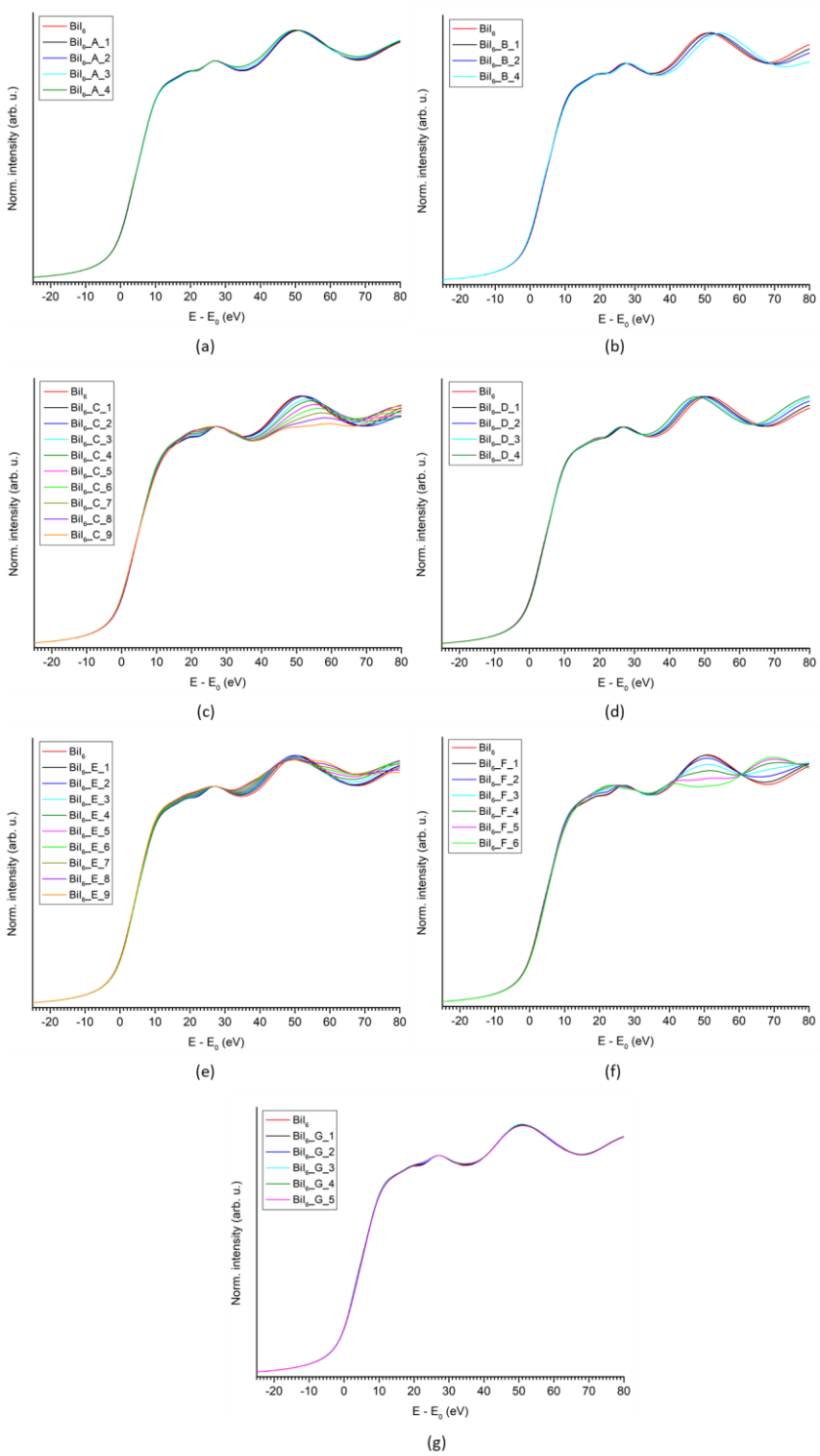

Figure A 3.5. Simulated XANES spectra at the Bi L_3-edge of reference BiI_6 octahedron, and different modes of octahedral distortion: (a) skewing; (b) isotropic compression; (c) axial compression; (d) isotropic expansion; (e) axial elongation; (f) equatorial elongation and axial compression; (g) symmetric change of the equatorial I−Bi−I angle.

4. Isovalent Substitution of Lead

*Adapted from J. Mater. Chem. C **2024**, 12, 12951, with permission from the Royal Society of Chemistry (RSC), Copyright 2024.*

4.1. Introduction: Tin-based HPs

Tin-based perovskites, together with germanium-based ones, represented the first experimentally demonstrated alternatives to LHPs. Since Sn and Ge belong to the same group as Pb in the periodic table and share a similar electronic configuration, this kind of substitution is almost obvious. The chemical affinity between Pb and Sn enables the formation of isostructural perovskite frameworks, making these materials natural candidates for lead substitution in halide perovskites.[124]

DFT calculations of the band structure of $MASnI_3$ predict that the cubic polymorph exhibits a direct bandgap of 1.55 eV, slightly higher than that of MAPI.[214] The VBM is mainly determined by the antibonding hybridization of Sn 5s and I 5p states, while the CBM is primarily composed of Sn 5p and I 5p states. The MA cations do not directly contribute to the band edges, therefore, the bandgap of tin-based perovskites is largely governed by the Sn–X bonding.[215] Similarly to $MASnI_3$, $FASnI_3$ also exhibits a direct bandgap, with the VBM and CBM composed of the same Sn and I orbitals.[134,216] In $FASnI_3$, the longer Sn−I bond length, resulting from the larger ionic size of the FA cation, weakens the antibonding interactions between the I 5p and Sn 5s orbitals, leading to a downward shift of the VBM relative to $MASnI_3$. Consequently, $FASnI_3$ exhibits a slightly wider bandgap, in contrast to its lead counterpart.[217] In general, among Sn-based materials, only $CsSnI_3$, $MASnI_3$, $FASnI_3$, and $FASnI_2Br$ exhibit bandgaps in the range of 1.2–1.6 eV, making them particularly suitable for single-junction solar cells. The bandgap does not vary significantly upon changing only the A-site cation, whereas substantial variations are observed following halide substitution. In particular, replacing iodine with bromine in these compositions allows a continuous

tuning of the bandgap from 1.3 to 2.4 eV, enabling optimal application in both single-junction and tandem solar cells.[218]

Although tin can theoretically replace lead in perovskite structures due to its similarity to lead in both electronic configuration and ionic radius, tin-based PSCs exhibit significantly lower long-term air stability instead, when compared to their lead-based counterparts.[124] Kanatzidis and Snaith groups were the first to employ tin-based HPs as the active layer in solar cells, achieving efficiencies of 5.73% and 6.4% with $MASnI_{3-x}Br_x$ and $MASnI_3$, respectively.[219,220] Koh et al. were the first to employ $FASnI_3$ as the active layer in solar cells, achieving a PCE of 2.10%.[221] The low efficiency of these materials arises from the tendency of tin, a fourth-period element, to readily lose the electrons of its lone pair, resulting in poor chemical stability due to oxidation from the +2 to the more stable +4 oxidation state.[124,125,127] Several studies have therefore focused on improving device performance through additive engineering since. For instance, the incorporation of metallic tin[222] or additives such as pyrazine,[223] ammonium hypophosphite,[224] trihydrazine dihydriodide,[225] phenylhydrazine hydrochloride,[226] as well as the use of π-conjugated organic molecules[227] and polymers,[228,229] has been shown to passivate defects, suppress the oxidation of Sn^{2+} to Sn^{4+}, improve film morphology, and increase the PCE to approximately 11%. $CsSnI_3$ perovskite solar cells achieved much lower PCE than the afore mentioned tin perovskite solar cells, mainly due to a fast degradation from the photoactive B-γ-$CsSnI_3$ to the yellow polymorph structure, which subsequently transforms to the photoinactive Cs_2SnI_6 due to a rapidly self-doping reaction from Sn^{2+} to Sn^{4+}. Nevertheless, these perovskites are of interest due to their higher air stability compared to organic tin-based perovskites.[230] The adoption of strategies similar to those applied to $MASnI_3$ and $FASnI_3$ has enabled improvements in both stability and efficiency, with PCE values reaching approximately 7%.[124] Another strategy for stabilizing these materials is the mixing of cations at the A-site, which has been shown to be effective in improving the efficiency of lead-based perovskite solar cells. In the case of tin-based counterparts, numerous research groups have investigated the effect of commonly used mixed cations, such as MA/FA, ethylenediammonium, hydrazinium, dimethylammonium, 2-hydroxyethylammonium, and BA, among others. Some of these cations have led to the formation of low-dimensional structures, which have proven to be crucial for the development of tin-based PSCs.[124] However, their photophysical properties are not yet fully understood, primarily due to their structural complexity, and a better understanding could open new and promising opportunities for optoelectronic applications.

In this chapter, the focus is therefore placed on the substitution of lead with tin in the $(TMSO)_3Pb_{3x}Bi_{2(1-x)}I_9$ series, addressing the critical issue of Pb toxicity. Building on the materials described in the previous chapter, new tin-based one-dimensional halide pseudo-perovskite materials were prepared, and a thorough structural characterization was conducted. Although chemically similar to lead, tin presents the challenge of easy oxidation from Sn^{2+} to Sn^{4+}, one of the main limitations of tin-based perovskites. XAS analysis at the Sn K-edge provided promising results, showing that doping the B site with bismuth progressively reduces tin oxidation, ultimately suppressing it almost entirely, thus enabling the development of more stable and potentially higher-performing materials. Notably, Bi^{3+} not only stabilizes tin in its +2 oxidation state but also reduces the bandgap from 2.75 eV to 1.96 eV. Finally, the resulting $(TMSO)_3Sn_{3x}Bi_{2(1-x)}I_9$ materials were also assessed for potential applications as piezoresistive materials, highlighting additional functional capabilities of these systems.

A benchmark in the field of piezoelectric perovskites is represented by $Pb(Ti,Zr)O_3$, employed as a piezoelectric actuator.[231] To avoid the use of lead, Bi-based perovskites, such as $BiFeO_3$ and $(Bi_{0.5}Na_{0.5})TiO_3$, have been studied for their excellent piezoelectric properties.[232] A recent example of a lead-free piezoelectric perovskite is the $0.3BaTiO_3$-$0.1Bi(Mg_{1/2}Ti_{1/2})O_3$-$0.6BiFeO_3$ ceramic, whose piezoelectric response arises from the combined partial ordering of off-centered Bi ions, which adjust their positions under the application of an external electric field.[233] In this context, halide perovskites have demonstrated excellent piezoelectric and ferroelectric properties, comparable to those of conventional inorganic piezoelectric materials.[234] For instance, the piezoelectric properties of MAPI thin films were investigated via piezoelectric force microscopy.[235] Other examples include $CsPbBr_3$ thin films[236] and the two-dimensional hybrid ferroelectric perovskite $(4\text{-aminotetrahydropyran})_2PbBr_4$ $[(ATHP)_2PbBr_4]$.[237] The interplay between electrical and mechanical responses in halide perovskites is still far from being fully understood, limiting their full implementation in real strain-sensing devices. A major challenge concerns the stability of these materials in air and the reproducibility under ambient conditions.[238] To date, no studies have reported on hybrid halide perovskite thin films with piezoresistive properties that would facilitate their integration into sensor devices.

Thin films of the resulting $(TMSO)_3Sn_{3x}Bi_{2(1-x)}I_9$ halide pseudo-perovskites were prepared via spin coating on ITO/PET substrates, exhibiting significant variations in morphology and piezoresistive properties as a function of Bi^{3+} content, reaching an optimized value closely correlated with the formation of Bi-induced vacant cation sites. The observed features were

explained in terms of the surface morphology analyzed by AFM, highlighting the key role of Bi^{3+}. Microstructural and electrical effects after strain were further investigated using SEM and EIS, emphasizing the crucial role of microcracks and delamination in the observed bending strain response.

4.2. Synthesis and Structural Characterization of Sn/Bi OHP

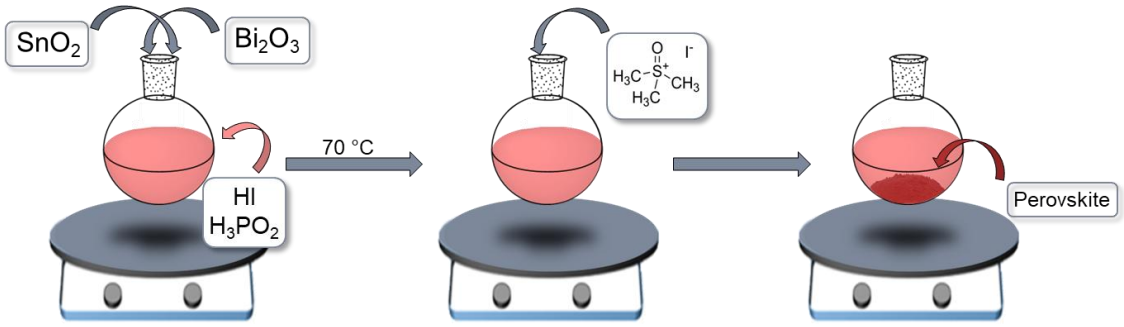

Scheme 4.1. Scheme of the synthesis of all samples.

The synthesis of $(TMSO)_3Sn_{3x}Bi_{2(1-x)}I_9$ powders was carried out by precipitation from an aqueous solution, following the procedure previously established for the lead-based analogues. The synthesis method, described in detail in the Appendix, is shown in **Scheme 4.1**. In this case, the substitution of bismuth occurs within the $(TMSO)SnI_3$ lattice according to the quasi-chemical reaction:

$$3Sn_{Sn}^{x} + 2BiI_3 \rightarrow 2Bi_{Sn}^{\bullet} + V_{Pb}'' + 3SnI_2 \qquad (4.1)$$

The resulting solid solutions are therefore best represented by the formula $(TMSO)_3Sn_{3x}Bi_{2(1-x)}I_9$, with $0 \leq x \leq 1$. The compositions corresponding to $x = 0$ and $x = 1$ represent the pure tin $(TMSO)SnI_3$ and pure bismuth $(TMSO)_3Bi_2I_9$ compounds, respectively (**Figure 4.1**).

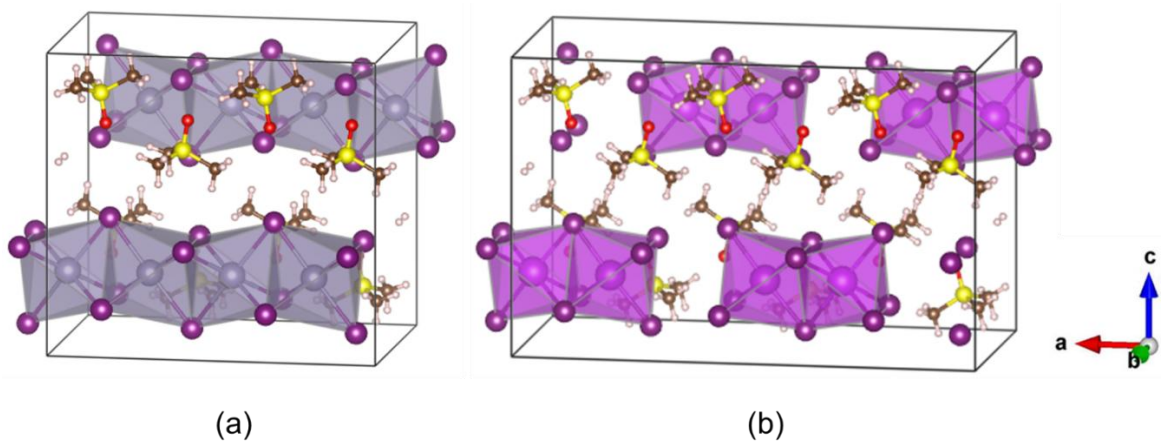

Figure 4.1. (a) Undoped $TMSO_8Sn_8I_{24}$ 2 × 1 × 1 supercell. (b) $(TMSO)_3Bi_2I_9$ supercell. Iodine atoms are in violet, SnI_6 octahedra are in gray, BiI_6 octahedra in pink. Carbon, sulfur, oxygen, and hydrogen atoms are in brown, yellow, red, and white, respectively. The octahedral chains are aligned along the *a* direction.

Intermediate compositions, characterized by mixed Bi^{3+}/Sn^{2+} ratios, retain structural isomorphism with the end members, in agreement with previous studies on analogous lead-based systems discussed in Chapter 3, namely $(TMSO)_3Pb_{3x}Bi_{2(1-x)}I_9$.[182,183,202,239] The structure and possible arrangements of Sn/Bi/vacancies in the eight metal cation sites of a 2 x 1 x 1 supercell of these samples have been outlined in detail in the Chapter 3. The only significant difference lies in the replacement of Pb with Sn, which does not substantially affect the crystal structure (**Table 4.1**).

Table 4.1. Labels and crystal structure for all samples. Bi0 and Bi100 represent the samples in absence of Bi and Sn, respectively. Crystal system: orthorhombic. Space group: *Pnma*. Uncertainty is reported in parentheses.

Labels	a (Å)	b (Å)	c (Å)	V (Å^3)
Bi0	7.7631(3)	11.1739(4)	14.382(1)	1247.6(1)
Bi25	7.7040(4)	11.1815(8)	14.385(1)	1239.2(2)
Bi50	7.6431(7)	11.180(1)	14.375(3)	1228.5(3)
Bi75	7.5256(6)	11.213(1)	14.406(1)	1215.7(2)
Bi100	7.4534(4)	11.2149(6)	14.4017(8)	1203.8(1)

X-ray diffraction patterns exhibit minor, predictable shifts in peak positions as a function of stoichiometry. Specifically, increasing the bismuth content results in a contraction of the unit

cell along the *a*-axis, causing the diffraction peaks (hkl with h ≠ 0) to shift toward higher angles. For instance, the 213 reflection peak shifts from 30.5° in Bi0 to 31.1° in Bi100, as shown in the inset of **Figure 4.2**. Furthermore, notable peak broadening is observed in intermediate compositions like Bi50 and Bi75, whereas 0kl peaks, which are less sensitive to cation disorder, remain largely unchanged in position and shape.

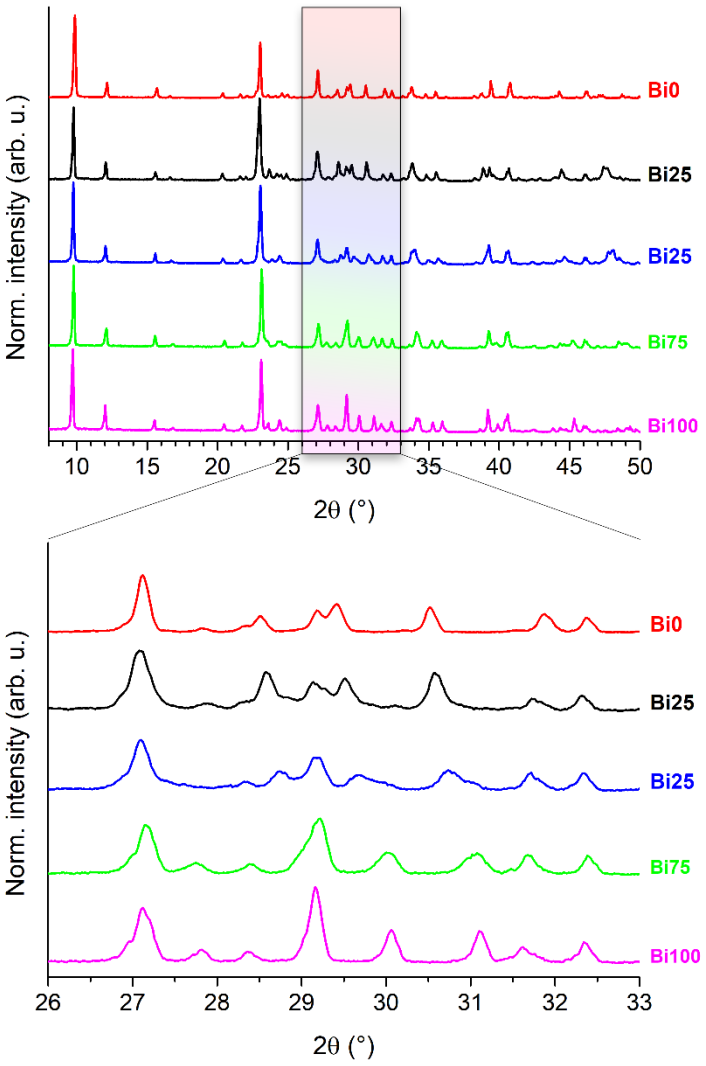

Figure 4.2. XRD data of $(TMSO)SnI_3$, mixed sample $(TMSO)_3Sn_{3x}Bi_{2(1-x)}I_9$ ($0 < x < 1$), and the $(TMSO)_3Bi_2I_9$ crystal phases in the 8−50° 2θ range (bottom to top) with an enlargement of the 26−33° section, where the peak shift discussed in the text is more evident.

Lattice parameters, reported in **Table 4.1**, vary with the Bi/Sn ratio. Parameters *b* and *c*, orthogonal to the metal-halide chains, remain relatively constant, while the *a* lattice

parameter decreases linearly with increasing Bi content. This behavior reflects the influence of both ionic radius differences and the presence of vacancies, which contribute to a reduced periodicity along the *a* axis. The actual Bi content in each sample was estimated by interpolation, by using the end-members as fixed points (**Figure 4.3**). The stoichiometries obtained were then confirmed by XRF analysis, showing strong agreement with values derived from XRD analysis (**Table 4.2**).

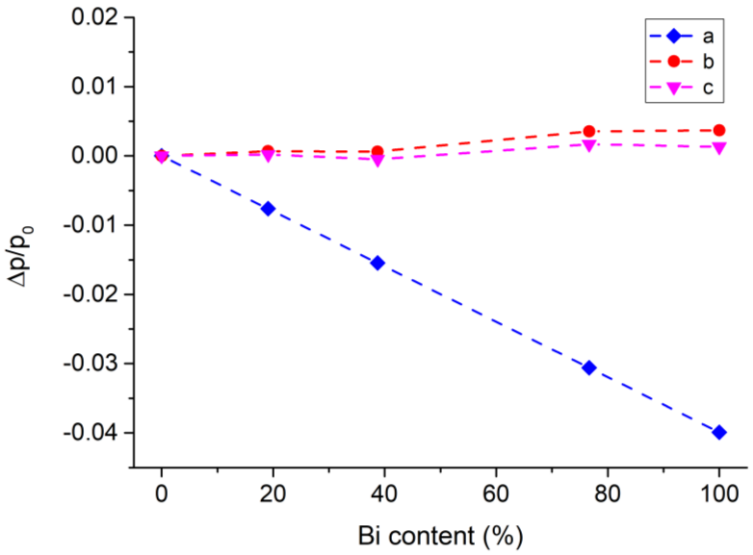

Figure 4.3. Lattice parameter relative variation vs %Bi [Bi content (%)], in the form of $\Delta p/p_0$ (where p = a, b, c, and p_0 values are taken with reference to the $(TMSO)SnI_3$ species, that with x = 0) for the $(TMSO)_3Sn_{3x}Bi_{2(1-x)}I_9$ series. The uncertainty on $\Delta a/a_0$ is 10^{-4}.

Table 4.2. x values for the intermediate compositions $(TMSO)_3Sn_{3x}Bi_{2(1\_x)}I_9$ formula, obtained from XRD and XRF respectively.

	XRD			XRF		
Labels	**x**	**%Bi**	**Formula**	**x**	**%Bi**	**Formula**
Bi25	0.81	19	$(TMSO)_3Sn_{2.42}Bi_{0.38}I_9$	0.82	18	$(TMSO)_3Sn_{2.46}Bi_{0.36}I_9$
Bi50	0.61	39	$(TMSO)_3Sn_{1.84}Bi_{0.77}I_9$	0.57	43	$(TMSO)_3Sn_{1.71}Bi_{0.86}I_9$
Bi75	0.23	77	$(TMSO)_3Sn_{0.69}Bi_{1.54}I_9$	0.24	76	$(TMSO)_3Sn_{0.72}Bi_{1.52}I_9$

4.3. X-ray Absorption and Optical Spectroscopy of Sn/Bi OHP

The experimental Bi L_3-edge and Sn K-edge XANES spectra are shown in **Figure 4.4**. A first analysis reveal that the Bi L_3-edge (**Figure 4.4b**) features differ markedly from those of BiI_3, indicating that significant radiation-induced decomposition to simple iodides does not occur. The spectra across all Bi-containing samples are quite similar. Regarding the Sn K-edge (**Figure 4.4a**), most samples exhibit spectra that differ from SnI_2, with the notable exception of Bi0, where the absorption edge shifts to higher energy. This indicates partial oxidation of Sn(II) to Sn(IV), likely forming SnO_2, which is further confirmed by EXAFS analysis. This oxidation appears to be caused by the synchrotron beam and may be assisted by trace moisture present in the boron nitride matrix. Importantly, this phenomenon is exclusive to the Bi-free sample; in contrast, increasing bismuth concentrations lead to a substantial reduction in SnO_2 formation.

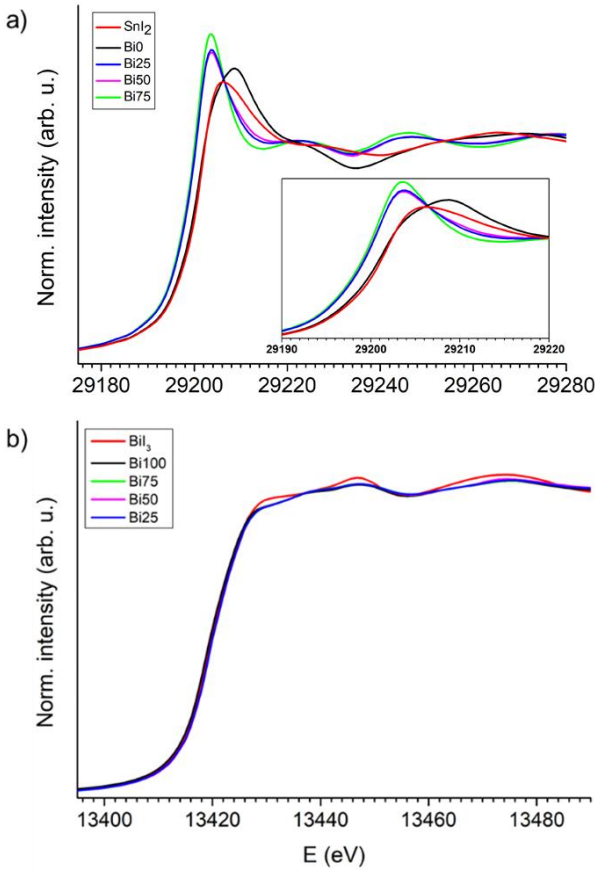

Figure 4.4. Experimental XANES spectra of all samples at the (a) Sn K-edge and (b) Bi L_3-edge compared with their respective precursor.

EXAFS spectra (**Figure 4.5**) confirm a pronounced Sn−O contribution in Bi0, which diminishes dramatically with more Bi, becoming nearly undetectable in Bi75. This suggests that bismuth plays a protective role, inhibiting the photooxidation of Sn(II). Further evidence of tin oxidation in Bi0 and the absence of this phenomenon in Bi75 comes from XRD measurements taken before and after synchrotron exposure (**Figure 4.6**). The XRD pattern of Bi75 after XAFS shows distinct peaks corresponding to boron nitride, which was used as a diluent during pellet preparation and is indicated by red asterisks. The Bi75 sample retains its diffraction pattern without shifts, confirming the absence of oxidation upon exposure to the X-ray beam.

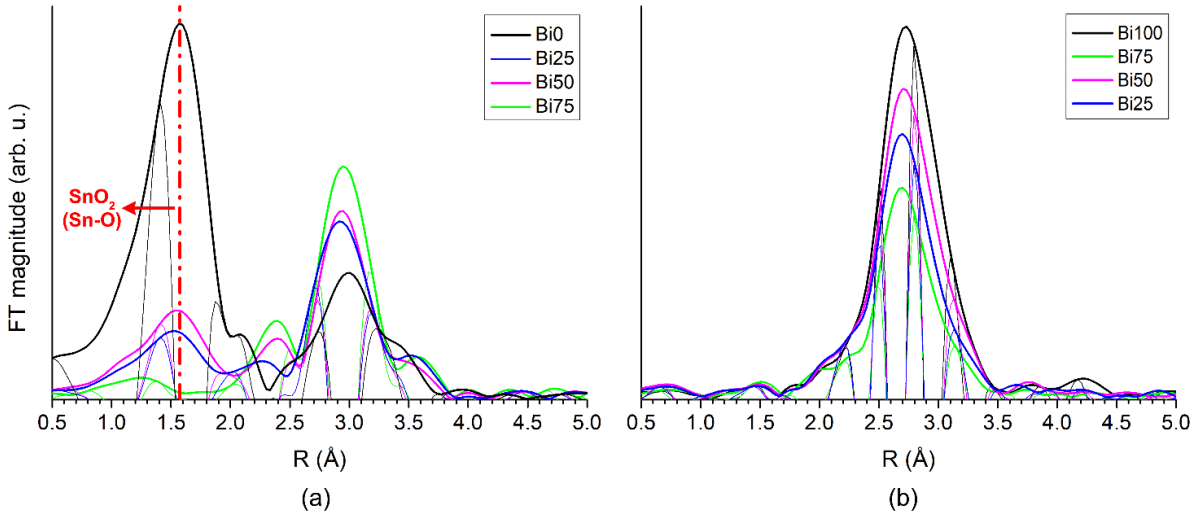

Figure 4.5. (a) Sn K-edge and (b) Bi L_3-edge Fourier-transformed EXAFS spectra of samples. The Sn−O signal due to the oxidation of tin in SnO_2 is marked with a red line.

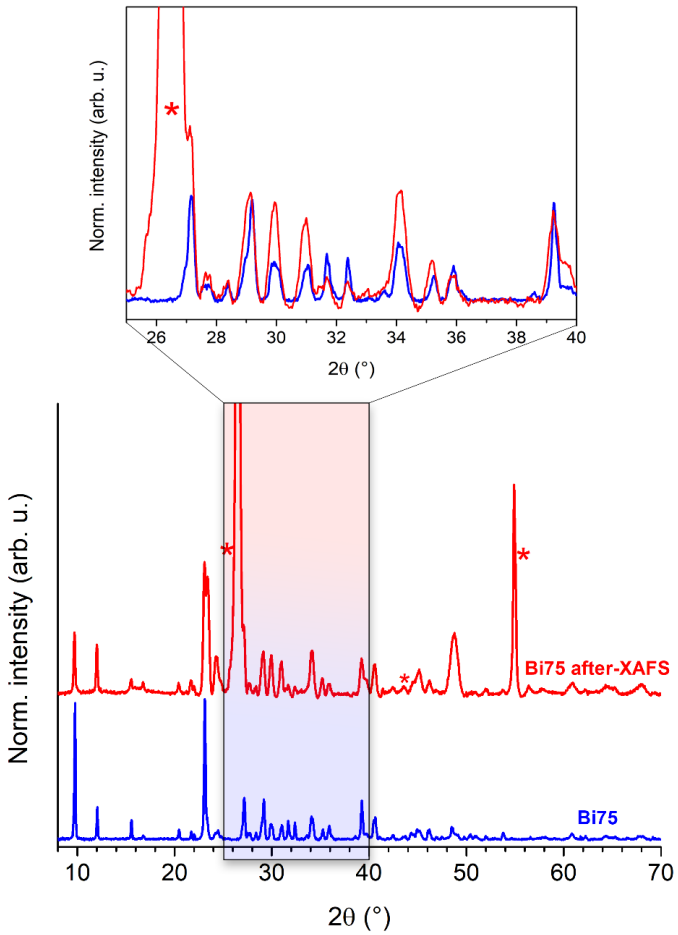

Figure 4.6. Diffraction data of Bi75 pre (blue) and after (red) XAFS with an enlargement of the 25-40° section, where the congruence of the position of the peaks is more evident.

To assess any changes following thin film fabrication, XPS measurements were conducted on freshly deposited films. **Figure 4.7** shows the Bi 4f region of the Bi75 sample, indicating a significant reduction (ca. 23%) of Bi(III) to Bi(0). The asymmetric peak shape suggests delocalization of electrons, hinting at metallic bonding between Bi(0) atoms. While such effects have previously been attributed to X-ray exposure,[240,241] this is unlikely here. Powdered samples exposed to the same Al Kα radiation for double the time showed no signs of reduction, supporting the idea that the observed reduction originates from the solution or suspension environment.[241]

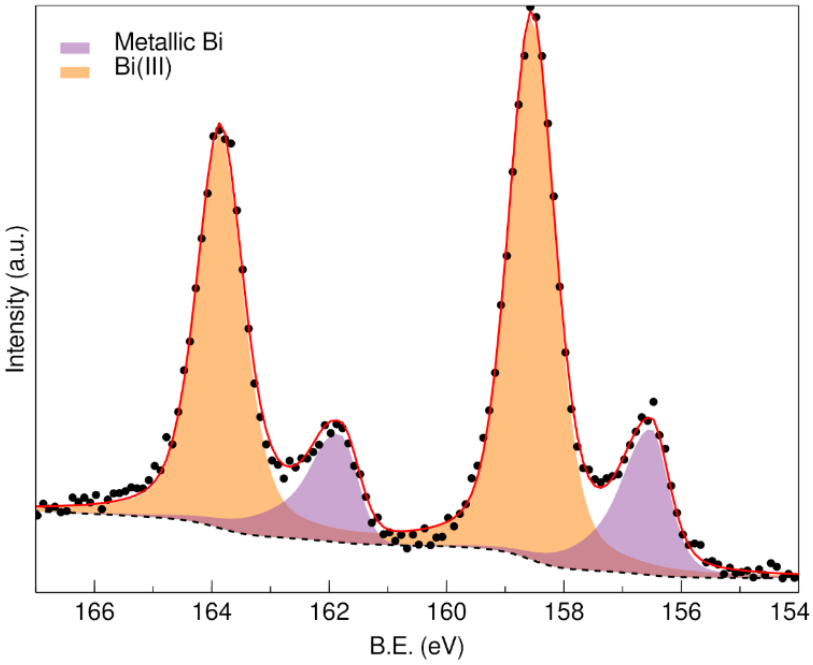

Figure 4.7. Bi75 XPS spectrum in the Bi 4f region.

UV-vis-NIR reflectance spectra of the bulk powders (**Figure 4.8**) exhibit consistent trends, with increased diffuse reflectance near 350 nm corresponding to higher Bi content. Optical band gaps (E_g) were determined from Tauc plots (**Figure 4.9**) and follow a U-shaped trend with increasing Bi content (**Figure 4.10**). The minimum band gap of 1.96 eV is observed in Bi75, extending the trend previously found in the Pb/Bi series,[202] and showing even lower gaps when Sn is used instead of Pb. This non-monotonic trend is likely due to the competing interplay of structural and/or electronic effects (e.g. spin-orbit coupling vs. lattice strain, as observed in $(MA)_3Sb_{1\_x}Bi_xI_9$).[242]

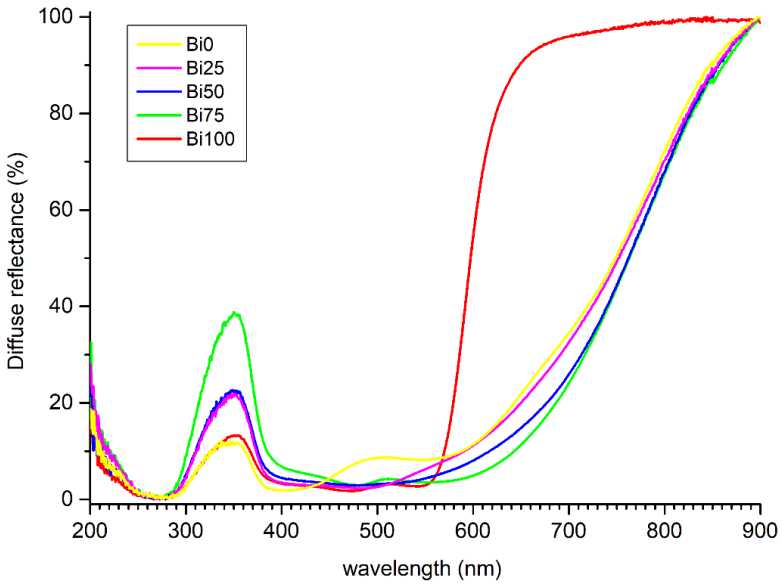

Figure 4.8. UV-vis-NIR reflectance spectra of all bulk powder samples.

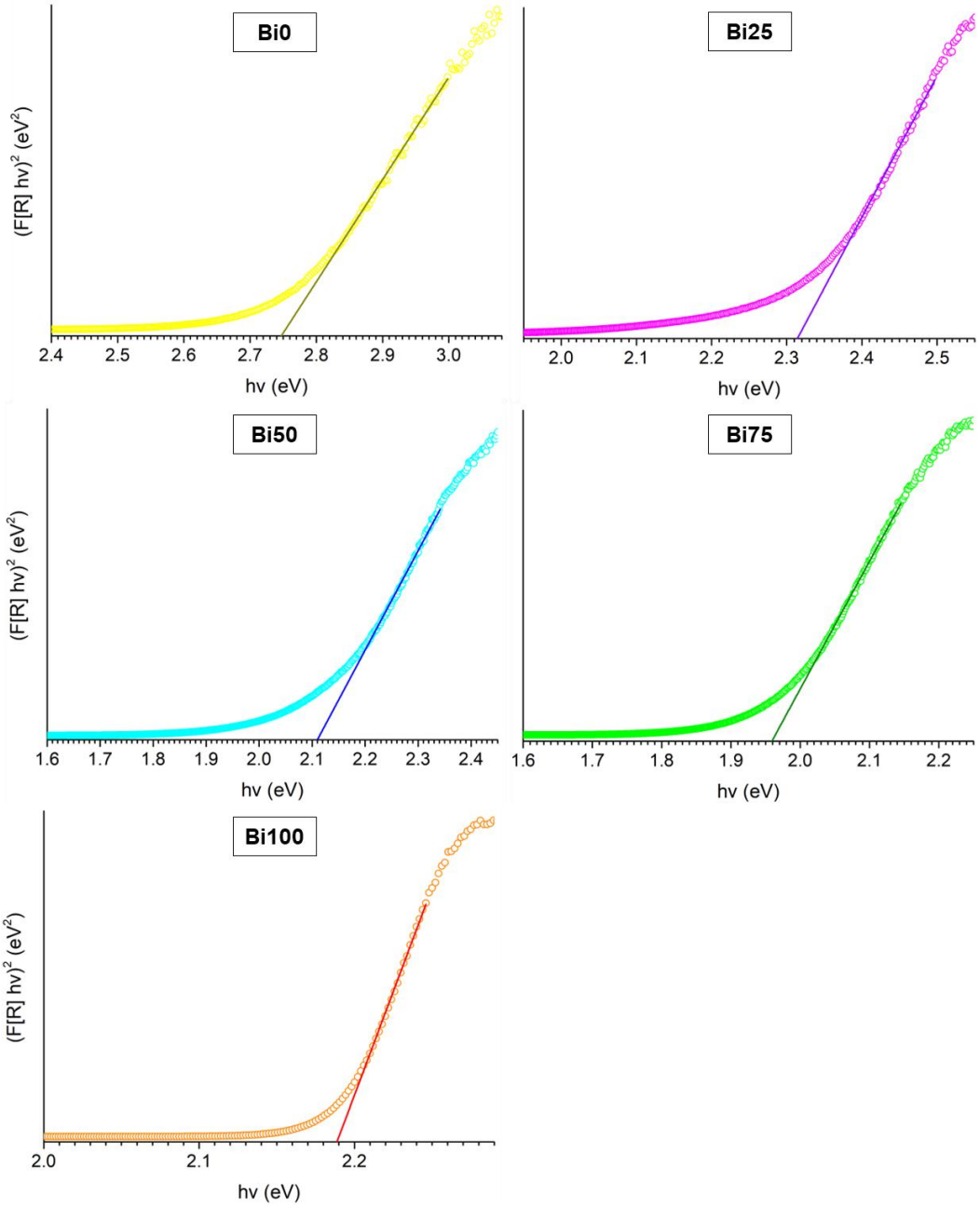

Figure 4.9. Tauc Plots of (a) $(TMSO)SnI_3$, (b-d) $(TMSO)_3Sn_{3x}Bi_{2(1-x)}I_9$ ($0 < x < 1$), and (e) $(TMSO)_3Bi_2I_9$.

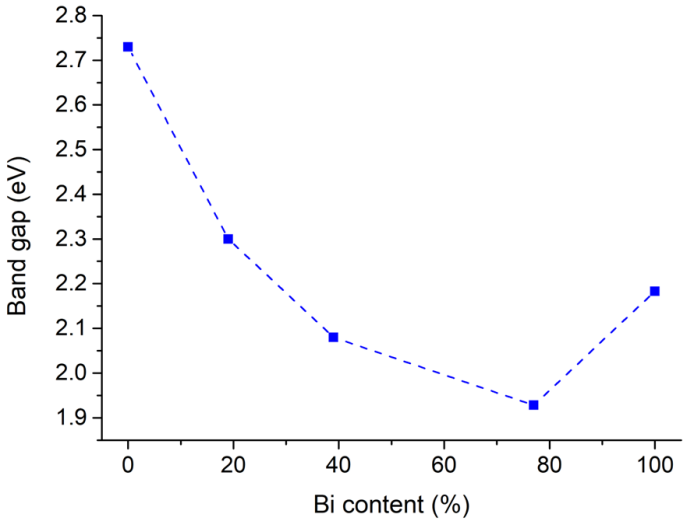

Figure 4.10. Bulk powders optical band gap as a function of %Bi.

SEM analysis was also performed on the powder samples (**Figure 4.11**). It is noteworthy that even a slight variation in bismuth content leads to a substantial difference in the morphology of the various compositions. In the absence of bismuth (Bi0), the grains appear predominantly polygonal with smooth surfaces; in some cases, however, a clear layered structure can be distinguished. The Bi25 and Bi50 samples exhibit very similar morphologies, yet distinctly different from Bi0: in these cases, the predominant morphology is acicular or lamellar, with a noticeable increase in the acicular component in Bi50 compared to Bi25. The Bi75 sample shows another pronounced morphological change, with grains adopting polyhedral shapes; some crystals display symmetric geometries with sharp, angular contours reminiscent of octahedra, while others appear more irregular. Finally, the Bi100 sample is characterized by the presence of large, thick blocks or compact plate-like structures.

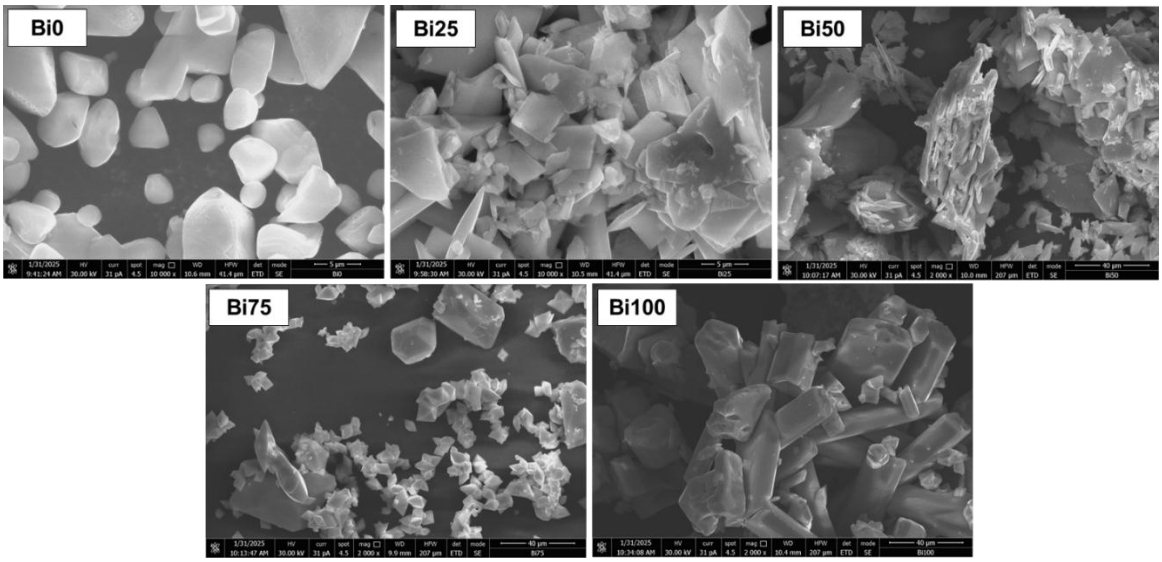

Figure 4.11. SEM images of all $(TMSO)_3Sn_{3x}Bi_{2(1-x)}I_9$ powders.

4.4. Application of Sn/Bi OHP as Piezoresistive Strain Sensors

These materials were finally tested for potential use in the field of bending sensors. To this end, the powders were deposited on ITO/PET substrates by spin coating. The flexible substrates were mounted on a 3D-printed foldable device (**Figure A 4.6**) with one end fixed, allowing bending at different angles (0°, 30°, 60°, 90°) with a bending radius of 10 mm, for the acquisition of I–V curves (**Figure 4.12**). A first analysis reveals that the initial bending step (0-30°) results in a decrease in current slope for all the samples. Specifically, the ITO control sample shows a current variation of approximately 1.66 mA, while the Bi50 and Bi100 samples exhibit relatively minor current changes (0.32 and 0.78 mA, respectively). In contrast, the remaining samples show more significant variations, with Bi0, Bi25, and Bi75 experiencing changes of 3.38, 4.72, and 2.97 mA, respectively. In the bending range between 30 and 90°, the ITO sample displays a current variation of approximately 1 mA for each step, whereas Bi25 shows no significant variations, despite having the largest initial current change. Bi0, on the other hand, exhibits changes of about 1.2 mA for each step, slightly higher than the control. Bi75 maintains a 3 mA variation in the second bending step, which subsequently increases to 3.68 mA in the final bending step, demonstrating tripled sensitivity compared to the substrate alone.

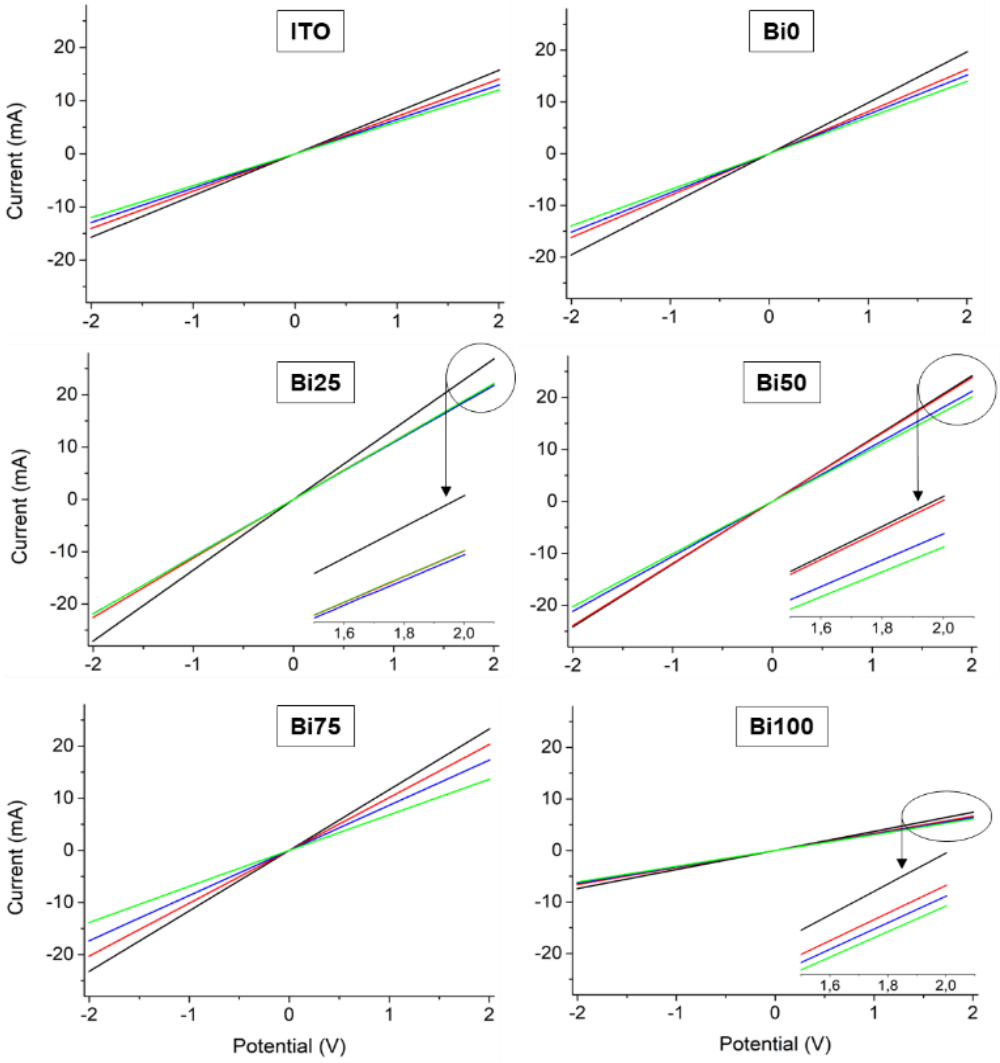

Figure 4.12. I-V characteristic curves detected on the ITO/PET substrate and on all samples at different bending angles: 0° (black lines), 30° (red lines), 60° (blue lines), 90° (light green lines).

A rigorous statistical analysis, based on the average of 16 different scans, was then conducted to assess the decrease in current values measured at +2 V (**Figure 4.13**). The diverse electrical responses can be attributed to both the varying bismuth concentration and the different morphology and roughness of the films. Indeed, the gauge factors for bending at the different bismuth concentration were calculated as $(\Delta R/R)/\varepsilon$ where ε, ΔR, and R are the strain applied to the sensor, resistance variation at ε strain, and initial resistance at zero strain, respectively.[242] The strain can be estimated by the equation $\varepsilon = h/2R$, where h is the ITO/PET thickness of the substrate (about 150 mm) and R is the bending radius, equal to 16, 14, and 12 mm for bending angles of 30°, 60°, and 90°, respectively. The highest value of B70 was observed for Bi75 and Bi100 to be compared with the Bi0, Bi25 and Bi50 and ITO control samples that all showed lower gauge factor values, equal to 50, 24, 13 and 40, respectively.

Notably, Bi100 showed an almost constant gauge factor at all the different bending strains, whereas Bi75 reached a value as high as 110 at 90° bending. The most promising sample, Bi75, underwent a series of multiple bending tests from 0 to 90° (**Figure 4.14**) to evaluate the repeatability and durability of the sensor under repeated stress conditions. The sensor demonstrated excellent long-term repeatability, confirming its suitability as a suitable candidate for this type of device.

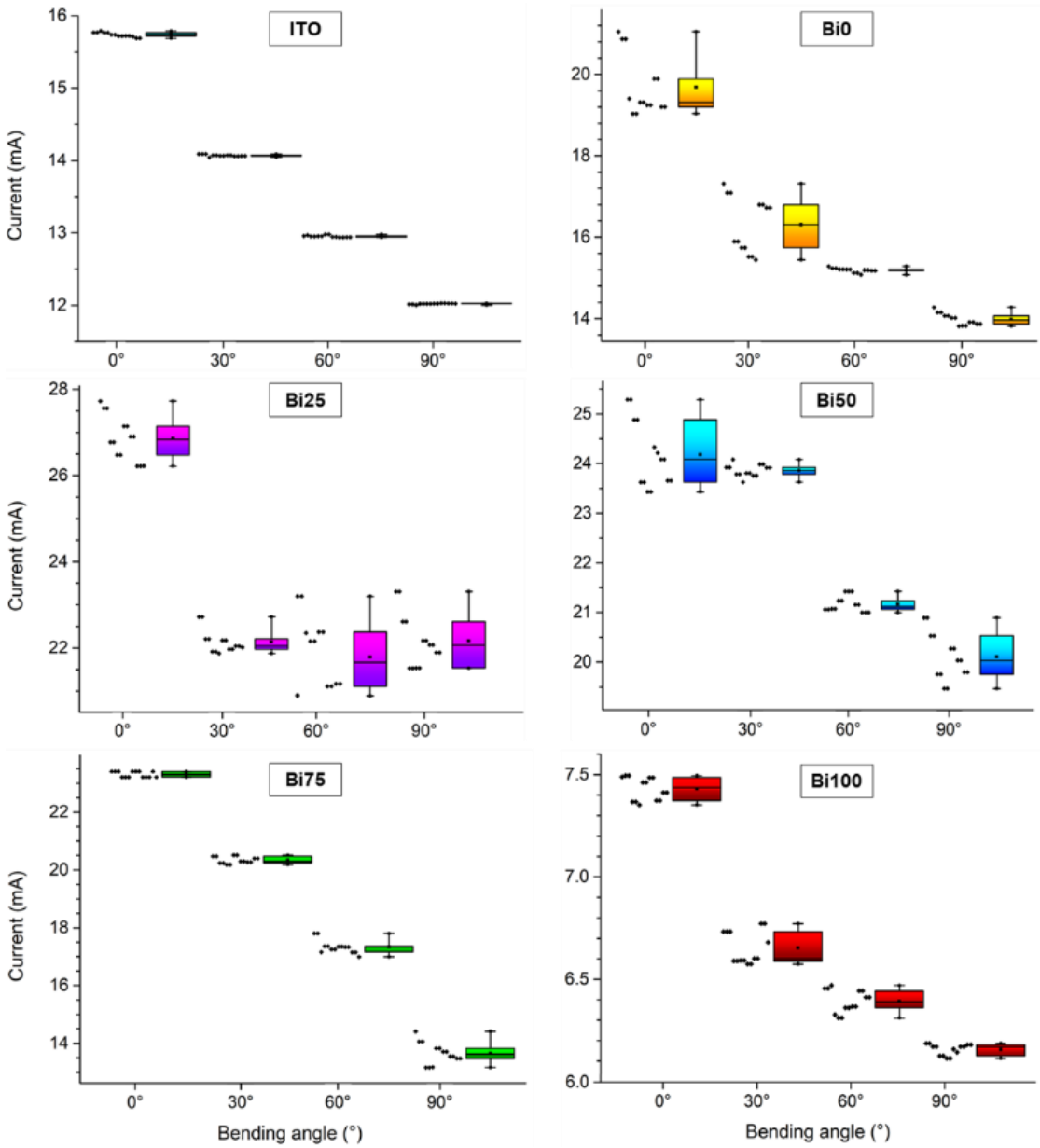

Figure 4.13. Statistical box plots, for the ITO/PET substrate and for all samples, of the fourteen measured current values along with their average at +2 V voltage bias.

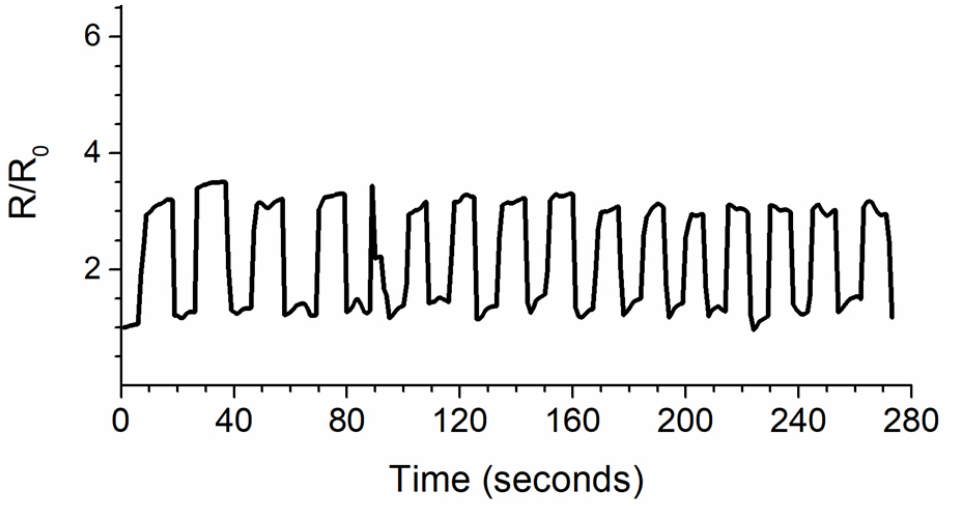

Figure 4.14. Electrical resistance response of multicycle 0-90° bending of the Bi75 sample.

The AFM imaging shows how the morphology of the film undergoes significant changes with different bismuth concentration, as with powders. Bi0 (**Figure 4.15a**) exhibits a peculiar grain shape, entirely different from the other compositions. Bi0 does not display good grain compactness and has a relatively high average roughness of 8.98 nm. Nevertheless, the I-V curves and the calculated gauge factor showed slightly better results than the ITO control. This can be explained by the fact that the film has an average grain size of 150 nm with a well-defined orientation, helping the grains move apart when bent, reducing the current, and then returning to their original position. In contrast, the Bi25, Bi50, and Bi100 samples did not yield positive responses in the I-V curves. Bi25 (**Figure 4.15b**), despite having a lower average roughness (4.75 nm) compared to Bi0, has a smaller average grain size of about 88.91 nm, and their distribution is rather discontinuous. Bi50 (**Figure 4.15c**), on the other hand, has a more compact and continuous grain distribution with an average size, equal to 93.74 nm, but it exhibits a higher average roughness of 9.22 nm. Bi100 (**Figure 4.15f**) presents the least favorable conditions for good electrical conduction, as it has the smallest average grain size, about 66 nm, a discontinuous grain distribution, and an average roughness of 8.2 nm. Bi75 (**Figure 4.15d-e**) displays a rather unique morphology. The film consists of very compact grains that are not easily distinguishable, leading to an extremely dense and continuous distribution, with distinctive tips about 8-12 nm. In this case, it is difficult to estimate the average grain size due to the compactness of the film. Despite the presence of these peaks, the film keeps an extremely low roughness of 0.86 nm.

Thus, the dense, compact, and continuous grain network combined with the low roughness explains why this sample performs better than others.

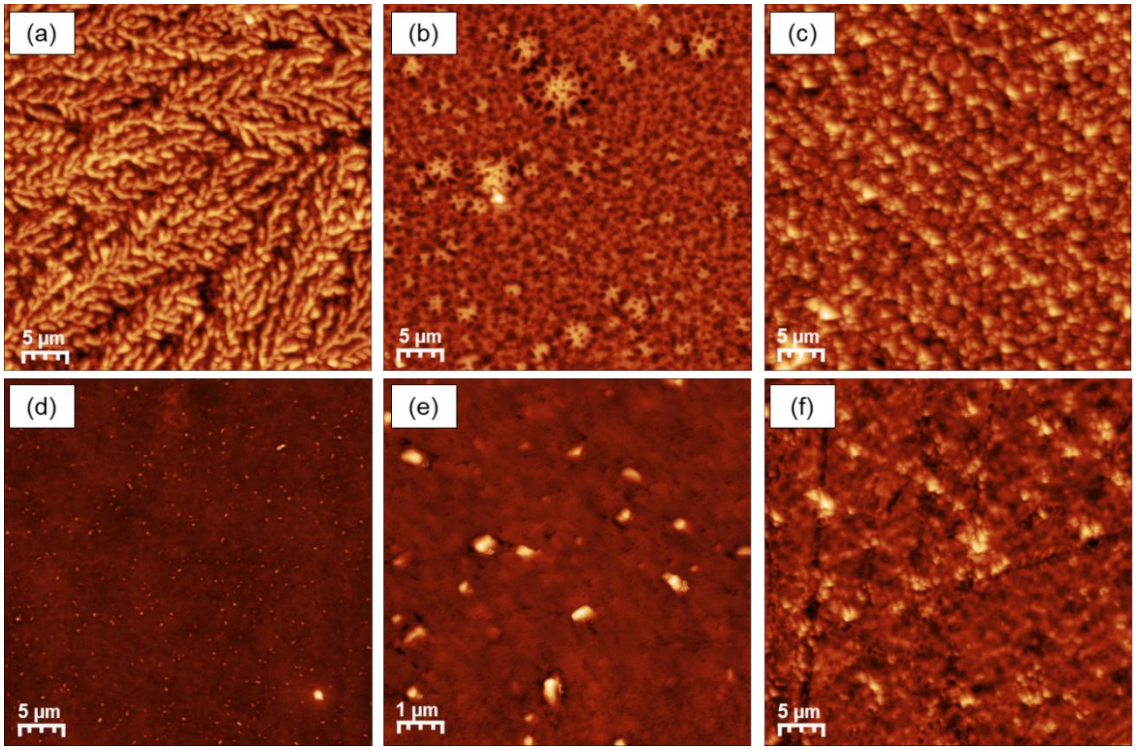

Figure 4.15. AFM top images of (a) Bi0, (b) Bi25, (c) Bi50, (d) Bi75, (e) enlargement of Bi75, (f) Bi100.

The SEM analysis reveals the morphological difference of the Bi75 sensor before and after bending (**Figure 4.16**). Considering that the sample exhibits a dense, uninterrupted network of grains, bending in this case, probably does not result in their separation, but rather causes them to slide. Once the device is returned to its resting state, this sliding leads to the formation of raised microstructures which are extremely oriented, all parallel to each other. Indeed, the presence of sliding conductive networks has already been studied in previous piezoresistive sensors that introduced lubricants such as fullerene[243] or MoS_2 particles,[244] resulting in a significative enhancement of piezosensing performances with respect to films without lubricity. Once the device is returned to its resting state, this sliding leads to the formation of oriented raised microstructures, all parallel to each other. The direction of strain is approximately parallel to the direction at which the bending strain is applied.

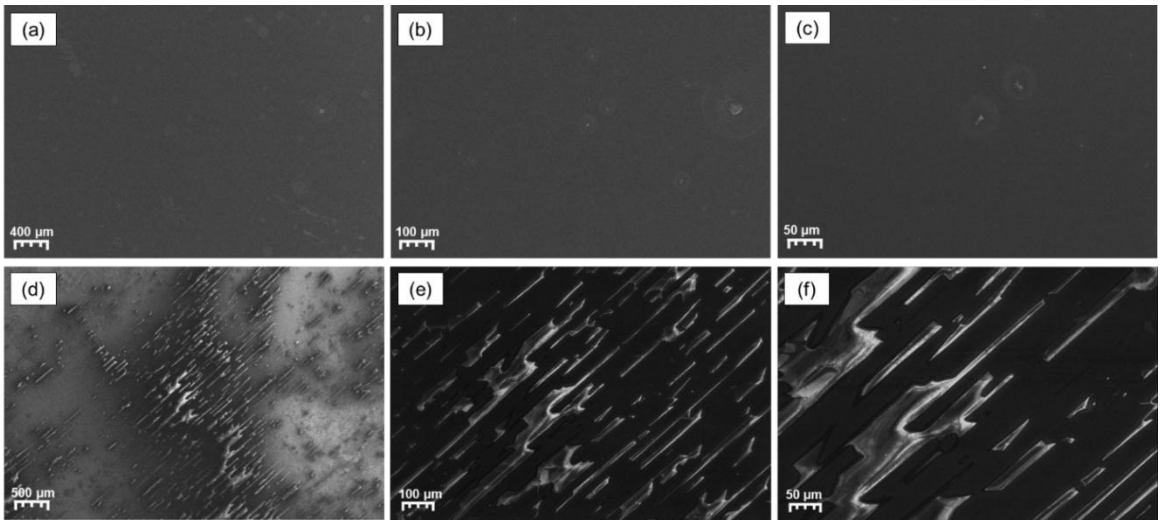

Figure 4.16. Top-view SEM images of (a-c) Bi75 before bending, (d-f) Bi75 after bending.

EIS characterization was carried out on the Bi75 sample before and after the application of the bending strain. The sample before the bending strain showed an almost totally resistive response (**Figure 4.17a**), resulting in a model circuit ($X^2 = 0.0012$) with a resistance (R_{film}) with of 294 ± 2 Ω, hinting to a current flow through unperturbed resistive paths. The EIS analysis on the sample after the 0°–90°–0° bending cycles shows a significant increase of the total impedance of the system in the imaginary component as well. This results in an electrical model in which a resistance is put in parallel to a capacitance (circuit 1, $X^2 = 0.005$, see **Figure 4.17b**), or to a pseudo-capacitance (circuit 2, $X^2 = 0.004$, see Fig. SI), also defined as CPE. The impedance of a CPE is described by:

$$\frac{1}{Q_0 \omega^n} e^{-\frac{\pi}{2}ni} \qquad (4.2)$$

where $Q_0 = 1/|Z|$ and $0 < n < 1$. These two circuits, however, provide results which are not statistically different. Indeed, the resistance of the film after the bending strain (R_{film}') is 36.7 kΩ (±0.01%) for circuit 1 and 36.8 kΩ (±0.01%) for circuit 2. The capacitance value of 3.1 pF (±1.5%) is found for circuit 1, whereas a pseudo impedance of the CPE equal to 4.6 pF (±13.4%) and n = 0.973 (±0.95%) is found for circuit 2. To further ensure the stability, linearity and casualty of both EIS data, a satisfactory Kramers–Kroning test was also performed, i.e. $X^2 < 10^{-5}$ for the pristine Bi75 sample and $X^2 < 10^{-4}$ for the stressed sample. Accordingly, these values agree well with a picture in which the perovskite is affected by defect propagation after the bending stress, leading to microcracks and delamination at the microscale as shown by SEM characterization. These microscale defects concentrate charge

carriers in solid films in accordance with previous EIS models,[245] ultimately reducing the overall conductivity of the films after the application of bending stress.

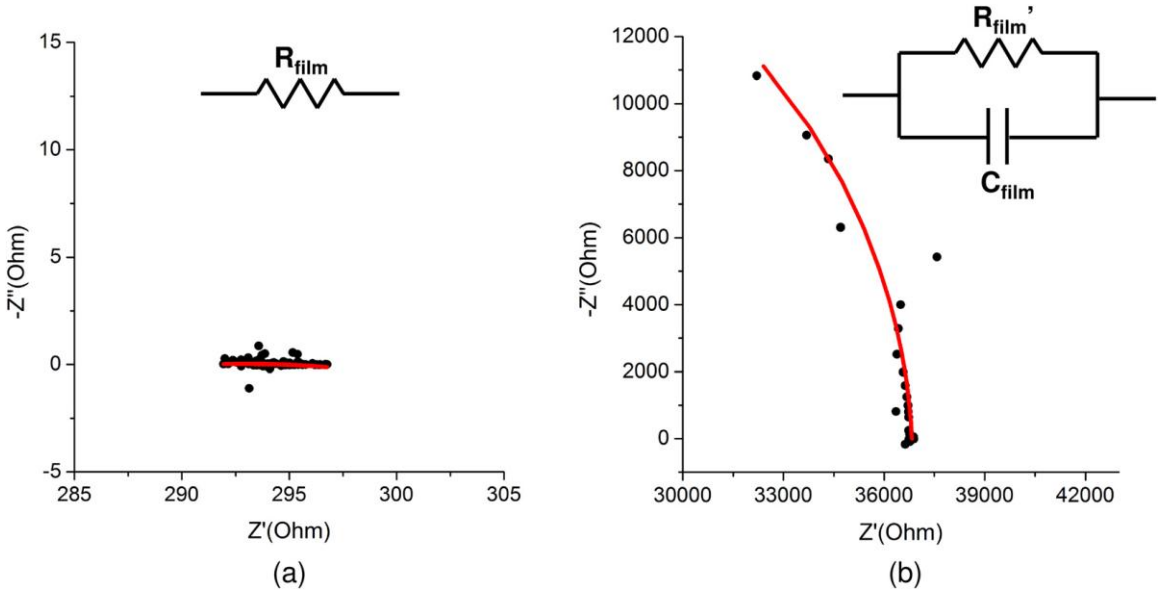

Figure 4.17. Nyquist plots and relative fits of Bi75 bending sensors (a) before and (b) after 0°-90°-0° bending cycles. The best fits for model circuits are marked with a red solid lines.

This chapter shows the synthesis of a novel lead-free hybrid organic–inorganic perovskite $(TMSO)_3Sn_{3x}Bi_{2(1-x)}I_9$ ($0 \leq x \leq 1$) formed by combining Bi^{3+} and Sn^{2+} in different ratio. The Bi^{3+} dependent piezoresistivity of the thin films grown on ITO/PET flexible supports is studied as a function of the Bi^{3+} concentration. Bi^{3+} induces the formation of vacant cation sites in the crystalline cell, leading to shrinkage of the crystalline cell along the *a* axis. This control of the cell size is the key to guide the control of the thin film morphology from separated grains to compact, dense features that are piezo-responsive. The films produced with low amount or no Bi^{3+} display piezoresistive properties similar or even worse than the ITO control, while when Bi^{3+} is the predominant metal ion, the corresponding piezoresistive features are improved. An optimal composition is found in Bi75, at which the perovskite bandgap can be lowered to 1.96 eV, and the gauge factor improves by increasing the bending strain, from 30 to 62 and 110 at 0.4%, 0.5% and 0.6% strains, respectively. This composition shows an almost flat surface with compact grains and vertical tips, which under the application of bending strain is expected to produce sliding of the grains and film delamination, as confirmed by SEM. These observations can be explained by considering that the sliding grains piezoresistive mechanism likely observed in Bi75 resembles the one

observed in graphene conductive networks, where fullerene[243] or MoS_2 lubricant particles[244] increase strain sensitivity at higher ranges with respect to films without lubricity by favouring film sliding. On the contrary, all the other perovskite compositions show nanoscale grains. Indeed, perovskite films containing only Bi^{3+} and no Sn^{2+} show a discontinuous grain distribution, resulting in a surprising constant gauge factor around 65 at all the investigated bending strains which is significantly better than the control ITO, especially at small bending angles. Such constant response of the perovskite containing only Bi^{3+} and no Sn^{2+} can be due to the bending induced separation of grains which is known to produce an increase in relative resistance R/R_0 change of the film in accord with physical models used for conductor-filled polymer composites.[246] This study shows a first step towards the tailored design of a lead-free halide perovskite where the introduction of bismuth ions triggers unprecedented piezoresistive properties to prepare bending sensors requiring sensitivity to small and high bending angles, which can find applications for wearable electronics and soft robotics.

4.5. Appendix

Materials

Hydroiodic acid (HI,57% w/w aqueous stabilized with 1.5 w/w H_3PO_2), hypophosphorous acid (H_3PO_2, 50% w/w aqueous solution), tin oxide (SnO, 99%), and trimethylsulfoxonium iodide ($((CH_3)_3SO)I$, >98%) were purchased from Alfa Aesar. Anhydrous ethanol (C_2H_6O, >99%), bismuth oxide (Bi_2O_3, 99.9%), dimethylformamide (DMF, 99.8%), and isopropyl alcohol (C_3H_8O, 99.7%) were purchased from Sigma-Aldrich. All materials were used without further purification.

$(TMSO)_3Sn_{3x}Bi_{2(1-x)}I_9$ synthesis

Samples with general formula $(TMSO)_3Pb_{3x}Bi_{2(1-x)}I_9$ were synthetized through precipitation from aqueous solution. The corresponding metal oxides were dissolved in 5 mL of HI and 1 mL of H_3PO_2. The stoichiometric quantities for each reaction are described in **Table A 4.1**. The solutions were heated to 70 °C to dissolve all-metal oxides, resulting in a clear solution. (TMSO)I powder was added to the solutions, causing the immediate precipitation of a powder. All powders were decanted for 24 h and then filtered, under vacuum, through 0.45 μm polypropylene filters (Millipore) and washed with anhydrous ethanol. The powders obtained were dried at 40 °C overnight.

Table A 4.1. Stoichiometric quantities used for the $(TMSO)_3Pb_{3x}Bi_{2(1-x)}I_9$ synthesis.

Label	Formula from XRD	$TMSO^+$ mmol	Sn^{2+} mmol	Bi^{3+} mmol
Bi0	$(TMSO)SnI_3$	1	1	--
Bi25	$(TMSO)_3Sn_{2.42}Bi_{0.38}I_9$	1	0.75	0.25
Bi50	$(TMSO)_3Sn_{1.84}Bi_{0.77}I_9$	1	0.5	0.5
Bi75	$(TMSO)_3Sn_{0.69}Bi_{1.54}I_9$	1	0.25	0.75
Bi100	$(TMSO)_3Bi_2I_9$	1	--	1

XRD

XRD patterns of $(TMSO)_3Sn_{3x}Bi_{2(1-x)}I_9$ powders were acquired with a Rigaku Miniflex 600 diffractometer using Ni-filtered Cu Kα radiation (λ=1.5418 Å) and analyzed with Rietveld refinement using GSASII.[213] All samples were refined with an orthorhombic *Pnma* structure and all lattice parameters obtained from refining are reported in **Table A 4.1**. The Rietveld refinements are shown in **Figure A 4.1**-**Figure A 4.5**.

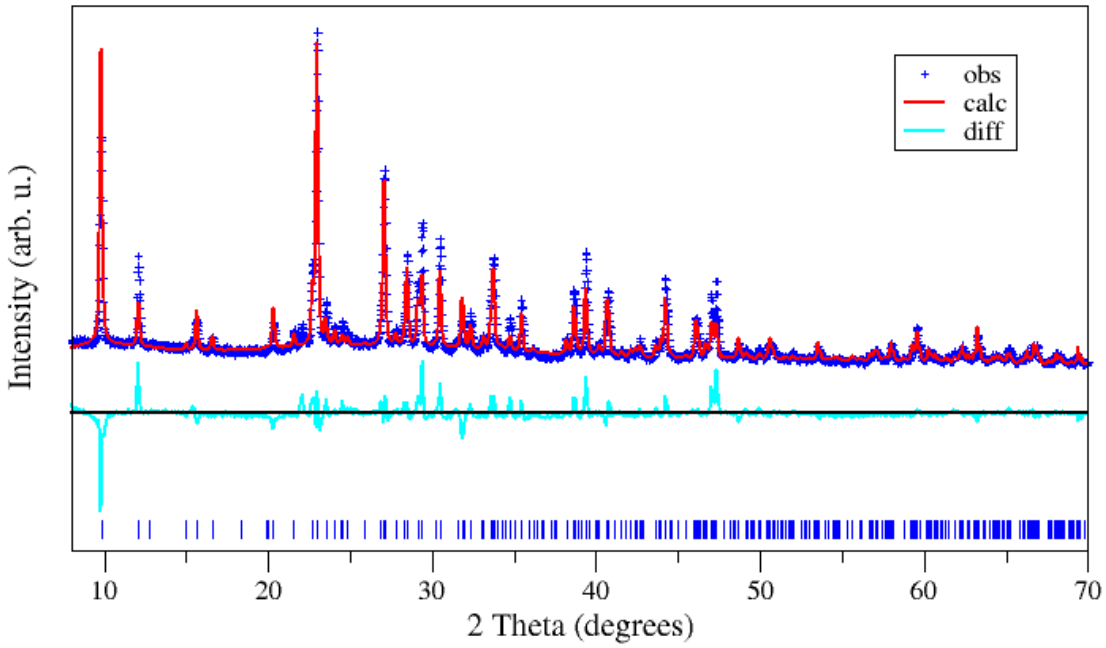

Figure A 4.1. Rietveld refinement plot for $(TMSO)SnI_3$ (Bi0). Experimental data (blue), calculated pattern (red), residual (cyan).

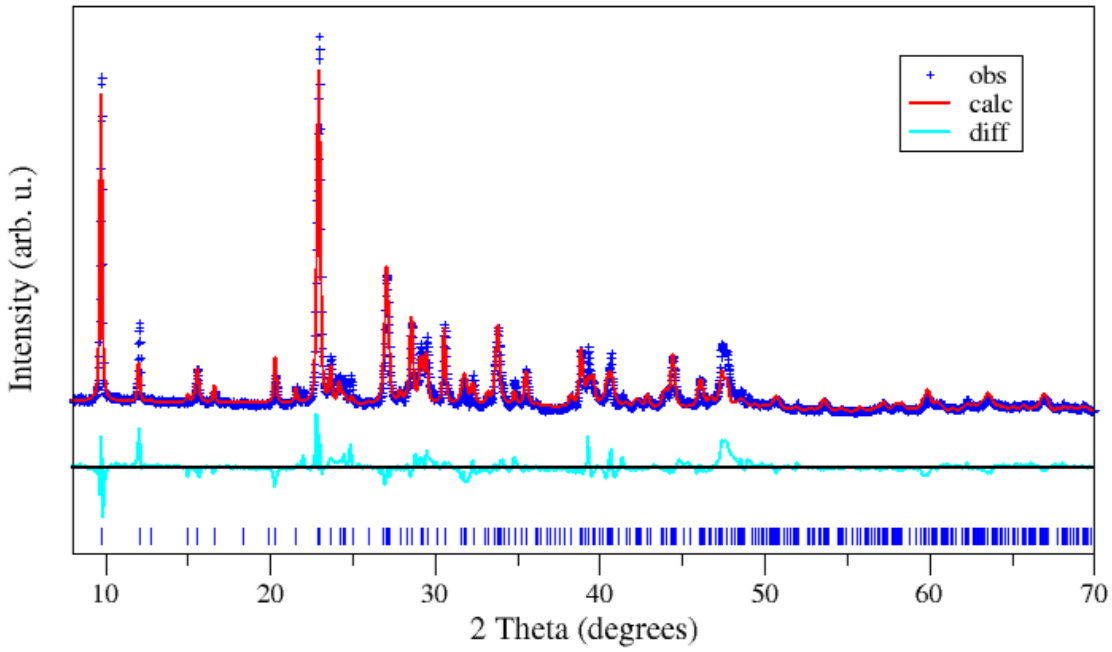

Figure A 4.2. Rietveld refinement plot for $(TMSO)_3Sn_{2.42}Bi_{0.38}I_9$ (Bi25). Experimental data (blue), calculated pattern (red), residual (cyan).

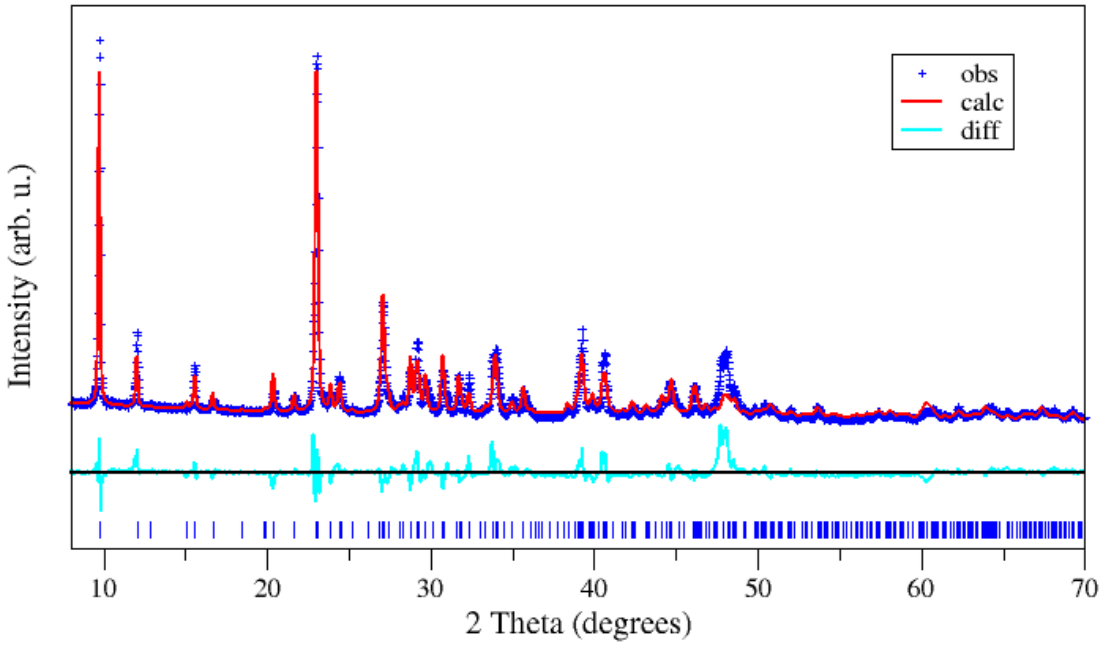

Figure A 4.3. Rietveld refinement plot for $(TMSO)_3Sn_{1.84}Bi_{0.77}I_9$ (Bi50). Experimental data (blue), calculated pattern (red), residual (cyan).

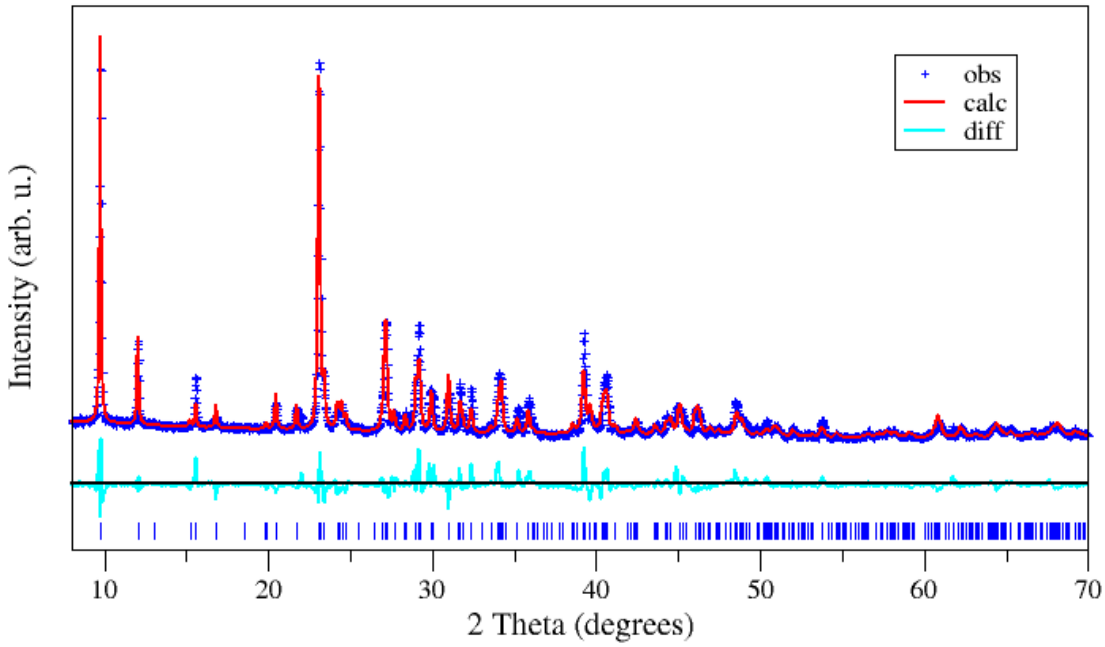

Figure A 4.4. Rietveld refinement plot for $(TMSO)_3Sn_{0.69}Bi_{1.54}I_9$ (Bi75). Experimental data (blue), calculated pattern (red), residual (cyan).

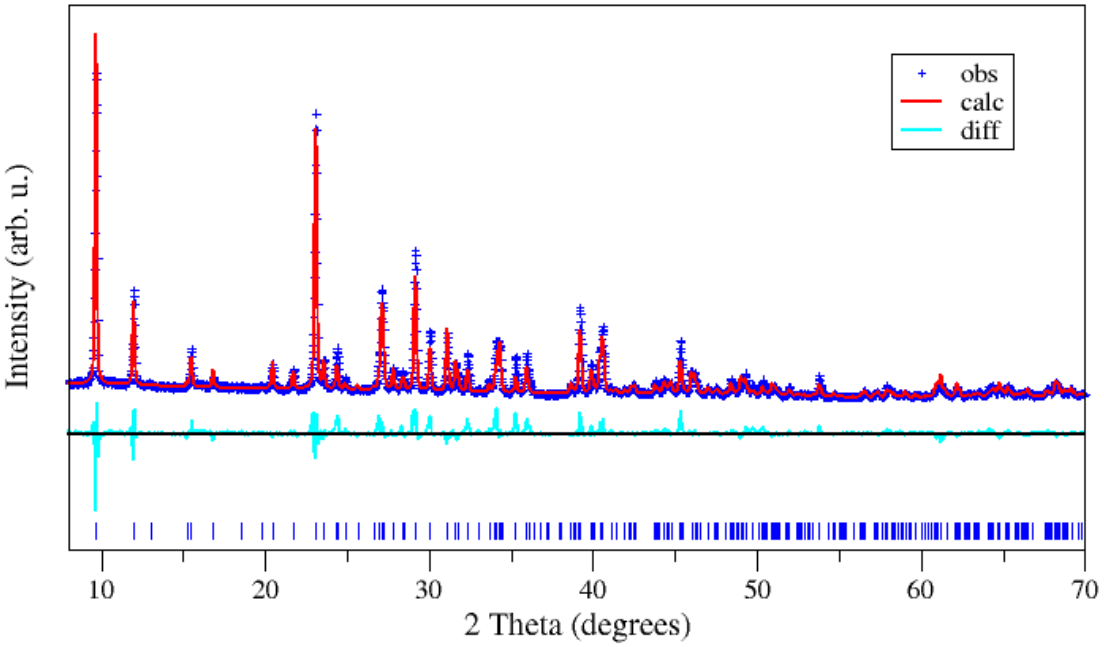

Figure A 4.5. Rietveld refinement plot for $(TMSO)_3Bi_2I_9$ (Bi100). Experimental data (blue), calculated pattern (red), residual (cyan).

Thin films deposition

Thin films were prepared by dissolving the powder with a concentration of 40 mg mL^{-1} in DMF, stirring the solution at 30 °C until a clear solution was obtained. The solution was filtered through 0.22 μm Millipore PTFE syringe filter. Then, 100 mL of solution were spin-coated for 20 s at 4000 rpm using an Ossila system on 1 mm-thick and 24 x 24 mm^2 ITO/PET substrates. Before film deposition, the substrates were sonicated in isopropyl alcohol for 10 min and treated in an ozone cleaner for 30 min.

XRF

XRF was performed on the powders of the three mixed-metal phases with formula $(TMSO)_3Sn_{3x}Bi_{2(1-x)}I_9$. The powders were deposited on a polycarbonate film and analyzed with a MiniPal2 XRF spectrometer (PANalytical), working with a Cr anode at 30 kV and 3 mA, using an Ag filter. X-ray fluorescence lines were measured for Sn ($K_{\alpha 1}$ line, at 25.2 keV) and Bi ($L_{\alpha 1}$, $L_{\beta 1}$ and $L_{\gamma 1}$ lines, at 10.8, 13.0 and 15.2 keV, respectively). Intensity calibration was performed using an equimolar amount of Sn and Bi, using a $(TMSO)SnI_3$ and $(TMSO)_3Bi_2I_9$ mixture.

XAS

XAS spectra at Bi L_3-edge and Sn K-edge were acquired at the BM08 beamline of ESRF. Spectra were acquired in transmission mode on samples cooled at 100 K with a liquid nitrogen cryostat. Each sample was measured on a grid of nine spots ca. 1 mm apart to minimize beam exposure, with each scan lasting about 40 min, and all scans averaged afterwards. For each sample, pellets were prepared by dilution with boron nitride.

XPS

XPS spectra of the deposited thin film were acquired with a PHI5000 VersaProbe II apparatus (ULVAC-PHI, Japan) equipped with an Al K_α anode (1486.6 eV); spectra were collected at high energy resolution (0.05 eV) using a 100 mm beam (25 W), collecting and analyzing in FAT mode electrons with a 45° take off angle, while compensating the electrical charging with both electrons and Ar^+ ions low energy beams.

UV-vis-NIR

UV-vis-NIR reflectance spectra of the $(TMSO)_3Sn_{3x}Bi_{2(1-x)}I_9$ powders were measured in the 200–800 nm range using a Jasco V-770 spectrophotometer equipped with an integrating sphere. The Kubelka–Munk function *F*[R] was calculated from the reflectance spectrum, using the *F*[R] = (1 - R)2/2R relationship. Taking *F*[R] as the representative of the sample absorbance spectrum, extrapolation of the linear portion of the $(F[R]\ h\nu)^2$ vs. $h\nu$ plot on the $h\nu$ axis provided experimentally accessible direct band gap values (Tauc plots).
All transmission mode UV-vis spectra on films deposited on 24 x 24 mm^2 glass substrates, using the latter as blank, were recorded with a Analytik Jena Specord S600 spectrophotometer in the range of 300–650 nm.

Electrical and impedance characterizations

The electrical and impedance characterizations were conducted using a instrument Metrohm Autolab PGSTAT 128 N potentiostat/galvanostat. The electrical response of the sensors was acquired as current-potential (I-V) analyses with a two-electrode connection, linked to the two ends of the ITO 24 x 24 mm^2 active area, connected by crocodile clips (**Figure A 4.6**). The sensing electrode (S) was short-circuited with the reference electrode (RE), to avoid Ohmic losses. The potential range used was from -2 to +2 V with a scanning speed equal to 0.1 V s^{-1}. The sensors were placed on a custom 3D-printed folding device, with a 10 mm sized curvature radius. The bending measurements were performed by affixing the sensors to Kapton tape at both ends. Specifically, one end was securely fixed with Kapton tape, while the other was adjusted to vary the angular position, corresponding to the sensor movement on the folding device. The samples were placed on the folding device, and their behavior was analyzed under static conditions at bending angles equal to 0°, 30°, 60°, and 90°. At each bending step, the folding device is elongated by approximately 5 mm. For each angle, 14 repeated measurements were performed on each sample. Electrochemical impedance spectroscopy (EIS) measurements were carried out in the frequency range comprised between 0.05 Hz and 500 kHz, using a sine wave at 10 mV potential and 0 V bias. The fit of the equivalent circuits from the EIS data was carried out with the Nova 2.1.5 software. Measurements of electrical resistance variations were acquired with a PeakTech 2025 multimeter.

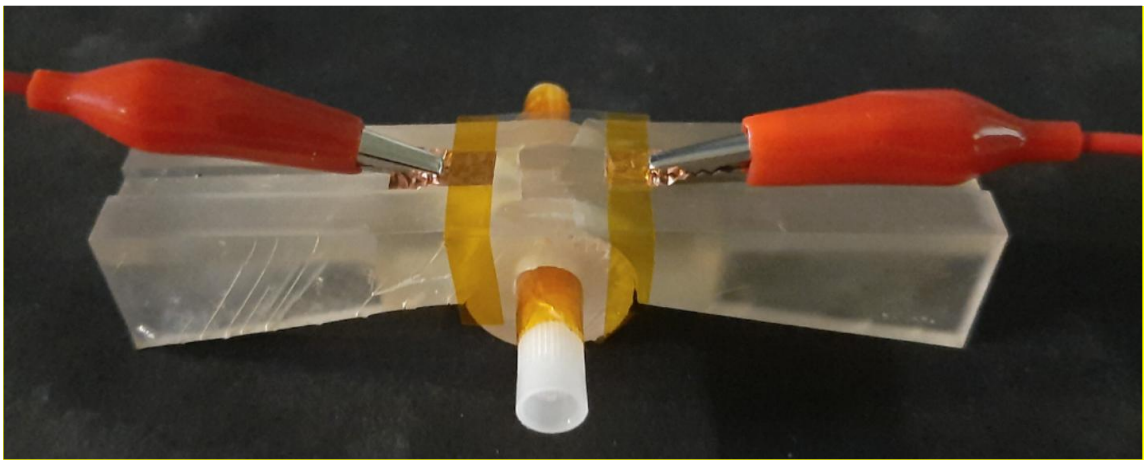

Figure A 4.6. Optical photograph of the piezoresistive sensor mounted on the bending device.

AFM and SEM

AFM was acquired in air with a Bruker Dimension FastScan Bio microscope equipped with a closed-loop scanner (X, Y, Z maximum scan ranges: 35 mm, 35 mm, 3 mm, respectively). The scans were obtained in soft tapping mode in air, by using Bruker FASTSCAN-A probes with a nominal diameter of 5 nm. AFM images were obtained with a pixel resolution comparable to the tip size. The images were analyzed using Gwyddion 2.62.[247] Average roughness was evaluated over the full 5 x 5 μm^2 image with the Otsu grain marking algorithm. SEM was performed in secondary electron mode using a FEI Versa 3D microscope with 10 kV acceleration.

5. Heterovalent Substitution of Lead, part 1: Halide Double Perovskites

5.1. Introduction: Composition and Properties of HDPs

HDPs, derived from the +1/+3 alternate heterovalent substitution of Pb^{2+} and characterized by the general formula $A_2B^+B^{3+}X_6$, represent the most extensively studied alternatives to LHPs. Most of HDPs exhibit very good chemical stability, and achieve highly tunable optoelectronic properties through doping and alloying.[99,157,248,249] Although still not competitive with their lead-based counterparts in photovoltaics, HDPs have nevertheless attracted significant interest in the materials chemistry community, particularly in the form of capped nanosized crystals,[159] for applications such as light emission,[250–252] photodetection,[253] X-ray detection,[254] solar-to-heat conversion,[255] or photocatalysis.[256]

In both simple and double perovskites alike, the A-site cation typically does not directly contribute its orbitals to the electronic states of the VB and the CB, maintaining a completely ionic interaction with the octahedral framework.[257,258] In simple perovskites, the connected $[BX_6]^{4-}$ units are the fundamental building block of the band structure of the materials,[257] whereas in HDPs the electronic states are constructed from the combination of $[BX_6]^{5-}$ and $[BX_6]^{3-}$ units.[258] This breakage of B-site symmetry leads to a significantly larger number of possible electronic structures in HDPs compared to single perovskites. Beyond generating a greater diversity of electronic structures, the loss of B-site symmetry can also fundamentally alter the nature of the band-edge optical transition in double perovskites. In LHPs, the bandgap can be interpreted as a LMCT transition between states with dominant X(p)

character in the VB (with minor Pb(s) contribution), and states with Pb(p) orbital character in the CB.[149] Similar LMCT-type transitions are also observed in some HDPs, however, in many cases, the main transitions exhibit a pronounced MMCT character.[258] Modulating this MMCT transition in HDPs through appropriate selection of B^{+}/B^{3+} combinations provides a powerful means to control the band gap.[149,259]

These diverse electronic behaviors can be categorized into three main groups, as outlined in **Figure 5.1**:[99,260] type 1) indirect band gaps, commonly observed in systems with B^{+} = Ag, Cu, Au (group 11 elements) and B^{3+} = Sb or Bi (group 15 elements), as $Cs_2AgBiCl_6$; type 2) direct band gaps with parity-forbidden transitions at all k-points, due to identical parity of the VBM and CBM, as seen in compositions with B^{+} = alkali metals, B^{3+} = In (or other group 13 elements), like Cs_2KInCl_6; type 3) direct band gaps with parity-forbidden transitions only at the band edges, but allowed transitions at other k-points, typically found in systems with B^{+} = Ag (or other group 11 elements) and B^{3+} = In^{3+} (or group 13 elements), as $Cs_2AgInCl_6$; type 4) direct band gaps with allowed weak transitions, tipically observed in systems with B^{+} = alkali metals and B^{3+} = Sb, Bi (or group 15 elements), like Cs_2KBiCl_6.

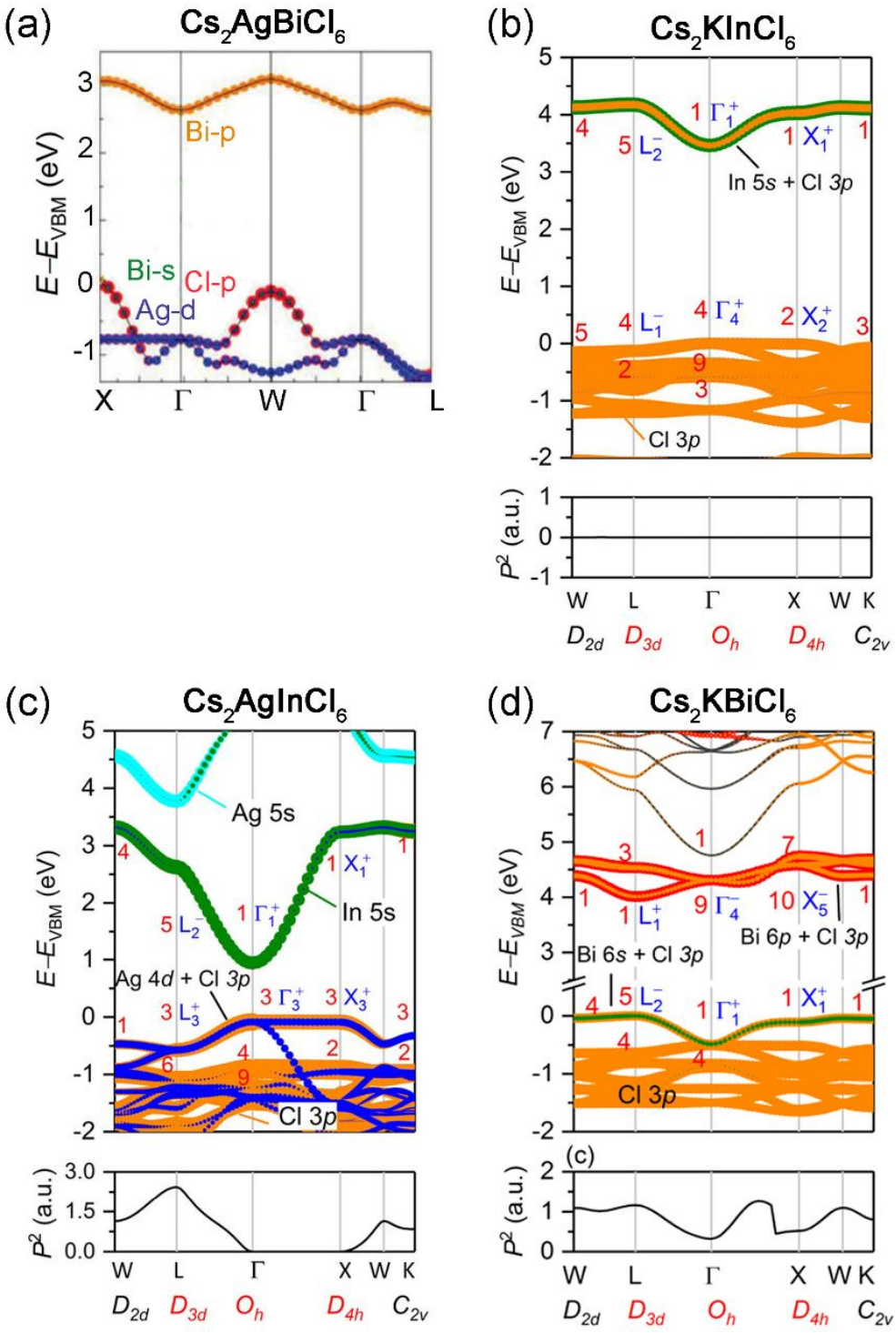

Figure 5.1. DFT-calculated band structures (at the PBE level) for: (a) $Cs_2AgBiCl_6$ (type 1; E_g=2.57 eV); (b) Cs_2KInCl_6 (type 2; E_g=3.57 eV); (c) $Cs_2AgInCl_6$ (type 3; E_g=1.03 eV); (d) Cs_2KBiCl_6 (type 4; E_g=4.01 eV). Black and red symbols below high-symmetry k-points correspond to the point groups without and with inversion symmetry, respectively. Panel a is adapted from ref. [261], with permission from WILEY-VCH Verlag GmbH & Co. KgaA, Copyright 2019. Panels b, c, and d, are reproduced from ref. [260] with permission from American Chemical Society, Copyright 2017.

Direct bandgaps with symmetry-forbidden transitions (e.g., from T_3^+ to T_1^+) result in weak optical absorption. However, it is important to emphasize that these can be advantageous for solar absorber materials if allowed transitions exist near the band edge.[149,259] Furthermore, a narrow forbidden region does not significantly impair light absorption, but it can slow down recombination, as carriers are funneled into the forbidden region, thereby providing long carrier lifetimes that are beneficial for charge extraction.[149]

Double perovskites are also highly tolerant hosts for alloying, and the effects of sub-stoichiometric substitution of a wide range of B-site cations have been extensively explored in a large body of recent literature.[157,262–267,267,268] Isoelectronic alloys involve the substitution of a cation in the host structure with an impurity cation having the same electronic configuration. Consequently, no change in the symmetry of the bandgap is expected, only a modification of its magnitude. For example, in $Cs_2AgBi_{1-x}Sb_xX_6$, the bandgap gradually decreases with increasing Sb^{3+} substitution, but remains indirect across the entire compositional range. This reduction in the bandgap is due to the higher energy of the Sb 5s orbital compared to Bi 6s, and to the stronger Sb(5s)–Cl(3p) coupling, which raises the VB. Conversely, the Sb 5p orbital is lower in energy than Bi 6p, and its weaker coupling with Cl 3p lowers the CB, resulting in a reduced bandgap with higher Sb^{3+} content.[268,269] In non-isoelectronic alloys, the impurity does not have the same electronic configuration as the cation it replaces, and therefore, at sufficiently high levels of alloying, both the symmetry and the magnitude of the bandgap are modified. In the alloy $Cs_2AgBi_{1-x}In_xX_6$,[268,270] a $4d^{10}5s^0$ cation (In^{3+}) replaces a $6s^26p^0$ cation (Bi^{3+}). The substitution with In^{3+} leads to the formation of a new conduction band, arising from the empty In 5s orbitals, which exhibits a minimum at the Γ point.[260] Meanwhile, the removal of Bi^{3+} from the structure reduces the antibonding contribution of its 6s orbitals to the valence band at the X point, thereby lowering the VBM. Across most of the solid-solution range, the bandgap is indirect from X to Γ, but once a sufficient amount of Bi^{3+} is removed from the system, the bandgap becomes direct at the Γ point.[268]

The bandgap and properties of interest for optoelectronic applications, such as the exciton binding energy, undergo drastic changes as the dimensions are reduced.[271,272] For this reason, significant advances have been achieved in the field of colloidal HDP NCs in terms of controlled shape and composition synthesis, self-assembly, understanding of optical properties, and applications in optoelectronic devices.[273] Unlike their bulk counterparts, the optical properties of colloidal NCs can be tuned not only through composition but also via quantum confinement effects.[274–277] HDP NCs are predominantly synthesized via solution-

processing techniques, primarily relying on the use of long-chain ligands that selectively adsorb onto the surface of the perovskite nanoparticles.[273,278] The ligands serve a dual purpose: firstly, due to their large size, these cations cannot be incorporated into the perovskite crystal structure, thereby inducing self-termination of nanocrystal growth; secondly, they passivate and protect the newly formed crystal facets.[277] Due to their high surface-to-volume ratio, the optical and optoelectronic performance, as well as the colloidal stability of LHP NCs, largely depend on their surface chemistry, particularly the ligands and surface termination. The most commonly used capping ligands are long-chain alkylamines and alkyl acids, specifically the OLAM and OA pair.[279–281] The OA/OLAM acid-base pair initially transforms into oleate anions and oleylammonium cations through proton transfer, which subsequently bind to the surface of the NCs, while the ligands also facilitate the dissolution of the precursors in the solvent, thereby initiating the formation of colloidal NCs.[275,282–284] Unfortunately, NCs often exhibit much lower PLQYs compared to their bulk counterparts. This discrepancy is commonly attributed to incomplete surface passivation of the colloidal NCs after synthesis and/or washing, leading to the presence of undercoordinated ions at the surface, which in turn can give rise to mid-gap electronic states.[273,274,285,286] For this reason, over the years, several studies have focused on exploring various strategies, such as optimizing the ratios of metal precursors and OA/OLAM capping, or employing alternative ligand molecules, to achieve effective surface passivation of LHP NCs, with the aim of enhancing colloidal stability and PLQY, as well as imparting new properties and functionalities to the materials.[274]

The preparation of high-quality HDP NCs with precise control over size, shape, and optical properties is most effectively achieved through the HI and LARP methods. In the HI method, precursors are dissolved in a high-boiling solvent under heating, stirring, and degassing, followed by the rapid injection of additional reactants to induce nucleation, and a temporally separated NCs growth.[287–289] Critical parameters governing the size, size distribution, and morphology of colloidal NCs synthesized by HI include: 1) the surfactant-to-precursor ratio; 2) the injection temperature of the cationic or anionic precursor; 3) the reaction time; and 4) the precursor concentration.[14,279,290]

In the LARP route, precursors are dissolved under supersaturated conditions and subsequently reprecipitated in the presence of ligands, resulting in the formation and growth of colloidal NCs with dimensions ranging from tens to several hundreds of nanometers.[14,291,292] For the colloidal synthesis of lead-free perovskite NCs, the HI approach

has been the most employed, despite being less environmentally friendly, while reports of their preparation with LARP are scarce.[14]

In this chapter, three different HDP NCs with B^+ = Ag, Na, K and B^{3+} = Bi, along with their intermediate alloys, are analyzed from a structural and optical point of view. These NCs were synthesized using the conventional HI method with the OA/OLAM ligand pair. The choice of monovalent cations was motivated by the aim of evaluating how their identity influences the structure and optical properties of the HDPs. In particular, the progressive substitution of Ag^+ with Na^+ in $Cs_2AgBiCl_6$ was first studied to analyze the effect of a non-isoelectronic substitution (Ag^+: $4d^{10}5s^0$; Na^+: $2p^63s^0$). Subsequently, Na^+ was gradually replaced with K^+, which presents the same electronic configuration, in order to investigate also the effect of isoelectronic substitution on the properties of the HDPs. The three monovalent cations (Ag^+, Na^+, K^+) were subsequently combined with In^{3+} to evaluate how its $4d^{10}5s^0$ electronic configuration affects the structure and optical properties compared to bismuth, which exhibits an $6s^26p^0$ configuration. These compositions, however, were synthesized using the same OA/OLAM ligand pair but following a different synthetic approach. Although the HI method effectively results in NCs with good control over size and shape, it also has important drawbacks, including limited reproducibility due to high operator dependency, infeasibility for large-scale production, and the frequent requirement for inert conditions. Moreover, its compositional tunability (i.e., the key to exploiting HDPs) is limited, since introducing a dopant or adjusting the amount of an alloying cation requires setting up an entirely new reaction. A multistep synthetic strategy was thus developed for the preparation of HDP NC colloids, enabling the formation of high-purity nanocrystalline phases that, unlike conventional one-pot methods, allow rapid and efficient compositional engineering by facilitating cation substitution within the three-dimensional HDP lattices, a crucial step toward obtaining materials with tailored optoelectronic properties.

5.2. Synthesis and Characterization of Bi-based HDP NCs

$Cs_2AgBiCl_6$ nanocrystals were synthesized using the HI method. The corresponding metal acetates were dissolved in a mixture of OA, OLAM, and ODE under vacuum. After heating, TMSCl was swiftly injected at 170 °C, and the reaction mixture was cooled after 10 s. The resulting NCs were purified through successive centrifugation and redispersion steps, finally obtaining a suspension containing the pure NCs. The substitution of Ag^+ ions with Na^+ was carried out through a series of syntheses in which the stoichiometric ratio of the starting Ag and Na acetates was varied (see the Appendix for details), yielding alloys with the formula $Cs_2Ag_{1-x}Na_xBiCl_6$ ($0 \leq x \leq 1$), up to the complete replacement of Ag^+ ($x = 1$) and the formation of $Cs_2NaBiCl_6$ (**Scheme 5.1**). In a similar manner, K^+ ions were gradually substituted for Na^+ ions, yielding alloys with the formula $Cs_2Na_{1-x}K_xBiCl_6$ ($0 \leq x \leq 1$), up to the complete replacement of Na^+ ($X= 1$) and the formation of Cs_2KBiCl_6. (**Table 5.1**).

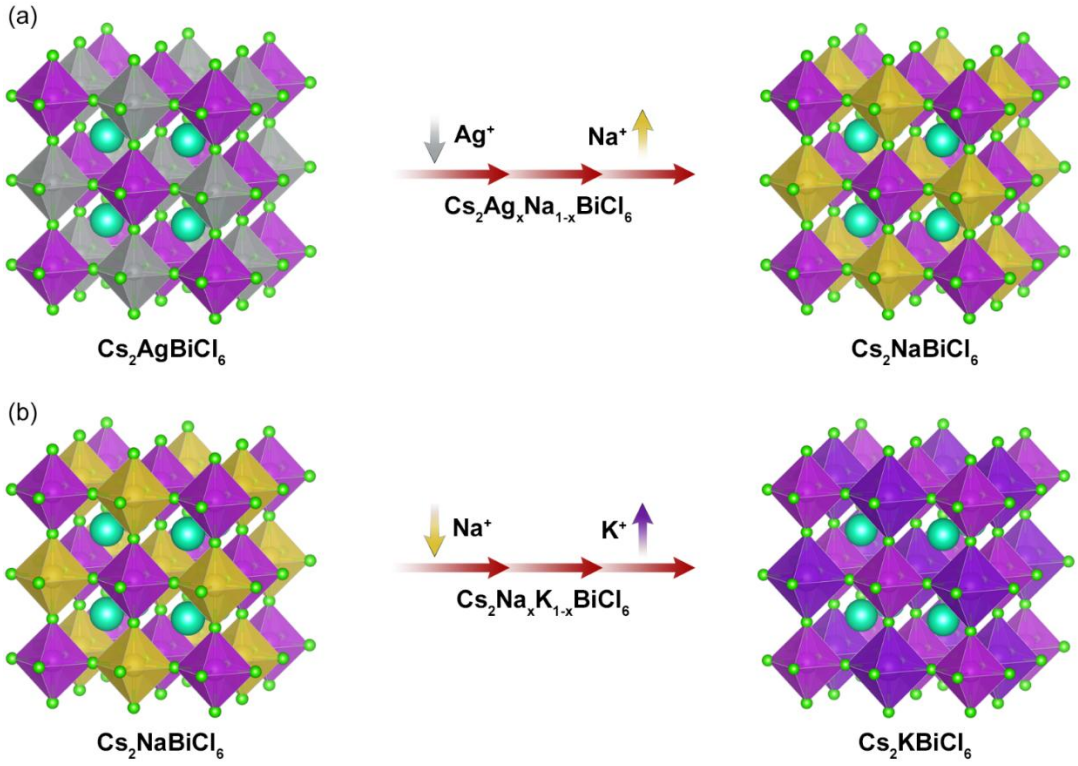

Scheme 5.1. Bi-containing HDP solid solutions described in this chapter. (a) Na^+ doping in $Cs_2AgBiCl_6$, and (b) K^+ doping in $Cs_2NaBiCl_6$. Chlorine atoms are in green, cesium atoms in teal, $BiCl_6$ octahedra in purple, $AgCl_6$ octahedra in grey, $NaCl_6$ octahedra in yellow and KCl_6 octahedra in dark violet.

Table 5.1. Labels, stoichiometry (determined by ICP-OES) and crystal structure of $Cs_2(Ag,Na,K)BiCl_6$ NCs. Space group: *Fm-3m*. Uncertainty is reported in parentheses.

Labels	Formula	Crystal data	
		a = b = c (Å)	V (Å^3)
Ag100	$Cs_2AgBiCl_6$	10.800(1)	1259.9(3)
Ag75	$Cs_2Ag_{0.83}Na_{0.17}BiCl_6$	10.8062(7)	1261.9(2)
Ag50	$Cs_2Ag_{0.4}Na_{0.6}BiCl_6$	10.823(9)	1267.8(3)
Ag25	$Cs_2Ag_{0.24}Na_{0.76}BiCl_6$	10.826(7)	1268.9(2)
Na100	$Cs_2NaBiCl_6$	10.8372(7)	1272.7(2)
K25	$Cs_2K_{0.27}Na_{0.73}BiCl_6$	10.872(1)	1285.2(4)
K50	$Cs_2K_{0.41}Na_{0.59}BiCl_6$	10.927(2)	1304.7(9)
K75	$Cs_2K_{0.7}Na_{0.3}BiCl_6$	11.043(2)	1346.7(9)
K100	Cs_2KBiCl_6	11.136(2)	1381(1)

The XRD patterns of $Cs_2AgBiCl_6$ nanocrystals with different Na^+ fractions are shown in **Figure 5.2a**. The XRD results reported in **Table 5.1** show that $Cs_2AgBiCl_6$ NCs with varying sodium contents exhibit a cubic double perovskite structure in the *Fm-3m* space group.[289] As the Na^+ content increases, the diffraction peaks shift toward smaller 2θ angles. Furthermore, with increasing Na^+ incorporation, the intensity of the (111) diffraction peak gradually increases (see magnified view in **Figure 5.2a**), since the structure factor for this reflection is proportional to the difference in average atomic scattering factors between Na and Ag atoms in the B-site. This trend proves the formation of $Cs_2Ag_{1-x}Na_xBiCl_6$ NCs in intermediate Na/Ag compositions.[293]

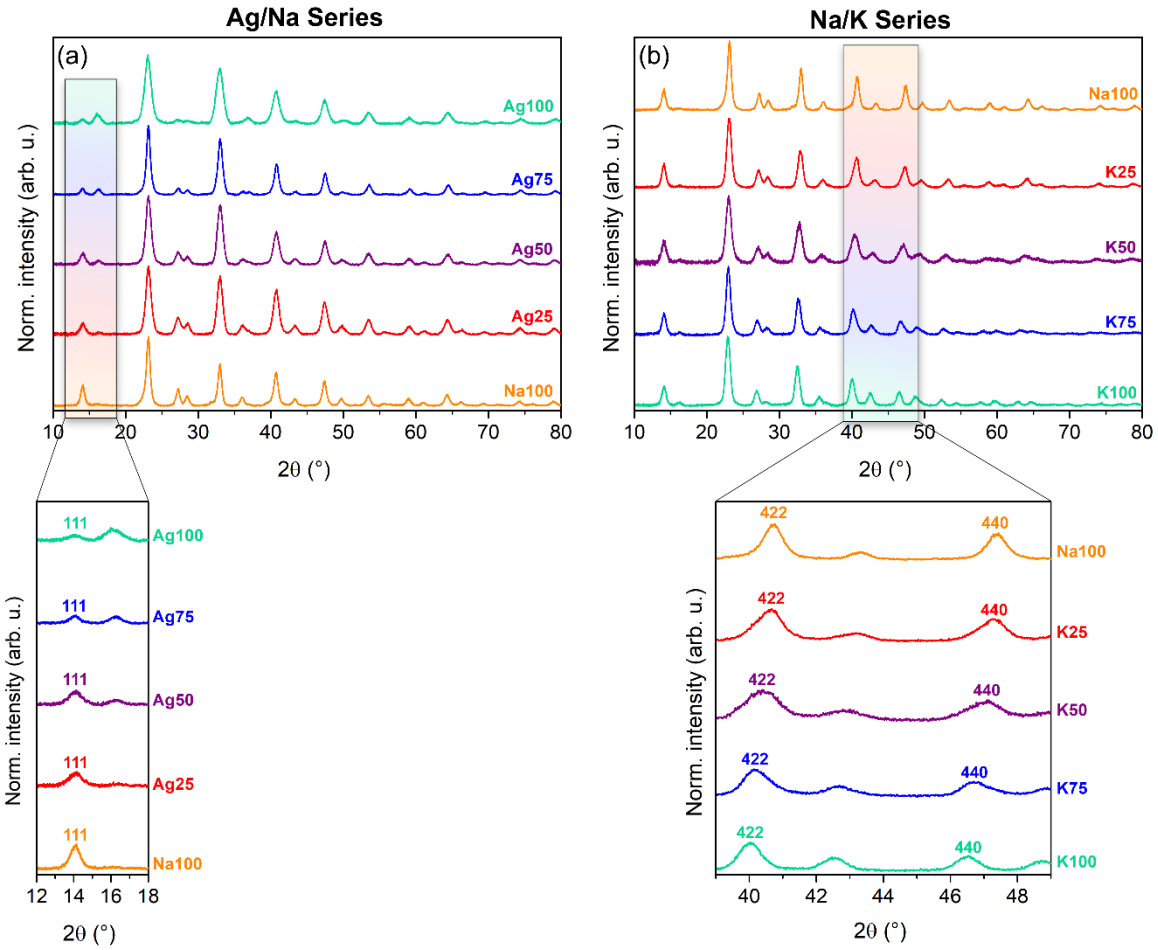

Figure 5.2. (a) XRD patterns of $Cs_2Ag_{1-x}Na_xBiCl_6$ with an enlargement of the 12-18° range, where the peak (111) discussed in the text is more evident. (b) XRD patterns of $Cs_2Na_{1-x}K_xBiCl_6$ with an enlargement of the 39-49° section, where the peaks discussed in the text are more evident.

The Rietveld refinement of the structures indicates that the substitution of Ag^+ with Na^+ induces a small but significant lattice expansion (**Figure 5.3a**), increasing from 10.800(1) Å for $Cs_2AgBiCl_6$ NCs to 10.8372(7) Å for $Cs_2NaBiCl_6$ NCs (**Table 5.1**). This lattice expansion might be somewhat unexpected if one considers the tabulated ionic radii for six-coordinated Ag^+ (1.15 Å) and Na^+ (1.02 Å).[294] However, it can be attributed to the shorter observed Ag−Cl bond length (2.708 Å), which is partially covalent,[267] compared to the Na−Cl bond length (2.736 Å) which exhibits a more ionic character.[146,295] The expansion can thus be attributed to the greater covalent character of the Ag−Cl bond compared to the Na−Cl bond. **Figure 5.2b** shows the XRD patterns of the $Cs_2Na_{1-x}K_xBiCl_6$ NCs. The results indicate that all compositions retain the typical cubic structure of $Cs_2NaBiCl_6$ NCs. The magnified region highlights the diffraction peaks at 40.7° and 47.4°, corresponding to the (422) and (440) crystal planes, respectively. As the K^+ content increases, the XRD peaks gradually shift toward lower 2θ angles, reaching 40.04° and 46.52°, respectively. This shift

toward lower angles is due to the replacement of smaller Na^+ ions with larger K^+ ions. The incorporation of K^+ into the crystal lattice therefore leads to a lattice expansion (**Figure 5.3b**), as confirmed by the unit cell parameters obtained through Rietveld refinement (**Table 5.1**).

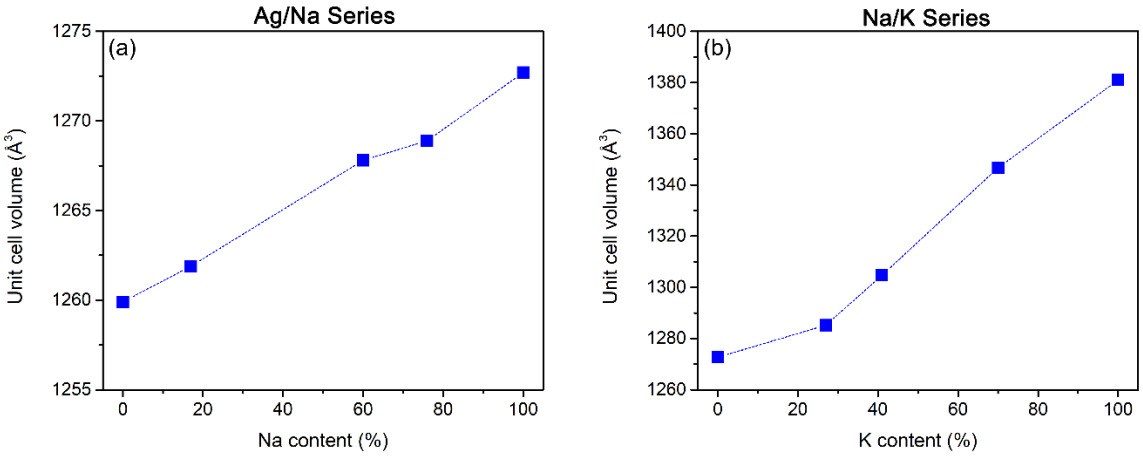

Figure 5.3. Unit cell volume as a function of (a) Na content in the $Cs_2Ag_{1-x}Na_xBiCl_6$ series and (b) K content in the $Cs_2Na_{1-x}K_xBiCl_6$ series. Error bars are not shown as they are smaller than the square markers.

For $Cs_2AgBiCl_6$, the VBM exhibits Cl 3p, Ag 4d, and Bi 6s character at the Γ point, while the CBM shows Bi 6p, Cl 3p, and Ag 5s character at the L point, resulting in an indirect band gap.[296,297] The situation is different for $Cs_2(Na,K)BiCl_6$. The CBM mainly originates from Bi 6p and Cl 3p orbitals at the L point with even parity (L^+), while the VBM is also located at the L point but with odd parity (L^-) and mainly derives from Bi 6s and Cl 3p states. Consequently, these two compositions exhibit a direct bandgap and do not show parity-forbidden transitions at the band edges.[260]

The UV–vis absorption spectra of Ag100 with different Na^+ incorporation levels are shown in **Figure 5.4a**. The absorption spectrum of Ag100 shows the characteristics of an indirect bandgap semiconductor with an excitonic peak at 369 nm, followed by a broad tail extending up to ~500 nm.[147,298] The absorption peak originates from the direct bismuth s-p transition,[287,299] while the absorption tail mainly corresponds to the trap-state-related transition and indirect band gap transition, which has an at least partially Ag s-d character.[287,298,299] The surface trap-state transition can be tuned by surfactants such as OA, therefore, the estimation of the indirect bandgap by means of a Tauc plot is not reliable.[248,300]

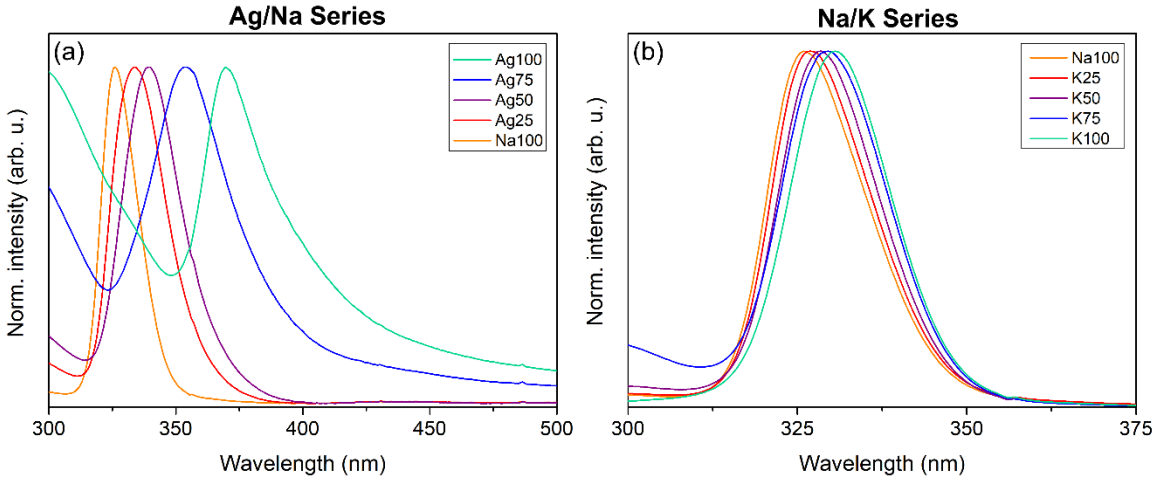

Figure 5.4. UV-vis spectra of the (a) $Cs_2Ag_{1-x}Na_xBiCl_6$ NCs and of the (b) $Cs_2Na_{1-x}K_xBiCl_6$ NCs, dispersed in toluene.

Figure 5.5a shows the fitting of the experimental absorption coefficient to the Tauc equation, using an exponent of 1/2 ($\gamma = 2$) for the indirect bandgap of Ag100. The shallow absorption region begins at about 1.5 eV and is followed by a sharp increase in absorption near 2.7 eV, the indirect bandgap is therefore between these two values, but it cannot be estimated precisely, falling within the range of various experimental indirect bandgaps reported in the literature.[146,147,298,301,302] With increasing Na^+ incorporation, the excitonic absorption peak undergoes a pronounced blue shift, shifting from 369 to 326 nm, which corresponds to an increase in the excitonic absorption energy from 3.36 eV to 3.80 eV. This behavior, as well as the change in bandgap type from indirect to direct, can be attributed to the contribution of Ag 5s and Ag 4d orbitals to the CBM and VBM of $Cs_2AgBiCl_6$, thereby modulating the electronic structure of the nanocrystals. **Figure 5.4b** shows the UV–vis absorption spectra of $Cs_2Na_{1-x}K_xBiCl_6$ NCs. The incorporation of K^+ induces a slight red shift, moving the peak from 326 to 330.5 nm. **Figure 5.5b-c** shows the fitting of the experimental absorption coefficient to the Tauc equation, using an exponent of 2 ($\gamma = 1/2$) for the direct band gap of Na100 and K100, yielding band gap values of 3.66 eV and 3.62 eV, respectively. This is consistent with the character of the VBM and CBM, which is mainly determined by Bi and Cl orbitals in both compositions, so the substitution of Na^+ with K^+ does not lead to significant changes in the bandgap.[260]

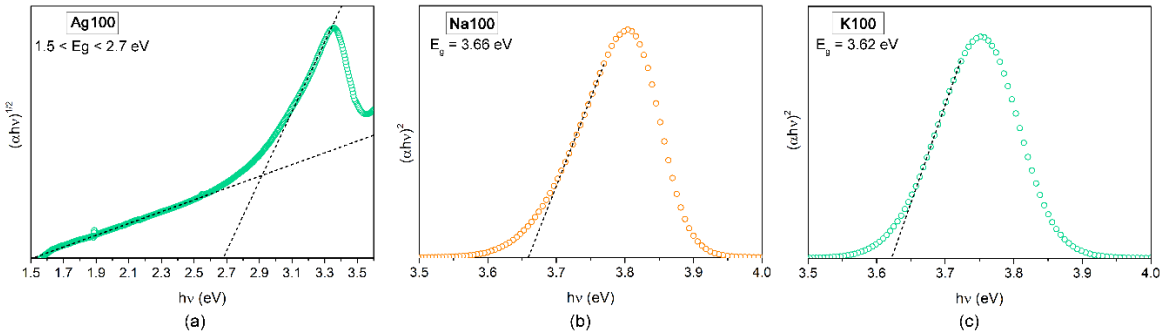

Figure 5.5. Tauc Plots of the three end members (a) $Cs_2AgBiCl_6$, (b) $Cs_2NaBiCl_6$, and (c) Cs_2KBiCl_6, obtained by fitting the strong absorption tails and, for $Cs_2AgBiCl_6$, the shallow absorption tail.

5.3. X-ray Absorption Spectroscopy of Bi-based HDP NCs

Figure 5.6 shows the HERFD-XANES spectra acquired at the Ag L_3-edge and the K K-edge for the $Cs_2Ag_{1-x}Na_xBiCl_6$ and $Cs_2Na_{1-x}K_xBiCl_6$ series, respectively. The spectra for the Ag L_3-edge all exhibit the same profile. In particular, the edge peak appears at 3351 eV, followed by a second pronounced peak at approximately 3359 eV. These two peaks are separated by two shoulders at 3354 and 3356 eV, with the first being more pronounced in spectra with higher sodium content and tending to disappear when sodium is completely absent. It is noteworthy, however, that systematic variations are observed between 3350 and 3354 eV: in particular, the minimum at 3352 eV is shallower for Ag100 and becomes progressively more pronounced as Ag^+ is replaced by Na^+. The Ag L_3-edge corresponds to transitions from the $2p_{3/2}$ orbitals to various unoccupied states, mainly Ag 5s, and is sensitive to the covalency of the Ag–Cl bond. Therefore, this systematic variation can be attributed to a change in the average covalency of the Ag–Cl bond due to the increased content of Na^+ ions, which alter the covalency of the Bi–Cl bond and, in turn, that of the Ag–Cl bond. However, the Ag L_3-edge shape is consistent with a $AgCl_6$ octahedral coordination, and is in good agreement with the long-range structure determined by XRD.[303] The K K-edge does not show significant variations among the $Cs_2Na_{1-x}K_xBiCl_6$ NCs, however an interesting feature emerges. Ideally, in HDPs, potassium should be octahedrally coordinated by six chlorine atoms. In $Cs_2NaBiCl_6$, sodium and bismuth have very similar ionic radii in octahedral coordination (Na^+: 1.02 Å; Bi^{3+}: 1.03 Å),[294] making the $NaCl_6$ and $BiCl_6$ octahedra dimensionally comparable and favoring a well-balanced structure. The substitution of Na^+ with K^+ involves a significant increase in the ionic radius (K^+: 1.38 Å),[294] the ideal octahedral coordination of potassium is no longer preserved, resulting in a strongly distorted geometry. The HERFD-XANES spectra show a single transition, at the absorption edge (≈3612 eV): on the contrary, two distinct transitions (due to the octahedral crystal field splitting) are visible in the spectra of octahedrally coordinated K^+,[304] These observations suggest that the local symmetry is lower than the long-range structure probed by XRD, e.g. in a trigonal bipyramid symmetry arising from a pronounced anisotropic distortion along one diagonal of the octahedron.[304,305] The discrepant evidence from the short-range coordination environment and the long-range structure will need further work to eventually build a comprehensive model.

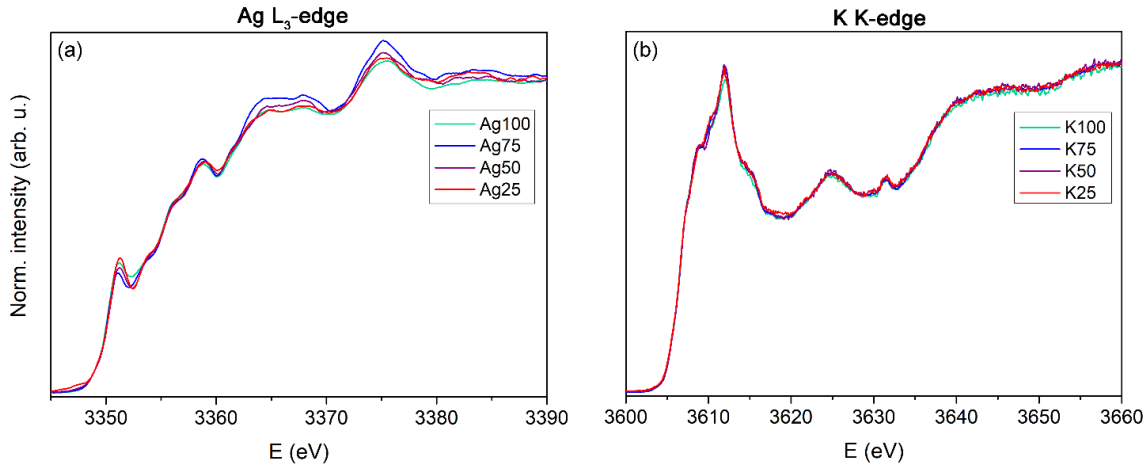

Figure 5.6. HERFD-XANES spectra on the (a) Ag L_3-edge for $Cs_2Ag_{1-x}Na_xBiCl_6$ NCs and (b) K K-edge for $Cs_2Na_{1-x}K_xBiCl_6$ NCs.

Figure 5.7 shows the chlorine K-edge for both solid solutions of Bi-containing HDPs. In Cl K-edge studies reported in the literature, a well-defined pre-edge feature is attributed to a ligand-to-metal transition from Cl 1s to partially occupied or unoccupied metal orbitals. Due to the localized nature of the Cl 1s orbital, this transition can exhibit significant intensity only if the final-state orbitals of the metal contain a significant component of Cl 3p character, a necessary condition is therefore the presence of sufficient spatial overlap between the chlorine and metal orbitals, in the absence of which the transition cannot occur. Consequently, since orbital hybridization is interpreted as a proxy for metal-chloride covalency, this pre-edge peak provides a direct estimate of metal–ligand covalency.[306–308] In both series of samples, two pre-edge peaks are observed at 2818.5 and 2824 eV, respectively. These pre-edge features can be interpreted as dominated by transitions towards Bi 6p states. In particular, the Bi 6p states, further hybridized with the Cl 3p orbitals, are split into Bi $6p_{1/2}$ and Bi $6p_{3/2}$,[309] giving rise to the two pre-edge peaks. The first pre-edge peak at 2819.5 eV has the highest intensity in Na100, and progressively decreases with the substitution of Ag^+ in the first series and K^+ in the second, although in the latter case the variation is less pronounced. Since the Na–Cl interaction is essentially ionic, it does not affect the covalent character of the Bi–Cl bond responsible for the transition. In contrast, Ag^+ exhibits a significant covalent interaction with chlorine, which reduces the hybridization between Cl 3p and Bi 6p orbitals, as the Cl 3p are also partially involved in bonding with Ag 4d orbitals. This results in a reduced orbital overlap between Bi 6p and Cl 3p in Ag100 compared to Na100.

In the Na/K series, the change of the pre-edge peak is less evident, due to the similar ionicity of Na–Cl and K–Cl bonds. However, the K–Cl bond should be more ionic than Na–Cl and therefore lead to greater covalency of the Bi–Cl bond, which is not reflected in the observed spectra, so it is likely that ionic radii and overlap effects are more important than ionicity in this case. The main edge shows two contributions at 2823.5-2824 eV, whose relative intensity shifts in the Ag/Na series, likely due to changing charge transfer in the M–Cl bonds. In the Na/K series, the main edge shows a consistent shape (since the B^{+}–Cl bond is always ionic), and exhibits just a 0.5 eV shift to lower energy in K100. The quantitative modeling of these edge changes will require further studies to fully correlate them with specific electronic transitions and chemical effects.

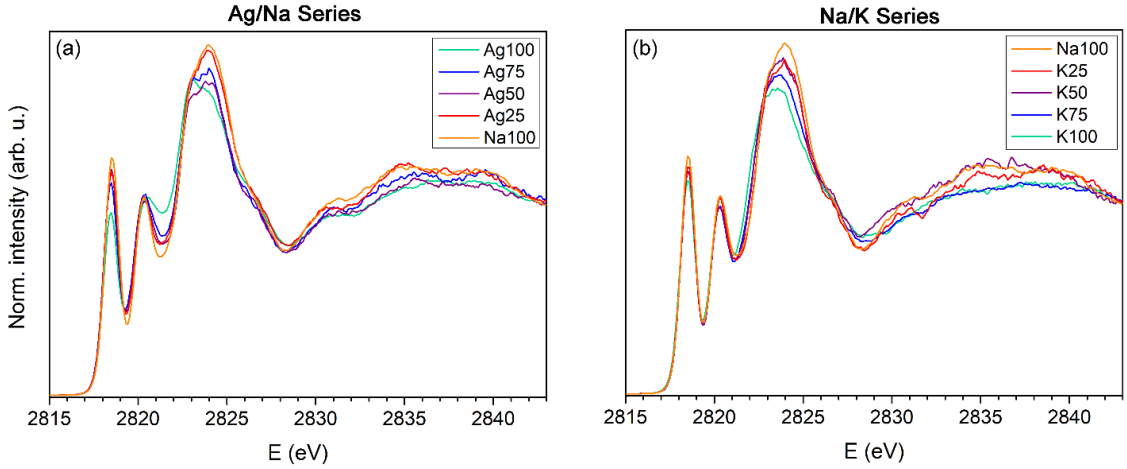

Figure 5.7. HERFD-XANES spectra on the Cl K-edge for (a) $Cs_2Ag_{1-x}Na_xBiCl_6$ NCs and (b) $Cs_2Na_{1-x}K_xBiCl_6$ NCs.

5.4. Multistep Synthesis of In-based HDP NCs

The newly developed approach used for the synthesis of $Cs_2B^+InCl_6$ (where B^+ = Ag, Na, K) is depicted in **Scheme 5.2**. A base solvent was prepared as a common medium to dissolve precursor stock solutions by mixing ODE, OLAM, and OA. The mixture was stirred, heated at 140 °C, and degassed under vacuum. Precursor stock solutions for the target elements were prepared in separate vials by dissolving the corresponding metal precursors in the base solvent at 140 °C until complete dissolution was achieved. The precursor stock solutions can then be stored in air and at room temperature and are used as cation reservoirs to prepare NCs with bespoke compositions as needed. To synthesize the $Cs_2(Ag,Na,K)InCl_6$ NCs, the required amount of each stock solution were mixed in a septum-sealed vial ad heated at 170 °C under nitrogen. Subsequently, a preheated stock solution of BzCl was injected (**Scheme 5.2b**), and after 10 s the reaction was rapidly quenched by cooling in an ice–water bath. The resulting NCs were purified through successive centrifugation and redispersion steps, finally the suspension containing the pure NCs was stored under nitrogen atmosphere.

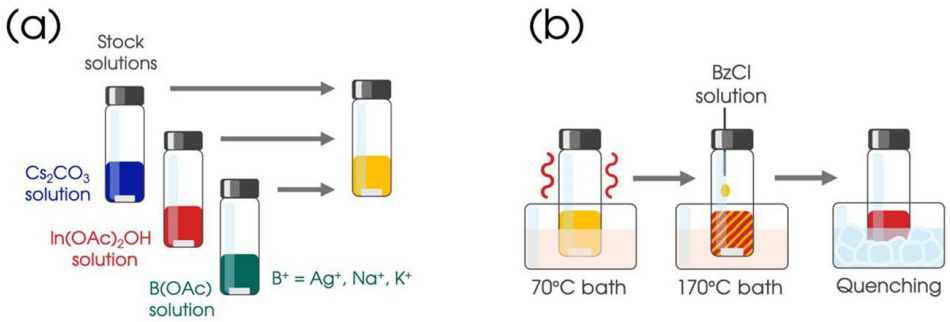

Scheme 5.2. Multistep synthesis of $Cs_2(Ag,Na,K)InCl_6$ NCs.

As confirmed by the XRD data, $Cs_2AgInCl_6$ and $Cs_2NaInCl_6$ NCs crystallize in the elpasolite *Fm-3m* structure, with no detectable secondary phases (**Figure 5.8**). The successful substitution of Ag^+ with Na^+ is evidenced by the appearance of the (111) peak, as also observed in the Bi-containing HDPs discussed above. The lattice parameter (**Table 5.2**) obtained from the Rietveld refinement of the structures further shows that, in this case as well, the replacement of Ag^+ with Na^+ induces a small but significant lattice expansion, from 10.4773(2) Å for $Cs_2AgInCl_6$ to 10.5283(3) Å for $Cs_2NaInCl_6$ NCs, which can be attributed to the greater covalent character of the Ag−Cl bond compared to that of Na−Cl.

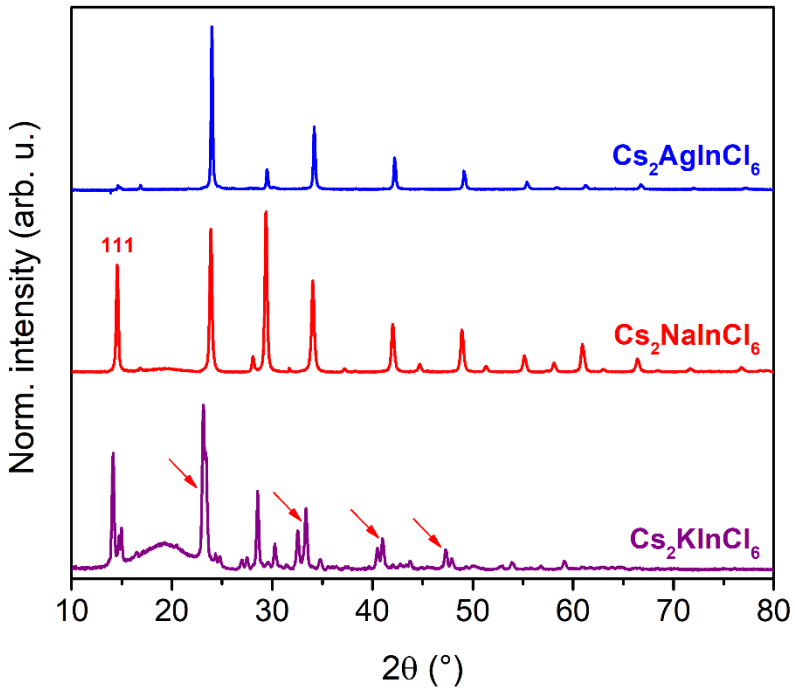

Figure 5.8. XRD data of $Cs_2AgInCl_6$ (blue line), $Cs_2NaInCl_6$ (red line), and Cs_2KInCl_6 (purple line). The red arrows mark the splitting of some Bragg reflections.

The case of Cs_2KInCl_6 is different and warrants a separate and more detailed discussion. A minor impurity phase, precipitated upon drying, is present and marked with red asterisks in the XRD patterns shown in the Appendix (**Figure A 5.13**). The XRD pattern in **Figure 5.8** shows a clear systematic splitting of the main reflections: in particular, the (220), (400), (422), and (440) reflections in cubic notation, observed at about 23.2°, 33.3°, 41°, and 47.3°, respectively, and marked with red arrows. This splitting is clearly inconsistent with the cubic elpasolite structure, which is instead perfectly apt to model the data of $Cs_2(Ag,Na)InCl_6$. The crystal structure of Cs_2KInCl_6 was therefore refined as a tetragonal HDP (space group: *I4/m*) with the unit cell parameters reported in **Table 5.2**. The structural model used for the refinement (CSD 2433763), shown in **Figure 5.9**, features octahedral coordination for all In^{3+} cations, 1/5 of which are rotated by 45° within the *ab*-plane along their 4-fold octahedral axes, as well as the same octahedral coordination for 1/5 of K^+ cations. The remaining 4/5 of K^+ adopt a distorted pentagonal bipyramidal coordination, and undergo a large displacement of ~0.84 Å from their ideal K^+Cl_6 position toward the rotated $InCl_6$ octahedron. A distorted seven- (and even 7+1)-fold coordination has been observed for K^+ in other

halides,[310,311] and is therefore attributed to the large difference in six-coordinate ionic radii between K^+ (1.38 Å) and In^{3+} (0.8 Å).[294]

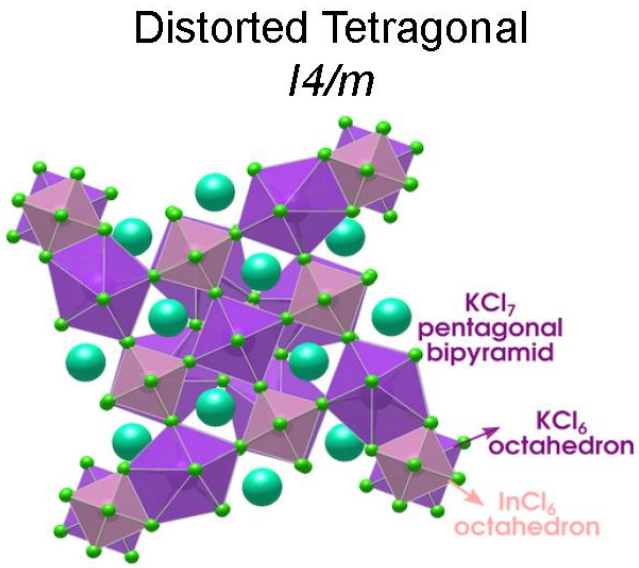

Figure 5.9. Distorted tetragonal structure (CSD 2433763) used for the refinement of Cs_2KInCl_6.

Table 5.2. Crystal structure for $Cs_2(Ag,Na)InCl_6$ NCs. Space group: *Fm-3m*. Crystal structure for Cs_2KInCl_6 NCs. Crystal system: tetragonal. Space group: *I4/m*. Uncertainty is reported in parentheses.

Samples	**Crystal data**		
	a = b = c (Å)		**V (Å^3)**
$Cs_2AgInCl_6$	10.4773(2)		1150.16(7)
$Cs_2NaInCl_6$	10.5283(3)		1167.0(1)
	a = b (Å)	**c (Å)**	**V (Å^3)**
Cs_2KInCl_6	16.9632(9)	10.9921(7)	3162.9(4)

The $Cs_2(Ag,Na,K)InCl_6$ NCs are all direct bandgap semiconductors with parity-forbidden transitions between the band edges. Specifically, for $Cs_2(Na,K)InCl_6$, the CBM originates from In 5s and Cl 3p orbitals, while the VBM derives from Cl 3p orbitals. Both the CBM and VBM are located at the Γ point and exhibit even parity (Γ^+). The band edge states at other k points also have the same parity. Consequently, only parity-forbidden transitions can occur between the band edges at all k points.[260] For $Cs_2AgInCl_6$, the VBM mainly originates from Ag 4d and Cl 3p orbitals, while the CBM mainly derives from delocalized In 5s states,

both located at the Γ point with even parity (Γ^+). However, the CB edge parity changes, while the VB edge parity remains unchanged, at k-points away from Γ. Consequently, $Cs_2AgInCl_6$ exhibits parity-forbidden transitions only between the CBM and VBM, with allowed transitions at other k-points.[260]

The absorption spectrum of $Cs_2AgInCl_6$ exhibits a strong peak at 266 nm followed by a broad tail extending up to ~400 nm (**Figure 5.10a**). Based on literature values for the bandgap of colloidal $Cs_2AgInCl_6$ NCs (ranging from 4.25 to 4.88 eV),[162] the broad feature at ~300 nm is attributed to a parity-allowed transition occurring between the valence band and the CBM.[312] **Figure 5.10b** shows the fitting of the experimental absorption coefficient to the Tauc equation using 2 as the exponent (γ = 1/2), yielding a bandgap of 4.384 eV. Furthermore, in agreement with Lee et al.,[312] a weak absorption shoulder at ~400 nm was also identified. The corresponding Tauc plot (inset of **Figure 5.10b**), using an exponent of 2/3 (γ = 3/2), suggests a transition energy of 3.289 eV, attributable to the (partially) parity-forbidden transition between the VBM and the CBM.

Another interesting feature observed is the relative absence of peaks in the optical absorption spectra of $Cs_2NaInCl_6$ and Cs_2KInCl_6. The calculated bandgap corresponding to a parity-forbidden transition is 2.92 eV for $Cs_2NaInCl_6$ and 3.42 eV for Cs_2KInCl_6, respectively 1.9 and 2.4 eV higher than the value calculated for $Cs_2AgInCl_6$ (0.99 eV). Considering the well-known underestimation of the DFT-simulated bandgap at the PBE level of theory (typically ~1.3-1.5 eV for wide-bandgap HDPs),[99,260] the corrected values for the lowest-energy parity-forbidden transitions were estimated to be approximately 4.1-4.3 eV (~302-288 nm) for $Cs_2NaInCl_6$ and 4.7-4.9 eV (~263-253 nm) for Cs_2KInCl_6. Consequently, the first parity-allowed transitions, occurring at even higher energies relative to the band edges, are expected to lie near or beyond the detectable range of the employed UV-vis experimental setup, thus explaining the relatively featureless absorption spectra observed for these compositions (**Figure 5.10a**).

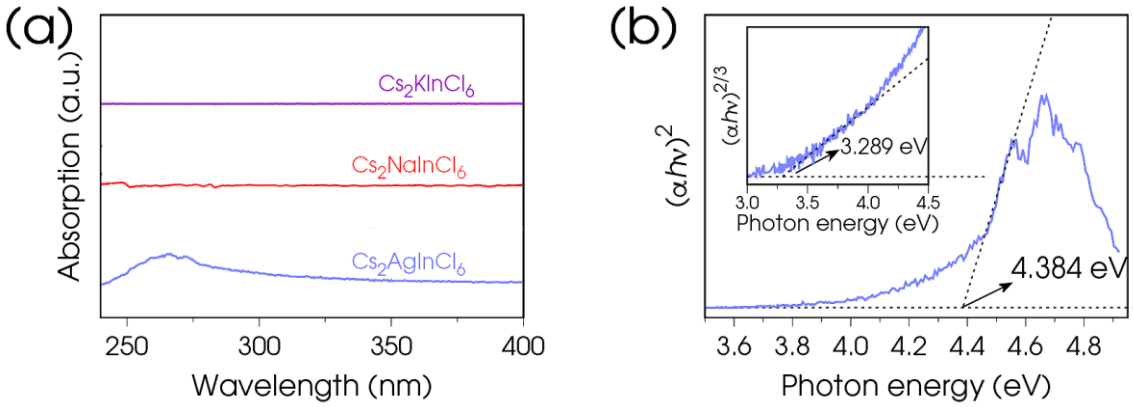

Figure 5.10. (a) UV-vis absorption spectra of selected $Cs_2(Ag,Na,K)InCl_6$ NCs dispersed in hexane. (b) Tauc plot of $Cs_2AgInCl_6$ NCs obtained by fitting the strong absorption tail. Inset: zoomed-in view of the lowest-energy absorption feature and the corresponding Tauc fit performed in the 3.4−4.0 eV range.

5.5. X-ray Absorption Spectroscopy of In-based HDP NCs

Figure 5.11 shows the HERFD-XANES spectra at the In L_3-edge and the Cl K-edge for the three $Cs_2(Ag,Na,K)InCl_6$ end-members. The In L_3-edge spectra of the three HDPs (**Figure 5.11**), all show a sharp peak at 3729 eV attributed to transitions from the In $2p_{3/2}$ state to unoccupied states with a predominant In 5s character, and minor In 5d contribution.[313] Two peaks are also clearly visible at approximately 3735 and 3737 eV, with the first being absent in Cs_2KInCl_6.[313] Two peaks are also clearly visible at approximately 3735 and 3737 eV in the main edge, the first being absent in Cs_2KInCl_6. This is likely due to the peculiar structure of Cs_2KInCl_6, in which 1/5 of the $InCl_6$ octahedra are rotated by 45° within the *ab*-plane along their 4-fold octahedral axes. However, the edge profile indicates that indium in these compositions adopts a fairly regular octahedral coordination with chloride anions, consistent with the results of the Rietveld refinement.[314]

The Cl K-edge, shown in the right panel of **Figure 5.11**, shows marked differences compared to the spectra of Bi-containing HDPs (**Figure 5.7**). In particular, just a single pre-edge is observed in this case (compared to the two pre-edges in the Bi HDPs) at 2819 eV. Unlike in Bi, where the transition from Cl 1s occurs to non-degenerate Bi 6p orbitals, this peak arises from the Cl 1s → In 5s transition, corresponding to the first unoccupied orbital with Cl 3p character.[315] In this case as well, the presence of silver, which participates in orbital overlap with the Cl 3p orbitals, reduces the covalency of the In–Cl bond compared to the two systems where silver is absent, resulting in a lower pre-edge intensity. For $Cs_2(Na,K)InCl_6$, however, the pre-edge intensities are very similar.

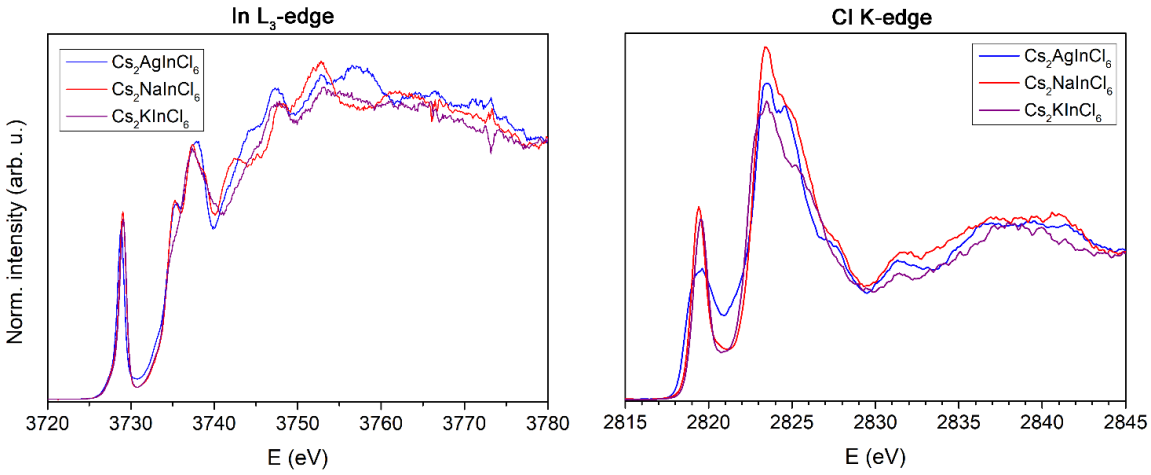

Figure 5.11. HERFD-XANES spectra of $Cs_2AgInCl_6$, $Cs_2NaInCl_6$ and Cs_2KInCl_6 on In L_3-edge (left panel) and on Cl K-edge (right panel).

The Ag L_3-edge of $Cs_2AgInCl_6$ (**Figure 5.12**) is very similar to that of $Cs_2AgBiCl_6$, but more structured, indicating an octahedral coordination of silver with the chlorine atoms. However, an additional peak at approximately 3352.5 eV is clearly visible, which is absent in the perovskite containing Bi^{3+}. From previous discussions, it is evident that the Bi–Cl bond has greater covalency than the In–Cl bond, implying a higher covalency of the Ag–Cl bond in the presence of In^{3+} compared to Bi^{3+}. Moreover, there is a significant difference in ionic radius between Bi^{3+} (1.03 Å) and In^{3+} (0.8 Å),[294] which consequently leads to differences in the size and distortions of the $AgCl_6$ octahedra in the two compositions. Understanding how this difference manifests in the spectrum remains a challenge and will require further detailed study.

In Cs_2KInCl_6, the K K-edge spectrum is highly structured and is very different from Cs_2KBiCl_6 (**Figure 5.12**). In Cs_2KInCl_6, in addition to the peak at 3612 eV, two well-defined peaks are observed at approximately 3607 and 3609 eV. In Cs_2KBiCl_6, the 3609 eV peak appears only as a shoulder, indicating negligible orbital splitting whose origin must still be clarified. The spectrum profile of Cs_2KInCl_6 is typical of an octahedral coordination with chlorine ligands, whereas potassium in Cs_2KBiCl_6 exhibits a highly distorted coordination.[305] However, this is in strong disagreement with the long-range structure previously discussed for Cs_2KInCl_6, in which only one fifth of the octahedra display octahedral coordination, while the remainder adopt a distorted pentagonal bipyramidal coordination. This behavior is intriguing and difficult to interpret without a more detailed study and possibly further experiments.

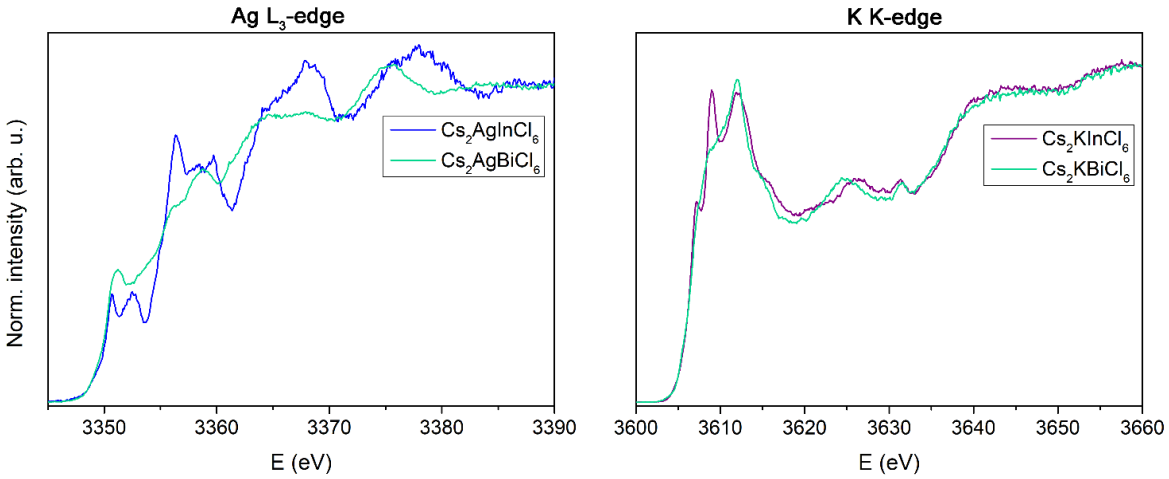

Figure 5.12. HERFD-XANES spectra of $Cs_2AgInCl_6$ compared with $Cs_2AgBiCl_6$ (Ag100) for the Ag L_3-edge (left panel) and Cs_2KInCl_6 compared with Cs_2KBiCl_6 (K100) for the K K-edge (right panel).

In conclusion, HDP NCs with different compositions were analyzed from a combined structural (both long-range and short-range) and functional (optical absorption) point of view, using Ag^+, Na^+, and K^+ in the B^+ site and In^{3+} and Bi^{3+} in the B^{3+} site, in order to evaluate how substitution at both the B^+ and B^{3+} sites affects the structure and bandgap. XRD shows that all compositions exhibit the cubic *Fm-3m* structure, as expected, except for Cs_2KInCl_6, which crystallizes in a tetragonal symmetry with distorted K coordination. The bandgap analysis is in good agreement with literature results: $Cs_2AgBiCl_6$ displays an absorption typical of an indirect bandgap, while $Cs_2(Na,K)BiCl_6$ show a direct bandgap. $Cs_2(In,Na,K)InCl_6$, on the other hand, exhibits a direct bandgap with a parity-forbidden transitions.

Local structural analysis performed via HERFD-XANES on the K and Cl K-edges and on the Ag and In L_3-edges reveals several aspects that require further investigation. While some spectral features are clear and in good agreement with other results, others remain uncertain or, as in the case of the K-edge, are in disagreement with the long-range structure for both compositions. In order to explain all the features, assign them to the different transitions, and understand the changes observed from one sample to another, given the scarce literature on these absorption edges, a more detailed study is currently in preparation, based on spectral modeling through *ab initio* simulations.

5.6. Appendix

Materials

1-octadecene (ODE, 90%), bismuth acetate ($Bi(OAc)_3$, 99%), cesium acetate (Cs(OAc), 97%), chlorotrimethylsilane (TMSCl, 97%), copper (II) acetate anhydrous ($Cu(OAc)_2$, 98%), oleic acid (OA, 90%) and oleylamine (OLAM, 80-90%) were purchased from Thermo Scientific. Toluene was purchased from J.T. Baker. Anhydrous sodium acetate (Na(OAc), ≥ 99%), ethyl acetate ($C_4H_8O_2$, 99.9%), potassium acetate (K(OAc), ≥99%), and silver acetate (Ag(OAc), 99%) were purchased from Carlo Erba Reagents. All materials were used without further purification.

Synthesis of Bi-based HDP NCs

The $Cs_2AgBiCl_6$ NCs were prepared with the HI method. Cs(OAc) (1 mmol), $Bi(OAc)_3$ (0.5 mmol) and Ag(OAc) (0.5 mmol) were placed in three-necked round-bottom flasks of 50 mL with OA (2.8 mL), OLAM (0.52 mL) and ODE (10 mL), the mixture was stirred at room temperature for about 10 minutes. The mixture was heated to 120 °C under vacuum for about 1h. The reaction mixture was heated under a nitrogen atmosphere, and TMSCl (0.4 ml) was swiftly injected at 170 °C and after 10 seconds cooled to room temperature in an ice-water bath. The reaction mixture was then decanted into a centrifugal tube and centrifuged at 6000 rpm for 20 min. The supernatant was removed, and the precipitate was redispersed in ethyl acetate (10 mL) with sonication, and centrifuged at 6000 rpm for 10 min. The supernatant was discarded. and the precipitate was finally redispersed in toluene (2 mL). The resulting suspension was stored in a closed vial under ambient conditions.

The $Cs_2NaBiCl_6$ and Cs_2KBiCl_6 NCs were prepared under the same experimental conditions by replacing Ag(OAc) with Na(OAc) and K(OAc), respectively. Mixed compositions $Cs_2Ag_{1-x}Na_xBiCl_6$ and $Cs_2Na_{1-x}K_xBiCl_6$ were synthesized following the same procedure by adjusting the ratio of the Ag/Na and Na/K metal precursors (**Table A 5.1**).

Table A 5.1. Stoichiometric quantities used for $Cs_2Ag_{1-x}Na_xBiCl_6$ and $Cs_2Na_{1-x}K_xBiCl_6$ NCs synthesis.

Label	Formula	Cs^+ mmol	Ag^+ mmol	Na^+ mmol	K^+ mmol	Bi^{3+} mmol
Ag100	$Cs_2AgBiCl_6$	1	0.5	--	--	0.5
Ag75	$Cs_2Ag_{0.83}Na_{0.17}BiCl_6$	1	0.375	0.125	--	0.5
Ag50	$Cs_2Ag_{0.4}Na_{0.6}BiCl_6$	1	0.25	0.25	--	0.5
Ag25	$Cs_2Ag_{0.24}Na_{0.76}BiCl_6$	1	0.125	0.375	--	0.5
Na100	$Cs_2NaBiCl_6$	1	--	0.5	--	0.5
K25	$Cs_2K_{0.27}Na_{0.73}BiCl_6$	1	--	0.375	0.125	0.5
K50	$Cs_2K_{0.41}Na_{0.59}BiCl_6$	1	--	0.25	0.25	0.5
K75	$Cs_2K_{0.7}Na_{0.3}BiCl_6$	1	--	0.125	0.375	0.5
K100	Cs_2KBiCl_6	1	--	--	0.5	0.5

Multistep synthesis of In-based HDP NCs

The synthesis of $Cs_2AgInCl_6$, $Cs_2NaInCl_6$ and Cs_2KInCl_6 NCs was performed using a modified HI method with a multistep approach. The stock solution of the BSv was prepared by mixing 100 mL of ODE, 6.6 mL of OLAM, and 25 mL of OA in a 250 mL two-neck round-bottom flask. The target molar ratio of OA to OLAM was 3.9:1. The mixture was stirred, heated in an oil bath at 140 °C, and degassed under vacuum. This same stock solution was used for all subsequent preparations. Stock solutions of each target element were prepared by individually dissolving the precursor salts in an appropriate volume of base solvent. The solutions were prepared in vials sized relative to the target volume. The stock solutions were prepared as follows:

Na: 0.0126 g (0.15 mmol) of Na(OAc) was dissolved in 3.1 mL of BSv and 1 mL of ODE;

K: 0.0151 g (0.15 mmol) of K(OAc) was dissolved in 3.1 mL of BSv and 1 mL of ODE;

In: 0.0384 g (0.15 mmol) of $In(OAc)_2OH$ was dissolved in 3.1 mL of BSv and 1 mL of ODE;

Cs: 0.0501 g (0.31 mmol) of Cs_2CO_3 was dissolved in 3.1 mL of BSv and 1 mL of ODE;

Ag: 0.0301 g (0.18 mmol) of Ag(OAc) and 0.0407 g (0.16 mmol) of PPh_3 was dissolved in 3.1 mL of BSv and 1 mL of ODE;

Cl: 1 mL (7.8 mmol) of BzCl was mixed at room temperature with 2 mL of BSv.

Dissolution was achieved by heating under stirring stirring in an oil bath at 140 °C (70 °C for the Ag stock solution).

In the typical synthesis of $Cs_2(Ag,Na,K)InCl_6$, 1 mL of the Cs stock solution, 1 mL of the B^+ stock solution, and 1 mL of the In stock solution were combined in a 10 mL vial. The resulting solution was preheated and stirred in an oil bath at 70 °C and degassed in vacuum. Simultaneously, the Cl stock solution was also heated to 70 °C. The reaction mixture was then raised to 170 °C for 3 minutes, at which point 150 µL of the preheated Cl stock solution was swiftly injected into the vial under vigorous stirring. After 10 seconds, the reaction was quenched by immersing the vial in an ice water bath. For purification, the reaction product was transferred to a centrifuge tube and centrifuged for 10 minutes at 4000 × g. The supernatant was discarded, and the precipitate was redispersed in ODE using a volume equal to that of the reaction mixture employed for purification. The suspension was centrifuged again for 10 minutes at 4000 × g, the supernatant was discarded, and the precipitate was finally redispersed in toluene. The resulting suspension was stored in a closed vial under ambient conditions.

XRD

XRD patterns of $Cs_2Na_{1-x}Ag_xBiCl_6$ and $Cs_2Na_{1-x}K_xBiCl_6$ NCs were acquired with a Rigaku Miniflex 600 diffractometer using Ni-filtered Cu Kα radiation (λ=1.5418 Å). A few droplets of each colloidal sample were deposited with the aid of a micropipette and dried in air within minutes. Rietveld refinements were performed using GSAS-II,[213] with $Cs_2AgBiCl_6$ (ICSD #291598) used as the starting structural model. The Rietveld refinements of these compositions are primarily influenced by the more intense low-angle peaks, which can lead to less accurate refinement of the high-angle peaks (**Figure A 5.1**-**Figure A 5.9**). Since the high-angle peaks are less affected by systematic effects, subsequent refinements were carried out in the 45–90° range for all compositions to obtain more reliable lattice parameters, reported in **Table 5.1**. An example of the Rietveld refinement in the $45° \leq 2\theta \leq 90°$ range is shown in **Figure A 5.10**.

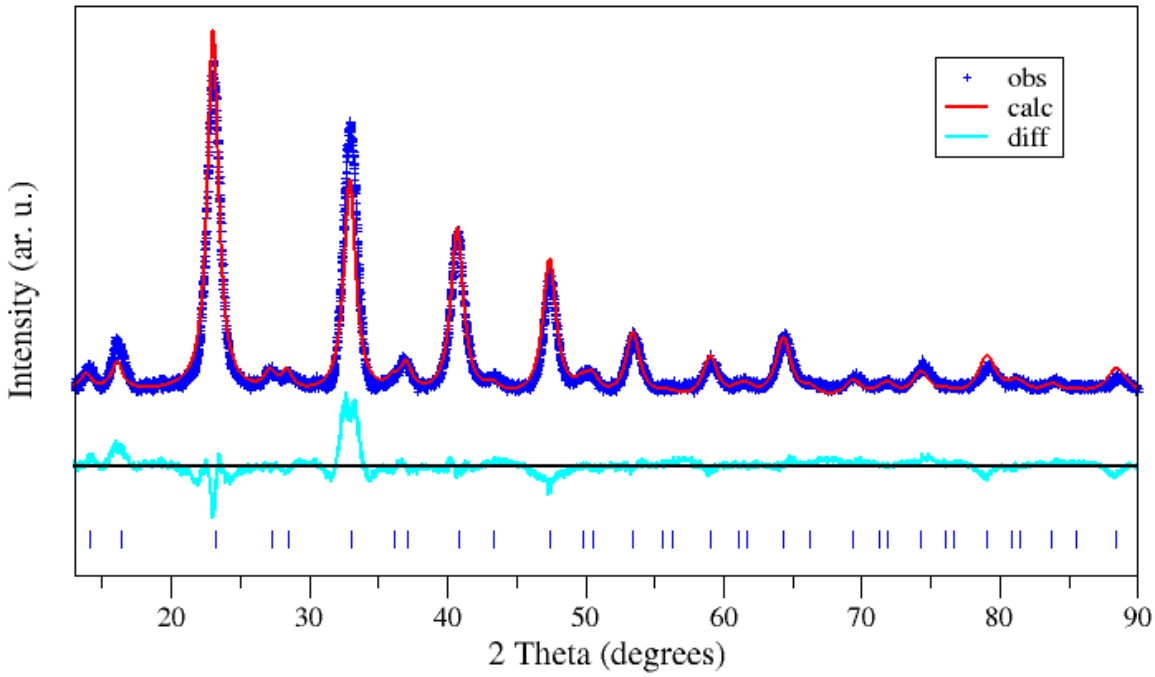

Figure A 5.1. Rietveld refinement plot for $Cs_2AgBiCl_6$ (Ag100). Experimental data (blue), calculated pattern (red), residual (cyan).

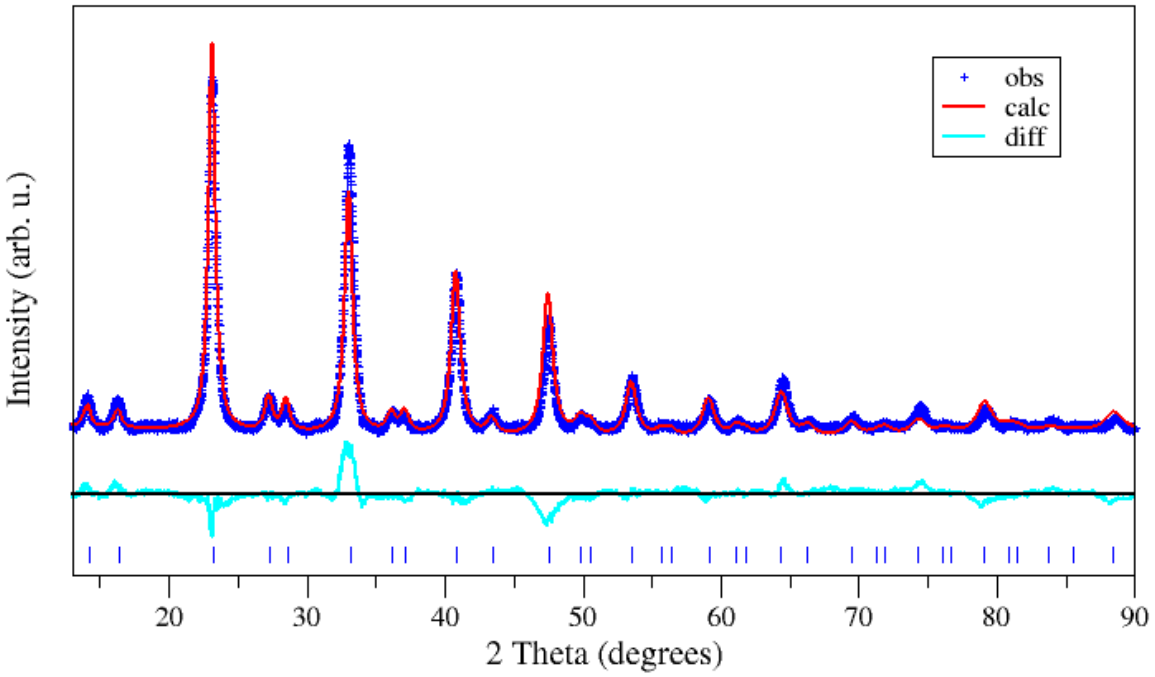

Figure A 5.2. Rietveld refinement plot for $Cs_2Ag_{0.83}Na_{0.17}BiCl_6$ (Ag75). Experimental data (blue), calculated pattern (red), residual (cyan).

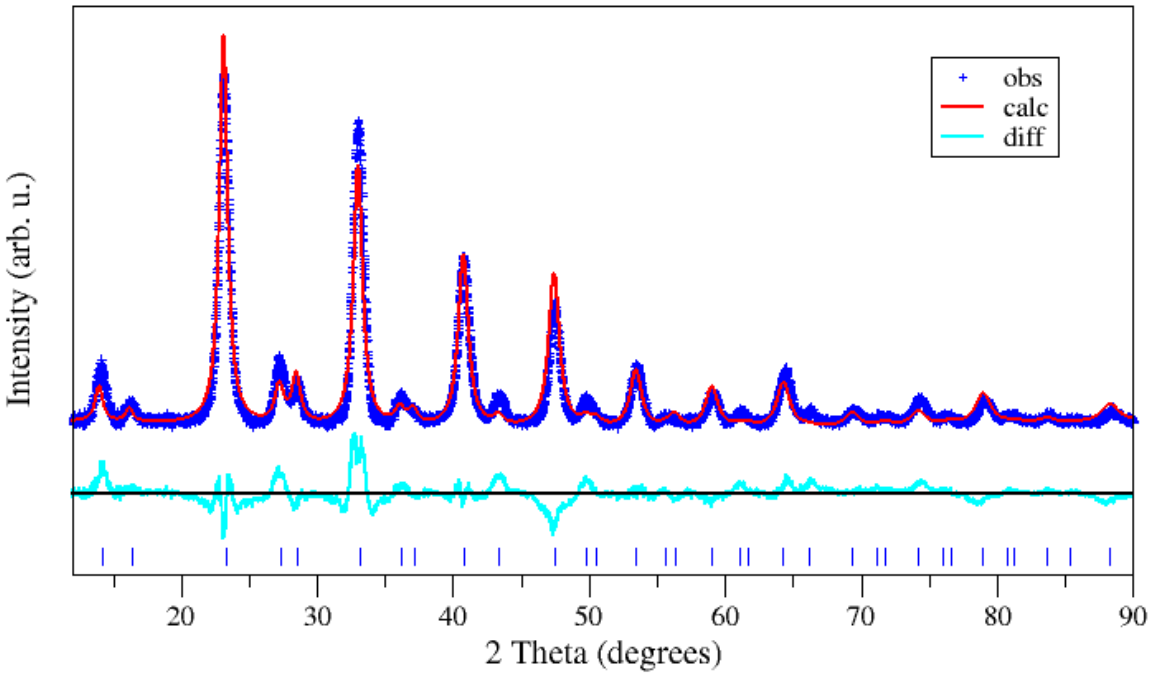

Figure A 5.3. Rietveld refinement plot for $Cs_2Ag_{0.4}Na_{0.6}BiCl_6$ (Ag50). Experimental data (blue), calculated pattern (red), residual (cyan).

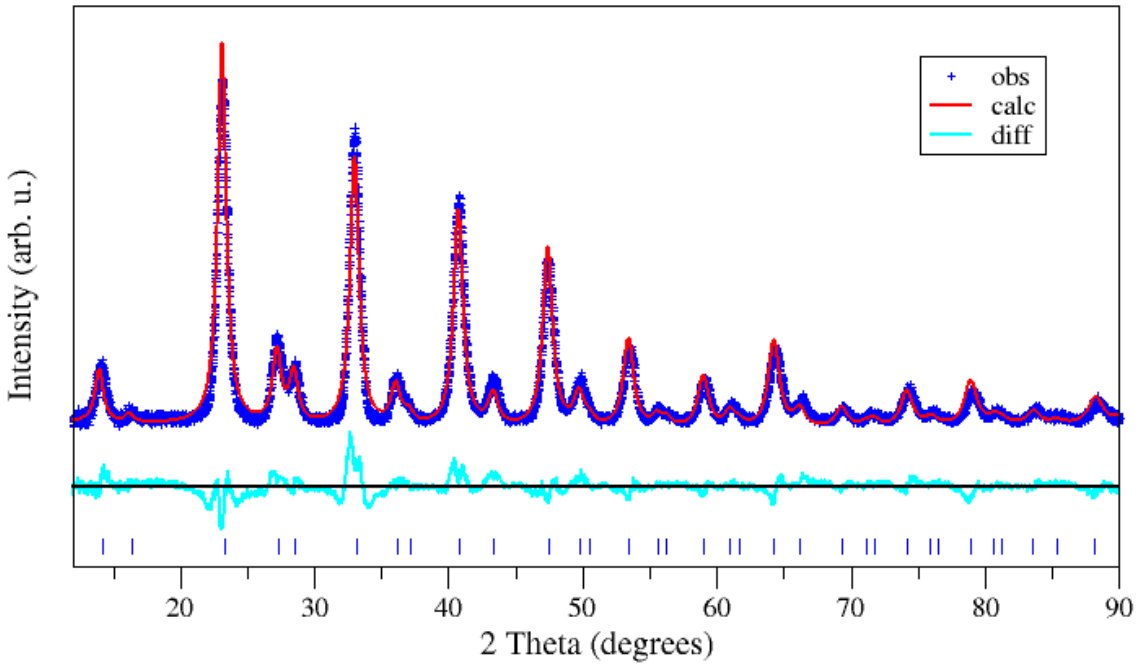

Figure A 5.4. Rietveld refinement plot for $Cs_2Ag_{0.24}Na_{0.76}BiCl_6$ (Ag25). Experimental data (blue), calculated pattern (red), residual (cyan).

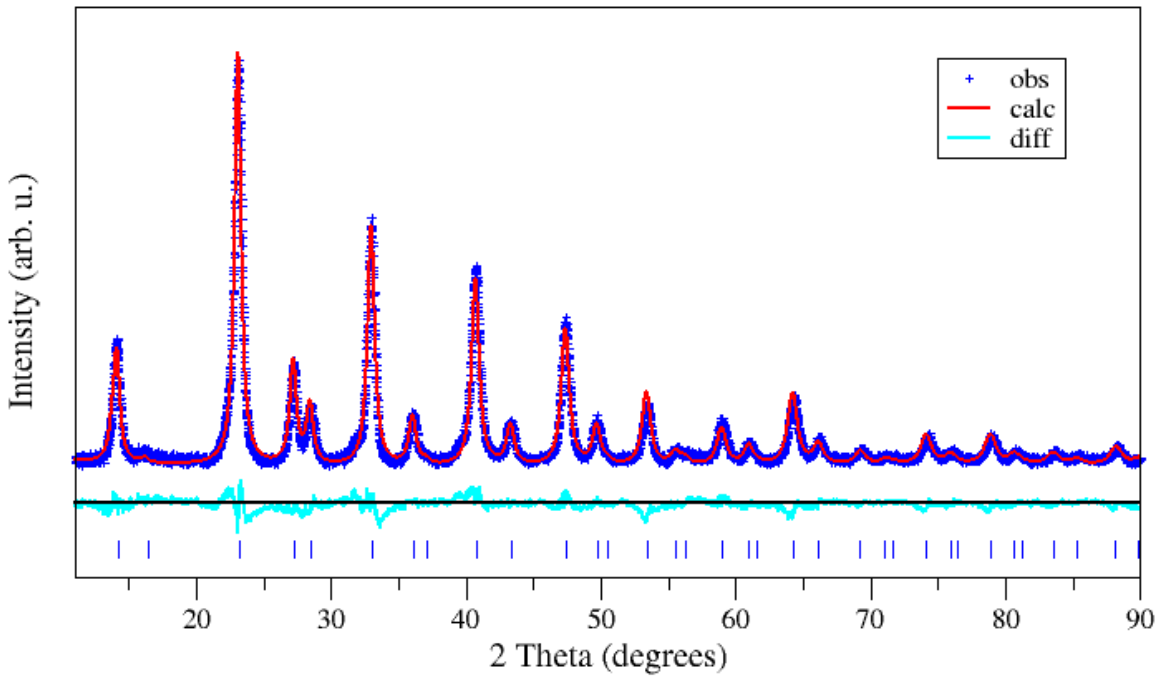

Figure A 5.5. Rietveld refinement plot for $Cs_2NaBiCl_6$ (Na100). Experimental data (blue), calculated pattern (red), residual (cyan).

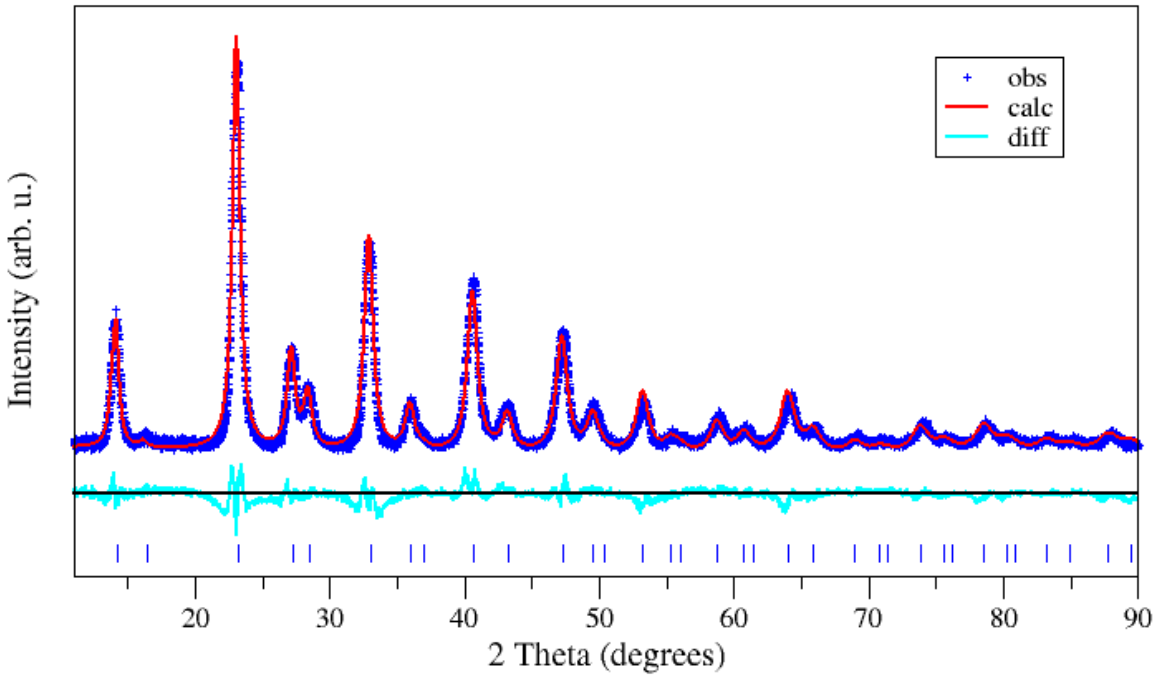

Figure A 5.6. Rietveld refinement plot for $Cs_2K_{0.27}Na_{0.73}BiCl_6$ (K25). Experimental data (blue), calculated pattern (red), residual (cyan).

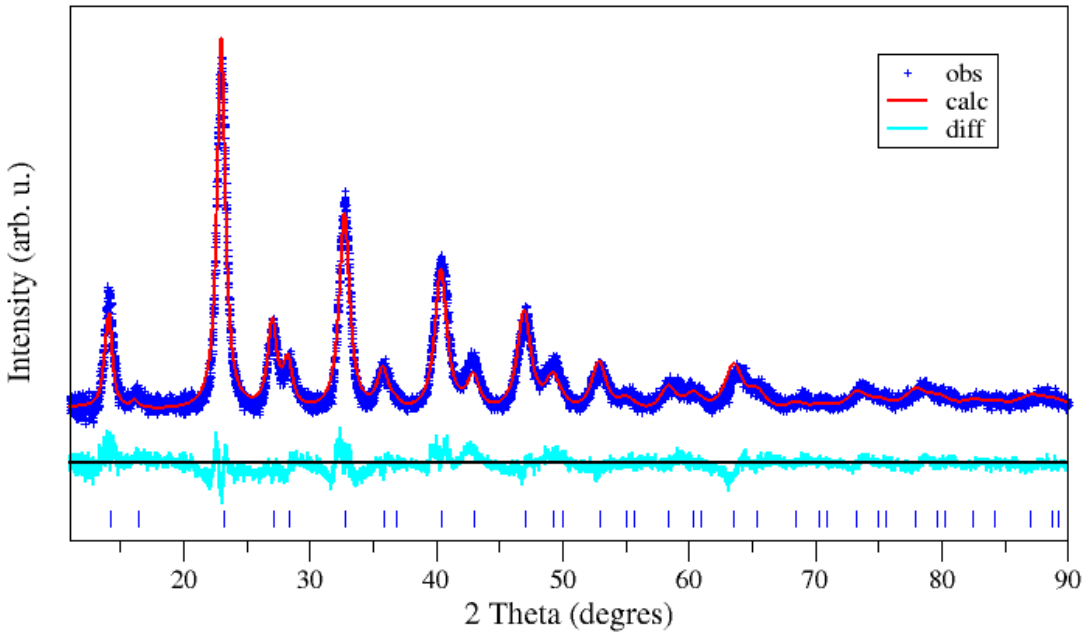

Figure A 5.7. Rietveld refinement plot for $Cs_2K_{0.41}Na_{0.59}BiCl_6$ (K50). Experimental data (blue), calculated pattern (red), residual (cyan).

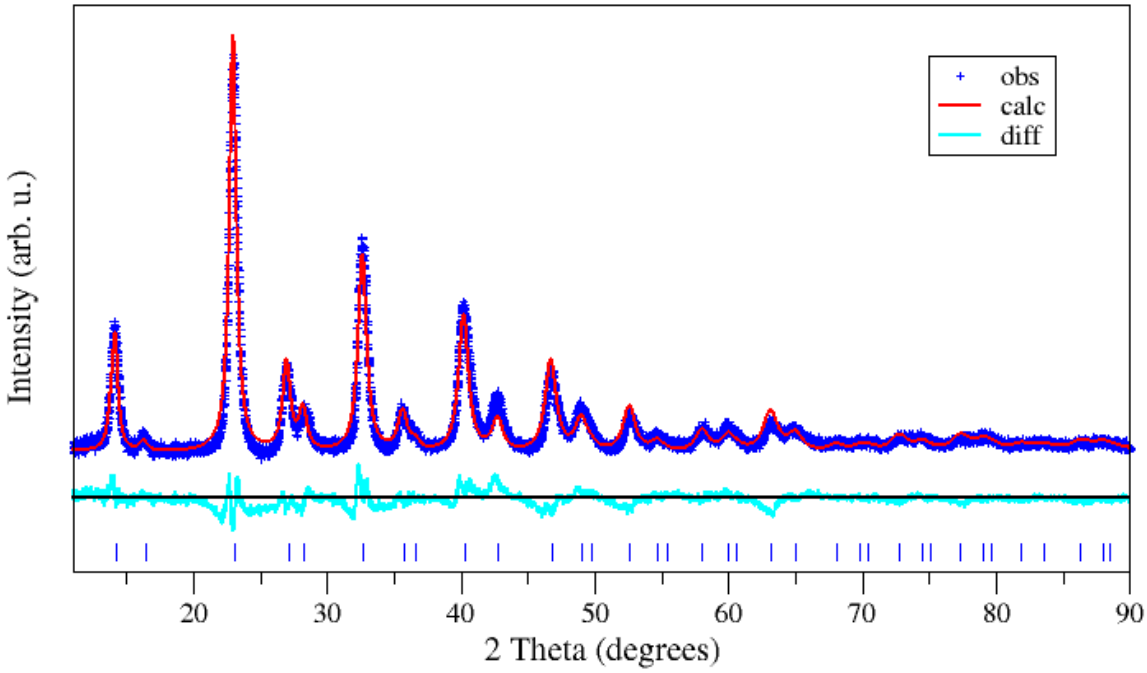

Figure A 5.8. Rietveld refinement plot for $Cs_2K_{0.7}Na_{0.3}BiCl_6$ (K75). Experimental data (blue), calculated pattern (red), residual (cyan).

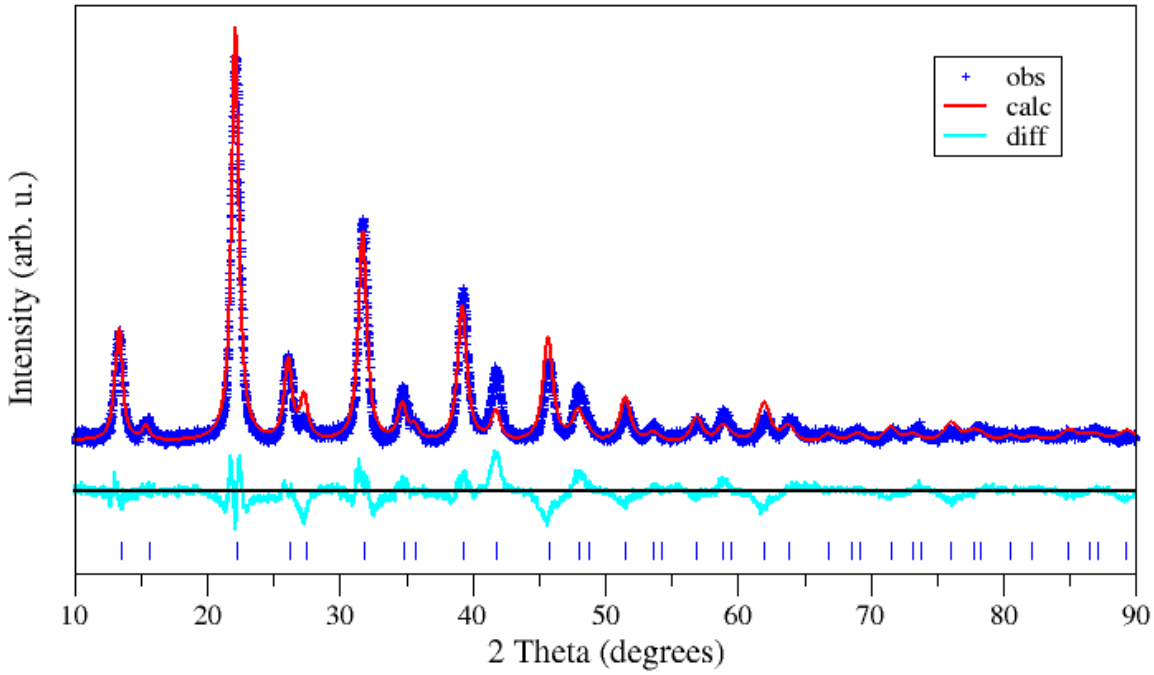

Figure A 5.9. Rietveld refinement plot for Cs_2KBiCl_6 (K100). Experimental data (blue), calculated pattern (red), residual (cyan).

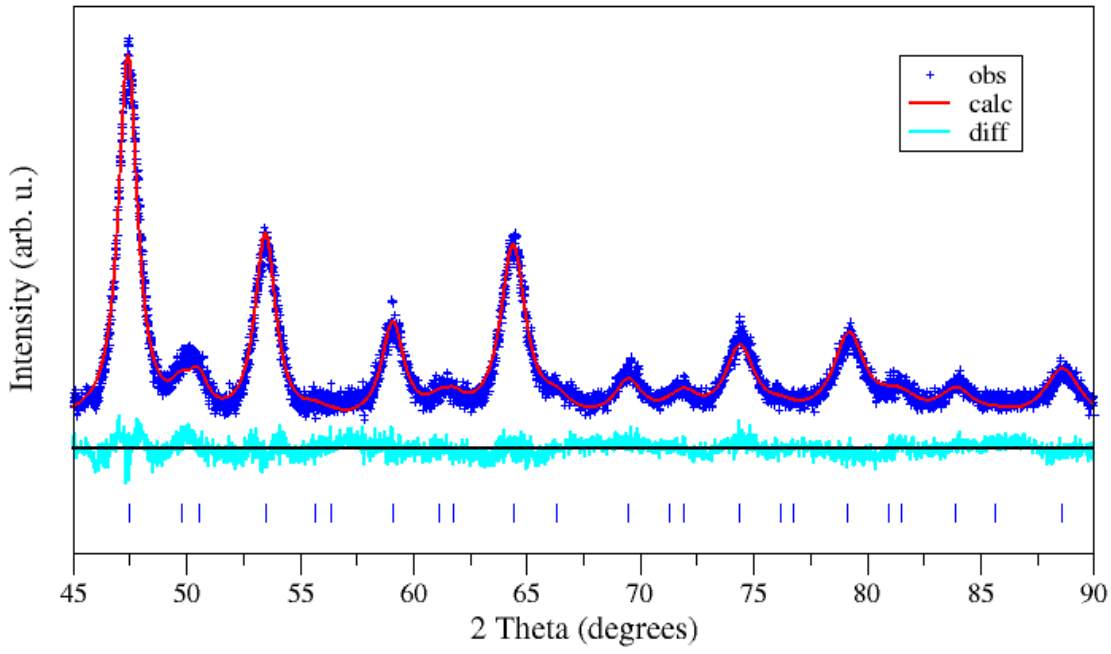

Figure A 5.10. Rietveld refinement plot in the $45° \leq 2\theta \leq 90°$ range for $Cs_2AgBiCl_6$ (Ag100). Experimental data (blue), calculated pattern (red), residual (cyan).

XRD data of $Cs_2(Ag,Na,K)InCl_6$ NCs were collected and analyzed on dried samples. A droplet of each colloidal sample was deposited on the surface of a silicon monocrystal zero-background plate with the aid of a micropipette and dried in air within minutes. The XRD diffractograms were collected using Cu-Kα radiation (λ = 1.5418 Å) on a Bruker AXS D8 Advance Diffractometer equipped with a Lynxeye detector operating at 40 kV and 40 mA. The Rietveld refinements (**Figure A 5.11**-**Figure A 5.13**) were performed with the TOPAS software.[316] The corresponding refined structural parameters are available in **Table 5.2**.

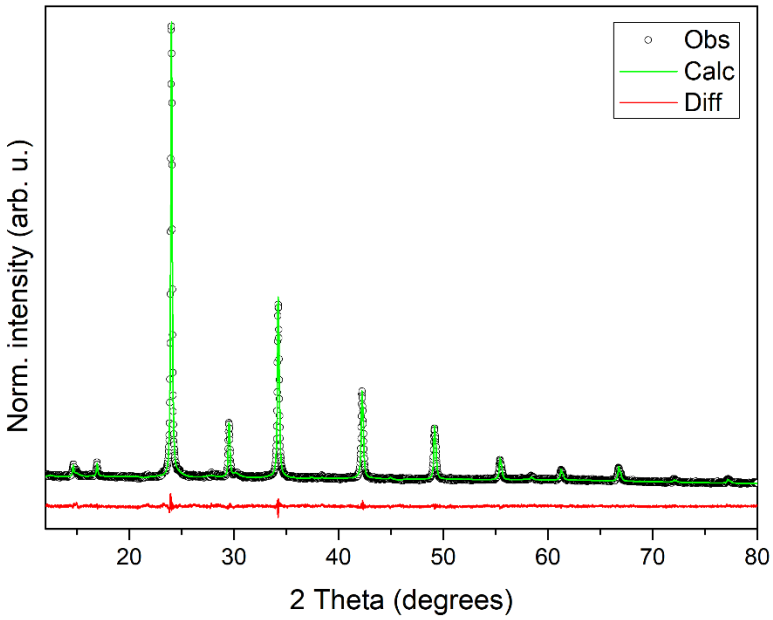

Figure A 5.11. Rietveld refinement plot for $Cs_2AgInCl_6$. Experimental data (black), calculated pattern (green), residual (red).

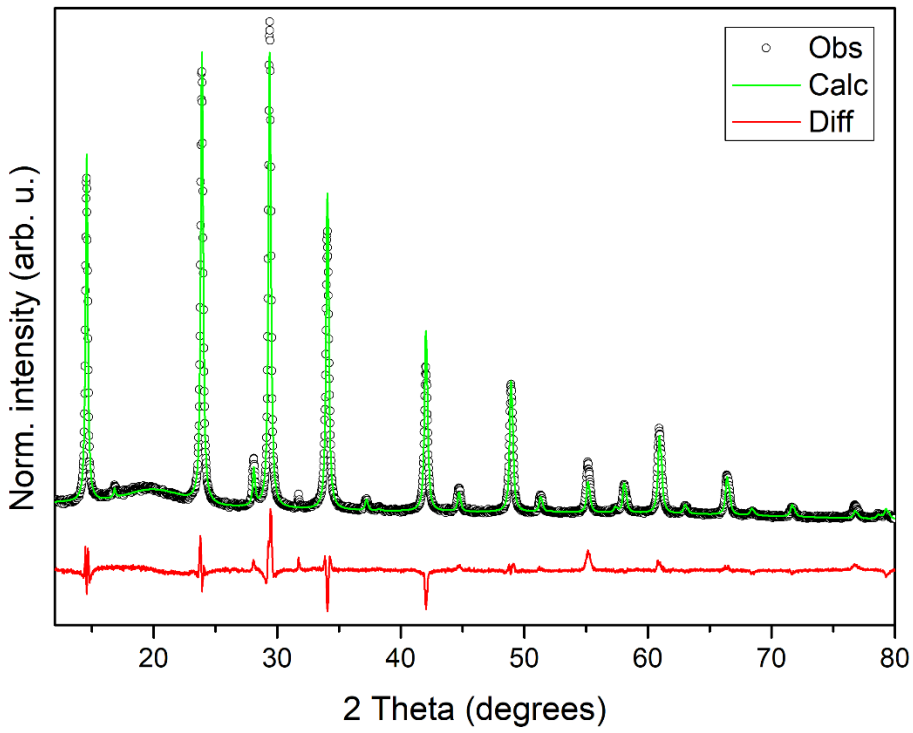

Figure A 5.12. Rietveld refinement plot for $Cs_2NaInCl_6$. Experimental data (black), calculated pattern (green), residual (red).

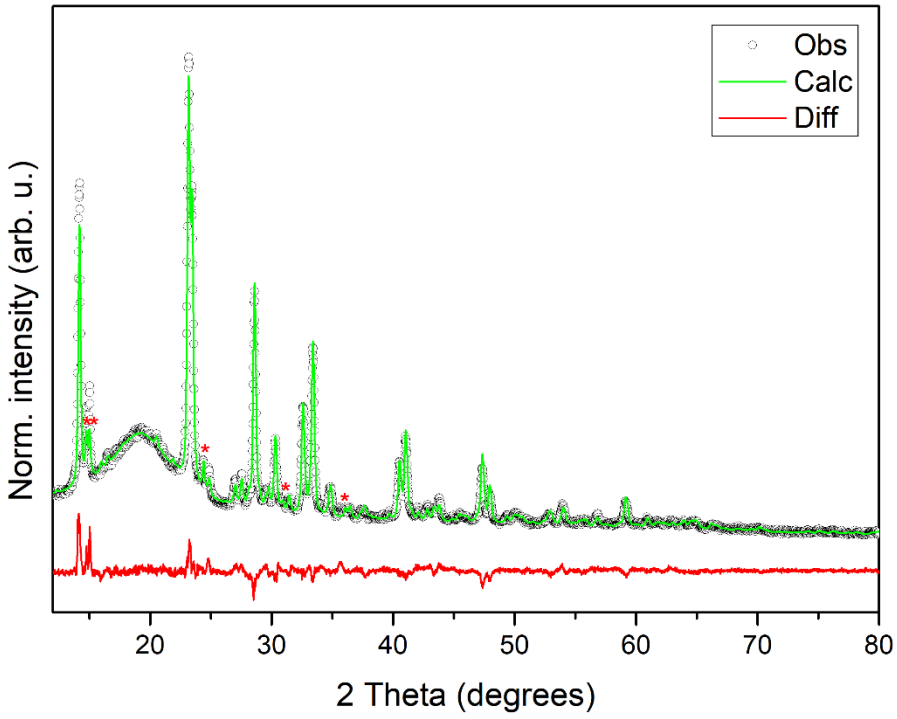

Figure A 5.13. Rietveld refinement plot for Cs_2KInCl_6. A minor impurity phase is present and marked with red asterisks. Experimental data (black), calculated pattern (green), residual (red).

ICP-OES

ICP-OES was performed to accurately quantify Bi, K, Na, Cs and Ag in the $Cs_2Na_{1-x}Ag_xBiCl_6$ and $Cs_2Na_{1-x}K_xBiCl_6$ NCs, using a Perkin-Elmer Optima 2100 ICP-OES spectrometer equipped with an autosampler model S10. WinLab 32 software (Perkin-Elmer) was used for the acquisition and processing of the data. The emission wavelengths used for Cs, Bi, Na, K, Ag were 455.531, 306.766, 330.237, 166.490, and 328.068 nm respectively. Calibration curves of ions were obtained by diluting a multielement standard solution. For the analysis, 5 mg of the dry samples were mineralized in 5 mL of concentrated HNO_3 until half of the volume evaporated. The remaining liquid was recovered quantitatively in a 10 mL graduated flask, then filled with distilled water. The stoichiometries obtained, reported in **Table 4.1**, are reported with two significant digits for simplicity, although the ions concentration measurements are accurate to the 10^{-3} level.

UV-vis

The UV-vis spectra of $Cs_2Ag_{1-x}Na_xBiCl_6$ and $Cs_2Na_{1-x}K_xBiCl_6$ NCs were acquired using a Analytik Jena Specord S600 spectrophotometer. The UV-vis spectra of Cs_2KInCl_6, $Cs_2AgInCl_6$ and $Cs_2NaInCl_6$ NCs were recorded by using a home-made custom setup at the University of Insubria. UV-vis absorption spectra allow for the direct estimation of the Tauc exponent by fitting the experimental absorption coefficient to the Tauc equation:[317]

$$[\mu_\alpha(\lambda)hv]^{\frac{1}{\gamma}} = A(hv - E_g)$$

where γ is the Tauc exponent, allowed transitions, and E_g the optical band gap. γ = 2 for indirect bandgap and γ = 1/2 for direct bandgap.

HERFD-XANES

HERFD-XANES spectra at the Cl and K K-edges and at the Ag and In L_3-edges were acquired at the ID26 beamline of ESRF, using the TEXS tender emission spectrometer, by collecting the KL_3 (Cl and K K-edge), and L_3M_5(Ag and In L_3-edge) emission lines, in high-energy resolution fluorescence detection mode. The dry sample was pressed with boron

nitride and measured at room temperature. Each sample was divided into a grid of around 400 spots, and several scans were carried out as needed to increase the statistics.

6. Heterovalent Substitution of Lead, part 2: Cu-based HDPs

*Adapted with permission from ACS Materials Lett. **2025**, 7, 3626−3633. Copyright 2025 American Chemical Society.*

6.1. Introduction: Cu in HDPs

In the broad landscape of HDP NCs, among the most widely used monovalent cations are Ag^+, Na^+, and K^+, whereas the use of Cu^+ has been investigated mainly from a theoretical perspective. A general theoretical evaluation of Cu-based HDPs has shown that their lower band gap compared to Ag-based HDPs comes at a trade-off: while $AgCl_6$ octahedra are stable, Cu^+ tends to adopt a lower coordination environment, as the Cu 3d states in the VBM lie at higher energy than the Ag 4d states.[318] Indeed, Wang et al. have recently proposed that $Cs_2CuSbCl_6$ NCs are metastable.[319] A recent review on copper-containing perovskites and perovskite-like structures (2D-0D) further highlighted that Cu-based HDPs remain mostly at the theoretical level due to stability concerns.[320] Within this generally unfavorable landscape, the report of $Cs_2CuSbCl_6$ NCs with a band gap of 1.66 eV in 2020 understandably sparked significant interest.[321] This was, in fact, the lowest band gap ever reported for an HDP, and $Cs_2CuSbCl_6$ has been the subject of renewed research efforts over the past five years: it has been employed as an archetypal HDP to illustrate topological states[322] and band structure,[323,324] prominently cited in HDP reviews,[320,325–327] and even used in photovoltaic device simulations.[328,329]

In this chapter, it is demonstrated that both the optical absorption spectra and the XRD pattern previously attributed to $Cs_2CuSbCl_6$ are in fact consistent with Cu-containing $Cs_3Sb_2Cl_9$, where LMCT and d-d electronic transitions within $[CuCl_3]^-$ clusters are responsible for the broad optical absorption centered at 530 nm. These conclusions are further supported by detailed XAS analysis and XANES simulations, which confirm the

formation of $Cs_3Sb_2Cl_9$ and the presence of Cu^{2+}. Finally, ab initio calculations are employed to substantiate the observation that $Cs_2CuSbCl_6$ is thermodynamically unstable towards decomposition, and that the incorporation of Cu^{2+} centers in $Cs_3Sb_2Cl_9$ does not result in an overall reduction of the band gap.

6.2. Synthesis of Cu-containing NCs and Laboratory Characterization

The complete characterization of the Cu-containing NCs, a combined experimental and theoretical approach was adopted. To first validate the $Cs_2CuSbCl_6$ NCs preparation, the synthesis method reported in ref. [321] was followed, obtaining the same optical absorption spectrum and XRD pattern as published. The experimental investigation was then complemented by *ab initio* XANES simulations as well as DFT and GW calculations of the total lattice energy and band structure, using Quantum ESPRESSO,[330–332] and Yambo.[333] Details of the experimental and computational procedures are reported in the Appendix. The NCs were prepared via simple HI method, dissolving the corresponding metal acetate in a mixture of OA, OLAM and ODE under vacuum. After heating, TMSCl was swiftly injected at 165 °C, and the reaction mixture was immediately cooled. The resulting NCs were then purified through successive centrifugation and redispersion steps, obtaining a similar purple colloidal suspension. The resulting XRD pattern indicates the formation of the trigonal $Cs_3Sb_2Cl_9$ phase instead of cubic $Cs_2CuSbCl_6$ (**Figure 6.1a**), which features very similar Bragg peaks. Repeated batches of the same sample sometimes also resulted in the formation of a minor fraction of $Cs_2CuSbCl_6$ (**Figure 6.1b**), which did not affect the optical absorption in the visible range (**Figure A 6.1**). When Cs and Sb react in the absence of Cu, two polymorphs of $Cs_3Sb_2Cl_9$ are formed (about 30% trigonal and 70% orthorhombic) (**Figure 6.1c**).

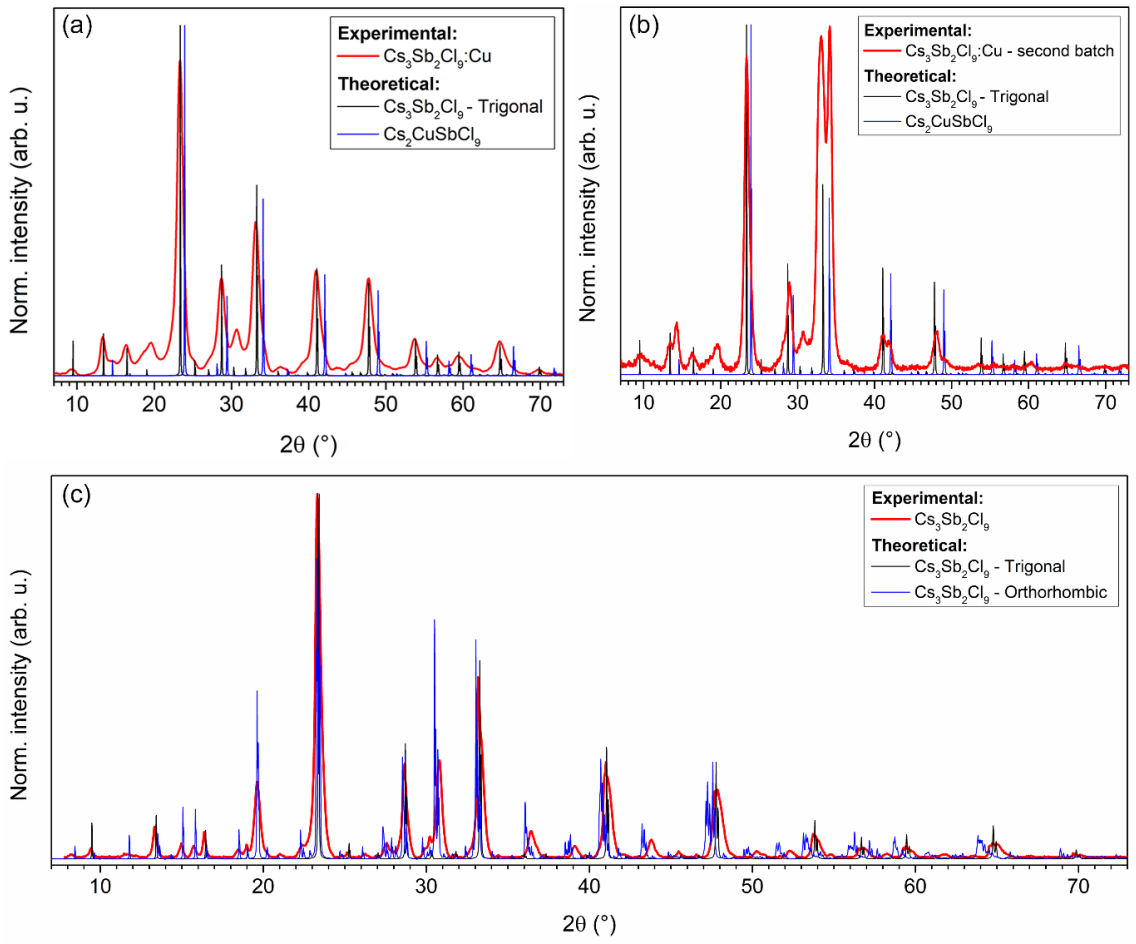

Figure 6.1. (a) XRD pattern (for λ=1.5418 Å), of the sample $Cs_3Sb_2Cl_9$:Cu compared with simulations of the XRD patterns of trigonal $Cs_3Sb_2Cl_9$ and $Cs_2CuSbCl_6$. (b-c) XRD pattern, using Cu Kα radiation (λ=1.5418 Å), of (b) a second batch of $Cs_3Sb_2Cl_9$:Cu compared with simulations of the XRD patterns of trigonal $Cs_3Sb_2Cl_9$ and $Cs_2CuSbCl_6$ and of (c) the experimental $Cs_3Sb_2Cl_9$ compared with simulations of the XRD patterns of trigonal and orthorhombic $Cs_3Sb_2Cl_9$.

When Cu is present, the sample is single-phase with just the trigonal polymorph. Since Cu directs the crystallization process towards this latter polymorph, it needs to be in the crystal lattice of $Cs_3Sb_2Cl_9$ (see **Figure A 6.2-Figure A 6.9** for the Rietveld refinements). The expected XRD patterns of trigonal $Cs_3Sb_2Cl_9$ and of the $Cs_2CuSbCl_6$ structure proposed previously (see SI of ref. [321]) are similar, which explains the misattribution of the Bragg peaks in ref. [321]. However, the $Cs_2CuSbCl_6$ structure proposed previously, with a cubic lattice parameter of 10.757 Å, involves very long Cu−Cl bonds at 2.61 Å (see **Figure A 6.10** for average Cu−Cl bond lengths in the literature). Most importantly, the proposed unit cell volume would be larger than the isostructural $Cs_2AgSbCl_6$ (10.664 Å),[145] despite Ag^+ being in fact much larger than Cu^+ (1.15 vs 0.77 Å). The DFT calculations confirm a monotonic reduction in the lattice parameter upon gradual substitution of Ag^+ by Cu^+, eventually

reaching a smaller value for $Cs_2CuSbCl_6$, in agreement with ionic size considerations (**Figure 6.2**).

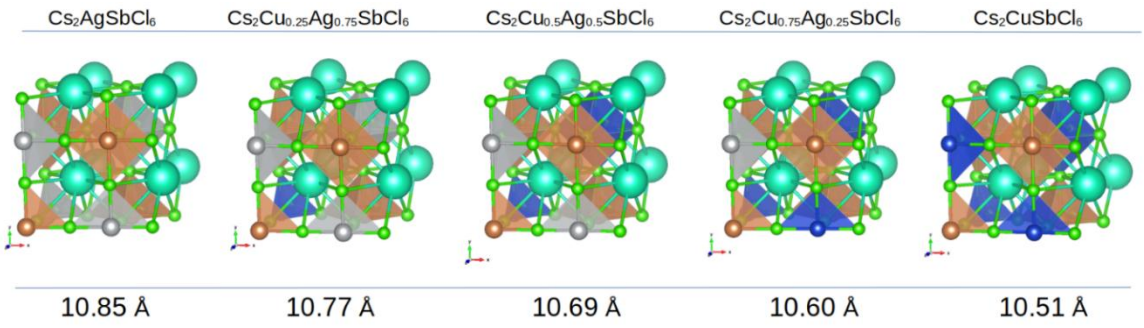

Figure 6.2. Optimized DFT lattice parameters of cubic mixed compositions of $Cs_2AgSbCl_6$ and $Cs_2CuSbCl_6$.

While no XRD data modeling was provided, Karmakar et al. showed that Cu^{2+} contracts the lattice parameter of polycrystalline $Cs_2AgSbCl_6$ up to 10% substitution, consistently with a lower ionic radius of Cu^{2+} compared to Ag^+.[266] Wang et al. reported metastable $Cs_2CuSbCl_6$ nanocrystals using modified ligand-assisted reprecipitation. Although the reported XRD data matched with a cubic perovskite symmetry, no lattice parameters were provided. In fact, they found a theoretically predicted structure with $[CuCl_3]^{2-}$ and $[SbCl_6]^{3-}$ polyhedra to be the most stable for Cu^+ and Sb^{3+}.[319]

The optical absorption spectrum of $Cs_3Sb_2Cl_9$:Cu (**Figure 6.3a**) displays a broad absorption peak centered around 530 nm, with a full width at half maximum of 170 nm, in agreement with the literature.[321] Such a broad absorption peak, attributed to the bandgap of $Cs_2CuSbCl_6$,[321] does not resemble a fundamental bandgap, which should not result in an absorption peak, nor an exciton in a semiconductor.[334] On the other hand, such broad absorption features are rather common for LMCT and d-d transitions in coordination complexes. For instance, Cu−Cl complexes exhibit various charge-transfer transitions from 350 to 635 nm.[335,336] In addition to the broad absorption at 530 nm, the $Cs_3Sb_2Cl_9$:Cu NCs also exhibit two absorption peaks at 304 nm and 361 nm:[159,337,338] these were not shown in ref. [321], due to the spectrum being cut below 400 nm. To investigate the nature of these lower-wavelength absorption peaks, further reactions were conducted with different ratios of Cs:Cu:Sb, namely 1:0:1, 1:1:0 and 0:0:1 (**Figure 6.3b**). The peaks below 400 nm are observed with a Cs:Cu:Sb ratio of 1:0:1, consistent with the direct and indirect band gaps of α- and β-$Cs_3Sb_2Cl_9$ at 2.85-2.9 eV.[339] The broad absorption band around 2.3 eV / 530 nm is

due to copper instead, and can be tentatively attributed to the incorporation of Cu into trigonal $Cs_3Sb_2Cl_9$. Extending the analysis into the NIR region, although the signal is relatively weak, an absorption shoulder can be discerned (**Figure 6.3c**), at 1.5 eV / 820 nm, with an intensity around 5% of that of the main peak at 2.3 eV / 530 nm. The shape and intensity ratio of these bands are consistent with LMCT and d-d transitions,[336,337,340] and they can only be due to Cu^{2+} ions in a d^9 configuration, as they are forbidden in d^{10} Cu^+ ions, providing additional evidence against the attribution of such band to the $Cs_2CuSbCl_6$ double perovskite. The only allowed localized electronic transition in Cu^+ (3d → 4s/p) is expected at 300 nm or lower.[341]

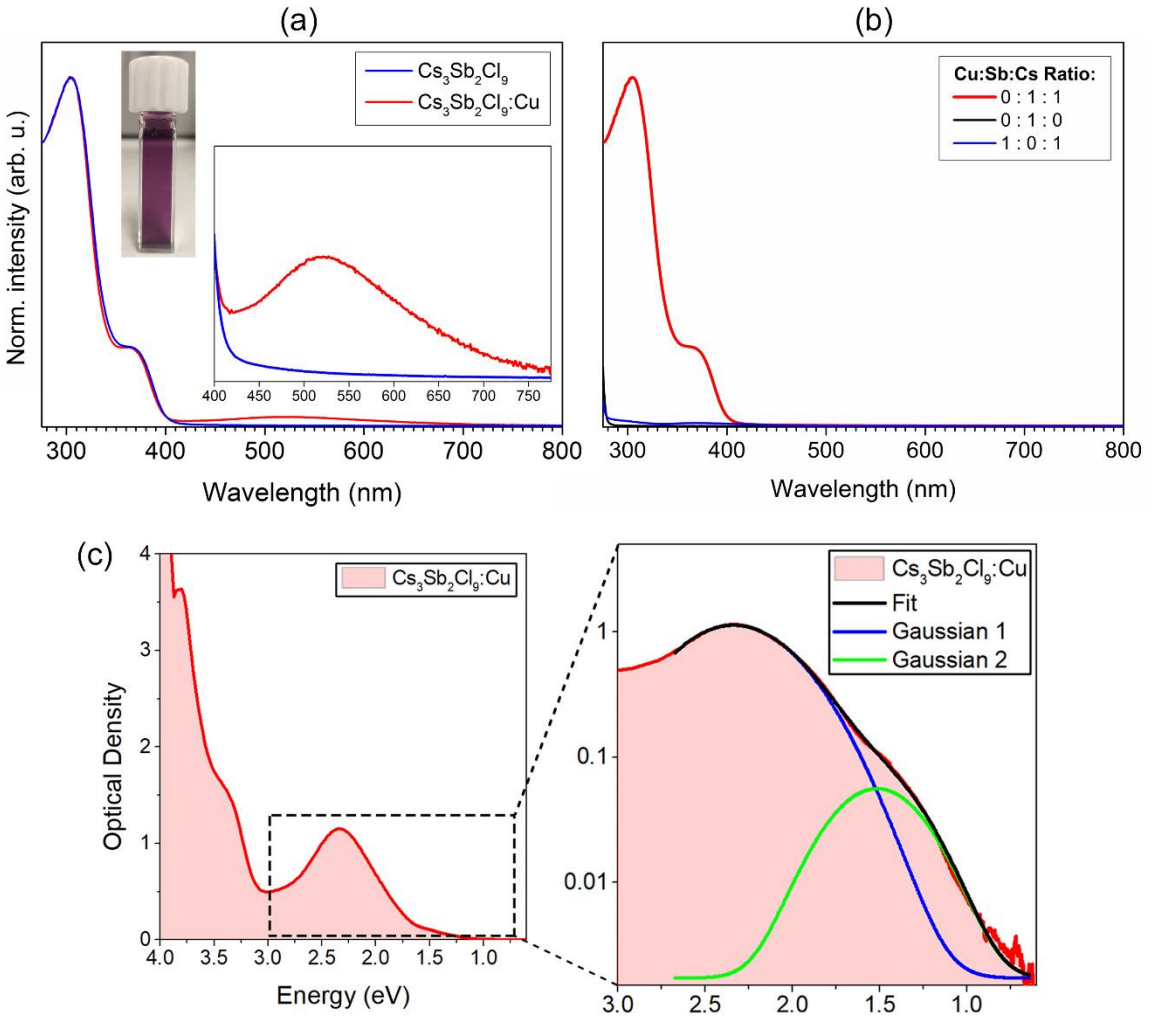

Figure 6.3. (a) UV-vis absorption spectrum of $Cs_3Sb_2Cl_9$:Cu compared with $Cs_3Sb_2Cl_9$. (b) UV-vis absorption spectra of reactions carried out in the absence of either Cu (red line) or Sb (blue line), and in the absence of Cu and Cs (black line). (c) UV-vis-NIR absorption spectrum of $Cs_3Sb_2Cl_9$:Cu.

TEM images (**Figure 6.4a**) confirm the effect of Cu in directing the growth $Cs_3Sb_2Cl_9$, resulting in a sharper size distribution and smaller average size (20 nm vs. 23 nm) (**Figure 6.4b**). Changing the Cu loading always results in the formation of trigonal $Cs_3Sb_2Cl_9$:Cu with different intensity of the 530 nm band relative to the 304 and 361 nm absorption transitions (**Figure 6.5a**), further proving that this band is due to Cu^{2+} centers in the structure. Once the Cu:Sb ratio reaches 2:1, the absorption spectrum changes radically (**Figure 6.5b**), since a new phase is formed, which XRD identifies as Cs_2CuCl_4 (**Figure 6.5c**).

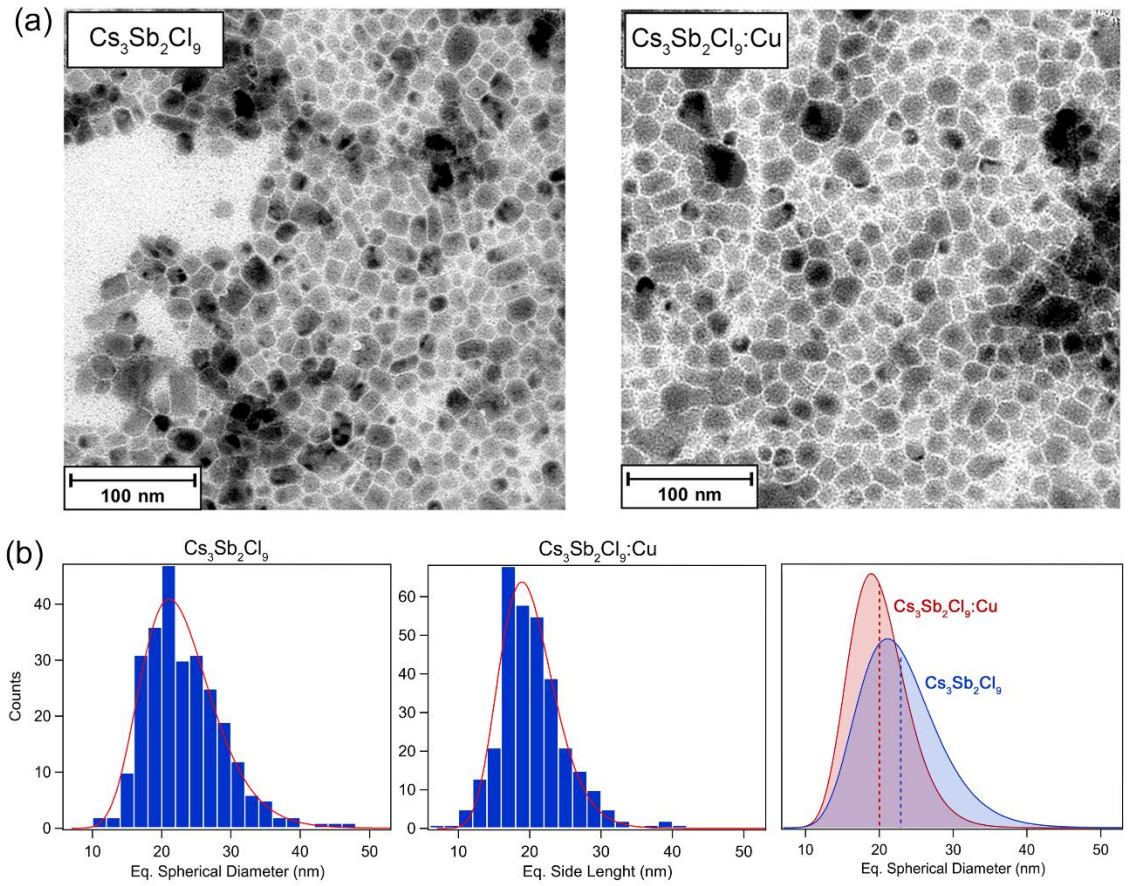

Figure 6.4. (a) TEM images of $Cs_3Sb_2Cl_9$ and $Cs_3Sb_2Cl_9$:Cu. (b) Nanoparticles distribution, fitted using a lognormal distribution, of the two samples and their comparison.

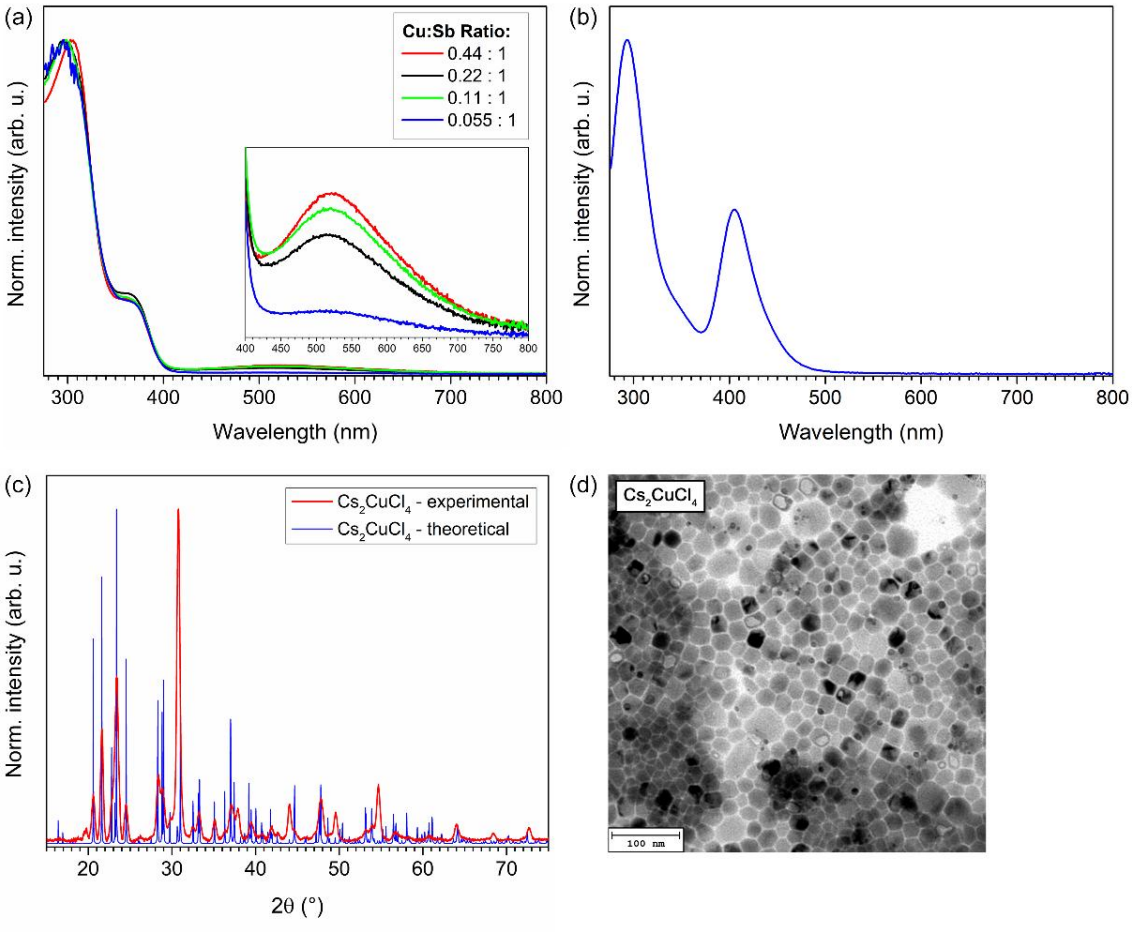

Figure 6.5. (a) UV-vis absorption spectra of reactions with lower Cu:Sb ratios compared to the reference reaction. (b) UV-vis absorption spectrum of Cs_2CuCl_4. (c) (b) XRD pattern of the experimental Cs_2CuCl_4 compared with simulation of the XRD patterns of Cs_2CuCl_4. (d) TEM images of Cs_2CuCl_4.

6.3. X-ray Absorption Spectroscopy on Cu-containing NCs

The Cu K-edge XANES of $Cs_3Sb_2Cl_9$:Cu and Cs_2CuCl_4 are shown in **Figure 6.6a**. Both samples exhibit a pre-edge peak at 8977 eV, attributed to a 1s → 3d electronic transition, which is dipole-forbidden and only occurs in Cu^{2+}, with the lowest intensity for D_{4h} coordination geometry and the highest for D_{2d}.[308] In contrast, Cu^+ species only exhibit an allowed 1s → 4p transition around 8983-8984 eV (8986-89 eV for Cu^{2+}), which is not evident in the present spectra.[342,343] This corroborates that copper is in the +2 oxidation state in $Cs_3Sb_2Cl_9$:Cu. Such a finding is again in contrast with a $Cs_2CuSbCl_6$ double perovskite, requiring Cu^+. Cai et al. reported the synthesis of $Cs_4CuSb_2Cl_{12}$ layered perovskite NCs featuring Cu(II)Cl_6 octahedra, confirmed by XRD and TEM, and attributed a 530 nm broad absorption to a direct band gap.[253] While the XRD patterns of $Cs_4CuSb_2Cl_{12}$ and our $Cs_3Sb_2Cl_9$:Cu sample are clearly different, the UV-vis absorption spectra are remarkably similar. In particular, also in the case of $Cs_4Cu_xAg_{2-2x}Sb_2Cl_{12}$ the intensity of the 530 nm band increases with Cu loading, suggesting it is also due to localized transitions at the Cu^{2+} site. From the EXAFS analysis (**Figure 6.6b-d**), Cu is coordinated by three Cl atoms at 2.29 Å in $Cs_3Sb_2Cl_9$:Cu, significantly shorter than the Cu−Cl distance of 2.61 Å in the HDP structure proposed in ref. [321].

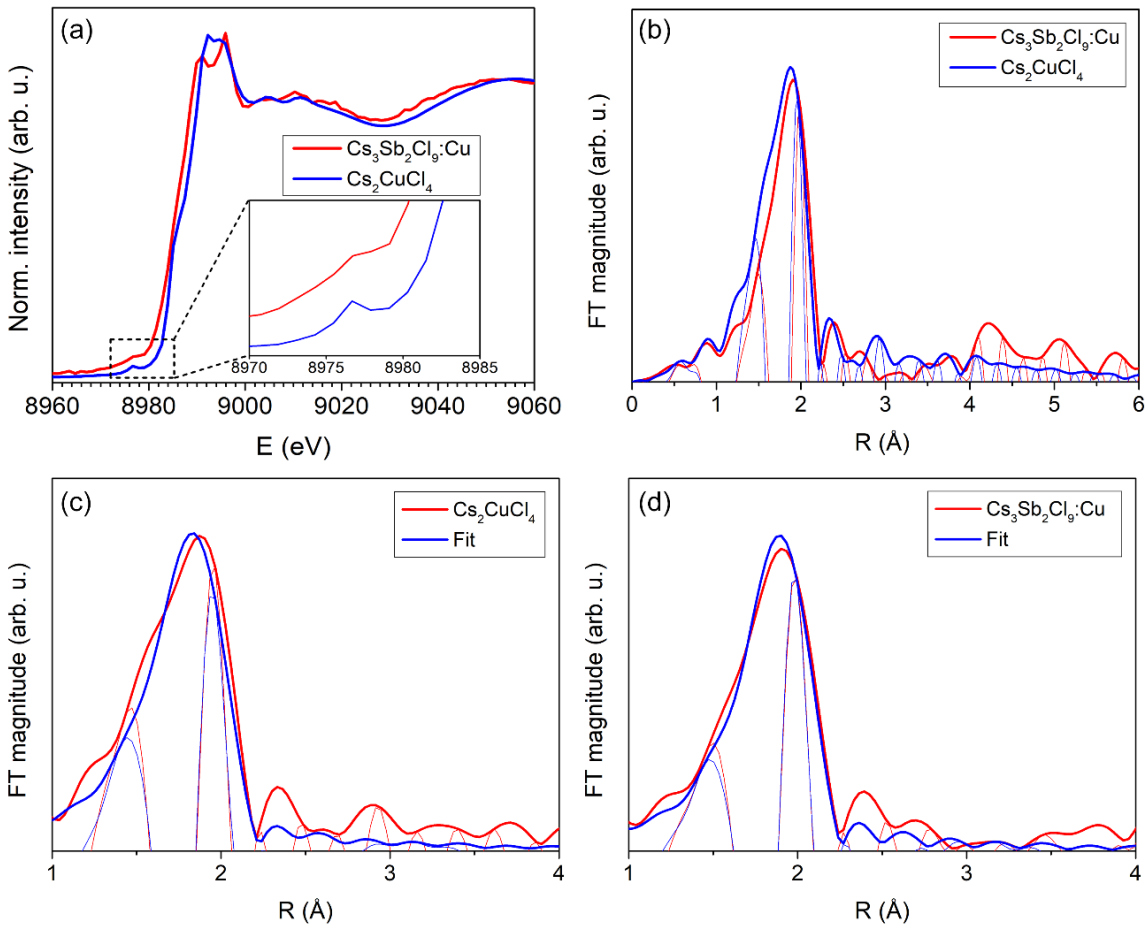

Figure 6.6. (a) XANES spectra of the Cu K-edge of $Cs_3Sb_2Cl_9$:Cu and experimental Cs_2CuCl_4. (b) Experimental Fourier-transformed EXAFS spectra (red) of $Cs_3Sb_2Cl_9$:Cu and Cs2CuCl4 at the Cu K-edge and best fit (blue) for (c) Cs_2CuCl_4 and (d) $Cs_3Sb_2Cl_9$:Cu. The modulus and imaginary phases are shown.

The XANES simulation of tetrahedral $CuCl_4$ clusters reproduces the experimental data of the experimental Cs_2CuCl_4, validating the model (**Figure A 6.11**). Since the experimental spectra for Cs_2CuCl_4 and $Cs_3Sb_2Cl_9$:Cu are very similar in the EXAFS region (as the coordinating atoms are the same), but differ significantly at the absorption edge, this suggests the Cu coordination geometry is not tetrahedral in $Cs_3Sb_2Cl_9$:Cu. To gain further insight into the local structure of copper, XANES simulations of various trial $CuCl_n$ clusters were compared with $Cs_3Sb_2Cl_9$:Cu, and the best agreement was found with a trigonal $CuCl_3$ complex (**Figure 6.7a**). Further simulations were performed varying the Cl−Cu−Cl dihedral angle from 120° (flat geometry) to 90° (trigonal pyramidal geometry). Decreasing the angle between 102 and 110° gives the best agreement with the experiment (**Figure 6.7b**), suggesting a distorted, trigonal pyramidal coordination environment. Finally, simulations of this $CuCl_3$ trigonal pyramid were performed by adjusting the electronic screening values on

the Cu photoabsorber (**Figure 6.7c**), and the best simulation is eventually reported in **Figure 6.8a**.

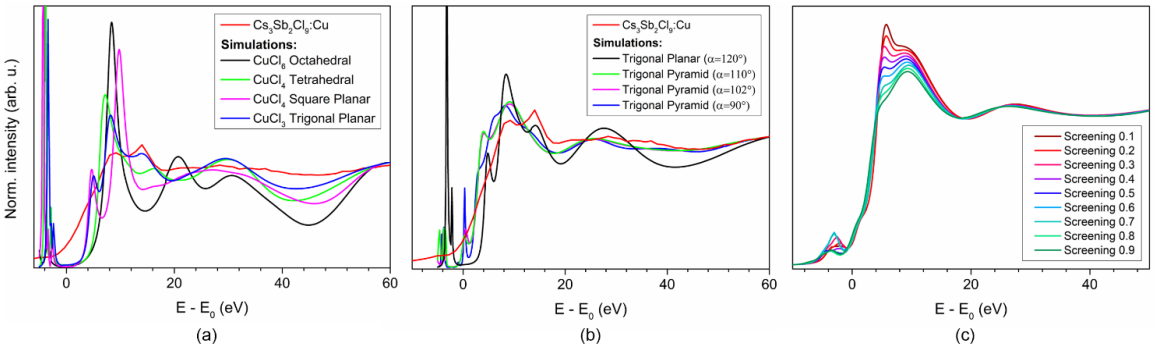

Figure 6.7. Cu K-edge XANES spectrum of $Cs_3Sb_2Cl_9$:Cu (red) compared with the (non-convoluted) XANES simulations of (a) several $CuCl_n$ complexes and (b) trigonal $CuCl_3$ cluster with different Cl−Cu−Cl angles (α). (c) XANES simulations of a trigonal pyramidal $CuCl_3$ cluster (α = 102°) with different values of the semi-empirical screening parameter of FDMNES.

This result provides strong evidence that in $Cs_3Sb_2Cl_9$:Cu copper is coordinated by three chloride ligands in a distorted trigonal pyramidal geometry, with a Cl−Cu−Cl angle around 104° and Cu−Cl bond lengths of about 2.29 Å. Such a coordination environment can be achieved in the trigonal $Cs_3Sb_2Cl_9$ lattice if Cu resides e.g. an empty Cs site with significant off-centering.

Cu^{2+} is much smaller than Cs^+, but a similar coordination was described by Kaiukov et al.[344] in the perovskite-related structure $Cs_3Cu_4In_2Cl_{13}$, with a polynuclear cluster of four tetrahedrally coordinated Cu in place of Cs. Similar arrangements, with less than four $CuCl_3$ units, can also accommodate in the Cs cavity with appropriate distortion. Further confirmation that Cu^{2+} does not sit in an octahedral environment is provided by the XANES of $CuCl_6$ octahedra (**Figure 6.8b**), which result in a completely different simulated spectrum, also ruling out the possible Sb/Cu substitution in $Cs_3Sb_2Cl_9$. One possible way to allocate the $[CuCl_3]^-$ unit in the $Cs_3Sb_2Cl_9$ lattice can be obtained by substituting two Cs^+ ions with one Cu^{2+} ion, resulting in $[CuCl_3]^-$ in-between the Sb octahedral layers, in which the Cu-Cl distances and angles are all in agreement with the EXAFS and XANES evidence (**Figure 6.8b-c**).

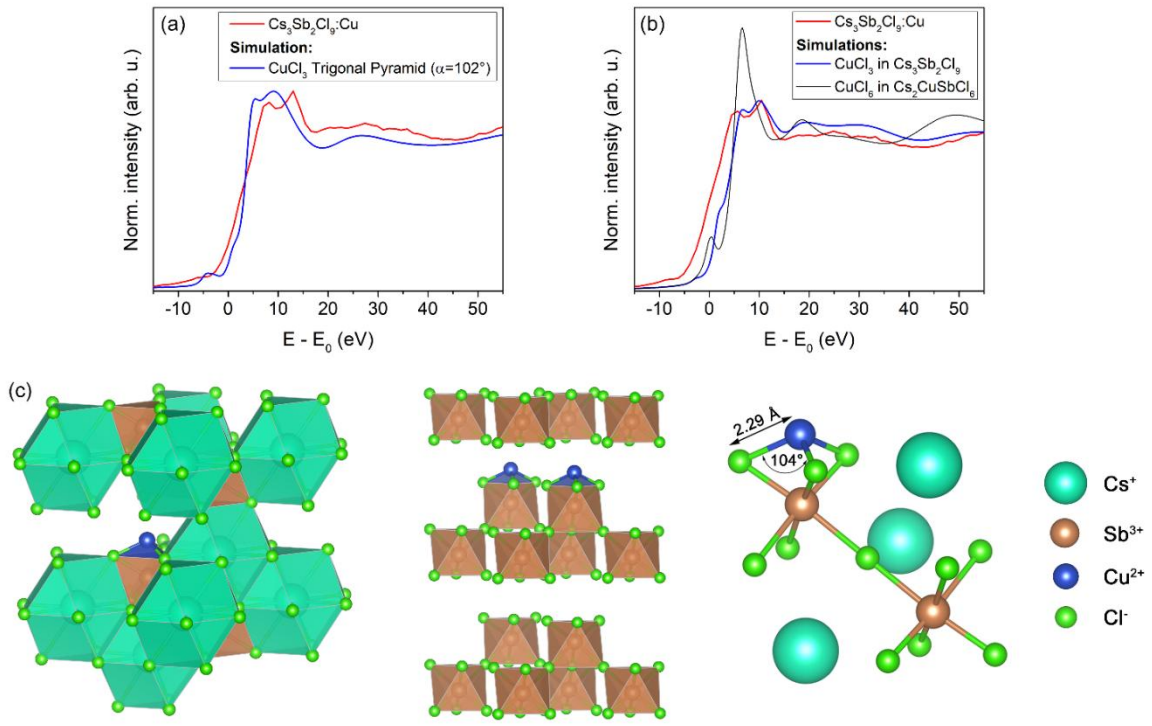

Figure 6.8. (a-b) XANES spectra for the Cu K-edge of $Cs_3Sb_2Cl_9$:Cu compared with (a) XANES simulation of $CuCl_3$ with α=102° and (b) XANES simulations of trigonal pyramidal $CuCl_3$ in $Cs_3Sb_2Cl_9$ and octahedral $CuCl_6$ in $Cs_2CuSbCl_6$. (c) Possible location of a trigonal pyramidal $[CuCl_3]^-$ center in the $Cs_3Sb_2Cl_9$ lattice. (See **Figure A 6.12** for possible locations).

Complementary evidence was collected also from the Sb K- and L_3-edges, and the Cl K-edge. The Sb L_3- (**Figure 6.9a**) and K-edge (**Figure 6.9b**) spectra have little difference between the two samples with and without Cu: the subtle variation in the post-edge region is attributable to the absence of the orthorhombic polymorph induced by the incorporation of Cu. The XANES simulations of trigonal $Cs_3Sb_2Cl_9$ show a good agreement with the experimental $Cs_3Sb_2Cl_9$, both at the Sb L_3- and K-edges (**Figure 6.9c-d**), confirming at the local level what is observed by XRD on the long range. Similarly, the experimental Sb L_3-edge spectrum of $Cs_3Sb_2Cl_9$:Cu (**Figure 6.9e**) does not match the simulations of the double perovskite $Cs_2CuSbCl_6$, but is instead well reproduced by the simulations of the trigonal $Cs_3Sb_2Cl_9$ (similarly for Sb K-edge, **Figure 6.9f**). This provides further confirmation on the coordination state of all Sb atoms.

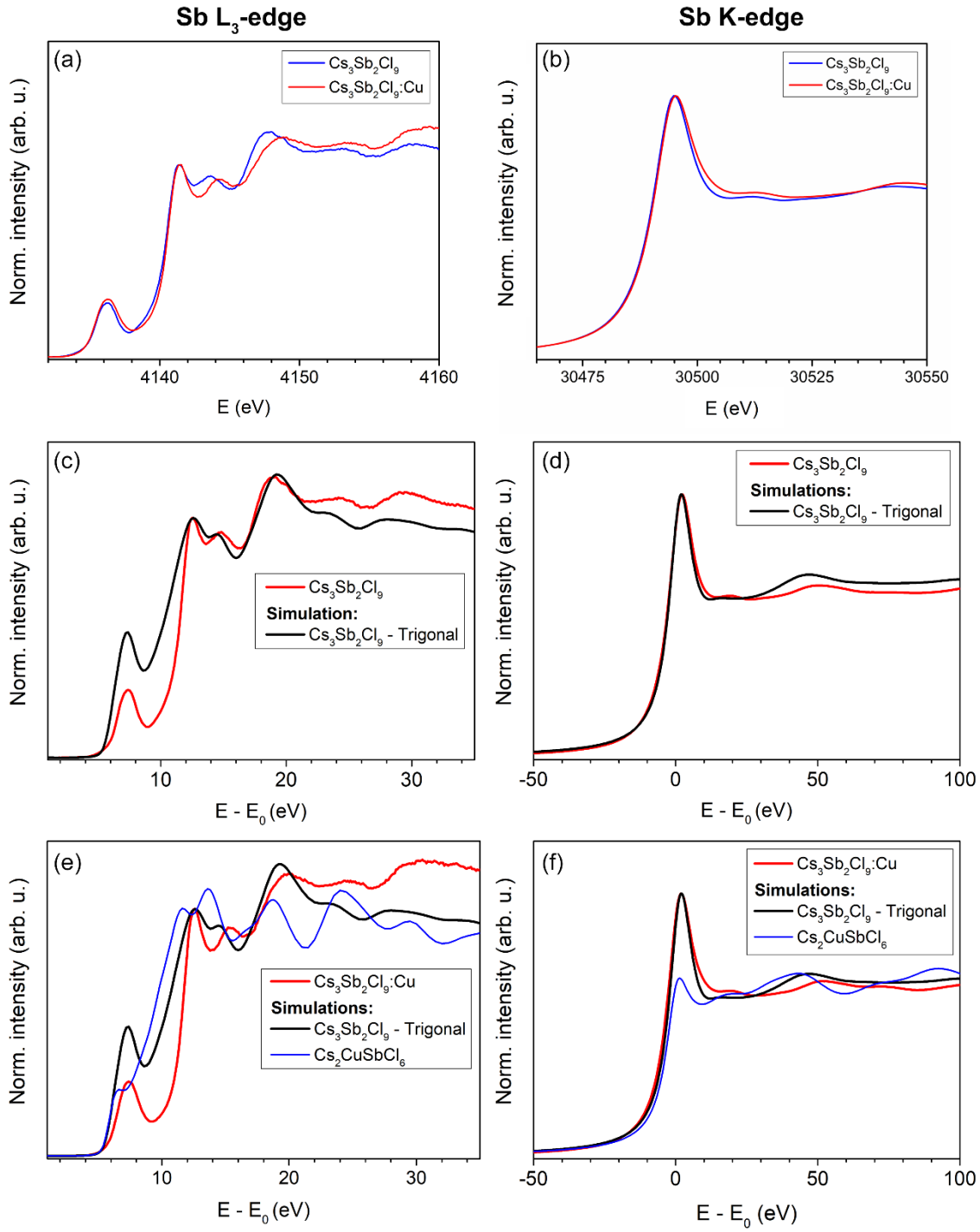

Figure 6.9. XANES spectra of experimental $Cs_3Sb_2Cl_9$ and $Cs_3Sb_2Cl_9$:Cu for (a) Sb L_3-edge and (b) Sb K-edge. (c-f) Comparison of experimental XANES spectra (red in all panels) with the simulated spectra of trigonal $Cs_3Sb_2Cl_9$ (black in all panels) and $Cs_2CuSbCl_6$ (blue in all panels). Experimental $Cs_3Sb_2Cl_9$ compared with a simulation of trigonal $Cs_3Sb_2Cl_9$ at the (c) Sb L_3-edge and (d) Sb K-edge. Experimental $Cs_3Sb_2Cl_9$:Cu, compared with trigonal $Cs_3Sb_2Cl_9$ and $Cs_2CuSbCl_6$ at the (e) Sb L_3-edge and (f) Sb K-edge.

The Cl K-edge probes all the bonds between chlorine and metals: the pre-edge transition observed at 2819 eV represents the transition from Cl 1s to hybridized empty states of Cl 3p and Cu 3d, and it then is assigned to Cu^{2+}–Cl by comparison with literature data on $CuCl_2$ and CuCl.[345] The intensity of this peak reflects the covalent character of the metal–chloride interaction, and it is notably absent in $Cs_3Sb_2Cl_9$ (**Figure 6.10**) where the Sb–Cl interaction is ionic.[308]

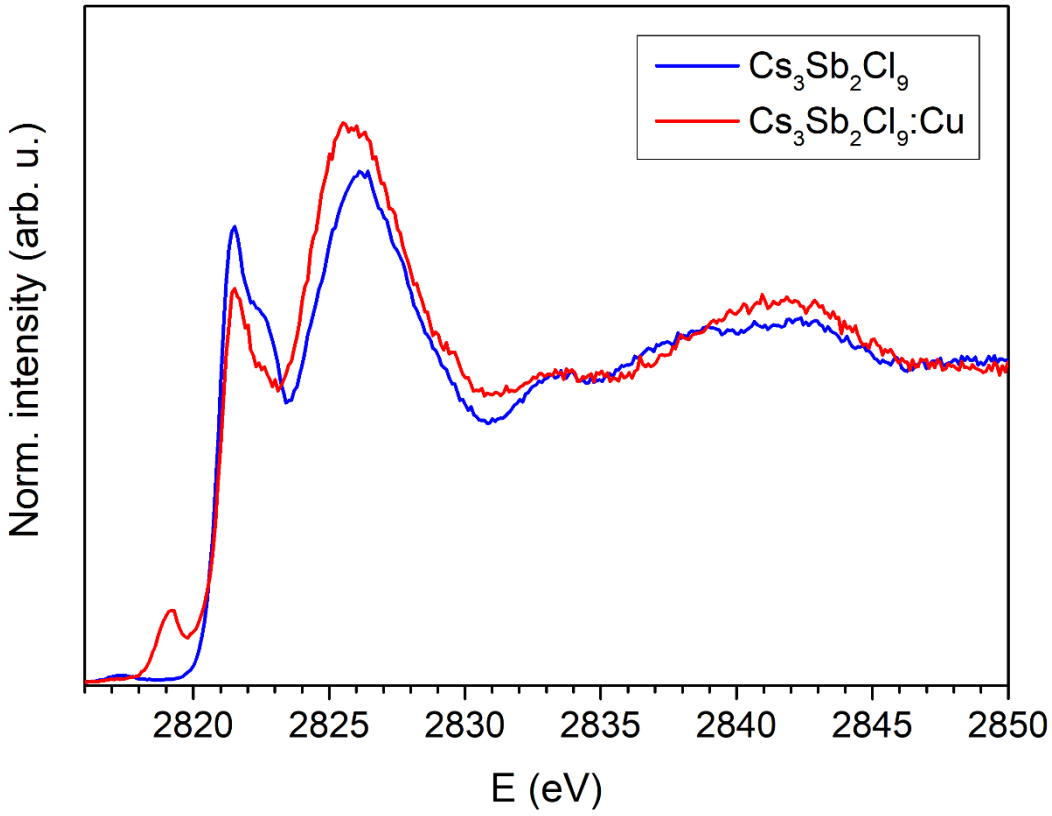

Figure 6.10. Experimental XANES spectra of $Cs_3Sb_2Cl_9$ and $Cs_3Sb_2Cl_9$:Cu at the Cl K-edge.

6.4. Stability and Electronic Structure through Calculations

To rationalize the experimental absence of the $Cs_2CuSbCl_6$ perovskite phase, we performed DFT calculations to assess its thermodynamic stability and electronic structure. Specifically, we computed the decomposition enthalpy into plausible ternary and binary compounds. To preserve stoichiometry and capture realistic decomposition pathways, we selected only a few specific ternary and binary compounds as likely decomposition products, based on their known stability within the Cs-Cu-Sb-Cl chemical space.

Figure 6.11a summarizes the decomposition enthalpies for various combinations of products. Several different pathways have negative enthalpy, indicating a high susceptibility of the Cu-based perovskite phase to decompose. The strongest driving force is found for decomposition into the ternary compounds with $Cs_3Sb_2Cl_9$, confirming its thermodynamic preference over the perovskite phase.

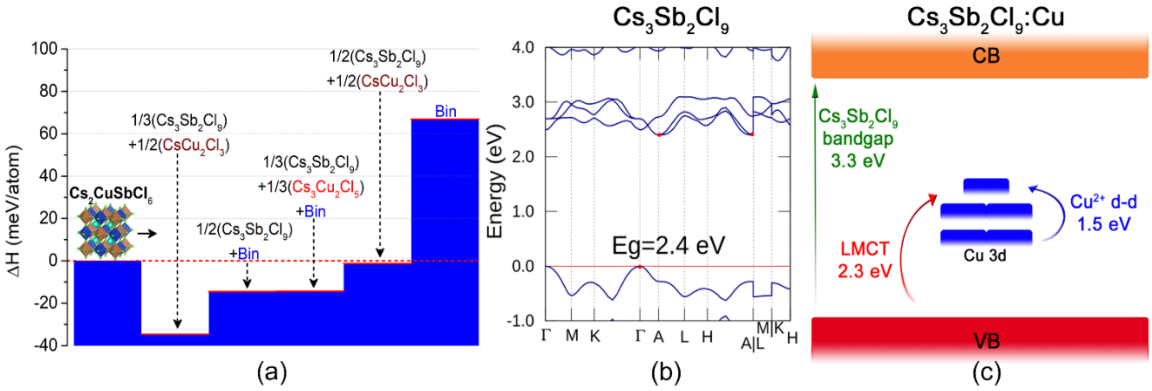

Figure 6.11. (a) Decomposition enthalpies of $Cs_2CuSbCl_6$ into different ternary and binary chlorides (labeled as Bin). (b) Electronic band structure of trigonal $Cs_3Sb_2Cl_9$ at the PBE level. (c) Schematic band diagram showing localized Cu 3d states in relation to $Cs_3Sb_2Cl_9$.

A deeper insight into the chemical origin of such instability comes from the band structure and pDOS of the Cu HDP compared with its Ag analogue, which on the contrary has been successfully synthesized in several reports and exhibits high thermodynamic stability, evidenced by positive decomposition enthalpies toward ternary and binary compounds (**Figure 6.12**).

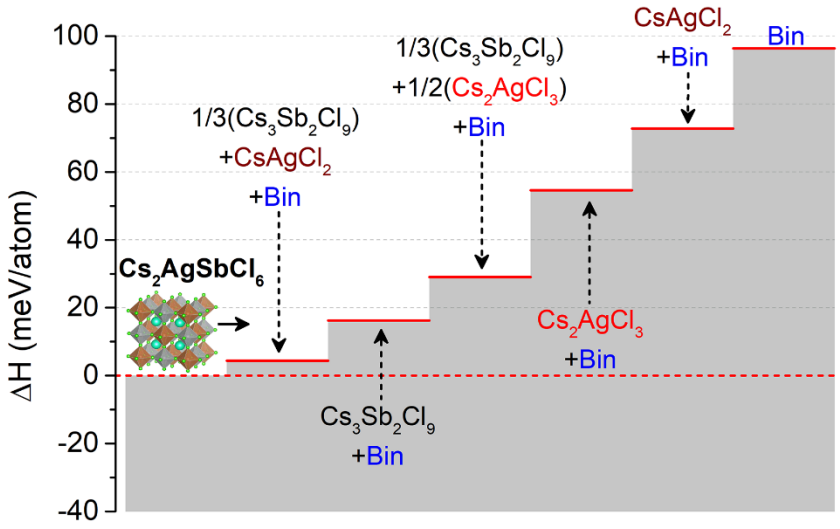

Figure 6.12. Decomposition enthalpies of $Cs_2AgSbCl_6$ into different ternary and binary chlorides (labeled as Bin).

The pDOS of cubic $Cs_2CuSbCl_6$ and $Cs_2AgSbCl_6$ calculated at the PBE level are shown in **Figure 6.13**. The main peaks of the Cu 3d states are located approximately 2 eV higher in energy than those of the Ag 4d states; this generally destabilizes the six-fold coordinated $CuCl_6$ octahedra.[318] Moreover, a stronger Ag *d* − Cl *p* coupling results from these states being closer in energy. In contrast, the larger separation between the Cu *d* and Cl *p* states reflects both weaker coupling and lower structural stability. These findings are all consistent with the decomposition enthalpy results, confirming the lower stability of the Cu HDP compared to its Ag analogue. Overall, both the lower stability and the lower band gap of $Cs_2CuSbCl_6$ (**Figure 6.14**) can ultimately be attributed to the higher energy of the Cu *d* states.[318] To obtain accurate band gap values, GW calculations on $Cs_2AgSbCl_6$ were performed, which show PBE underestimates the band gap by ~0.8 eV (**Figure 6.14**). Unfortunately, GW calculations fail to converge in the presence of Cu due to localized *d* states, which cause strong electronic correlations and sharp variations in the quasiparticle self-energy.

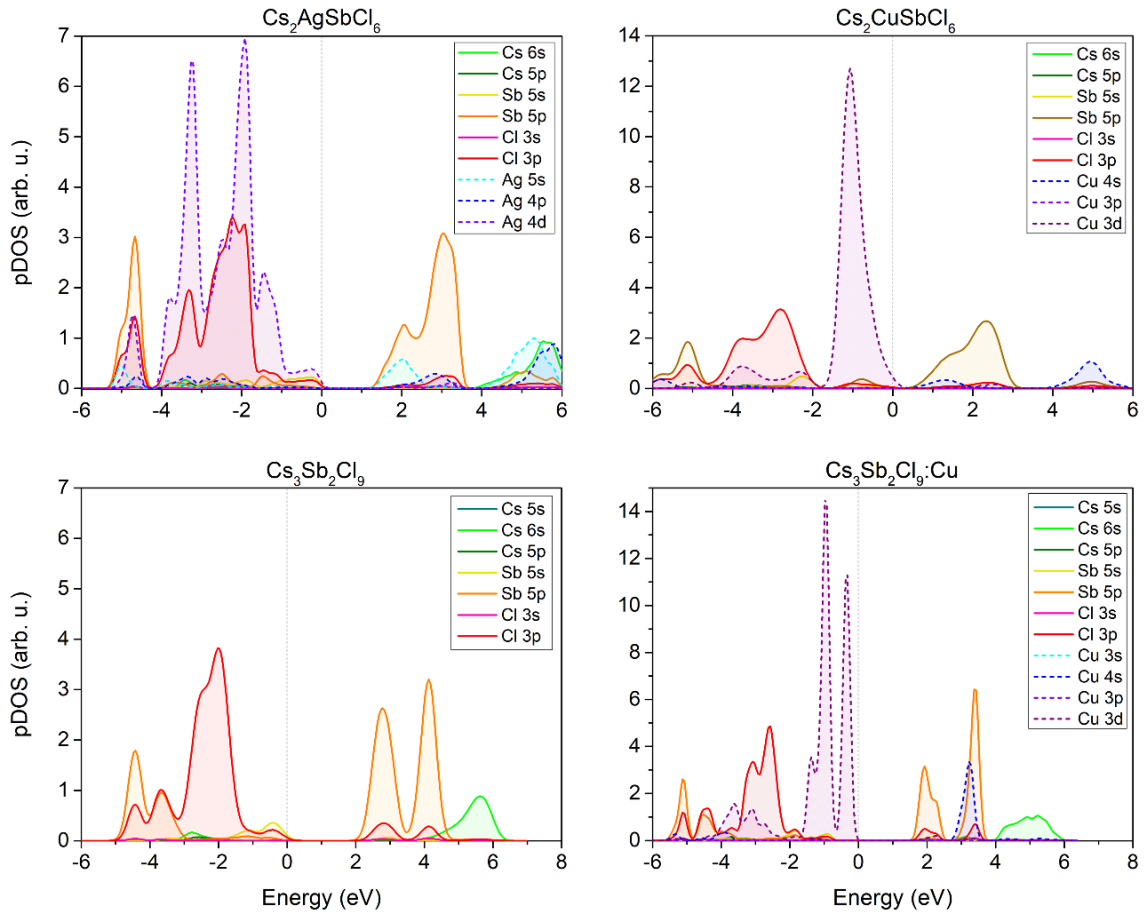

Figure 6.13. pDOS of $Cs_2CuSbCl_6$, $Cs_2AgSbCl_6$, trigonal $Cs_3Sb_2Cl_9$ and theoretical $Cs_3Sb_2Cl_9$:Cu at the PBE level. The valence band maximum is aligned to zero energy (dotted gray line) in all plots.

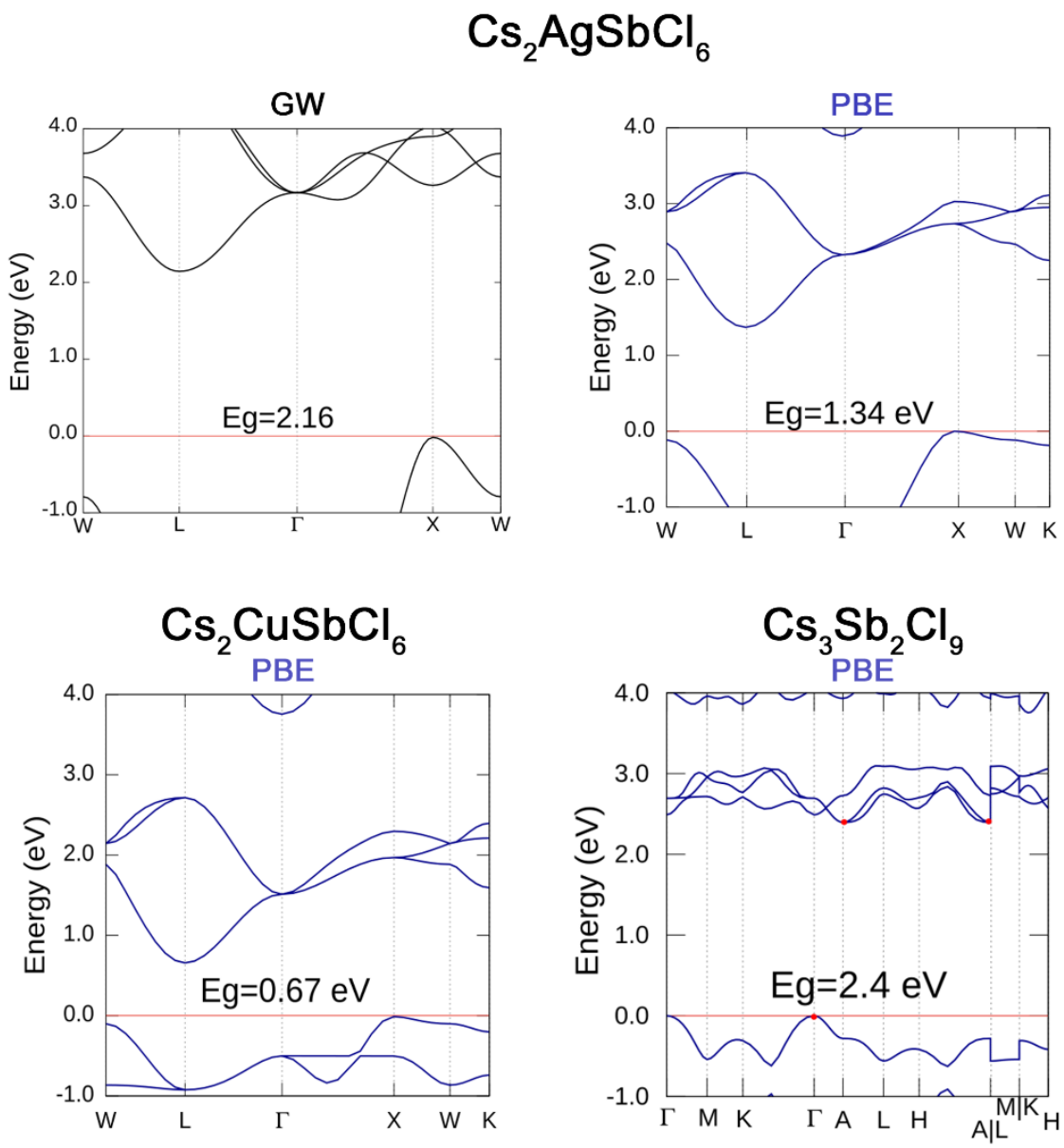

Figure 6.14. Electronic band structures of $Cs_2AgSbCl_6$ (at the PBE and GW levels of theory, upper panels), and of $Cs_2CuSbCl_6$ and trigonal $Cs_3Sb_2Cl_9$ (at the PBE level, lower panels).

We expect the defective $Cs_4CuSb_4Cl_{18}$ structure in **Figure 6.8c** to be one of the different possible configurations which average out over the long range. Through band structure and pDOS simulations, we investigated this structure configuration and compared it with the defect-free structure of $Cs_3Sb_2Cl_9$. The bands of $Cs_3Sb_2Cl_9$ show a gap of 2.4 eV (**Figure 6.11b**) that underestimated as expected from PBE calculations. The VBM is mainly composed of Cl p and Sb 5s states, while the CBM originates primarily from Sb p and Cl p states (**Figure 6.13**). As Cu^{2+} in the $3d^9$ configuration is not fully occupied, this configuration plays a key role and may give rise to magnetization effects and Hubbard

corrections necessary (DFT+U). Under these conditions, the simulations are challenging and should be interpreted qualitatively. We first studied the system in the non-magnetic case, and found Cu 3d-derived doping states just above the Fermi energy (**Figure A 6.13**), which can be associated with two possible electronic transitions: either from Cl ligand states (i.e., near the Fermi level) or from other Cu 3d electrons (above the Fermi level), as illustrated in the scheme in **Figure 6.11c**. When magnetization is included the calculations show agreement with the non-magnetic results (**Figure A 6.13**). Some Cu 3d-derived doping states appear in the middle of the band gap, while others states exhibit a minor influence, attributed to the overlap of Cu 3d states with Sb s/p and Cl p states at the VBM, while showing no contribution to the CBM, confirming the presence of two optical absorption peaks in the visible and NIR range. On the other hand, DFT+U correction did not yield physically meaningful results in our system, likely due to the instability of the magnetic configuration induced by the partially filled Cu 3d orbitals, which prevented proper convergence and led to unphysical solutions. The applicability of DFT+U corrections in this system remains an open question and warrants further investigation in future studies.

With a combination of XRD, XANES, EXAFS, and optical spectroscopy, we conclude that Cu-doped $Cs_3Sb_2Cl_9$ NCs are formed instead of $Cs_2CuSbCl_6$ from one-pot hot injection, confirming DFT predictions of limited stability for the HDP. Instead, we propose an overall structure bringing together the evidence from long-range and short-range X-ray techniques, in which Cu^{2+} in trigonal pyramidal coordination sits off-centered in empty Cs^{+} sites. The peculiar broad optical absorption in the visible range, previously attributed to a low bandgap of the double perovskite, is rather due to isolated LMCT and d-d transitions at the Cu^{2+} site in $Cs_3Sb_2Cl_9$, which is a wide bandgap semiconductor.

6.5. Appendix

Materials

1-octadecene (ODE, 90%), antimony (III) acetate ($Sb(OAc)_3$, 97%), cesium acetate (Cs(OAc), 97%), chlorotrimethylsilane (TMSCl, 97%), copper (II) acetate anhydrous ($Cu(OAc)_2$, 98%), oleic acid (OA, 90%) and oleylamine (OLAM, 80-90%) were purchased from Thermo Scientific. Toluene was purchased from J.T. Baker. n-hexane (>98.5%) was purchased from Carlo Erba Reagents. All materials were used without further purification.

Cu-containing NCs synthesis

To prepare $Cs_3Sb_2Cl_9$:Cu NCs, 0.65 mmol Cs(OAc), 0.22 mmol $Cu(OAc)_2$, and 0.5 mmol $Sb(OAc)_3$ were placed in three-necked round-bottom flasks of 50 mL with OA (2.9 ml), OLAM (0.65 ml) and ODE (10 ml), the mixture was stirred at room temperature for about 10 minutes.[321] The mixture was heated to 105 °C under vacuum for about 1h. The reaction mixture was heated under a nitrogen atmosphere, and TMSCl (0.4 ml) was swiftly injected at 165 °C and immediately cooled to room temperature in an ice-water bath. The reaction mixture is then decanted into a centrifugal tube and centrifuged at 9000 rpm for 10 min. The supernatant was removed. The precipitate was redispersed in 10 mL toluene with sonication and centrifuged at 9000 rpm for 10 min. The supernatant was discarded. The precipitate was redispersed in 10 mL hexane with sonication and centrifuged at 5000 rpm for 10 min. The supernatant obtained has a purple color and was assumed to contain the NCs, while the precipitate was discarded.

The synthesis described above was then also repeated without either $Cu(OAc)_2$ or $Sb(OAc)_3$, respectively, or without both $Cu(OAc)_2$ or $Sb(OAc)_3$, and also with different amounts of $Cu(OAc)_2$. In total, five syntheses were performed with Cu:Sb ratios 0.055:1, 0.11:1, 0.22:1, 0.44:1, 2:1. When not specified otherwise, a Cu:Sb ratio of 0.44:1 was used, and this latter synthesis was repeated two times to check for reproducibility. The different experimental conditions of all syntheses are summarized in **Table A 6.1**.

Table A 6.1. Cation amounts and resulting copper-antimony molar ratios for each reaction.

$Cu(OAc)_2$ mmol	$Sb(OAc)_3$ mmol	Cs(OAc) mmol	Cu:Sb Ratio
0.22	0.5	0.65	0.44:1*
0	0.5	0.65	0:1
0	0.5	0	0:1 (Without Cs)
0.22	0	0.65	1:0
0.0275	0.5	0.65	0.055:1
0.055	0.5	0.65	0.11:1
0.11	0.5	0.65	0.22:1
1	0.5	0.65	2:1

* Reference cation ratio from ref.[321].

UV-vis-NIR

For the Cu-based samples absorption spectra were recorded using a Cary 60 UV-Vis Spectrophotometer (Agilent Technologies) and a LAMBDA 1050+ (PerkinElmer).

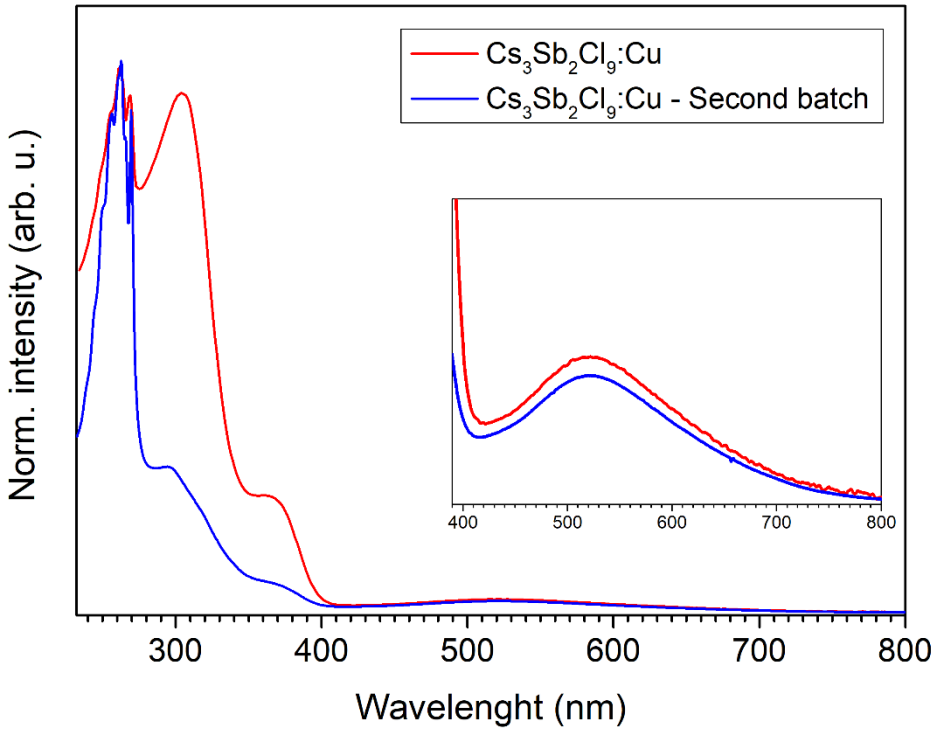

Figure A 6.1. UV-vis absorption spectra of two different batches of $Cs_3Sb_2Cl_9$:Cu synthesis.

XRD

XRD patterns of experimental $Cs_3Sb_2Cl_9$, Cs_2CuCl_4 and $Cs_3Sb_2Cl_9$:Cu - second batch were collected using Cu Kα radiation (λ=1.5418 Å) on a Rigaku Miniflex diffractometer equipped with a DTEX detector operating at 30 kV and 10 mA. A few droplets of each colloidal sample were deposited on the surface of a silicon monocrystal zero-background plate with the aid of a micropipette and dried in air within minutes. All datasets were collected in the $4.8° \leq 2\theta \leq 80°$ range, with a 2θ-step of 0.05°. For the $Cs_3Sb_2Cl_9$:Cu sample, XRD data was collected on a laboratory X-ray scattering setup using Mo Kα radiation (0.71 Å) from a microfocus X-ray source (Xenos) collimated to a beam size of ≈1 × 1 mm. Dispersions of NCs in n-hexane were drop-casted onto adhesive tape (3 m Scotch Magic 810) and measured in transmission mode after drying. The data was collected using a Dectris Pilatus 100K detector. The pattern was transformed to Cu Kα for comparison. The VESTA software[346] was used to simulate the diffraction patterns of trigonal α-$Cs_3Sb_2Cl_9$ (ICSD #22075),[347] orthorhombic β-$Cs_3Sb_2Cl_9$ (ICSD #2066),[348] and Cs_2CuCl_4 (ICSD #15699).[349] Starting from these structural models, Rietveld refinements were performed using the experimental data in the $8.5° \leq 2\theta \leq 72°$ range with the TOPAS software (**Figure A 6.2**-**Figure A 6.9**).[316] In **Table A 6.2** all the refined parameters are reported, together with the corresponding best fits for the different models refined against the data for the samples $Cs_3Sb_2Cl_9$ and $Cs_3Sb_2Cl_9$:Cu (two batches, one collected in transmission and one in Bragg-Brentano geometry). For the latter, a spherical harmonics description was used to describe the (weak) preferred orientation effects found in the experimental data. Given the limitations in laboratory data quality and the complexity of the samples (often exhibiting the co-presence of multiple phases), the atomic coordinates were fixed to the values reported in the corresponding Crystallographic Information Files.

Table A 6.2. Lattice parameters of each phase and respective R_p derived from Rietveld refinements.

Sample	Trigonal $Cs_3Sb_2Cl_9$			Orthorhombic $Cs_3Sb_2Cl_9$				Cubic $Cs_2CuSbCl_6$		R_p %
	a (Å)	c (Å)	%*	a (Å)	b (Å)	c (Å)	%*	a (Å)	%*	
$Cs_3Sb_2Cl_9$	7.620(3)	9.276(7)								43.47
				18.647(7)	7.543(2)	3.192(6)				22.84
	7.620(2)	9.318(5)	33.00(2)	18.620(4)	7.593(1)	3.028(1)	67.00(2)			14.56
$Cs_3Sb_2Cl_9$:Cu	7.630(9)	9.33(2)								16.48
								10.785(1)		20.94
$Cs_3Sb_2Cl_9$:Cu - Second batch	7.56(2)	9.25(4)								33.32
								10.672(8)		30.63
	7.681(5)	9.196(6)	82.00(3)					10.478(5)	18.00(3)	19.96

* Contribution of each crystalline phase in the mixed-phase Rietveld refinement.

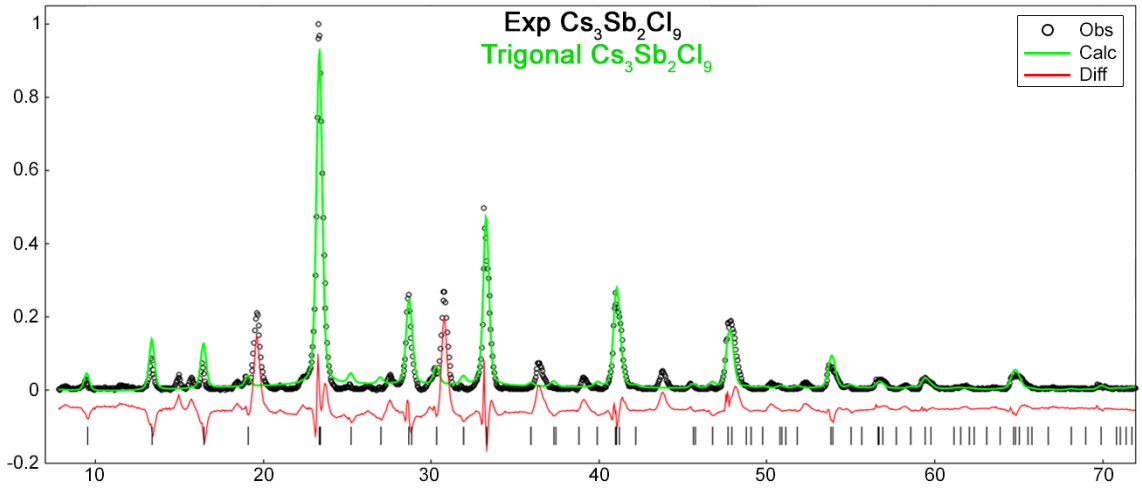

Figure A 6.2. Rietveld refinement of the experimental $Cs_3Sb_2Cl_9$ performed with trigonal $Cs_3Sb_2Cl_9$. Experimental data (black), calculated pattern (green), residual (red).

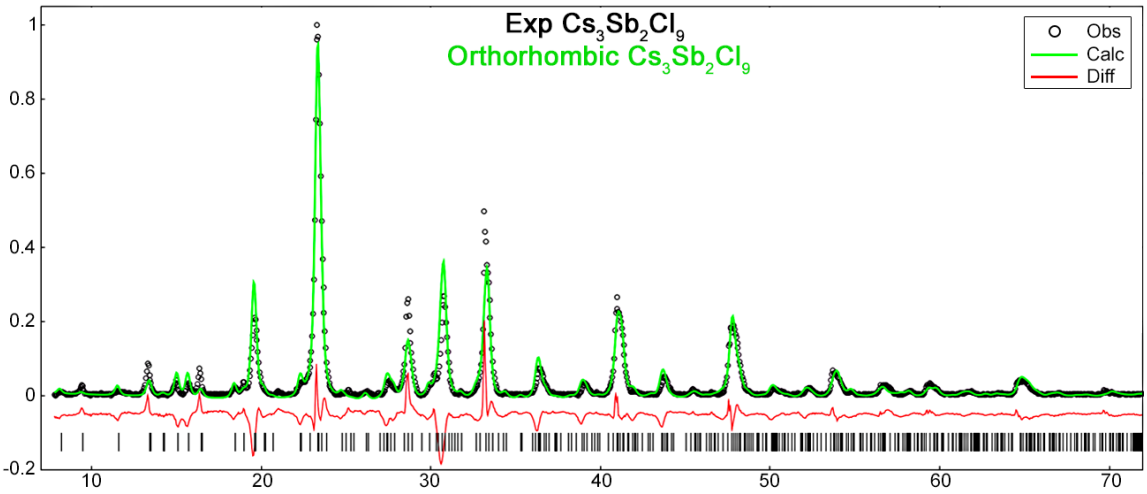

Figure A 6.3. Rietveld refinement of the experimental $Cs_3Sb_2Cl_9$ performed with orthorhombic $Cs_3Sb_2Cl_9$. Experimental data (black), calculated pattern (green), residual (red).

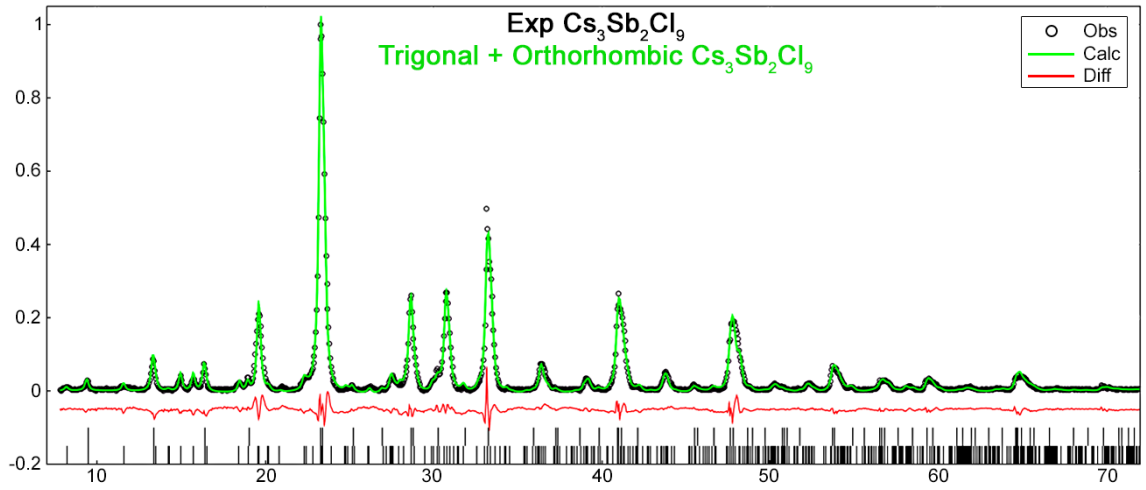

Figure A 6.4. Rietveld refinement of the experimental $Cs_3Sb_2Cl_9$ performed with the two phases, trigonal and orthorhombic, of $Cs_3Sb_2Cl_9$. Experimental data (black), calculated pattern (green), residual (red).

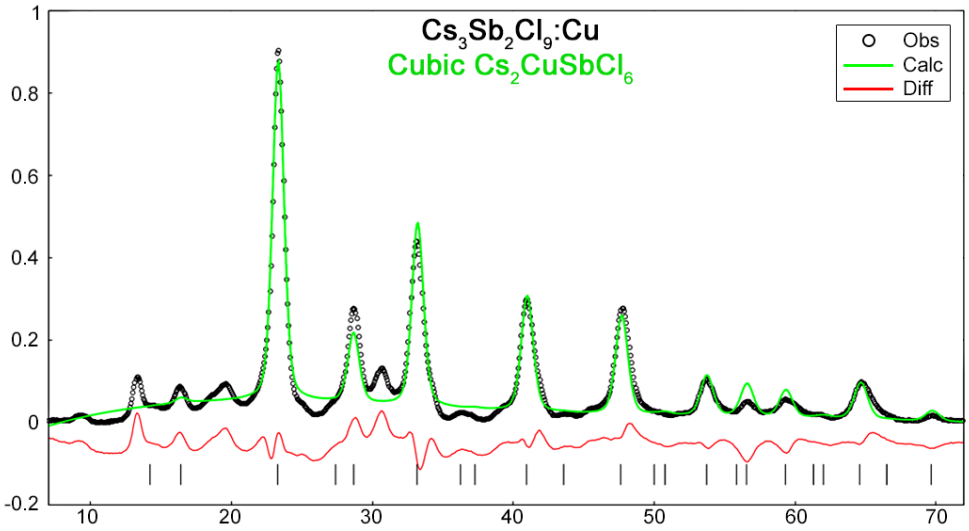

Figure A 6.5. Rietveld refinement of the sample $Cs_3Sb_2Cl_9$:Cu performed with cubic $Cs_2CuSbCl_6$. Experimental data (black), calculated pattern (green), residual (red).

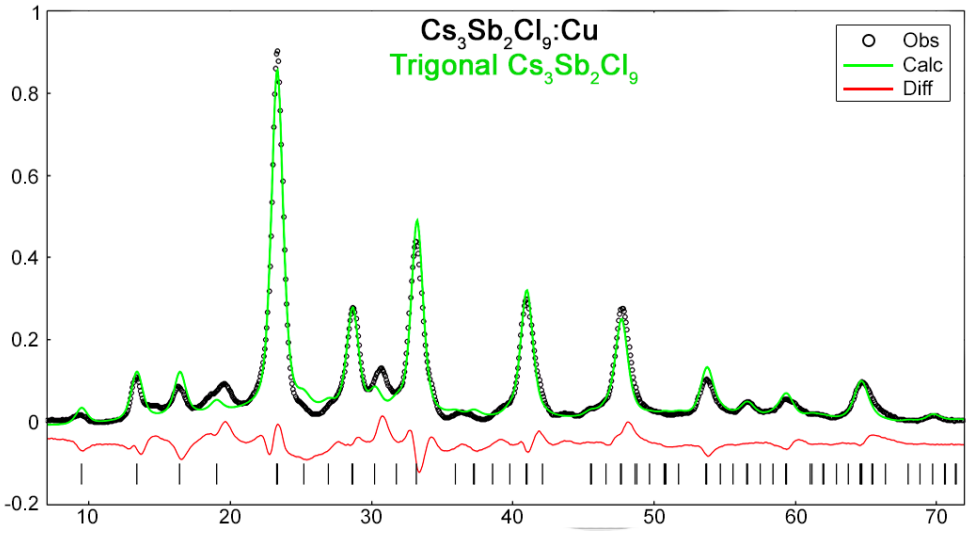

Figure A 6.6. Rietveld refinement of the sample $Cs_3Sb_2Cl_9$:Cu performed with trigonal $Cs_3Sb_2Cl_9$. Experimental data (black), calculated pattern (green), residual (red).

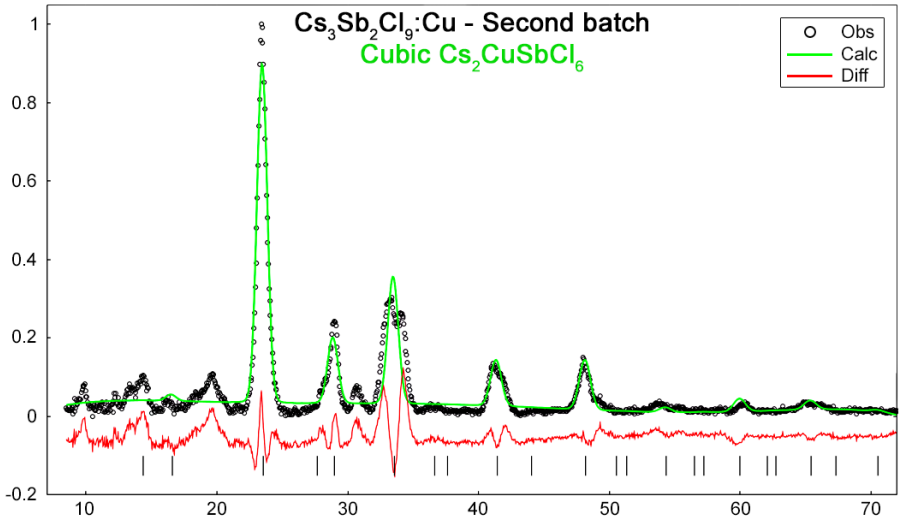

Figure A 6.7. Rietveld refinement of the second batch of the sample $Cs_3Sb_2Cl_9$:Cu performed with cubic $Cs_2CuSbCl_6$. Experimental data (black), calculated pattern (green), residual (red).

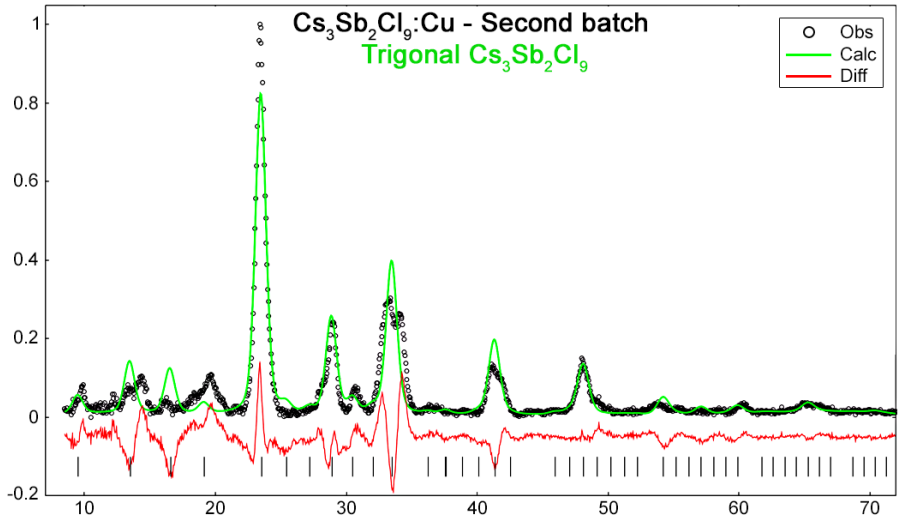

Figure A 6.8. Rietveld refinement of the second batch of the sample $Cs_3Sb_2Cl_9$:Cu performed with trigonal $Cs_3Sb_2Cl_9$. Experimental data (black), calculated pattern (green), residual (red).

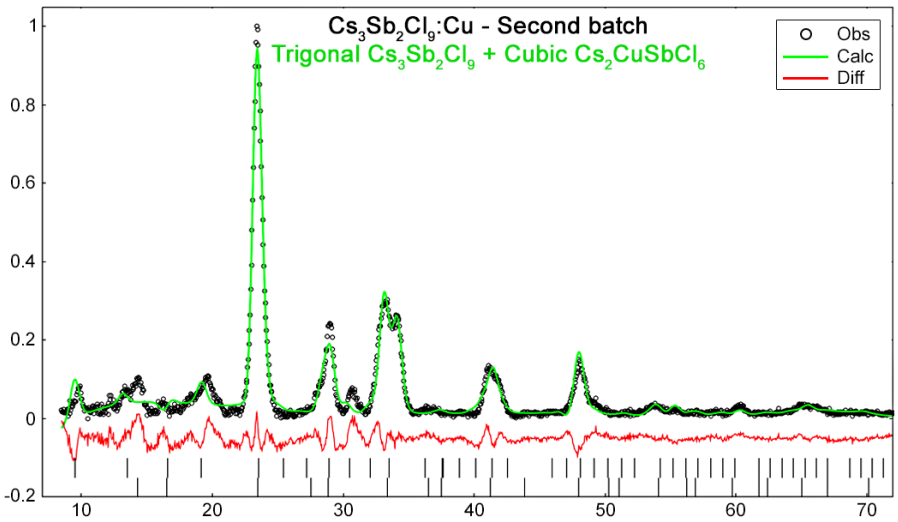

Figure A 6.9. Rietveld refinement of the second batch of the sample $Cs_3Sb_2Cl_9$:Cu performed with trigonal $Cs_3Sb_2Cl_9$ and cubic $Cs_2CuSbCl_6$. Experimental data (black), calculated pattern (green), residual (red).

Cu−Cl bond length distributions

The Cu−Cl bond lengths from the Cambridge Structural Database follow a slightly skewed distribution which peaks at 2.25 Å: this is not a bimodal curve that could be used to discriminate between Cu^{+}−Cl and Cu^{2+}−Cl. In particular, the Cu^{+}−Cl bond length distribution also peaks at 2.25 Å, while such a histogram is unreliable for Cu^{2+}−Cl because very few data sources specify the +2 oxidation state, while confirming the 2.25 Å average.

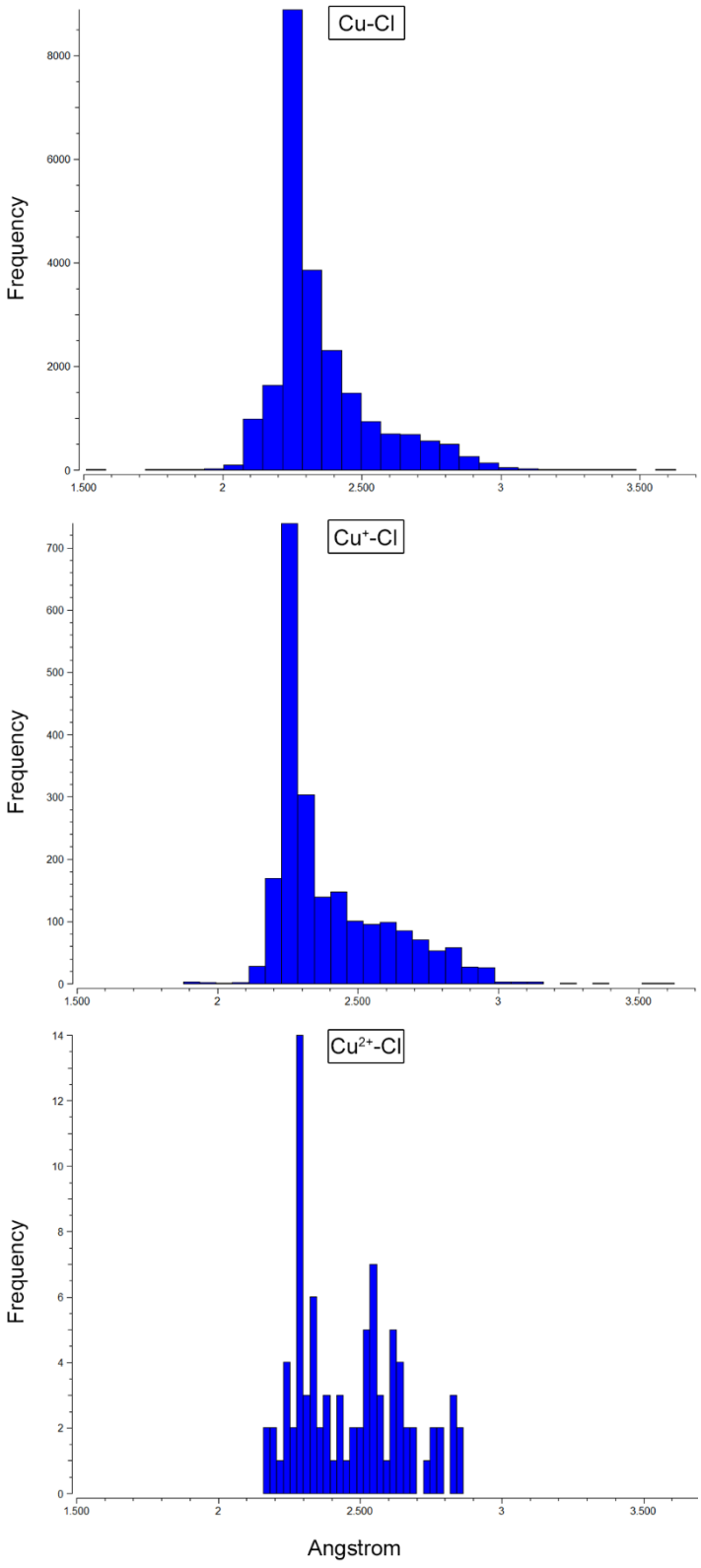

Figure A 6.10. Cu−Cl bond length distribution from the Cambridge Structural Database. Top: Cu−Cl for all oxidation states; middle: Cu^{+}−Cl; bottom: Cu^{2+}−Cl. The latter plot is marred by the fact most data entries do not specify copper in the +2 oxidation state.

TEM

TEM images were obtained using a JEOL JEM-1011 microscope operating at 80 keV. TEM samples were prepared by drop-casting NC solutions onto copper TEM grids. Segmentation of the nanoparticles (NPs) in the TEM images was performed using ImageDataExtractor by Yildirim and Cole.[350] For the segmentation, uncertainty threshold was kept at 0.0125, and 50 Monte Carlo samples for Bayesian inference were used. The output projected NPs areas were then converted in the equivalent diameter of the sphere projecting the same area. The resulting distribution was fitted using a lognormal distribution.

XAS

XAS spectra were acquired at the Cl, Cu and Sb K-edges and at the Sb L_3-edge. The Cl K-edge and Sb L_3-edge were acquired in HERFD-XANES mode at the ID26 beamline of ESRF, using the TEXS tender emission spectrometer, by collecting the KL_3 (Cl K-edge), and L_3M_5 (Sb L_3-edge) emission lines, in high-energy resolution fluorescence detection mode. The Sb K-edge was acquired in transmission mode at 80 K at the SAMBA beamline of Synchrotron SOLEIL. The Cu K-edge spectra of the suspensions were acquired at room temperature in fluorescence mode at the BM23 beamline of ESRF. For the Cl K-edge and Sb L_3-edge, the dry sample was pressed with boron nitride and cooled at 12 K to minimize radiation damage. For the Sb K-edge, the dry sample was pressed with boron nitride and cooled at 80 K.

EXAFS

The EXAFS analysis was performed using theoretical Cu−Cl scattering paths from the Cs_2CuCl_4 cluster. The parameters obtained are shown in the following table.

Table A 6.3. Local structure parameters determined from X-ray absorption spectroscopy (EXAFS). N, R and σ^2 are coordination number, interatomic distance and Debye-Waller factor, respectively. Fittings were performed in R space from about 0.5 to 2.9 Å. Estimated uncertainty is reported in parentheses.

Sample	N	R (Å)	σ^2 (Å^2)	R-factor (%)
Cs_2CuCl_4	4	2.250(5)	0.008(1)	18.55
$Cs_3Sb_2Cl_9$:Cu	3	2.289(5)	0.007(1)	12.84

XANES simulations

The XANES spectra of $CuCl_n$ isolated clusters (**Figure 6.7a-b**) were simulated with the FDM approach, with a R_{max} of 4 Å, fixing the vacuum potential parameter V_{max} at -6.0 eV to account for the potential outside the cluster. For the trigonal pyramid clusters $CuCl_3$ (with α = 102°), different values of the screening parameter were subsequently employed to estimate the partial screening of the core-hole charge. The creation of a core-hole on the absorbing atom induces a strong perturbation in the local electronic potential. However, this core-hole does not act as a fully +1 charge for the photoelectron, since other electrons and neighboring atoms partially screen its effect. The effect of the screening parameter on the simulations is shown in **Figure 6.7c**. An intermediate screening value of 0.5 provided the best agreement with experimental XANES spectra for the trigonal pyramidal cluster $CuCl_3$. This is consistent with a situation where partial screening arises from electron density of the surrounding Cl^- ligands. The XANES spectra of the extended solids were simulated with periodic boundary conditions using the *Green* function approach with muffin tin potentials, where the SCF function and the R_{max} parameter were increased until convergence, achieved around 8-9 Å.

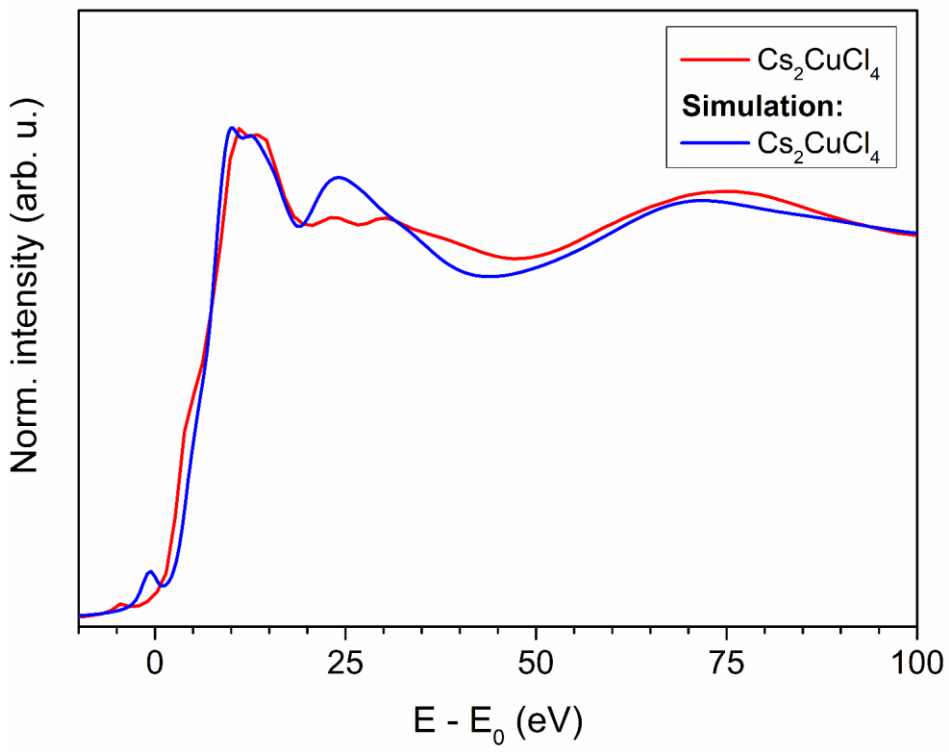

Figure A 6.11. XANES spectra for the Cu K-edge of experimental Cs_2CuCl_4 compared with the XANES simulation of Cs_2CuCl_4.

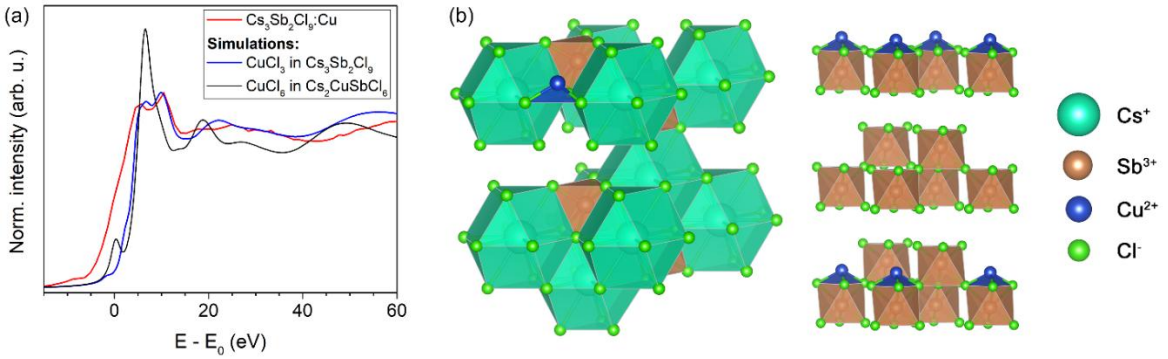

Figure A 6.12. (a) XANES simulations of trigonal pyramidal $CuCl_3$ in $Cs_3Sb_2Cl_9$ and octahedral $CuCl_6$ in $Cs_2CuSbCl_6$. (b) Possible location of a trigonal pyramidal $[CuCl_3]^-$ center, located within the antimony layer of the $Cs_3Sb_2Cl_9$ lattice.

Computational Methods

DFT calculations were carried out using the Quantum ESPRESSO software package,[330–332] employing the PAW method[351] and the PBE exchange-correlation functional within the GGA.[352] The structural optimizations were performed with convergence criteria set to reduce the forces on individual atoms below 0.001 Ry/a_0, where a_0 denotes the Bohr radius and Ry the Rydberg constant. The Brillouin zone was sampled using a G-centered Monkhorst-Pack grid chosen to achieve a k-point spacing of approximately 0.15 $Å^{-1}$. Band structures were calculated using QE with the PBE functional. Based on the fully optimized structures, quasiparticle corrections were subsequently obtained within the GW approximation using the Yambo code.[333,353] Scalar-relativistic PAW pseudopotentials from the PSLibrary were employed in combination with the PBE exchange-correlation functional.[354] The kinetic energy cutoff for the wavefunctions was set to 100 Ry, while the charge density cutoff was set as 400 Ry. These cutoff parameters were tested for convergence individually for each structure. The SCF calculations were performed with a convergence threshold of 1.0×10^{-6} Ry.

Decomposition Enthalpy

The PBE functional, because of its favorable balance between accuracy and computational cost, is widely adopted for evaluating thermodynamic stability.[99,318] In this thesis, total energies (E_T) of Ag- and Cu-based HDPs were calculated using PBE, and their

decomposition enthalpies (ΔH) were determined as the energy difference between the HDP and its most probable decomposition products:

$$\Delta H = E_T[products] - E_T[HDP]$$

Negative values of ΔH indicate thermodynamic instability with respect to decomposition, whereas positive values suggest inherent stability. The magnitude of ΔH reflects the degree of stability or instability, with large negative values indicating high decomposition propensity and large positive values indicating robust thermodynamic stability. Given the multicationic nature of HDPs, decomposition pathways involving binary and ternary phases were considered for a comprehensive stability assessment.

An analysis of decomposition enthalpies for $Cs_2AgSbCl_6$ is presented in **Figure 6.12**. Ag-based perovskites exhibit positive enthalpies with respect to decomposition into binary or ternary products, consistent with significant thermodynamic stability. The ternary compounds analyzed were $Cs_3Sb_2Cl_9$ (*P–3m1*), $CsAgCl_2$ (*P4/nmm1*), and Cs_2AgCl_3 (*Pnma*), along with the binary compounds CsCl, $SbCl_3$, and AgCl. Conversely, Cu-based perovskites were analyzed in relation to the ternary compounds $Cs_3Sb_2Cl_9$ (*P–3m1*), $CsCu_2Cl_3$ (*Cmcm*), $Cs_3Cu_2Cl_3$ (*Pnma*) and binary CsCl, CuCl, $SbCl_3$. Most of the decomposition pathways exhibit negative ΔH values, particularly toward $Cs_3Sb_2Cl_9$, indicating a stronger thermodynamic driving force for decomposition (see **Figure 6.11a**).

Electronic Structure Calculations

The electronic band structure and projected density of states were computed using the PBE functional, which, despite its well-known underestimation of band gaps, reliably describes band dispersion and electronic states. To obtain more accurate band gap estimates for pristine $Cs_2AgSbCl_6$, many-body perturbation theory within the GW approximation was applied, as implemented in the Yambo code.[333] In contrast, GW calculations failed to converge for all Cu-containing phases due to the presence of localized Cu *d* states, which induce strong electronic correlations and sharp variations in the quasiparticle self-energy.[355–357]

Figure 6.14 shows the GW and PBE band structures of $Cs_2AgSbCl_6$, along with the PBE band structures of $Cs_2CuSbCl_6$, $Cs_3Sb_2Cl_9$, and $Cs_3Sb_2Cl_9$:Cu (nominal composition $Cs_4CuSb_4Cl_{18}$). It is well established that GGA functionals (like PBE) underestimate the bandgap of all semiconductors and insulators significantly. We chose not to apply ad hoc corrections like hybrid functionals, as they necessarily add a certain arbitrariness in the

degree of Hartree-Fock exchange used. PBE, on the other hand, has proved reliable on structure and thermodynamics, and it is nonetheless useful to derive chemical trends even if bandgaps are not accurate. From the comparison of the band structure of $Cs_2AgSbCl_6$ at the PBE and GW levels of theory, it can be estimated that in these compounds, the bandgap is underestimated with PBE by about 0.8 eV.

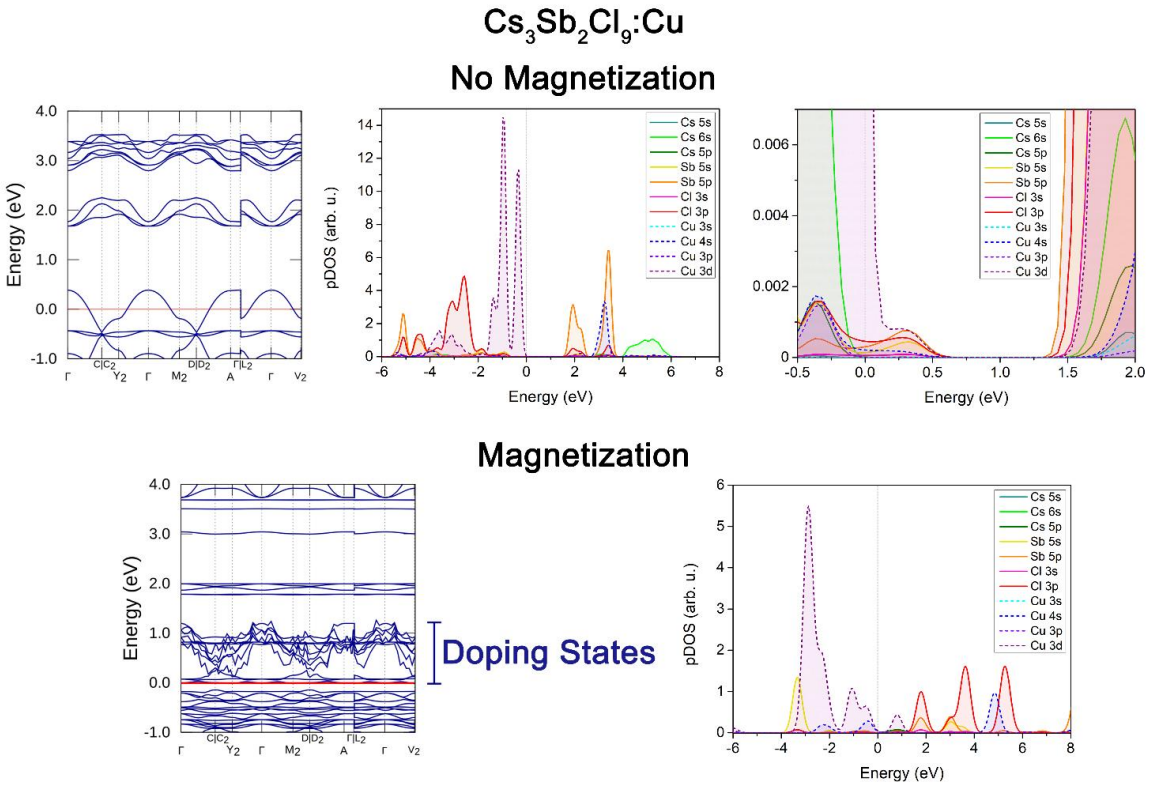

Figure A 6.13. Electronic band structures and pDOS of $Cs_3Sb_2Cl_9$:Cu ($Cs_4CuSb_4Cl_{18}$) at the PBE level without magnetization (above) and with magnetization (below) due to the unpaired electron at the Cu^{2+} site. The red line in the band structure represents the Fermi energy.

Assessment of the beam-induced radiation damage at ID26

For the X-ray absorption measurements carried out at ID26, considering the higher interaction cross-section at relatively low energies and the focused beam, an *ad hoc* procedure was followed to assess radiation damage: each sample was divided into a grid of around 400 spots, and several scans were carried out as needed to increase the statistics. Repeated 10-second spectra were acquired on each spot, averaging separately all the first spectra on each spot ("fresh") and all the subsequent spectra on each spot ("damaged"). It is

found that the variation between fresh and damaged spectra is negligible compared to the variation between different compounds.

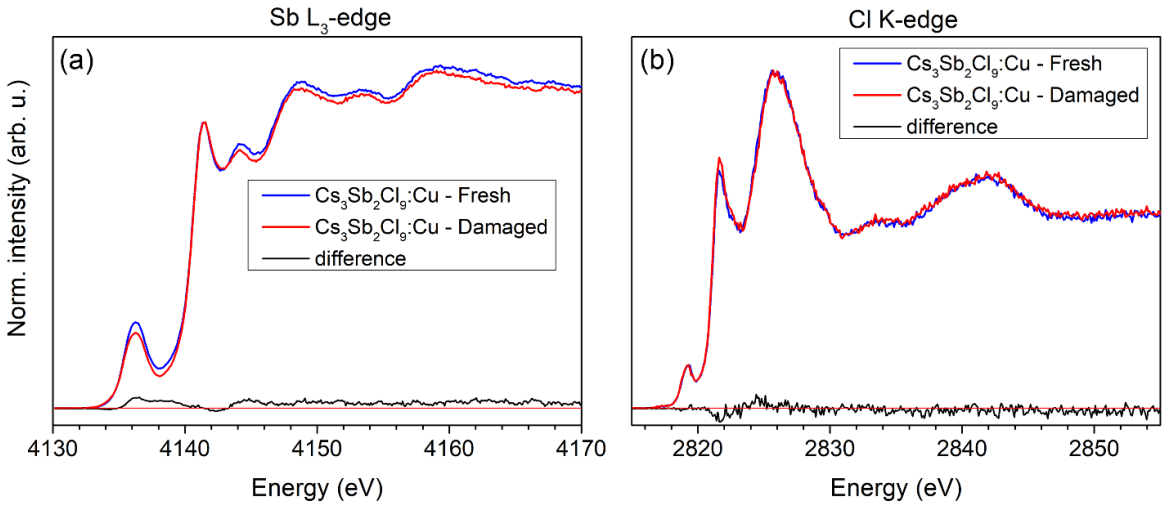

Figure A 6.14. HERFD-XANES spectra of $Cs_3Sb_2Cl_9$:Cu: fresh spots and previously exposed spots (blue and red, respectively) and their difference (black), for a) Sb L_3-edge and b) Cl K-edge.

7. Conclusions and Future Work

The main purpose of this work is the exploration and development of chemical strategies aimed at overcoming the intrinsic limitations of LHPs, i.e., the low stability of organic cations commonly used for OLHPs, and the toxicity of lead. After design, synthesis and laboratory characterization, all the materials studied, either as powders or nanocrystals, were investigated using synchrotron-based techniques, with a particular focus on XAS, which represents an ideal complement to diffraction methods and enables detailed knowledge of the local structure around each element.

The first line of investigation involved a substitution of the organic amines with TMSO, in order to improve the stability of lead-based perovskites. The substitution of the organic cation imparts enhanced stability to the resulting $TMSOPbI_3$ 1D perovskite under ambient conditions for at least one month, overcoming the typical stability limitations associated with MA and FA. Subsequently, doping of the B-site with Bi^{3+} was also investigated, with the formation of $(TMSO)_3Pb_{3x}Bi_{2(1-x)}I_9$ solid solutions, which promotes the formation of point defects that preferentially cluster in Bi−(V)−Bi arrangements along the linear metal halide chains. However, the reduced connectivity of octahedrons in one dimension hinders their applicability in photovoltaics. Nevertheless, by combining XAS experiments and simulations, using these 1D perovskite Pb/Bi solid solutions as model compounds, we demonstrated that XANES spectra of different absorption edges are highly sensitive to subtle structural features of the local metal-halogen coordination geometry, while remaining largely unaffected by long-range multiple-scattering effects that typically dominate the near-edge region. Extending this approach in the future to other halide perovskites should enable direct structural correlations, providing a valuable complement to other techniques.

Afterwards, different strategies were pursued in parallel to replace lead with non-toxic metals. The substitution was first done using Sn(II) in the $(TMSO)_3Pb_{3x}Bi_{2(1-x)}I_9$ series. Although chemically similar to lead, tin presents the challenge of easy oxidation from Sn^{2+} to Sn^{4+}, one of the main limitations of tin-based perovskites. Through XAS analysis we

demonstrated that doping the B site with bismuth progressively reduces tin oxidation, ultimately suppressing it almost entirely, thus enabling the development of more stable and potentially higher-performing materials. Subsequently, the resulting $(TMSO)_3Sn_{3x}Bi_{2(1-x)}I_9$ perovskites were tested for potential use as strain sensors. When Bi^{3+} is present in large concentrations, the piezoresistive response is very good, achieving excellent results for the Bi75 composition. This study shows a first step towards the tailored design of a lead-free halide perovskite to prepare bending sensors requiring sensitivity to small and high bending angles, which can find applications for wearable electronics and soft robotics.

The second substitution strategy was carried out through a heterovalent approach, substituting divalent lead with monovalent (Ag^+, Na^+, and K^+) and trivalent (Bi^{3+} and In^{3+}) cations to double perovskite nanocrystals. These exhibit very good chemical stability, and have highly tunable optoelectronic properties through doping and alloying. Using different combinations of cations in the B^+ and B^{3+} sites, HDPs with different bandgaps were obtained, demonstrating how even a simple ion substitution can cause significant variations in the properties of these materials. In particular, $Cs_2AgBiCl_6$ displays an indirect bandgap, while $Cs_2(Na,K)BiCl_6$ show a direct bandgap. $Cs_2(In,Na,K)InCl_6$, on the other hand, exhibit a direct bandgap with a parity-forbidden transitions. The switch from a transition metal to an alkali metal therefore involves a drastic change. Similarly, replacing Bi^{3+} with In^{3+} causes a substantial change in VBM and CBM, with the same monovalent cation. In the last line of investigation, Cu^+ and Sb^{3+} were used in an attempt to synthesize the double perovskite $Cs_2CuSbCl_6$, to explain its very peculiar optical absorption spectrum reported in the literature. However, with a combination of XRD, XANES, EXAFS, and optical spectroscopy, we demonstrated that the XRD trace of Cu-doped $Cs_3Sb_2Cl_9$ NCs was incorrectly attributed to $Cs_2CuSbCl_6$, confirming DFT predictions of limited stability for the HDP. Therefore we have proposed an overall structure bringing together the evidence from long-range and short-range X-ray techniques, in which Cu^{2+} in trigonal pyramidal coordination sits off-centered in empty Cs^+ sites and we demonstrated that the peculiar broad optical absorption in the visible range, previously attributed to a low bandgap of the double perovskite, is rather due to isolated LMCT and d-d transitions at the Cu^{2+} site in $Cs_3Sb_2Cl_9$, a wide bandgap semiconductor.

This work demonstrates that conventional characterization techniques can often be insufficient for the advanced study of complex materials, both from a structural and an electronic point of view. A detailed understanding of crystal structure, the presence of defects and distortions, as well as substitution mechanisms and their impact on structure, is crucial

to clarifying how structural variations are reflected in optical and electrical properties and, consequently, to exploiting this knowledge in the development of more efficient and sustainable materials. In this context, characterization using advanced techniques such as XAS spectroscopy in general, and HERFD-XANES in particular, allows the structure to be investigated from a chemical and electronic point of view down to the atomic scale, providing, in combination with conventional techniques, a complete and detailed picture of the material. Unfortunately, these techniques are still rarely used in the field of HPs. This work therefore aims to promote their use, since in many cases they reveal important details that are fundamental to understanding the structure and would otherwise remain hidden, as demonstrated in Chapter 6. However, analyzing XAS data is not always straightforward or immediate, and often requires modelling of the acquired spectra in order to understand the spectral characteristics and transitions in detail.

The local structural analysis performed via HERFD-XANES on the K and Cl K-edges and on the Ag and In L_3-edges on the Bi- and In-based HDP NCs brought to light several aspects that still require further investigation. While some spectral features are clear and in good agreement with other results, others remain not completely understood or, in some cases, in disagreement with the long-range structure. In particular, the Cl K-edge revealed important chemical and electronic information, such as greater covalency of the Bi–Cl bond in the presence of alkali metals compared to the presence of Ag^+. However, the systematic variations in the main peak observed between the different compositions still require a coherent explanation. The Ag L_3-edge confirmed the octahedral coordination of the monovalent cation in both compositions analyzed, $Cs_2AgBiCl_6$ and $Cs_2AgInCl_6$. However, the spectra show significant differences due to the substitution of the trivalent metal, which induces both chemical and electronic variations, such as changes in the covalency of the Ag–Cl bond and the orbital hybridization, as well as structural variations, influencing the distortion of the $AgCl_6$ octahedra. A detailed analysis of Cs_2KBiCl_6 and Cs_2KInCl_6, which show conflicting evidence between the long-range and short-range structures, will be of particular interest. While XRD analysis shows cubic symmetry for Cs_2KBiCl_6, HERFD-XANES analysis on the K K-edge reveals a strongly distorted coordination shell instead, compared to the typical octahedral coordination expected. Conversely, in Cs_2KInCl_6, which exhibits a tetragonal structure, with potassium displaying pentagonal bipyramidal coordination, HERFD-XANES data instead suggest a regular octahedral coordination for potassium. These contradictions are particularly interesting because they could highlight

how distortions can exist within a material that cannot be detected using long-range structural techniques, but which are crucial to fully understanding its properties.

In order to explain the spectral features, assign them to the different transitions, and understand the changes observed from one sample to another, given the limited literature available on these absorption edges, more comprehensive simulations are in order. Furthermore, it will be interesting to extend combined HERFD-XANES and Total Scattering experiments on compositions containing potassium at different temperatures, to investigate in depth the local and long-range structure and its variations. HPs often exhibit phase transitions, as demonstrated for Cs_2KInCl_6, which is cubic at 400 K. For Cs_2KInCl_6, further experiments could clarify whether octahedral coordination is maintained at both low and high temperatures. If it remains unchanged at high temperatures, this would confirm the Rietveld analysis at 400 K. On the other hand, if the octahedral coordination were not maintained at low temperatures, this would suggest that the measurement at room temperature induced a phase transition from tetragonal to cubic, possibly caused by the beam. This would pave the way for further experiments to accurately determine the temperature at which the phase transition occurs.

By combining *ab initio* simulations with new data acquired through HERFD-XANES, together with established characterization techniques, it will be possible to obtain detailed information on both the local and long-range structure of these materials, providing an accurate and comprehensive picture of their structural and optoelectronic properties.

8. Acknowledgments

I gratefully acknowledge:

- The European Synchrotron Radiation Facility for provision of beamtime, travel support, and access to the computing cluster;
- ELETTRA Sincrotrone Trieste, Synchrotron SOLEIL for provision of beamtime;
- The ATeN Center (University of Palermo) for accesso to SEM and AFM facilities;
- The Italian Ministry of University and Research (MUR) for financial support under grant PRIN2022 ‘‘Novel SUstainable double PER ovskites: multiscale characterization from the atomic structure to functional properties (SU-PER)’’;
- The ISCRA program for provision of parallel computing resources on the Leonardo supercomputer, owned by the EuroHPC Joint Undertaking and hosted by CINECA (Italy).

I would like to thank the following:

- B. Detlefs (ESRF), for outstanding support before, during and after several HERFD-XANES measurements;
- A. Puri (ESRF), J. Orsilli (ESRF), E. Fonda (Soleil) for technical support during the XAS measurements;
- All group members of Chair for Photonics and Optoelectronics led by Prof. J. Feldmann at Ludwig-Maximilians-Universitat (LMU), and especially Q. Akkerman, for they hospitality and support during my stay in Munich;
- The Rädler Chair (LMU) for providing access to the electron microscope and Prof. E. Cortes (LMU) for access to the Vis-NIR spectrometer;
- The group of Prof. F. Bertolotti, at the University of Insubria (Como, Italy) and N. Dengo, for the synthesis of $Cs_2(Ag,Na,K)InCl_6$ NCs, XRD and UV-vis measurements and Rietveld refinements of $Cs_2(Ag,Na,K)InCl_6$ and Cu-containing NCs;
- Finally, my supervisors for their support during this long project.

9. References

1 Y. Liu, W. Wang, J. Yang and S. Li, *Adv. Sustain. Syst.*, 2018, **2**, 1800046.

2 O. H. Ando Junior, A. L. O. Maran and N. C. Henao, *Renew. Sustain. Energy Rev.*, 2018, **91**, 376–393.

3 Y. Zhan, Q. Cheng, Y. Song and M. Li, *Adv. Funct. Mater.*, 2022, **32**, 2200385.

4 G. van T. Amelinckx, D. van Dyck, J. van Landuyt, in *Handbook of Microscopy Set*, 1996, pp. 145–205.

5 G. van T. Amelinckx, D. van Dyck, J. van Landuyt, in *Handbook of Microscopy Set*, 1996, pp. 207–233.

6 N.-G. Park, M. Grätzel, T. Miyasaka, K. Zhu and K. Emery, *Nat. Energy*, 2016, **1**, 16152.

7 A. Fakharuddin, M. K. Gangishetty, M. Abdi-Jalebi, S.-H. Chin, A. R. bin Mohd Yusoff, D. N. Congreve, W. Tress, F. Deschler, M. Vasilopoulou and H. J. Bolink, *Nat. Electron.*, 2022, **5**, 203–216.

8 V. Kumar, A. Kathiravan and M. A. Jhonsi, *Nano Energy*, 2024, **125**, 109523.

9 Q. A. Akkerman, G. Rainò, M. V Kovalenko and L. Manna, *Nat. Mater.*, 2018, **17**, 394–405.

10 S. Toso, D. Baranov and L. Manna, *Acc. Chem. Res.*, 2021, **54**, 498–508.

11 Y. Wang, Y. Wang, T. A. S. Doherty, S. D. Stranks, F. Gao and D. Yang, *Nat. Rev. Chem.*, 2025, **9**, 261–277.

12 H. Huang, M. I. Bodnarchuk, S. V Kershaw, M. V Kovalenko and A. L. Rogach, *ACS Energy Lett.*, 2017, **2**, 2071–2083.

13 Q. Zhang and Y. Yin, *ACS Cent. Sci.*, 2018, **4**, 668–679.

14 J. Shamsi, A. S. Urban, M. Imran, L. De Trizio and L. Manna, *Chem. Rev.*, 2019, **119**, 3296–3348.

References

15 S. P. Senanayak, B. Yang, T. H. Thomas, N. Giesbrecht, W. Huang, E. Gann, B. Nair, K. Goedel, S. Guha, X. Moya, C. R. McNeill, P. Docampo, A. Sadhanala, R. H. Friend and H. Sirringhaus, *Sci. Adv.*, 2025, **3**, e1601935.

16 G. Xing, N. Mathews, S. Sun, S. S. Lim, Y. M. Lam, M. Grätzel, S. Mhaisalkar and T. C. Sum, *Science*, 2013, **342**, 344–347.

17 Q. Dong, Y. Fang, Y. Shao, P. Mulligan, J. Qiu, L. Cao and J. Huang, *Science*, 2015, **347**, 967–970.

18 B. Saparov and D. B. Mitzi, *Chem. Rev.*, 2016, **116**, 4558–4596.

19 G. E. Eperon, G. M. Paternò, R. J. Sutton, A. Zampetti, A. A. Haghighirad, F. Cacialli and H. J. Snaith, *J. Mater. Chem. A*, 2015, **3**, 19688–19695.

20 Y. Zhao and K. Zhu, *Chem. Soc. Rev.*, 2016, **45**, 655–689.

21 Q. Xue, R. Xia, C. J. Brabec and H.-L. Yip, *Energy Environ. Sci.*, 2018, **11**, 1688–1709.

22 A. Roy, A. Ghosh, S. Bhandari, S. Sundaram and T. K. Mallick, *Buildings*, 2020, 10, 129.

23 L. Protesescu, S. Yakunin, S. Kumar, J. Bär, F. Bertolotti, N. Masciocchi, A. Guagliardi, M. Grotevent, I. Shorubalko, M. I. Bodnarchuk, C.-J. Shih and M. V Kovalenko, *ACS Nano*, 2017, **11**, 3119–3134.

24 F. Yan, S. T. Tan, X. Li and H. V. Demir, *Small*, 2019, **15**, 1902079.

25 Y. Fu, H. Zhu, A. W. Schrader, D. Liang, Q. Ding, P. Joshi, L. Hwang, X.-Y. Zhu and S. Jin, *Nano Lett.*, 2016, **16**, 1000–1008.

26 Y.-L. Tong, Y.-W. Zhang, K. Ma, R. Cheng, F. Wang and S. Chen, *ACS Appl. Mater. Interfaces*, 2018, **10**, 31603–31609.

27 Y. Gao, C. Huang, C. Hao, S. Sun, L. Zhang, C. Zhang, Z. Duan, K. Wang, Z. Jin, N. Zhang, A. V Kildishev, C.-W. Qiu, Q. Song and S. Xiao, *ACS Nano*, 2018, **12**, 8847–8854.

28 L. Dou, Y. (Micheal) Yang, J. You, Z. Hong, W.-H. Chang, G. Li and Y. Yang, *Nat. Commun.*, 2014, **5**, 5404.

29 S. Tsarev, D. Proniakova, X. Liu, E. Wu, G. J. Matt, K. Sakhatskyi, L. L. A.

Ferraresi, R. Kothandaraman, F. Fu, I. Shorubalko, S. Yakunin and M. V Kovalenko, *Nature*, 2025, **642**, 592–598.

30 K. Sakhatskyi, A. Bhardwaj, G. J. Matt, S. Yakunin and M. V Kovalenko, *Adv. Mater.*, 2025, **37**, 2418465.

31 H. Wei, Y. Fang, P. Mulligan, W. Chuirazzi, H.-H. Fang, C. Wang, B. R. Ecker, Y. Gao, M. A. Loi, L. Cao and J. Huang, *Nat. Photonics*, 2016, **10**, 333–339.

32 M. Wu, N. Haji Ladi, Z. Yi, H. Li, Y. Shen and M. Wang, *Energy Technol.*, 2020, **8**, 1900744.

33 Y. Nakamura, N. Shibayama, K. Fujiwara, T. Koganezawa and T. Miyasaka, *ACS Mater. Lett.*, 2022, **4**, 2409–2414.

34 A. Senocrate, T. Acartürk, G. Y. Kim, R. Merkle, U. Starke, M. Grätzel and J. Maier, *J. Mater. Chem. A*, 2018, **6**, 10847–10855.

35 N. Aristidou, I. Sanchez-Molina, T. Chotchuangchutchaval, M. Brown, L. Martinez, T. Rath and S. A. Haque, *Angew. Chemie Int. Ed.*, 2015, **54**, 8208–8212.

36 W. Zhou, P. Han, X. Zhang, D. Zheng, S. Yang, Y. Yang, C. Luo, B. Yang, F. Hong, D. Wei, R. Lu and K. Han, *J. Phys. Chem. Lett.*, 2020, **11**, 6463–6467.

37 C. Pipitone, S. Carlotto, M. Casarin, A. Longo, A. Martorana and F. Giannici, *J. Mater. Chem. C*, 2022, **10**, 1458–1469.

38 D. Phuyal, M. Safdari, M. Pazoki, P. Liu, B. Philippe, K. O. Kvashnina, O. Karis, S. M. Butorin, H. Rensmo, T. Edvinsson, L. Kloo and J. M. Gardner, *Chem. Mater.*, 2018, **30**, 4959–4967.

39 M. Safdari, D. Phuyal, B. Philippe, P. H. Svensson, S. M. Butorin, K. O. Kvashnina, H. Rensmo, L. Kloo and J. M. Gardner, *J. Mater. Chem. A*, 2017, **5**, 11730–11738.

40 D. Phuyal, S. M. Jain, B. Philippe, M. B. Johansson, M. Pazoki, J. Kullgren, K. O. Kvashnina, M. Klintenberg, E. M. J. Johansson, S. M. Butorin, O. Karis and H. Rensmo, *J. Mater. Chem. A*, 2018, **6**, 9498–9505.

41 M. A. Smith, M. Chen, Z. Dai, C. Antolini, G. K. Jayasekara, S. K. Yadavalli, B. J. Reinhart, N. P. Padture and D. Hayes, *ACS Appl. Energy Mater.*, 2021, **4**, 4327–4332.

42 C. Vorwerk, C. Hartmann, C. Cocchi, G. Sadoughi, S. N. Habisreutinger, R. Félix, R. G. Wilks, H. J. Snaith, M. Bär and C. Draxl, *J. Phys. Chem. Lett.*, 2018, **9**, 1852–1858.

43 W. S. Drisdell, L. Leppert, C. M. Sutter-Fella, Y. Liang, Y. Li, Q. P. Ngo, L. F. Wan, S. Gul, T. Kroll, D. Sokaras, A. Javey, J. Yano, J. B. Neaton, F. M. Toma, D. Prendergast and I. D. Sharp, *ACS Energy Lett.*, 2017, **2**, 1183–1189.

44 A. Babaei and A. Nasr Esfahani, *Electricity*, 2024, 5, 734–750.

45 H.-L. Daniela-Abigail, M. I. Vega-De-Lille, J. C. Sacramento-Rivero, C. Ponce-Caballero, A. El-Mekaoui and F. Navarro-Pineda, *Renew. Energy Focus*, 2024, **51**, 100649.

46 F. Roccaforte and M. Leszczynski, *Nitride Semiconductor Technology: Power Electronics and Optoelectronic Devices*, Wiley-VCH, 2020.

47 E. F. Schubert, in *Wiley Encyclopedia of Electrical and Electronics Engineering*, 2014, pp. 1–10.

48 George Domingo, *Semiconductor Basics: A Qualitative, Non-mathematical Explanation of How Semiconductors Work and How They are Used*, Wiley, 2020.

49 C. Gayner and K. K. Kar, *Prog. Mater. Sci.*, 2016, **83**, 330–382.

50 Y. Liu, W. Wang, J. Yang and S. Li, *Adv. Sustain. Syst.*, 2018, **2**, 1–15.

51 A. K. Jena, A. Kulkarni and T. Miyasaka, *Chem. Rev.*, 2019, **119**, 3036–3103.

52 W. Xiang, S. (Frank) Liu and W. Tress, *Energy Environ. Sci.*, 2021, **14**, 2090–2113.

53 D. Nodari, Z. Qiao, F. Furlan, O. J. Sandberg, K. Vandewal and N. Gasparini, *Nat. Rev. Mater.*, 2025, **10**, 842–856.

54 Y. He, L. Matei, H. J. Jung, K. M. McCall, M. Chen, C. C. Stoumpos, Z. Liu, J. A. Peters, D. Y. Chung, B. W. Wessels, M. R. Wasielewski, V. P. Dravid, A. Burger and M. G. Kanatzidis, *Nat. Commun.*, 2018, **9**, 1609.

55 L. Protesescu, S. Yakunin, M. I. Bodnarchuk, F. Krieg, R. Caputo, C. H. Hendon, R. X. Yang, A. Walsh and M. V Kovalenko, *Nano Lett.*, 2015, **15**, 3692–3696.

56 T. Qiao and D. H. Son, *Acc. Chem. Res.*, 2021, **54**, 1399–1408.

57 G. Rainò, N. Yazdani, S. C. Boehme, M. Kober-Czerny, C. Zhu, F. Krieg, M. D.

Rossell, R. Erni, V. Wood, I. Infante and M. V Kovalenko, *Nat. Commun.*, 2022, **13**, 2587.

58 A. Dey, J. Ye, A. De, E. Debroye, S. K. Ha, E. Bladt, A. S. Kshirsagar, Z. Wang, J. Yin, Y. Wang, L. N. Quan, F. Yan, M. Gao, X. Li, J. Shamsi, T. Debnath, M. Cao, M. A. Scheel, S. Kumar, J. A. Steele, M. Gerhard, L. Chouhan, K. Xu, X. Wu, Y. Li, Y. Zhang, A. Dutta, C. Han, I. Vincon, A. L. Rogach, A. Nag, A. Samanta, B. A. Korgel, C.-J. Shih, D. R. Gamelin, D. H. Son, H. Zeng, H. Zhong, H. Sun, H. V. Demir, I. G. Scheblykin, I. Mora-Seró, J. K. Stolarczyk, J. Z. Zhang, J. Feldmann, J. Hofkens, J. M. Luther, J. Pérez-Prieto, L. Li, L. Manna, M. I. Bodnarchuk, M. V Kovalenko, M. B. J. Roeffaers, N. Pradhan, O. F. Mohammed, O. M. Bakr, P. Yang, P. Müller-Buschbaum, P. V Kamat, Q. Bao, Q. Zhang, R. Krahne, R. E. Galian, S. D. Stranks, S. Bals, V. Biju, W. A. Tisdale, Y. Yan, R. L. Z. Hoye and L. Polavarapu, *ACS Nano*, 2021, **15**, 10775–10981.

59 F. Montanarella and M. V Kovalenko, *ACS Nano*, 2022, **16**, 5085–5102.

60 P. Palomaki, *IEEE Spectr.*, 2022, **59**, 52–53.

61 K. Bourzac, *Nature*, 2013, **493**, 283.

62 P. Patel, *IEEE Spectr.*, 2012, **49**, 14–17.

63 J.-K. Chen, Q. Zhao, N. Shirahata, J. Yin, O. M. Bakr, O. F. Mohammed and H.-T. Sun, *ACS Mater. Lett.*, 2021, **3**, 845–861.

64 L. De Trizio, I. Infante and L. Manna, *Acc. Chem. Res.*, 2023, **56**, 1815–1825.

65 T. Wu, C.-W. Sher, Y. Lin, C.-F. Lee, S. Liang, Y. Lu, S.-W. Huang Chen, W. Guo, H.-C. Kuo and Z. Chen, *Appl. Sci.*, 2018, 8, 1557.

66 S. W. Eaton, M. Lai, N. A. Gibson, A. B. Wong, L. Dou, J. Ma, L.-W. Wang, S. R. Leone and P. Yang, *Proc. Natl. Acad. Sci.*, 2016, **113**, 1993–1998.

67 H. Zhu, Y. Fu, F. Meng, X. Wu, Z. Gong, Q. Ding, M. V Gustafsson, M. T. Trinh, S. Jin and X.-Y. Zhu, *Nat. Mater.*, 2015, **14**, 636–642.

68 B. Tang, G. Li, X. Ru, Y. Gao, Z. Li, H. Shen, H. Yao, F. Fan and J. Du, *Nano Lett.*, 2022, **22**, 658–664.

69 V. M. Goldschmidt, *Naturwissenschaften*, 1926, **14**, 477–485.

References

70 D. Weber, *J. Chem. Sci.*, 1978, **33**, 862–865.

71 H. Wells, *Zeitschrift für Anorg. Chemie*, 2004, **3**, 195–210.

72 D. Weber, *J. Chem. Sci.*, 1978, **33**, 1443–1445.

73 C. Moure and O. Peña, *Prog. Solid State Chem.*, 2015, **43**, 123–148.

74 C. Li, X. Lu, W. Ding, L. Feng, Y. Gao and Z. Guo, *Acta Crystallogr. Sect. B*, 2008, **64**, 702–707.

75 W. Travis, E. N. K. Glover, H. Bronstein, D. O. Scanlon and R. G. Palgrave, *Chem. Sci.*, 2016, **7**, 4548–4556.

76 K. Tanaka, T. Takahashi, T. Ban, T. Kondo, K. Uchida and N. Miura, *Solid State Commun.*, 2003, **127**, 619–623.

77 J. Even, L. Pedesseau, J.-M. Jancu and C. Katan, *J. Phys. Chem. Lett.*, 2013, **4**, 2999–3005.

78 H. Jin, J. Im and A. J. Freeman, *Phys. Rev. B*, 2012, **86**, 121102.

79 Z. Xiao, Z. Song and Y. Yan, *Adv. Mater.*, 2019, **31**, 1–22.

80 Edward D Palik, *Handbook of optical constants of solids*, San Diego : Academic Press, 1998.

81 M. A. Green, E. D. Dunlop, M. Yoshita, N. Kopidakis, K. Bothe, G. Siefer, X. Hao and J. Y. Jiang, *Prog. Photovoltaics Res. Appl.*, 2018, **26**, 427.

82 Y. Zhao, W. Zhou, Z. Han, D. Yu and Q. Zhao, *Phys. Chem. Chem. Phys.*, 2021, **23**, 94–106.

83 J. Ibaceta-Jaña, M. Chugh, A. S. Novikov, H. Mirhosseini, T. D. Kühne, B. Szyszka, M. R. Wagner and R. Muydinov, *J. Phys. Chem. C*, 2022, **126**, 16215–16226.

84 K. L. Svane, A. C. Forse, C. P. Grey, G. Kieslich, A. K. Cheetham, A. Walsh and K. T. Butler, *J. Phys. Chem. Lett.*, 2017, **8**, 6154–6159.

85 A. Garrote-Márquez, L. Lodeiro, R. Suresh, N. Cruz Hernández, R. Grau-Crespo and E. Menéndez-Proupin, *J. Phys. Chem. C*, 2023, **127**, 15901–15910.

86 A. Garrote-Márquez, L. Lodeiro, N. C. Hernández, X. Liang, A. Walsh and E. Menéndez-Proupin, *J. Phys. Chem. C*, 2024, **128**, 20947–20956.

87 X. Guo and C. Burda, *Coord. Chem. Rev.*, 2016, **320**–**321**, 53–65.

88 Y. Wang, T. Gould, J. F. Dobson, H. Zhang, H. Yang, X. Yao and H. Zhao, *Phys. Chem. Chem. Phys.*, 2014, **16**, 1424–1429.

89 H.-S. Kim, C.-R. Lee, J.-H. Im, K.-B. Lee, T. Moehl, A. Marchioro, S.-J. Moon, R. Humphry-Baker, J.-H. Yum, J. E. Moser, M. Grätzel and N.-G. Park, *Sci. Rep.*, 2012, **2**, 591.

90 T. Baikie, Y. Fang, J. M. Kadro, M. Schreyer, F. Wei, S. G. Mhaisalkar, M. Graetzel and T. J. White, *J. Mater. Chem. A*, 2013, **1**, 5628–5641.

91 C. Motta, F. El-Mellouhi, S. Kais, N. Tabet, F. Alharbi and S. Sanvito, *Nat. Commun.*, 2015, **6**, 7026.

92 F. Hao, C. C. Stoumpos, R. P. H. Chang and M. G. Kanatzidis, *J. Am. Chem. Soc.*, 2014, **136**, 8094–8099.

93 K. T. Butler, J. M. Frost and A. Walsh, *Mater. Horizons*, 2015, **2**, 228–231.

94 J. Hu, L. Yang and J. Zhang, *Sol. RRL*, 2023, **7**, 2300187.

95 H. Chen, Y. Chen, T. Zhang, X. Liu, X. Wang and Y. Zhao, *Small Struct.*, 2021, **2**, 2000130.

96 H.-S. Kim and N.-G. Park, *Adv. Energy Mater.*, 2025, **15**, 2400089.

97 M. RaeisianAsl, S. F. K. S. Panahi, M. Jamaati and S. S. Tafreshi, *Int. J. Energy Res.*, 2022, **46**, 13117–13151.

98 T. M. Koh, K. Fu, Y. Fang, S. Chen, T. C. Sum, N. Mathews, S. G. Mhaisalkar, P. P. Boix and T. Baikie, *J. Phys. Chem. C*, 2014, **118**, 16458–16462.

99 D. F. Macias-Pinilla and F. Giannici, *ACS Appl. Mater. Interfaces*, 2025, **17**, 20501–20518.

100 C.-H. Chen, S.-N. Cheng, L. Cheng, Z.-K. Wang and L.-S. Liao, *Adv. Energy Mater.*, 2023, **13**, 2204144.

101 K. Hong, Q. Van Le, S. Y. Kim and H. W. Jang, *J. Mater. Chem. C*, 2018, **6**, 2189–2209.

102 Q. A. Akkerman and L. Manna, *ACS Energy Lett.*, 2020, **5**, 604–610.

103 P. Zhu and J. Zhu, *InfoMat*, 2020, **2**, 341–378.

104 C. C. Stoumpos, L. Mao, C. D. Malliakas and M. G. Kanatzidis, *Inorg. Chem.*, 2017, **56**, 56–73.

105 X. Li, H. Dong, G. Volonakis, C. C. Stoumpos, J. Even, C. Katan, P. Guo and M. G. Kanatzidis, *Chem. Mater.*, 2022, **34**, 6541–6552.

106 J.-W. Lee, S. Tan, S. Il Seok, Y. Yang and N.-G. Park, *Science*, 2025, **375**, eabj1186.

107 G. Wu, R. Liang, Z. Zhang, M. Ge, G. Xing and G. Sun, *Small*, 2021, **17**, 2103514.

108 Y. Han, S. Yue and B.-B. Cui, *Adv. Sci.*, 2021, **8**, 2004805.

109 B. Li, F. Xia, B. Du, S. Zhang, L. Xu, Q. Su, D. Zhang and J. Yang, *Adv. Sci.*, 2024, **11**, 2310263.

110 C. C. Stoumpos, D. H. Cao, D. J. Clark, J. Young, J. M. Rondinelli, J. I. Jang, J. T. Hupp and M. G. Kanatzidis, *Chem. Mater.*, 2016, **28**, 2852–2867.

111 L. Mao, W. Ke, L. Pedesseau, Y. Wu, C. Katan, J. Even, M. R. Wasielewski, C. C. Stoumpos and M. G. Kanatzidis, *J. Am. Chem. Soc.*, 2018, **140**, 3775–3783.

112 H. Lin, C. Zhou, Y. Tian, T. Siegrist and B. Ma, *ACS Energy Lett.*, 2018, **3**, 54–62.

113 C. Liang, H. Gu, Y. Xia, Z. Wang, X. Liu, J. Xia, S. Zuo, Y. Hu, X. Gao, W. Hui, L. Chao, T. Niu, M. Fang, H. Lu, H. Dong, H. Yu, S. Chen, X. Ran, L. Song, B. Li, J. Zhang, Y. Peng, G. Shao, J. Wang, Y. Chen, G. Xing and W. Huang, *Nat. Energy*, 2021, **6**, 38–45.

114 D. Duan, C. Ge, M. Z. Rahaman, C.-H. Lin, Y. Shi, H. Lin, H. Hu and T. Wu, *NPG Asia Mater.*, 2023, **15**, 8.

115 S. Driessen, S. Sarigul-Ozbek, C. M. Sutter-Fella and S. Tao, *J. Phys. Energy*, 2024, **6**, 42001.

116 Y. Zhang, J. Liu, Z. Wang, Y. Xue, Q. Ou, L. Polavarapu, J. Zheng, X. Qi and Q. Bao, *Chem. Commun.*, 2016, **52**, 13637–13655.

117 C. Ge, J.-F. Lu, M. Singh, A. Ng, W. Yu, H. Lin, S. Satapathi and H. Hu, *Sol. RRL*, 2022, **6**, 2100879.

118 M. Z. Rahaman, S. Ge, C.-H. Lin, Y. Cui and T. Wu, *Small Struct.*, 2021, **2**,

2000062.

119 L. Gao, I. Spanopoulos, W. Ke, S. Huang, I. Hadar, L. Chen, X. Li, G. Yang and M. G. Kanatzidis, *ACS Energy Lett.*, 2019, **4**, 1763–1769.

120 S. Sun, M. Lu, X. Gao, Z. Shi, X. Bai, W. W. Yu and Y. Zhang, *Adv. Sci.*, 2021, **8**, 2102689.

121 X. Gao, X. Zhang, W. Yin, H. Wang, Y. Hu, Q. Zhang, Z. Shi, V. L. Colvin, W. W. Yu and Y. Zhang, *Adv. Sci.*, 2019, **6**, 1900941.

122 C. Zhou, H. Lin, Y. Tian, Z. Yuan, R. Clark, B. Chen, L. J. van de Burgt, J. C. Wang, Y. Zhou, K. Hanson, Q. J. Meisner, J. Neu, T. Besara, T. Siegrist, E. Lambers, P. Djurovich and B. Ma, *Chem. Sci.*, 2018, **9**, 586–593.

123 J. Huang, H. Xiang, R. Ran, W. Zhou, W. Wang and Z. Shao, *Renew. Sustain. Energy Rev.*, 2024, **191**, 114187.

124 M. Pitaro, E. K. Tekelenburg, S. Shao and M. A. Loi, *Adv. Mater.*, 2022, **34**, 2105844.

125 C. C. Stoumpos, L. Frazer, D. J. Clark, Y. S. Kim, S. H. Rhim, A. J. Freeman, J. B. Ketterson, J. I. Jang and M. G. Kanatzidis, *J. Am. Chem. Soc.*, 2015, **137**, 6804–6819.

126 T. Krishnamoorthy, H. Ding, C. Yan, W. L. Leong, T. Baikie, Z. Zhang, M. Sherburne, S. Li, M. Asta, N. Mathews and S. G. Mhaisalkar, *J. Mater. Chem. A*, 2015, **3**, 23829–23832.

127 W.-F. Yang, F. Igbari, Y.-H. Lou, Z.-K. Wang and L.-S. Liao, *Adv. Energy Mater.*, 2020, **10**, 1902584.

128 I. Chung, B. Lee, J. He, R. P. H. Chang and M. G. Kanatzidis, *Nature*, 2012, **485**, 486–489.

129 K. Yamada, S. Funabiki, H. Horimoto, T. Matsui, T. Okuda and S. Ichiba, *Chem. Lett.*, 1991, **20**, 801–804.

130 W. Ke, C. C. Stoumpos and M. G. Kanatzidis, *Adv. Mater.*, 2019, **31**, 1803230.

131 Y. Takahashi, R. Obara, Z.-Z. Lin, Y. Takahashi, T. Naito, T. Inabe, S. Ishibashi and K. Terakura, *Dalt. Trans.*, 2011, **40**, 5563–5568.

132 G. Laurita, D. H. Fabini, C. C. Stoumpos, M. G. Kanatzidis and R. Seshadri, *Chem. Sci.*, 2017, **8**, 5628–5635.

133 C. C. Stoumpos, C. D. Malliakas and M. G. Kanatzidis, *Inorg. Chem.*, 2013, **52**, 9019–9038.

134 S. Kahmann, O. Nazarenko, S. Shao, O. Hordiichuk, M. Kepenekian, J. Even, M. V Kovalenko, G. R. Blake and M. A. Loi, *ACS Energy Lett.*, 2020, **5**, 2512–2519.

135 A. Filippetti, S. Kahmann, C. Caddeo, A. Mattoni, M. Saba, A. Bosin and M. A. Loi, *J. Mater. Chem. A*, 2021, **9**, 11812–11826.

136 H.-H. Fang, S. Adjokatse, S. Shao, J. Even and M. A. Loi, *Nat. Commun.*, 2018, **9**, 243.

137 T. Leijtens, R. Prasanna, A. Gold-Parker, M. F. Toney and M. D. McGehee, *ACS Energy Lett.*, 2017, **2**, 2159–2165.

138 Z. Xiao, W. Meng, J. Wang and Y. Yan, *ChemSusChem*, 2016, **9**, 2628–2633.

139 H. Tang, Y. Xu, X. Hu, Q. Hu, T. Chen, W. Jiang, L. Wang and W. Jiang, *Adv. Sci.*, 2021, **8**, 2004118.

140 C. J. Bartel, J. M. Clary, C. Sutton, D. Vigil-Fowler, B. R. Goldsmith, A. M. Holder and C. B. Musgrave, *J. Am. Chem. Soc.*, 2020, **142**, 5135–5145.

141 N. Elliott and L. Pauling, *J. Am. Chem. Soc.*, 1938, **60**, 1846–1851.

142 L. R. Moras, *J. Inorg. Nucl. Chem.*, 1974, **36**, 3876–3878.

143 G. Volonakis, A. A. Haghighirad, R. L. Milot, W. H. Sio, M. R. Filip, B. Wenger, M. B. Johnston, L. M. Herz, H. J. Snaith and F. Giustino, *J. Phys. Chem. Lett.*, 2017, **8**, 772–778.

144 M. Retuerto, T. Emge, J. Hadermann, P. W. Stephens, M. R. Li, Z. P. Yin, M. Croft, A. Ignatov, S. J. Zhang, Z. Yuan, C. Jin, J. W. Simonson, M. C. Aronson, A. Pan, D. N. Basov, G. Kotliar and M. Greenblatt, *Chem. Mater.*, 2013, **25**, 4071–4079.

145 T. T. Tran, J. R. Panella, J. R. Chamorro, J. R. Morey and T. M. McQueen, *Mater. Horizons*, 2017, **4**, 688–693.

146 E. T. McClure, M. R. Ball, W. Windl and P. M. Woodward, *Chem. Mater.*, 2016, **28**, 1348–1354.

147 A. H. Slavney, T. Hu, A. M. Lindenberg and H. I. Karunadasa, *J. Am. Chem. Soc.*, 2016, **138**, 2138–2141.

148 G. Meyer, *Prog. Solid State Chem.*, 1982, **14**, 141–219.

149 N. R. Wolf, B. A. Connor, A. H. Slavney and H. I. Karunadasa, *Angew. Chemie Int. Ed.*, 2021, **60**, 16264–16278.

150 A. E. Fedorovskiy, N. A. Drigo and M. K. Nazeeruddin, *Small Methods*, 2020, **4**, 1900426.

151 C. J. Bartel, C. Sutton, B. R. Goldsmith, R. Ouyang, C. B. Musgrave, L. M. Ghiringhelli and M. Scheffler, *Sci. Adv.*, 2026, **5**, eaav0693.

152 L. A. Muscarella and E. M. Hutter, *ACS Energy Lett.*, 2022, **7**, 2128–2135.

153 L. Chu, W. Ahmad, W. Liu, J. Yang, R. Zhang, Y. Sun, J. Yang and X. Li, *Nano-Micro Lett.*, 2019, **11**, 16.

154 F. Giustino and H. J. Snaith, *ACS Energy Lett.*, 2016, **1**, 1233–1240.

155 Z. Liu, J. Zito, M. Ghini, L. Goldoni, M. Prato, H. Bahmani Jalali, I. Infante, L. De Trizio and L. Manna, *Nano Lett.*, 2022, **22**, 8567–8573.

156 A. Noculak, V. Morad, K. M. McCall, S. Yakunin, Y. Shynkarenko, M. Wörle and M. V Kovalenko, *Chem. Mater.*, 2020, **32**, 5118–5124.

157 J. Luo, X. Wang, S. Li, J. Liu, Y. Guo, G. Niu, L. Yao, Y. Fu, L. Gao, Q. Dong, C. Zhao, M. Leng, F. Ma, W. Liang, L. Wang, S. Jin, J. Han, L. Zhang, J. Etheridge, J. Wang, Y. Yan, E. H. Sargent and J. Tang, *Nature*, 2018, **563**, 541–545.

158 J. Zhou, X. Rong, P. Zhang, M. S. Molokeev, P. Wei, Q. Liu, X. Zhang and Z. Xia, *Adv. Opt. Mater.*, 2019, **7**, 1801435.

159 Q. Fan, G. V Biesold-McGee, J. Ma, Q. Xu, S. Pan, J. Peng and Z. Lin, *Angew. Chemie Int. Ed.*, 2020, **59**, 1030–1046.

160 S. Ghosh, H. Shankar and P. Kar, *Mater. Adv.*, 2022, **3**, 3742–3765.

161 F. Locardi, M. Cirignano, D. Baranov, Z. Dang, M. Prato, F. Drago, M. Ferretti, V. Pinchetti, M. Fanciulli, S. Brovelli, L. De Trizio and L. Manna, *J. Am. Chem. Soc.*, 2018, **140**, 12989–12995.

162 Y. Liu, Y. Jing, J. Zhao, Q. Liu and Z. Xia, *Chem. Mater.*, 2019, **31**, 3333–3339.

163 J. Nie, H. Li, S. Fang, B. Zhou, Z. Liu, F. Chen, Y. Wang and Y. Shi, *Cell Reports Phys. Sci.*, 2022, **3**, 100820.

164 F. Locardi, E. Sartori, J. Buha, J. Zito, M. Prato, V. Pinchetti, M. L. Zaffalon, M. Ferretti, S. Brovelli, I. Infante, L. De Trizio and L. Manna, *ACS Energy Lett.*, 2019, **4**, 1976–1982.

165 S. Li, Q. Hu, J. Luo, T. Jin, J. Liu, J. Li, Z. Tan, Y. Han, Z. Zheng, T. Zhai, H. Song, L. Gao, G. Niu and J. Tang, *Adv. Opt. Mater.*, 2019, **7**, 1901098.

166 N. S. M. Viswanath and W. Bin Im, *ACS Appl. Opt. Mater.*, 2025, **3**, 578–600.

167 T. Li, X. Zhao, D. Yang, M.-H. Du and L. Zhang, *Phys. Rev. Appl.*, 2018, **10**, 41001.

168 C. Freysoldt, B. Grabowski, T. Hickel, J. Neugebauer, G. Kresse, A. Janotti and C. G. de Walle, *Rev. Mod. Phys.*, 2014, **86**, 253–305.

169 J. M. Thomas, *Nature*, 2012, **491**, 186–187.

170 W. L. Tan and C. R. McNeill, *Appl. Phys. Rev.*, 2022, **9**, 21310.

171 D. Attwood, *Soft X-Rays and Extreme Ultraviolet Radiation: Principles and Applications*, Cambridge University Press, Cambridge, 1999.

172 J. Schwinger, *Phys. Rev.*, 1949, **75**, 1912–1925.

173 E. Mitchell, P. Kuhn and E. Garman, *Structure*, 1999, **7**, R111–R121.

174 ESRF, https://www.esrf.fr/home/UsersAndScience/Publications/Highlights/esrf-highlights-2024.html.

175 Carlo Lamberti and Jeroen A. van Bokhoven, *X-Ray Absorption and X-Ray Emission Spectroscopy*, 1st editio., 2016.

176 P. Bruno, J.-C. Biasci, C. Detlefs, R. Dimper, M. Krisch, G. Martínez-Criado, M. Mezouar, C. Nevo, Q. Qin, P. Raimondi, H. Reichert, F. Sette, J. Susini, P. Tafforeau and C. Yildirim, *Eur. Phys. J. Plus*, 2024, **139**, 928.

177 P. Cloetens, J. Daillant, C. Detlefs, J. Drnec, J. Frey, J.-A. Hernandez, V. Honkimaki, M. Krisch, G. Martínez-Criado, J. McCarthy, M. Mezouar, M. Di Michiel, E. Mitchell, A. Pacureanu, Q. Qin, D. de Sanctis, F. Sette, P. Tafforeau, R. Torchio, Y. Watier, J. Wright and C. Yildirim, *Synchrotron Radiat. News*, 2025, **38**,

4–9.

178 Bunker and Grant, *Introduction to XAFS: A Practical Guide to X-ray Absorption Fine Structure Spectroscopy*, Cambridge University Press, 2010.

179 J. E. Penner-Hahn, *Compr. Coord. Chem. II*, 2003, **2**, 159–186.

180 M. Newville, *Rev. Mineral. Geochemistry*, 2014, **78**, 33–74.

181 S. Virga, G. Arrabito, V. Ferrara, M. Scopelliti, A. Longo, B. Pignataro and F. Giannici, *J. Mater. Chem. C*, 2024, **12**, 12951–12961.

182 S. Virga, A. Longo, C. Pipitone and F. Giannici, *J. Phys. Chem. C*, 2023, **127**, 18058–18066.

183 C. Pipitone, S. Carlotto, M. Casarin, A. Longo, A. Martorana and F. Giannici, *J. Mater. Chem. C*, 2022, **10**, 1458–1469.

184 M. Rovezzi and P. Glatzel, *Semicond. Sci. Technol.*, 2014, **29**, 23002.

185 H. Asakura and T. Tanaka, *Chem. Lett.*, 2021, **50**, 1075–1085.

186 G. N. George and S. DeBeer, *Synchrotron Radiat. News*, 2025, **38**, 55–57.

187 F. M. F. de Groot, M. H. Krisch and J. Vogel, *Phys. Rev. B*, 2002, **66**, 195112.

188 S. Lafuerza, M. Retegan, B. Detlefs, R. Chatterjee, V. Yachandra, J. Yano and P. Glatzel, *Nanoscale*, 2020, **12**, 16270–16284.

189 P. Glatzel, E. Biasin, O. Filimonova and V. Marchuk, *Synchrotron Radiat. News*, 2025, **38**, 25–30.

190 B. Ravel and M. Newville, *J. Synchrotron Radiat.*, 2005, **12**, 537–541.

191 V. A. Solé, E. Papillon, M. Cotte, P. Walter and J. Susini, *Spectrochim. Acta Part B At. Spectrosc.*, 2007, **62**, 63–68.

192 K. V Klementev, *J. Phys. D. Appl. Phys.*, 2001, **34**, 209.

193 J. J. Rehr, J. J. Kas, F. D. Vila, M. P. Prange and K. Jorissen, *Phys. Chem. Chem. Phys.*, 2010, **12**, 5503–5513.

194 M. Rovezzi, A. Harris, B. Detlefs, T. Bohdan, A. Svyazhin, A. Santambrogio, D. Degler, R. Baran, B. Reynier, P. Noguera Crespo, C. Heyman, H.-P. Van Der Kleij, P. Van Vaerenbergh, P. Marion, H. Vitoux, C. Lapras, R. Verbeni, M. M. Kocsis, A.

Manceau and P. Glatzel, *J. Synchrotron Radiat.*, 2020, **27**, 813–826.

195 E. J. Jaeschke, S. Khan, J. R. Schneider and J. B. Hastings, *Synchrotron Light Sources and Free-Electron Lasers: Accelerator Physics, Instrumentation and Science Applications*, Springer Cham, 2016.

196 M. I. Saidaminov, I. Spanopoulos, J. Abed, W. Ke, J. Wicks, M. G. Kanatzidis and E. H. Sargent, *ACS Energy Lett.*, 2020, **5**, 1153–1155.

197 O. Bunău, A. Y. Ramos and Y. Joly, in *International Tables for Crystallography*, 2021, pp. 752–757.

198 O. Bunău and Y. Joly, *J. Phys. Condens. Matter*, 2009, **21**, 345501.

199 Y. Joly, *Phys. Rev. B*, 2001, **63**, 125120.

200 Y. Joly, A. Y. Ramos and O. Bunău, in *International Tables for Crystallography*, 2023, pp. 114–120.

201 F. Zhang and K. Zhu, *Adv. Energy Mater.*, 2020, **10**, 1902579.

202 C. Pipitone, F. Giannici, A. Martorana, G. García-Espejo, S. Carlotto, M. Casarin, A. Guagliardi and N. Masciocchi, *J. Phys. Chem. C*, 2021, **125**, 11728–11742.

203 M. Simenas, A. Gagor, J. Banys and M. Maczka, *Chem. Rev.*, 2024, **124**, 2281–2326.

204 L. N. Quan, M. Yuan, R. Comin, O. Voznyy, E. M. Beauregard, S. Hoogland, A. Buin, A. R. Kirmani, K. Zhao, A. Amassian, D. H. Kim and E. H. Sargent, *J. Am. Chem. Soc.*, 2016, **138**, 2649–2655.

205 D. S. Lee, J. S. Yun, J. Kim, A. M. Soufiani, S. Chen, Y. Cho, X. Deng, J. Seidel, S. Lim, S. Huang and A. W. Y. Ho-Baillie, *ACS Energy Lett.*, 2018, **3**, 647–654.

206 T. Niu, J. Lu, M.-C. Tang, D. Barrit, D.-M. Smilgies, Z. Yang, J. Li, Y. Fan, T. Luo, I. McCulloch, A. Amassian, S. (Frank) Liu and K. Zhao, *Energy Environ. Sci.*, 2018, **11**, 3358–3366.

207 D. Bi, P. Gao, R. Scopelliti, E. Oveisi, J. Luo, M. Grätzel, A. Hagfeldt and M. K. Nazeeruddin, *Adv. Mater.*, 2016, **28**, 2910–2915.

208 Y. Zhang, G. Grancini, Z. Fei, E. Shirzadi, X. Liu, E. Oveisi, F. F. Tirani, R. Scopelliti, Y. Feng, M. K. Nazeeruddin and P. J. Dyson, *Nano Energy*, 2019, **58**,

105–111.

209 F. Xu, M. Zhang, Z. Li, X. Yang and R. Zhu, *Adv. Energy Mater.*, 2023, **2203911**, 1–14.

210 Y. Tong, A. Najar, L. Wang, L. Liu, M. Du, J. Yang, J. Li, K. Wang and S. Liu, *Adv. Sci.*, 2022, **9**, 1–20.

211 C. Pipitone, S. Boldrini, A. Ferrario, G. Garcìa-Espejo, A. Guagliardi, N. Masciocchi, A. Martorana and F. Giannici, *Appl. Phys. Lett.*, 2021, **119**, 101104.

212 A. Gorczyca, V. Moizan, C. Chizallet, O. Proux, W. Del Net, E. Lahera, J.-L. Hazemann, P. Raybaud and Y. Joly, *Angew. Chemie Int. Ed.*, 2014, **53**, 12426–12429.

213 B. H. Toby and R. B. Von Dreele, *J. Appl. Crystallogr.*, 2013, **46**, 544–549.

214 P. Umari, E. Mosconi and F. De Angelis, *Sci. Rep.*, 2014, **4**, 4467.

215 C. Bernal and K. Yang, *J. Phys. Chem. C*, 2014, **118**, 24383–24388.

216 Z.-Q. Ma, H. Pan and P. K. Wong, *J. Electron. Mater.*, 2016, **45**, 5956–5966.

217 T. Shi, H.-S. Zhang, W. Meng, Q. Teng, M. Liu, X. Yang, Y. Yan, H.-L. Yip and Y.-J. Zhao, *J. Mater. Chem. A*, 2017, **5**, 15124–15129.

218 L. Huang and W. R. L. Lambrecht, *Phys. Rev. B*, 2013, **88**, 165203.

219 F. Hao, C. C. Stoumpos, D. H. Cao, R. P. H. Chang and M. G. Kanatzidis, *Nat. Photonics*, 2014, **8**, 489–494.

220 N. K. Noel, S. D. Stranks, A. Abate, C. Wehrenfennig, S. Guarnera, A.-A. Haghighirad, A. Sadhanala, G. E. Eperon, S. K. Pathak, M. B. Johnston, A. Petrozza, L. M. Herz and H. J. Snaith, *Energy Environ. Sci.*, 2014, **7**, 3061–3068.

221 T. M. Koh, T. Krishnamoorthy, N. Yantara, C. Shi, W. L. Leong, P. P. Boix, A. C. Grimsdale, S. G. Mhaisalkar and N. Mathews, *J. Mater. Chem. A*, 2015, **3**, 14996–15000.

222 F. Gu, S. Ye, Z. Zhao, H. Rao, Z. Liu, Z. Bian and C. Huang, *Sol. RRL*, 2018, **2**, 1800136.

223 S. J. Lee, S. S. Shin, Y. C. Kim, D. Kim, T. K. Ahn, J. H. Noh, J. Seo and S. Il Seok, *J. Am. Chem. Soc.*, 2016, **138**, 3974–3977.

224 J. Cao, Q. Tai, P. You, G. Tang, T. Wang, N. Wang and F. Yan, *J. Mater. Chem. A*, 2019, **7**, 26580–26585.

225 F. Li, H. Fan, J. Zhang, J.-H. Huang, P. Wang, C. Gao, L.-M. Yang, Z. Zhu, A. K.-Y. Jen, Y. Song and K.-J. Jiang, *Sol. RRL*, 2019, **3**, 1900285.

226 C. Wang, F. Gu, Z. Zhao, H. Rao, Y. Qiu, Z. Cai, G. Zhan, X. Li, B. Sun, X. Yu, B. Zhao, Z. Liu, Z. Bian and C. Huang, *Adv. Mater.*, 2020, **32**, 1907623.

227 T. Wu, X. Liu, X. He, Y. Wang, X. Meng, T. Noda, X. Yang and L. Han, *Sci. China Chem.*, 2020, **63**, 107–115.

228 G. Liu, C. Liu, Z. Lin, J. Yang, Z. Huang, L. Tan and Y. Chen, *ACS Appl. Mater. Interfaces*, 2020, **12**, 14049–14056.

229 X. Meng, J. Lin, X. Liu, X. He, Y. Wang, T. Noda, T. Wu, X. Yang and L. Han, *Adv. Mater.*, 2019, **31**, 1903721.

230 Z. Chen, J. J. Wang, Y. Ren, C. Yu and K. Shum, *Appl. Phys. Lett.*, 2012, **101**, 93901.

231 M. Budimir, D. Damjanovic and N. Setter, *Phys. Rev. B*, 2006, **73**, 174106.

232 M. H. Lee, D. J. Kim, J. S. Park, S. W. Kim, T. K. Song, M.-H. Kim, W.-J. Kim, D. Do and I.-K. Jeong, *Adv. Mater.*, 2015, **27**, 6976–6982.

233 Y. Kuroiwa, S. Kim, I. Fujii, S. Ueno, Y. Nakahira, C. Moriyoshi, Y. Sato and S. Wada, *Commun. Mater.*, 2020, **1**, 71.

234 H. Park, C. Ha and J.-H. Lee, *J. Mater. Chem. A*, 2020, **8**, 24353–24367.

235 M. Coll, A. Gomez, E. Mas-Marza, O. Almora, G. Garcia-Belmonte, M. Campoy-Quiles and J. Bisquert, *J. Phys. Chem. Lett.*, 2015, **6**, 1408–1413.

236 D. Bin Kim, K. H. Park and Y. S. Cho, *Energy Environ. Sci.*, 2020, **13**, 2077–2086.

237 X.-G. Chen, X.-J. Song, Z.-X. Zhang, P.-F. Li, J.-Z. Ge, Y.-Y. Tang, J.-X. Gao, W.-Y. Zhang, D.-W. Fu, Y.-M. You and R.-G. Xiong, *J. Am. Chem. Soc.*, 2020, **142**, 1077–1082.

238 H. Zhang, X. Fu, Y. Tang, H. Wang, C. Zhang, W. W. Yu, X. Wang, Y. Zhang and M. Xiao, *Nat. Commun.*, 2019, **10**, 1088.

239 C. Pipitone, F. Ursi, F. Giannici, A. Longo, A. Guagliardi, N. Masciocchi and A.

Martorana, *Nanotechnology*, 2022, **33**, 425703.

240 Ş. Süzer, *Appl. Spectrosc.*, 2000, **54**, 1716–1718.

241 H. Zhao, K. Chordiya, P. Leukkunen, A. Popov, M. Upadhyay Kahaly, K. Kordas and S. Ojala, *Nano Res.*, 2021, **14**, 1116–1125.

242 S. Chatterjee, J. Payne, J. T. S. Irvine and A. J. Pal, *J. Mater. Chem. A*, 2020, **8**, 4416–4427.

243 X. Shi, S. Liu, Y. Sun, J. Liang and Y. Chen, *Adv. Funct. Mater.*, 2018, **28**, 1800850.

244 H. Wang, J. Liu, H. Cui, Y. Liu, J. Zhu, H. Wang, G. Song, Z. Li and D. Chen, *ACS Appl. Electron. Mater.*, 2021, **3**, 1758–1770.

245 J. Soares Costa, M. Prestat, B. Tribollet, B. Lescop, S. Rioual, L. Holzer and D. Thierry, *ChemElectroChem*, 2020, **7**, 2055–2064.

246 X.-W. Zhang, Y. Pan, Q. Zheng and X.-S. Yi, *J. Polym. Sci. Part B Polym. Phys.*, 2000, **38**, 2739–2749.

247 D. Nečas and P. Klapetek, *Open Phys.*, 2012, **10**, 181–188.

248 B. Yang, J. Chen, S. Yang, F. Hong, L. Sun, P. Han, T. Pullerits, W. Deng and K. Han, *Angew. Chemie Int. Ed.*, 2018, **57**, 5359–5363.

249 Q. Liao, J. Chen, L. Zhou, T. Wei, L. Zhang, D. Chen, F. Huang, Q. Pang and J. Z. Zhang, *J. Phys. Chem. Lett.*, 2020, **11**, 8392–8398.

250 Q. Hu, G. Niu, Z. Zheng, S. Li, Y. Zhang, H. Song, T. Zhai and J. Tang, *Small*, 2019, **15**, 1903496.

251 Z. Rao, X. Zhao and X. Gong, *Adv. Funct. Mater.*, 2024, **34**, 2406424.

252 X. Li, D. Wang, Y. Zhong, F. Jiang, D. Zhao, S. Sun, P. Lu, M. Lu, Z. Wang, Z. Wu, Y. Gao, Y. Zhang, W. W. Yu and X. Bai, *Adv. Sci.*, 2023, **10**, 2207571.

253 T. Cai, W. Shi, S. Hwang, K. Kobbekaduwa, Y. Nagaoka, H. Yang, K. Hills-Kimball, H. Zhu, J. Wang, Z. Wang, Y. Liu, D. Su, J. Gao and O. Chen, *J. Am. Chem. Soc.*, 2020, **142**, 11927–11936.

254 Y. Wang, C. Wang, L. Men, Q. Hu and J. Xiao, *Inorg. Chem.*, 2024, **63**, 5734–5742.

255 Y. Wang, Y. Ji, Y. Yang, Z. Chen, H. Sun, X. Wang, Z. Zou and H. Huang, *ACS Energy Lett.*, 2024, **9**, 336–345.

256 Z. Liu, H. Yang, J. Wang, Y. Yuan, K. Hills-Kimball, T. Cai, P. Wang, A. Tang and O. Chen, *Nano Lett.*, 2021, **21**, 1620–1627.

257 M. G. Goesten and R. Hoffmann, *J. Am. Chem. Soc.*, 2018, **140**, 12996–13010.

258 A. H. Slavney, B. A. Connor, L. Leppert and H. I. Karunadasa, *Chem. Sci.*, 2019, **10**, 11041–11053.

259 A. H. Slavney, L. Leppert, A. Saldivar Valdes, D. Bartesaghi, T. J. Savenije, J. B. Neaton and H. I. Karunadasa, *Angew. Chemie Int. Ed.*, 2018, **57**, 12765–12770.

260 W. Meng, X. Wang, Z. Xiao, J. Wang, D. B. Mitzi and Y. Yan, *J. Phys. Chem. Lett.*, 2017, **8**, 2999–3007.

261 J. Xu, J.-B. Liu, B.-X. Liu, J. Wang and B. Huang, *Adv. Funct. Mater.*, 2019, **29**, 1805870.

262 K. P. Lindquist, S. A. Mack, A. H. Slavney, L. Leppert, A. Gold-Parker, J. F. Stebbins, A. Salleo, M. F. Toney, J. B. Neaton and H. I. Karunadasa, *Chem. Sci.*, 2019, **10**, 10620–10628.

263 N. N. K. and A. Nag, *Chem. Commun.*, 2018, **54**, 5205–5208.

264 B. F. Aull and H. P. Jenssen, *Phys. Rev. B*, 1986, **34**, 6647–6655.

265 A. H. Slavney, L. Leppert, D. Bartesaghi, A. Gold-Parker, M. F. Toney, T. J. Savenije, J. B. Neaton and H. I. Karunadasa, *J. Am. Chem. Soc.*, 2017, **139**, 5015–5018.

266 A. Karmakar, M. S. Dodd, S. Agnihotri, E. Ravera and V. K. Michaelis, *Chem. Mater.*, 2018, **30**, 8280–8290.

267 J. D. Majher, M. B. Gray, T. A. Strom and P. M. Woodward, *Chem. Mater.*, 2019, **31**, 1738–1744.

268 K. Du, W. Meng, X. Wang, Y. Yan and D. B. Mitzi, *Angew. Chemie Int. Ed.*, 2017, **56**, 8158–8162.

269 H. Chen, S. Ming, M. Li, B. Wang and J. Su, *J. Phys. Chem. C*, 2021, **125**, 11271–11277.

270 L. Schade, S. Mahesh, G. Volonakis, M. Zacharias, B. Wenger, F. Schmidt, S. V. Kesava, D. Prabhakaran, M. Abdi-Jalebi, M. Lenz, F. Giustino, G. Longo, P. G. Radaelli and H. J. Snaith, *ACS Energy Lett.*, 2021, **6**, 1073–1081.

271 M. V Kovalenko, L. Protesescu and M. I. Bodnarchuk, *Science*, 2017, **358**, 745–750.

272 D. Chen and X. Chen, *J. Mater. Chem. C*, 2019, **7**, 1413–1446.

273 I. López-Fernández, D. Valli, C.-Y. Wang, S. Samanta, T. Okamoto, Y.-T. Huang, K. Sun, Y. Liu, V. S. Chirvony, A. Patra, J. Zito, L. De Trizio, D. Gaur, H.-T. Sun, Z. Xia, X. Li, H. Zeng, I. Mora-Seró, N. Pradhan, J. P. Martínez-Pastor, P. Müller-Buschbaum, V. Biju, T. Debnath, M. Saliba, E. Debroye, R. L. Z. Hoye, I. Infante, L. Manna and L. Polavarapu, *Adv. Funct. Mater.*, 2024, **34**, 2307896.

274 N. Fiuza-Maneiro, K. Sun, I. López-Fernández, S. Gómez-Graña, P. Müller-Buschbaum and L. Polavarapu, *ACS Energy Lett.*, 2023, **8**, 1152–1191.

275 C. Otero-Martínez, D. García-Lojo, I. Pastoriza-Santos, J. Pérez-Juste and L. Polavarapu, *Angew. Chemie Int. Ed.*, 2021, **60**, 26677–26684.

276 H. Huang, L. Polavarapu, J. A. Sichert, A. S. Susha, A. S. Urban and A. L. Rogach, *NPG Asia Mater.*, 2016, **8**, e328–e328.

277 L. Polavarapu, B. Nickel, J. Feldmann and A. S. Urban, *Adv. Energy Mater.*, 2017, **7**, 1700267.

278 S. Krishnamurthy, P. Pandey, J. Kaur, S. Chakraborty, P. K. Nayak, A. Sadhanala and S. Ogale, *J. Phys. D. Appl. Phys.*, 2021, **54**, 133002.

279 L. Protesescu, S. Yakunin, M. I. Bodnarchuk, F. Krieg, R. Caputo, C. H. Hendon, R. X. Yang, A. Walsh and M. V Kovalenko, *Nano Lett.*, 2015, **15**, 3692–3696.

280 Y. Tong, E. Bladt, M. F. Aygüler, A. Manzi, K. Z. Milowska, V. A. Hintermayr, P. Docampo, S. Bals, A. S. Urban, L. Polavarapu and J. Feldmann, *Angew. Chemie Int. Ed.*, 2016, **55**, 13887–13892.

281 X. Li, Y. Wu, S. Zhang, B. Cai, Y. Gu, J. Song and H. Zeng, *Adv. Funct. Mater.*, 2016, **26**, 2435–2445.

282 H. Huang, Y. Li, Y. Tong, E.-P. Yao, M. W. Feil, A. F. Richter, M. Döblinger, A. L. Rogach, J. Feldmann and L. Polavarapu, *Angew. Chemie Int. Ed.*, 2019, **58**, 16558–

16562.

283 G. Almeida, L. Goldoni, Q. Akkerman, Z. Dang, A. H. Khan, S. Marras, I. Moreels and L. Manna, *ACS Nano*, 2018, **12**, 1704–1711.

284 Y. Zhang, T. D. Siegler, C. J. Thomas, M. K. Abney, T. Shah, A. De Gorostiza, R. M. Greene and B. A. Korgel, *Chem. Mater.*, 2020, **32**, 5410–5423.

285 C. Giansante and I. Infante, *J. Phys. Chem. Lett.*, 2017, **8**, 5209–5215.

286 I. du Fossé, S. ten Brinck, I. Infante and A. J. Houtepen, *Chem. Mater.*, 2019, **31**, 4575–4583.

287 Y. Bekenstein, J. C. Dahl, J. Huang, W. T. Osowiecki, J. K. Swabeck, E. M. Chan, P. Yang and A. P. Alivisatos, *Nano Lett.*, 2018, **18**, 3502–3508.

288 L. Zhou, Y.-F. Xu, B.-X. Chen, D.-B. Kuang and C.-Y. Su, *Small*, 2018, **14**, 1703762.

289 S. E. Creutz, E. N. Crites, M. C. De Siena and D. R. Gamelin, *Nano Lett.*, 2018, **18**, 1118–1123.

290 O. Vybornyi, S. Yakunin and M. V Kovalenko, *Nanoscale*, 2016, **8**, 6278–6283.

291 S. Wei, Y. Yang, X. Kang, L. Wang, L. Huang and D. Pan, *Chem. Commun.*, 2016, **52**, 7265–7268.

292 J. Shamsi, P. Rastogi, V. Caligiuri, A. L. Abdelhady, D. Spirito, L. Manna and R. Krahne, *ACS Nano*, 2017, **11**, 10206–10213.

293 M.-M. Yao, L. Wang, J.-S. Yao, K.-H. Wang, C. Chen, B.-S. Zhu, J.-N. Yang, J.-J. Wang, W.-P. Xu, Q. Zhang and H.-B. Yao, *Adv. Opt. Mater.*, 2020, **8**, 1901919.

294 R. Shannon, *Acta Cryst*, 1976, **32**, 751–767.

295 L. R. Morrs and W. R. Robinson, *Acta Crystallogr. Sect. B*, 1972, **28**, 653–654.

296 B. A. Connor, L. Leppert, M. D. Smith, J. B. Neaton and H. I. Karunadasa, *J. Am. Chem. Soc.*, 2018, **140**, 5235–5240.

297 Y. Cai, W. Xie, Y. T. Teng, P. C. Harikesh, B. Ghosh, P. Huck, K. A. Persson, N. Mathews, S. G. Mhaisalkar, M. Sherburne and M. Asta, *Chem. Mater.*, 2019, **31**, 5392–5401.

298 F. He, Y. Wang, T. Debnath, M. Döblinger, Q. A. Akkerman, J. Feldmann and A. Dey, *Adv. Opt. Mater.*, 2024, **12**, 2302898.

299 B. Yang, X. Mao, F. Hong, W. Meng, Y. Tang, X. Xia, S. Yang, W. Deng and K. Han, *J. Am. Chem. Soc.*, 2018, **140**, 17001–17006.

300 B. Yang, J. Chen, F. Hong, X. Mao, K. Zheng, S. Yang, Y. Li, T. Pullerits, W. Deng and K. Han, *Angew. Chemie Int. Ed.*, 2017, **56**, 12471–12475.

301 A. C. Dakshinamurthy and C. Sudakar, *Appl. Phys. Lett.*, 2021, **118**, 131902.

302 H. Gao, C. Wang, H. Shen, H. Zhou and X. Zhang, *RSC Adv.*, 2024, **14**, 37322–37329.

303 T. Miyamoto, H. Niimi, Y. Kitajima, T. Naito and K. Asakura, *J. Phys. Chem. A*, 2010, **114**, 4093–4098.

304 G. Cibin, A. Mottana, A. Marcelli and M. F. Brigatti, *Mineral. Petrol.*, 2005, **85**, 67–87.

305 C. M. Dutta and H. W. Huang, *Phys. Rev. Lett.*, 1980, **44**, 643–646.

306 T. Glaser, B. Hedman, K. O. Hodgson and E. I. Solomon, *Acc. Chem. Res.*, 2000, **33**, 859–868.

307 M. W. Löble, J. M. Keith, A. B. Altman, S. C. E. Stieber, E. R. Batista, K. S. Boland, S. D. Conradson, D. L. Clark, J. Lezama Pacheco, S. A. Kozimor, R. L. Martin, S. G. Minasian, A. C. Olson, B. L. Scott, D. K. Shuh, T. Tyliszczak, M. P. Wilkerson and R. A. Zehnder, *J. Am. Chem. Soc.*, 2015, **137**, 2506–2523.

308 S. E. Shadle, J. E. Penner-Hahn, H. J. Schugar, B. Hedman, K. O. Hodgson and E. I. Solomon, *J. Am. Chem. Soc.*, 1993, **115**, 767–776.

309 M. R. Filip, S. Hillman, A. A. Haghighirad, H. J. Snaith and F. Giustino, *J. Phys. Chem. Lett.*, 2016, **7**, 2579–2585.

310 A. M. Abakumov, G. King, V. K. Laurinavichute, M. G. Rozova, P. M. Woodward and E. V Antipov, *Inorg. Chem.*, 2009, **48**, 9336–9344.

311 G. King, A. M. Abakumov, P. M. Woodward, A. Llobet, A. A. Tsirlin, D. Batuk and E. V Antipov, *Inorg. Chem.*, 2011, **50**, 7792–7801.

312 W. Lee, S. Hong and S. Kim, *J. Phys. Chem. C*, 2019, **123**, 2665–2672.

References

313 X. Li, J. Liang, K. R. Adair, J. Li, W. Li, F. Zhao, Y. Hu, T.-K. Sham, L. Zhang, S. Zhao, S. Lu, H. Huang, R. Li, N. Chen and X. Sun, *Nano Lett.*, 2020, **20**, 4384–4392.

314 M.-O. Figueiredo, T. P. da Silva, D. De Oliveira and D. Rosa, *Minerals*, 2012, **2**, 426–434.

315 S. R. Combs, P. K. Todd, P. Gorai and A. E. Maughan, *J. Electrochem. Soc.*, 2022, **169**, 40551.

316 2005.

317 J. Tauc, R. Grigorovici and A. Vancu, *Phys. status solidi*, 1966, **15**, 627–637.

318 Z. Xiao, K.-Z. Du, W. Meng, D. B. Mitzi and Y. Yan, *Angew. Chemie Int. Ed.*, 2017, **56**, 12107–12111.

319 S. Wang, D. Han, C. Maheu, Z. Xu, A. Biewald, H. Illner, R. Hooijer, T. Mayer, A. Hartschuh, H. Ebert and T. Bein, *APL Mater.*, 2023, **11**, 41110.

320 J. Wen, K. Rong, L. Jiang, C. Wen, B. Wu, B. Sa, Y. Qiu and R. Ahuja, *Nano Energy*, 2024, **128**, 109802.

321 W. Zhou, P. Han, X. Zhang, D. Zheng, S. Yang, Y. Yang, C. Luo, B. Yang, F. Hong, D. Wei, R. Lu and K. Han, *J. Phys. Chem. Lett.*, 2020, **11**, 6463–6467.

322 S. Ding, S. Zhang, Y. Liu, X. Zhang, P. Wang, T. Tang, Z. Wu, Z. Cheng and T. Yang, *Appl. Mater. Today*, 2025, **43**, 102644.

323 A. J. Kale, R. Chaurasiya and A. Dixit, *ACS Appl. Energy Mater.*, 2022, **5**, 10427–10445.

324 S. Adhikari and P. Johari, *Phys. Rev. Mater.*, 2023, **7**, 75401.

325 P. Han and K. Han, *Energy & Fuels*, 2021, **35**, 18871–18887.

326 A. Pasha, A. S and R. G. Balakrishna, *J. Mater. Chem. A*, 2021, **9**, 17701–17719.

327 J. Jiang, Z. Du, H. Fu, W. Li, H. Zhang, H. Xie, J. Zheng and W. Yang, *Adv. Opt. Mater.*, 2024, **12**, 2401347.

328 H. El-assib, M. Alla, S. Tourougui, M. Alla, F. Elfatouaki, S. A. Dar, A. Chauhan, Naima, N. Chawki, N. Shrivastav, V. Manjunath, M. Rouchdi and B. Fares, *Renew. Energy*, 2025, **239**, 122092.

329 A. Pradhan, P. Subudhi and D. Punetha, *J. Power Sources*, 2025, **629**, 235999.

330 P. Giannozzi, O. Andreussi, T. Brumme, O. Bunau, M. Buongiorno Nardelli, M. Calandra, R. Car, C. Cavazzoni, D. Ceresoli, M. Cococcioni, N. Colonna, I. Carnimeo, A. Dal Corso, S. de Gironcoli, P. Delugas, R. A. J. DiStasio, A. Ferretti, A. Floris, G. Fratesi, G. Fugallo, R. Gebauer, U. Gerstmann, F. Giustino, T. Gorni, J. Jia, M. Kawamura, H.-Y. Ko, A. Kokalj, E. Küçükbenli, M. Lazzeri, M. Marsili, N. Marzari, F. Mauri, N. L. Nguyen, H.-V. Nguyen, A. Otero-de-la-Roza, L. Paulatto, S. Poncé, D. Rocca, R. Sabatini, B. Santra, M. Schlipf, A. P. Seitsonen, A. Smogunov, I. Timrov, T. Thonhauser, P. Umari, N. Vast, X. Wu and S. Baroni, *J. Phys. Condens. Matter*, 2017, **29**, 465901.

331 P. Giannozzi, O. Baseggio, P. Bonfà, D. Brunato, R. Car, I. Carnimeo, C. Cavazzoni, S. de Gironcoli, P. Delugas, F. Ferrari Ruffino, A. Ferretti, N. Marzari, I. Timrov, A. Urru and S. Baroni, *J. Chem. Phys.*, 2020, **152**, 154105.

332 P. Giannozzi, S. Baroni, N. Bonini, M. Calandra, R. Car, C. Cavazzoni, D. Ceresoli, G. L. Chiarotti, M. Cococcioni, I. Dabo, A. Dal Corso, S. de Gironcoli, S. Fabris, G. Fratesi, R. Gebauer, U. Gerstmann, C. Gougoussis, A. Kokalj, M. Lazzeri, L. Martin-Samos, N. Marzari, F. Mauri, R. Mazzarello, S. Paolini, A. Pasquarello, L. Paulatto, C. Sbraccia, S. Scandolo, G. Sclauzero, A. P. Seitsonen, A. Smogunov, P. Umari and R. M. Wentzcovitch, *J. Phys. Condens. Matter*, 2009, **21**, 395502.

333 D. Sangalli, A. Ferretti, H. Miranda, C. Attaccalite, I. Marri, E. Cannuccia, P. Melo, M. Marsili, F. Paleari, A. Marrazzo, G. Prandini, P. Bonfà, M. O. Atambo, F. Affinito, M. Palummo, A. Molina-Sánchez, C. Hogan, M. Grüning, D. Varsano and A. Marini, *J. Phys. Condens. Matter*, 2019, **31**, 325902.

334 M. Baranowski and P. Plochocka, *Adv. Energy Mater.*, 2020, **10**, 1903659.

335 P. K. Olshin, O. S. Myasnikova, M. V Kashina, A. O. Gorbunov, N. A. Bogachev, V. O. Kompanets, S. V Chekalin, S. A. Pulkin, V. A. Kochemirovsky, M. Y. Skripkin and A. S. Mereshchenko, *Chem. Phys.*, 2018, **503**, 14–19.

336 Y. Ishimura, Y. Nonaka, Y. Nishida and S. Kida, *Bull. Chem. Soc. Jpn.*, 1973, **46**, 3728–3733.

337 F. Luo, Y. Wu, J. Tong, D. Xu, G. Qin, F. Tian and X. Zhang, *Sci. China Technol. Sci.*, 2023, **66**, 1141–1151.

338 Y.-L. Liu, C.-L. Yang, M.-S. Wang, X.-G. Ma and Y.-G. Yi, *J. Mater. Sci.*, 2019, **54**, 4732–4741.

339 A. Pradhan, M. K. Jena and S. L. Samal, *ACS Appl. Energy Mater.*, 2022, **5**, 6952−6961.

340 M. Nakamura, M. Mikuriya, H. Okawa and S. Kida, *Bull. Chem. Soc. Jpn.*, 1981, **54**, 1825–1829.

341 T. F. Pascher, M. Ončák, C. van der Linde and M. K. Beyer, *Chem. – A Eur. J.*, 2020, **26**, 8286–8295.

342 R. V Singh, M. R. Pai, A. M. Banerjee, C. Nayak, S. Phapale, D. Bhattacharyya and A. K. Tripathi, *J. Therm. Anal. Calorim.*, 2022, **147**, 7063–7076.

343 F. X. Llabrés i Xamena, P. Fisicaro, G. Berlier, A. Zecchina, G. T. Palomino, C. Prestipino, S. Bordiga, E. Giamello and C. Lamberti, *J. Phys. Chem. B*, 2003, **107**, 7036–7044.

344 R. Kaiukov, G. Almeida, S. Marras, Z. Dang, D. Baranov, U. Petralanda, I. Infante, E. Mugnaioli, A. Griesi, L. De Trizio, M. Gemmi and L. Manna, *Inorg. Chem.*, 2020, **59**, 548–554.

345 T. Fujimori, Y. Tanino, M. Takaoka and S. Morisawa, *Anal. Sci.*, 2010, **26**, 1119–1125.

346 K. Momma and F. Izumi, *J. Appl. Crystallogr. - J APPL CRYST*, 2008, **41**, 653–658.

347 H. Yamatera and K. Nakatsu, *Bull. Chem. Soc. Jpn.*, 1954, **27**, 244.

348 K. Kihara and T. Sudo, *Acta Crystallogr. Sect. B*, 1974, **30**, 1088–1093.

349 B. Morosin and E. C. Lingafelter, *J. Phys. Chem.*, 1961, **65**, 50–51.

350 B. Yildirim and J. M. Cole, *J. Chem. Inf. Model.*, 2021, **61**, 1136–1149.

351 G. Kresse and D. Joubert, *Phys. Rev. B*, 1999, **59**, 1758–1775.

352 J. P. Perdew, K. Burke and M. Ernzerhof, *Phys. Rev. Lett.*, 1996, **77**, 3865–3868.

353 A. Marini, C. Hogan, M. Grüning and D. Varsano, *Comput. Phys. Commun.*, 2009, **180**, 1392–1403.

354 J. P. Perdew, A. Ruzsinszky, G. I. Csonka, O. A. Vydrov, G. E. Scuseria, L. A.

Constantin, X. Zhou and K. Burke, *Phys. Rev. Lett.*, 2008, **100**, 1–4.

355 D. A. Leon, A. Ferretti, D. Varsano, E. Molinari and C. Cardoso, *Phys. Rev. B*, 2023, **107**, 155130.

356 H. Jiang, R. I. Gomez-Abal, P. Rinke and M. Scheffler, *Phys. Rev. B*, 2010, **82**, 45108.

357 W. Gao, W. Xia, Y. Wu, W. Ren, X. Gao and P. Zhang, *Phys. Rev. B*, 2018, **98**, 45108.